Biomarkers of motor network excitability in amyotrophic lateral sclerosis

Evan Cyril Edmond

Green Templeton College
University of Oxford

A thesis submitted for the degree of Doctor of Philosophy

Trinity 2022

Abstract

Increased cortical excitability, associated with brain motor network alterations, has been consistently implicated in the pathology of amyotrophic lateral sclerosis (ALS). This thesis considers the application of multi-modal magnetic resonance imaging (MRI) to explore motor network excitability in ALS.

Chapter 3 describes a novel functional MRI (fMRI) study measuring motor task associated cortical activation and between-region functional connectivity in ALS. This showed hyper-activation in non-motor regions in rapidly progressive ALS. I also showed brain motor network connectivity remodelling linked to measures of functional decline across all ALS patients.

Chapter 4 describes a novel magnetic resonance spectroscopic imaging (MRSI) technique that quantifies neurochemical excitatory and inhibitory 'tone' with fine spatial resolution. I validated this technique in a cohort of healthy adults to describe physiological variation in excitability 'set-points' between motor regions and hemispheres, age-associated changes, and the relationship between excitability and motor network connectivity.

Chapter 5 applies the same MRSI technique to a cohort including ALS patients and presymptomatic carriers of the ALS-causing *C9orf72*-HRE mutation. I found altered excitatory and inhibitory tone in both ALS and *C9orf72*-HRE carriers, a novel finding with a notably lateralised pattern between the hemispheres. A disinhibited 'hot-spot' in the left motor hand area may precede disease in *C9orf72*-HRE carriers.

Chapter 6 integrates these task-fMRI and MRSI motor network excitability biomarkers using modern data science techniques. This generated a multifactorial marker reflecting changes most prominent in established ALS, as well as a more specific marker of motor cortex activation lateralisation that improved differentiation of presymptomatic individuals.

Motor network excitability alterations in ALS and presymptomatic disease are multifaceted, reflecting an early stage of compensated vulnerability, followed by established neurodegeneration with accompanying functional reorganisation. My findings argue for the inclusion of MRI-based techniques measuring motor network excitability in future translational studies in ALS and presymptomatic disease.

Biomarkers of motor network excitability in amyotrophic lateral sclerosis

Evan Cyril Edmond

Green Templeton College

University of Oxford

A thesis submitted for the degree of

Doctor of Philosophy

Trinity 2022

Acknowledgements

I must acknowledge the Dunhill Medical Trust and the Association of British Neurologists for funding this clinical research training fellowship. I am thankful for the opportunity to work at the Nuffield Department of Clinical Neurosciences and Wellcome Centre for Integrative Neuroimaging.

I am deeply grateful to my two supervisors - Professor Martin Turner and Professor Charlotte Stagg - for their support, inspiration, and patience. Martin's drive, passion, and encyclopaedic knowledge of ALS research are remarkable. Charlie is a warmly dedicated mentor to all, an unflappable leader in a crisis, and an inspiring intellectual. Completing this journey would not have been possible without you.

This work is greatly enriched by the open WIN community. Lunchtime chats were full of camaraderie and had a way of sparking new ideas for exploration. Will Clarke developed *FSL-MRS* from scratch - a staggering achievement. Paul McCarthy and Michiel Cottaar built *fslpy* and *file-tree*, among other projects, to the highest standards of scientific open source. My pull requests were tolerated.

To the Oxford ALS group, thank you for the inspiring and thought provoking discussions - Kevin, Matt, Jakub, Alex, Thanuja, and Emily in particular.

To the PING and wider Neuroplasticity groups - Ioana, Marleen, Bron, Patricia, Justin, Jake, Caro, Emily, Mel, and Alberto in particular - it is a privilege to be surrounded by people of the highest calibre. I look forward to our paths crossing again.

Appa, Mummy, and Eric. You have unconditionally supported every step I took. You patiently and lovingly passed on your knowledge, values and culture. I am forever indebted to you.

Bronwyn - your love and joy brighten the world around you. I am deeply grateful for your enduring support, inspiration, and sacrifice. There could be no better partner for adventures past and still to come.

Abstract

Increased cortical excitability, associated with brain motor network alterations, has been consistently implicated in the pathology of amyotrophic lateral sclerosis (ALS). This thesis considers the application of multi-modal magnetic resonance imaging (MRI) to explore motor network excitability in ALS.

Chapter 3 describes a novel functional MRI (fMRI) study measuring motor task associated cortical activation and between-region functional connectivity in ALS. This showed hyper-activation in non-motor regions in rapidly progressive ALS. I also showed brain motor network connectivity remodelling linked to measures of functional decline across all ALS patients.

Chapter 4 describes a novel magnetic resonance spectroscopic imaging (MRSI) technique that quantifies neurochemical excitatory and inhibitory 'tone' with fine spatial resolution. I validated this technique in a cohort of healthy adults to describe physiological variation in excitability 'set-points' between motor regions and hemispheres, age-associated changes, and the relationship between excitability and motor network connectivity.

Chapter 5 applies the same MRSI technique to a cohort including ALS patients and presymptomatic carriers of the ALS-causing *C9orf72*-HRE mutation. I found altered excitatory and inhibitory tone in both ALS and *C9orf72*-HRE carriers, a novel finding with a notably lateralised pattern between the hemispheres. A disinhibited 'hot-spot' in the left motor hand area may precede disease in *C9orf72*-HRE carriers.

Chapter 6 integrates these task-fMRI and MRSI motor network excitability biomarkers using modern data science techniques. This generated a multifactorial marker reflecting changes most prominent in established ALS, as well as a more specific marker of motor cortex activation lateralisation that improved differentiation of presymptomatic individuals.

Motor network excitability alterations in ALS and presymptomatic disease are multifaceted, reflecting an early stage of compensated vulnerability, followed by established neurodegeneration with accompanying functional reorganisation. My findings argue for the inclusion of MRI-based techniques measuring motor network excitability in future translational studies in ALS and presymptomatic disease.

Data attribution and related work

Some of the work presented in this thesis relates to published or submitted work, or involves novel analyses of existing datasets as follows.

- Sections of Chapter 1 are related to published review articles I have authored.
  - **Edmond EC**, Stagg CJ, Turner MR. Therapeutic non-invasive brain stimulation in amyotrophic lateral sclerosis: rationale, methods and experience. JNNP 2019;90:1131-1138.[1]
  - Dharmadasa T, Scaber J, **Edmond E**, et. al. Genetic testing in motor neurone disease. Practical Neurology 2022;22:107-116.[2]
- The dataset studied in Chapter 3 was acquired by Alexander Thompson, Ricarda Menke, and Malcolm Proudfoot for the BioMOx2 study. I performed a novel analysis of the task-fMRI data.
- The dataset studied in Chapter 4 was pooled, comprising parts (resting baseline conditions) of various datasets acquired by the PING group - Ioana F. Grigoras, Jacob Levenstein, Adam Steel, Caroline Nettekoven, Justin Andrushko, Emily Hinson, Melanie Fleming, and myself.
  - The analysis presented in this thesis has been pre-registered.
    Edmond EC et. al. Magnetic resonance spectroscopic imaging markers of inhibitory and excitatory motor cortical function in healthy individuals and those with ALS. OSF Registries 2021[3,4].
  - I contributed to a functional connectivity analysis in one task dataset, which has been prepared as a preprint[5]. This does not overlap with my thesis.
- The dataset studied in Chapters 5 and 6 was collected by myself - along with Patricia Cambalova and Thanuja Dharmadasa - as part of the Oxford *C9orf72* Cohort study. Other parts of this dataset have been analysed for submitted M.Sc. theses but are not included in this thesis (Patricia Cambalova analysed pilot transcranial magnetic stimulation data, while Daniel Kolsky analysed subcortical structures).

Contents

List of Figures

We are sometimes reproached for conducting incessant studies on the major neurological diseases which have up to now mostly been incurable. What use is it? ... People have questioned whether this is really medicine. ... But can you picture this? "Dear Patient, I am a doctor, it is true, but unfortunately I can do nothing for you, you belong to the category of the rejected with which we do not deal." No, our responsibility is otherwise. Let us keep looking in spite of everything. Let us keep searching. It is indeed the best method of finding, and perhaps thanks to our efforts, the verdict we will give such a patient tomorrow will not be the same we must give [them] today.

— Jean-Martin Charcot *lesson of Feb. 28, 1889, trans. Goetz 1987.*

1 Introduction

Contents

1.1 What is ALS?

This introductory chapter summarises the historic core clinical features of amyotrophic lateral sclerosis (ALS) and the modern discovery of the unifying neuropathological signature (TDP43). ALS now also encompasses a spectrum of cognitive features as well as both monogenic and polygenic risk factors. I will discuss what

magnetic resonance imaging (MRI) has shown us about ALS as a brain network disorder. Finally, I will discuss the research rationale and clinical potential of measuring motor network excitability in ALS patients and ALS-risk gene carriers.

1.1.1 A historic clinicopathological entity

The core clinical syndrome and pathology were described in a seminal lecture by Jean-Martin Charcot in 1874[6], a high point in a frenetic period of neurological discovery in the 19th century. Preceding Charcot, partial syndromes with only lower motor neuron features had been described and named "progressive muscular atrophy" (PMA)[7–9].

Charcot, however, presented a comprehensive account of the disease and gave it its name. He had assembled a case series of patients with "prototypical" clinical features and demonstrated post-mortem neuropathology in **both** spinal cord grey and white matter. This history is remarkable for the richness of the clinical and pathological descriptions of ALS, which remain recognisable and vivid to modern clinicians.

Lower motor neuron features

Lockhart Clarke had reported individual cases recognisable in retrospect as ALS, describing microscopic grey matter atrophy with abnormal cells in the anterior horns of the spinal cord and grossly damaged white matter in the lateral columns[10,11]. The clinical description included characteristic patterns of muscle wasting and weakness - features now considered indicative of lower motor neuron (LMN) dysfunction. The use of electrical stimulation foreshadowed modern application of electromyography (EMG) to demonstrate denervation.

> Her face began to waste and lose expression... weakness of the left hand and arm, as well as the right, and her legs dragged after her. Her voice changed; she did not pronounce words as usual; she never complained of any loss of sensation. ... She was able to shuffle about the house, but could not dress herself. She had almost completely lost the power of moving her left arm; ... The whole of the muscles of the back of the right scapula are apparently gone, and there is very little trace of those

> on the left side. There is a feeble action of each sterno-mastoid under the Faradaic current...[6]

Clarke also described typical examination features such as the pattern of tongue atrophy, speech disturbance, and tongue fasciculations.

> Her deglutition now became difficult... The palate moves little, and more as if blown than as if raised. She does not say ah! but makes a vague noise... The tongue is protruded badly... It is atrophied on each side, and in folds, reminding one of cerebral convolutions. It is also tremulous, and it does not seem to tremble as a whole, but in waves of tremulousness'.[11]

Weakness and wasting as described are the most common initial feature of ALS, focal in onset in 98% of patients[12] and usually spreading to adjacent body regions[13]. In approximately 75% of patients, ALS begins in the limbs, while in most of the rest bulbar muscles of speech and swallowing are the first affected[14] (Figure 1.1). Upper limb onset ALS begins in the dominant hand twice as often as the non-dominant hand[15], but this is not seen with lower limb onset. Respiratory weakness occurs first in a small (∼2%), but important, subgroup[16].

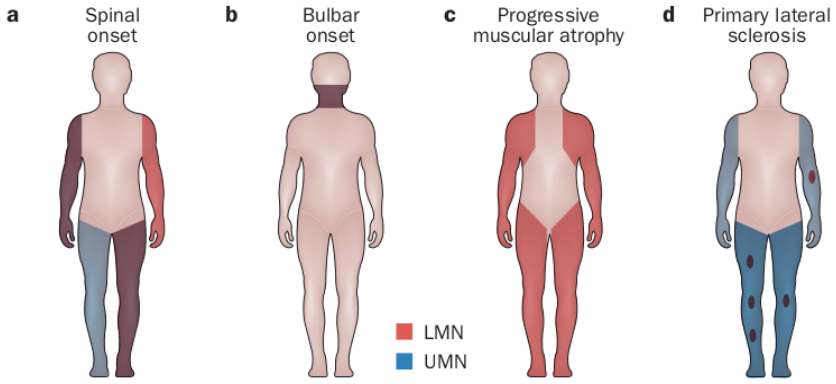

Figure 1.1: Variability in ALS disease onset includes site of onset as well as UMN vs. LMN predominance. Reused with permission from Swinnen, B et al. Nat. Rev. Neurol. 2014.

Upper motor neuron features

Charcot also described signs of upper motor neuron (UMN) dysfunction in ALS, including spasticity and disproportionate weakness not explainable by distal muscle

atrophy. Notably, brisk and pathological reflexes are not part of these descriptions as the examination techniques had not yet been developed.

> a) progressive atrophy invading the muscles; b) fibrillary contractions which are especially seen in the active period of the atrophy; c) the preservation of faradic contractility that the wasted muscles exhibit to the last moment. ... Other symptoms are ... first, motor weakness that occurs early and which, if it does not precede atrophy, at least is strikingly evident when the latter is not yet well-developed ... The extremities, more or less deprived of their natural movements, are usually in lateral sclerosis affected by rigidity at rest, resulting from what is called continual spasmodic contractures.[6]

More generally, upper and lower motor neurone features in ALS exist on a spectrum[17] - patients from either end with predominant UMN or LMN features tend to progress more slowly than those with both (Figure 1.3).

Natural history

Finally, Charcot also reported rapid and inexorable disease progression, and the role of respiratory and bulbar weakness in causing death.

> ... the comparative rapidity of its evolution, from the first symptom to the fatal end. This does not usually extend more than three years ... it is the rule that the four extremities are successively, and within a brief space of time, all stricken with paralysis accompanied by atrophy. ... We regularly find the disease extending to the bulbus, and it is nearly always to the paralysis of the bulbar nerves, more especially of the hypoglossus and pneumogastric, that the phenomena that determine death are to be attributed.[6]

Pooled data from a large repository of clinical trial data[14] for 8635 people with ALS shows mean disease duration of 23 months and mean delay from symptom onset to diagnosis of 11.6 months. While high inter-individual heterogeneity in outcome was seen in ALS patients who were clinically similar at onset, once a rate of functional decline was established, this tended to continue monotonically[18].

The evolution of ALS diagnostic criteria

Modern diagnostic criteria remain focused on clinical features. The 2019 Gold Coast criteria[19] for diagnosis of ALS require the following:

- Progressive motor impairment documented by history or repeated clinical assessment, preceded by normal motor function, and
- Presence of upper and lower motor neuron dysfunction in at least 1 body region, (with upper and lower motor neuron dysfunction noted in the same body region if only one body region is involved) or lower motor neuron dysfunction in at least 2 body regions, and
- Investigations excluding other disease processes

While previous iterations of consensus criteria[20–22] have suggested sub-categorisation based on the number of body regions involved, the 2019 criteria are simplified and return to the central features around which clinical diagnoses of ALS have been made historically.

In this thesis, two iterations of diagnostic criteria are used - contemporaneous with the time of participant recruitment. In Chapter 3 the 2000 revised El Escorial criteria[21] were used, while in the remaining chapters the 2008 Awaji algorithm was used.

Criticisms of the 1994 El Escorial criteria centred around its complexity - involving five sub-categories of "suspected", "possible", "laboratory-supported probable", "probable" and "definite" ALS[20]. While intended to standardise the diagnostic process and homogenise the cohorts recruited into multicenter clinical trials, several criticisms emerged. Initial trials restricting recruitment to "definite" or "probable" categories were challenging to recruit to in early disease[23,24], while more liberal categorisation increases sensitivity while maintaining specificity[25,26]. In head-to-head comparisons of all criteria sets on retrospective data, the largest increase in sensitivity occurs in the move from Awaji to Gold Coast criteria, while revised El Escorial criteria and Awaji perform similarly[26].

This progressed through three categories as “definite”/“probable”/“possible” in the 2000 revised El Escorial criteria to a single category of “ALS” with optional subcategorisation in 2008 Awaji and 2019 Gold Coast criteria. Earlier versions of criteria further resulted in confusion for patients and clinicians alike, where a confident clinical diagnosis of ALS is likely even in those with “possible” ALS[27].

Therefore, in Chapter 3, I included “definite”, “probable”, and “possible” groups according to 2000 revised El Escorial criteria. This represents a similar diagnostic threshold to that used in Chapters 5 and 6 - patients meeting 2008 Awaji criteria for “ALS”[26]. The latest Gold Coast criteria are likely to be similarly specific but more sensitive than the standards I have used - a potential limitation in the translation of my findings to future studies.

1.1.2 The core pathology of ALS

In the modern molecular taxonomy of neurodegeneration, ALS is characterised by a neuropathological signature of TAR DNA-binding protein 43 (TDP43). In ALS, TDP43 is consistently depleted from cell nuclei, mislocalised to the cytoplasm, and forms insoluble aggregates[28,29]. TDP43 binds to the trans-active response element in HIV DNA[30], but also to a wide range of other RNA and DNA targets within the cell nucleus. It is part of a class of heterogeneous nuclear ribonucleoproteins that regulate nuclear transcription and subsequent modifications including splicing. TDP43’s function and protein structure fundamentally shape its role in ALS pathogenesis. Typical distribution and appearances of TDP43 aggregates in the motor cortex are shown in Figure ??.

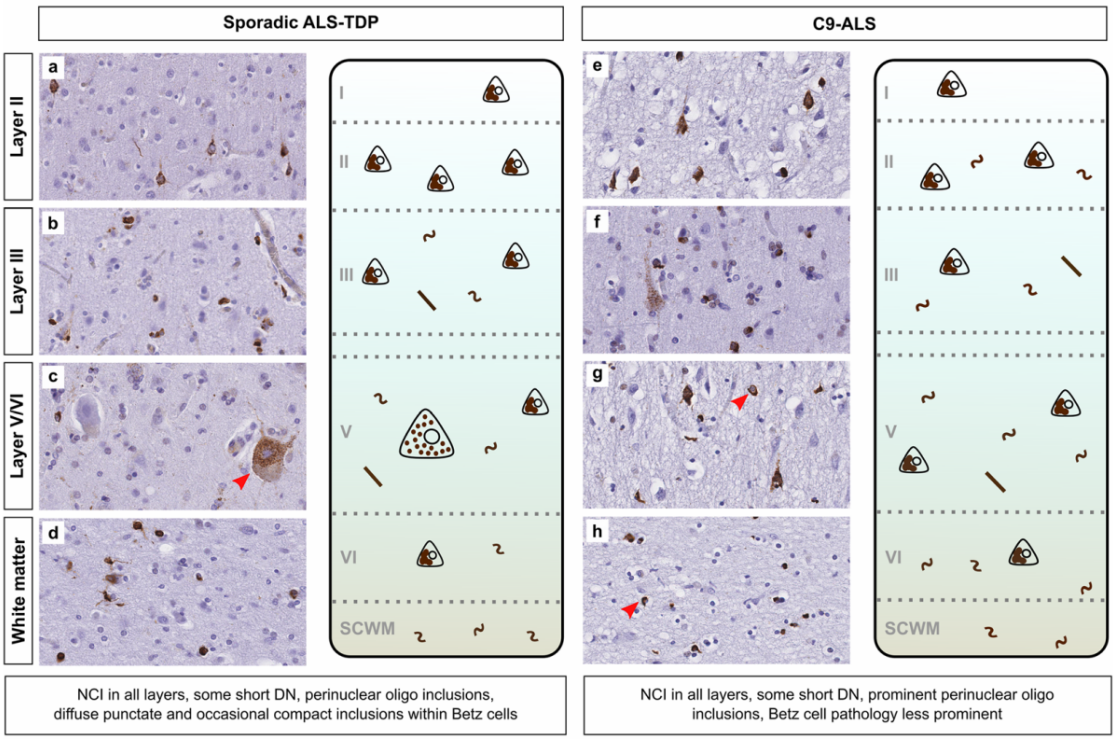

Figure 1.2: Left panel - typical inclusions seen in sporadic ALS. Right panel - typical inclusions seen in genetic ALS associated with *C9orf72* gene mutations (discussed later). NCI - neuronal cytoplasmic inclusions, DN - dystrophic neurites, SCWM - subcortical white matter. Figure reused from Nolan et al. Acta Neuropathologica Communications (2020) 8:98 under the Creative Commons CC BY license.

TDP43 autoregulation and its failure

TDP43 binds to a region in its own transcript, exerting negative feedback over its production[31,32]. The mechanism may be through promotion of unstable splice variants that are degraded within the cell nucleus[33,34]. Directly inhibiting autoregulation using a synthetic antisense oligonucleotide in mice led to increased TDP43 production and production of short fragments of TDP43 that were prone to cytoplasmic aggregation[35]. In a cellular hyperexcitability model using iPSC motor neurons, short fragment TDP43 isoforms lacking autoregulatory function accumulated, mislocalised to the cytoplasm, aggregated, and were neurotoxic[36]. TDP43 is also shown to accumulate in patients with mutations in the autoregulatory domain of the *TARDBP* gene[37].

Impaired nucleocytoplasmic transport

Failure of the normal processes for nuclear localisation of TDP43 may contribute to failure of autoregulation. TDP43 is normally actively shuttled into the nucleus through nuclear pores as cargo attached to karyopherin proteins[38]. Disrupting the TDP43 nuclear localisation signals in animal models can also trigger nuclear depletion, cytoplasmic mislocalisation and neurotoxicity[39]. Intriguingly, restoration of TDP43 nuclear localisation in an inducible mouse model produced functional recovery[40]. This link was originally discovered through siRNA knockdown screens in cellular models, and correlated with reduced expression of the same nuclear transport proteins in post-mortem spinal cord samples in ALS and brain samples in TDP43-associated FTD[41]. The presence of the *C9orf72* G4C2-HRE mutation (discussed in Section 1.1.4) is particularly strongly linked to deficits in nuclear import[42–45]. *C9orf72*-HRE derived dipeptide repeat proteins may initially increase cytosolic TDP43, triggerring further cascading nucleocytoplasmic transport defects[46].

Phase separation and aggregation

Once in the cytoplasm, the structural properties of the TDP43 protein predispose it to interact with the surrounding environment to transition from soluble to liquid, hydrogel or fibrillar aggregate states. At the carboxy- end of the TDP43 protein is a glycine-rich low-complexity domain that is similar to some yeast prion proteins[47][48]. Amino acid sequences within this region tend to form helical[49], low-complexity aromatic-rich kinked[50], and steric zipper[51] structures that may drive phase separation and fibril formation. The toxicity of TDP43 may depend strongly on its phase - within a yeast model, mutational variants that produced liquid-like condensates were most toxic, while aggregated TDP43 was protective[50].

Looking upstream and downstream from TDP43

TDP43 aggregation alone does not fully explain ALS. It occurs as a subset of ALS-related cellular pathology, with mitochondrial dysfunction, autophagy, calcium signalling and other pathways also implicated. Reports of TDP43 pathology in a

subset of patients with clinical Alzheimer's disease have created a new pathological entity - LATE[52]. However, the clinical syndrome of ALS remains strongly linked to TDP43, a common mechanism on which upstream factors converge, and from which downstream degeneration cascades. We still do not understand what originally makes the human motor system selectively vulnerable, and why this should begin in later life. Looking downstream, there is still a mechanistic gap between understanding why individual neurons die and explaining the full range of clinical manifestations of ALS.

1.1.3 The expanding ALS-FTD spectrum

Even before TDP43 was identified as the main constituent, ubiquitinated neuronal inclusions without tau were discovered in the brains of a small minority of patients with frank frontotemporal dementia (FTD) **and** ALS. A series of studies over the last 40 years have further identified more subtle deficits on cognitive battery testing in ALS[53–59]. Despite one negative finding[60], small, stereotyped deficits were generally reported in ∼30% of patients, with a small proportion (∼5%) having more severe impairment across many domains. Executive function, attention and verbal fluency were most commonly affected. Consensus criteria for diagnosis of cognitive impairment in ALS[61] have been developed in response to this previously under-acknowledged manifestation. ALS-specific screening questionnaires for clinic use have also been introduced and validated with the aim that routine cognitive screening will detect cognitive impairment and allow better patient care[62,63]. While subtle, these impairments can impact individual patients through treatment decision-making[64] and caregiver relationships[65], and the impact of behavioural changes may be greater[66].

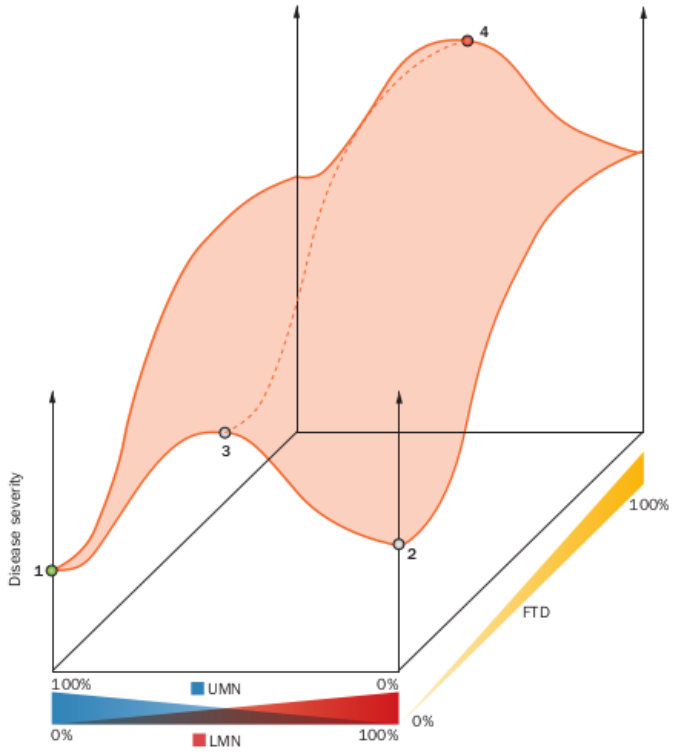

Figure 1.3: ALS phenotype occurs on a multidimensional spectrum, including upper vs. lower motor neurone predominance, and the degree of cognitive involvement. Pure motor phenotypes primary lateral sclerosis (1) and flail-limb (2) presentations have better prognosis than a prototypical ALS presentation (3), while combined ALS-FTD (4) is the most aggressive. Reused with permission from Swinnen, B et al. Nat. Rev. Neurol. 2014.

Outstanding controversy

Debates continue over the precise prevalence, clinical significance, and natural history of cognitive impairment in ALS. A recent multi-centre cross-sectional study reported lower scores for ALS-specific domains (executive, language, letter fluency) in more advanced disease[67]. This contradicts previous data from longitudinal studies suggesting that cognitive function remains stable despite variable rates of motor decline[68,69]. Large longitudinal studies are required to definitively conclude that cognition worsens with disease progression. One cognitive scale has even been proposed as a proxy readout for neuropathology, with potential applicability to clinical trial selection[70] - this could perhaps be validated in future by TDP43-targeted nuclear imaging.

1.1.4 Genetic drivers of ALS

The understanding of genetics in ALS has also expanded dramatically over the last 40 years. In European and North American cohorts, 5 - 10% of ALS is familial (fALS), generally inherited in an autosomal dominant pattern[71,72]. Causative mutations have been identified in 60 - 70% of these cases[73], most prominently in the *C9orf72*, *SOD1*, *TARDBP* and *FUS* genes. Additionally, mutations in these genes are identified in 7 - 10% of patients with sporadic ALS[74–76]. This likely underestimates the full genetic contribution in sporadic ALS - studies using twin or population register data estimate ∼50% heritability[77,78]. The number of genes linked to ALS is increasing over time - the Genomics England panel for ALS[79] (v1.59) includes 40 unique genes as of 2022. The 'hit-rate' of genetic testing in sporadic ALS will depend in practice on the genes tested for, the population tested and on what basis discovered variants are considered causal. As large array-based genetic screens are increasingly performed, figures of up to 21% have been reported[80]. However, this is counterbalanced by the decreasing certainty of causality for some rare mutations, and the designation of some mutations as variants of unknown significance. Such comprehensive/scattershot testing approaches will substratify and splinter the ALS population going forward. Those with clear single gene causes may be selected for targeted gene therapy clinical trials. When multiple or uncertain variants coexist in the same person, specialist genetic counselling and polygenic risk scoring may be required to reason through the clinical implications[2].

ALS genetics has similarly far-reaching implications for research. Two ALS genes in particular encapsulate the strengths and weaknesses of using mutations for modelling or sub-stratifying ALS.

SOD1

The initial discovery of superoxide dismutase 1 (*SOD1*)[81] mutations in fALS had mixed effects on the trajectory of ALS research as a whole. It established the idea that a single gene mutation can be sufficient to cause ALS, and that this

could be targeted by gene therapy[82,83]. However, *SOD1* associated ALS forms a small minority (∼2%) of cases, and is not characterised by TDP43 pathology. The assumption that *SOD1* ALS is broadly representative led to a generation of cellular and animal models that have not yielded therapies for sporadic ALS[84]. Nevertheless, clinical trials targeted at *SOD1*-related mechanisms continue in sporadic ALS[85]. The story of *SOD1* therefore represents a major pitfall in the attempts to generalise findings from genetic ALS to sporadic ALS. It likely comprises separate upstream disease processes that converge on a similar clinical but distinct pathological entity.

C9orf72

In contrast, *C9orf72* associated disease and derived models are more true to ALS as a whole. Its role was initially inferred through family linkage studies[86–88] and genome-wide association studies[89] identifying a chromosome 9 locus associated with ALS and FTD. Most healthy individuals carry 11 repeats or fewer of the GGGGCC hexanucleotide sequence within the first intron of the *C9orf72* gene. This is expanded in patients to more than 30 repeats - commonly hundreds or thousands. *C9orf72* mutations are the single most commonly identified monogenic cause - in 40% of patients with familial ALS and up to 7% with apparently sporadic ALS - though with notable geographic variation[90–94]. TDP43 pathology is present[95,96]. When the neuropathology is compared between sporadic ALS and monogenic forms, the *C9orf72*-HRE is the most similar in terms of overall burden, aggregate morphology and cortical layer specificity[97].

Altogether this makes studying models constructed using the *C9orf72*-HRE excellent for exploring upstream and early ALS disease mechanisms, with both loss and gain of function possible.

Loss of function The function of *C9orf72* was unknown prior to its association with ALS. Computational and proteomic studies have implicated its role in vesicle trafficking[98], specifically autophagy[99,100] - the targeted degradation of intracellular organelles. *C9orf72*-knockout mice do not show a motor phenotype - suggesting that its loss of function may not be a proximal cause of neuronal death[101]. However, the

(a) Sense **(b)** Antisense

Figure 1.4: DPRs can be produced by translation in either the sense or antisense direction, in several reading frames - named with letters coding for their constituent amino acids.

observed intracellular trafficking defects and immune system dysregulation[102] may increase cell vulnerability, reducing the number of subsequent insults required to produce disease[103].

Gain of function Two additional gain of function mechanisms have been proposed. The repeat expansion is transcribed into long, aggregation-prone, potentially toxic RNA. Furthermore, despite lacking a start codon, the repeat is translated through an unconventional mechanism - repeat associated non-AUG (RAN) translation[104,105] - producing potentially toxic dipeptide repeat (DPR) proteins (Figure 1.4).

What studying *C9orf72* adds to ALS research *C9orf72*-derived models have now been extensively used to demonstrate cellular recapitulation of in-vivo pathology[106–110], and applied to disease mechanism discovery[42,44,111–122] and high-throughput drug screening. A robust motor phenotype has been elusive in animal models using the entire mutated *C9orf72* gene with surrounding regulatory elements[123–127]. One study did demonstrate a motor phenotype and TDP-43 pathology[128], with inconsistent replicability in independent studies[129,130], provoking ongoing work on epigenetic and environmental modifiers.

As in other neurodegenerative diseases, challenges with translation have reinforced the need for more work with humanised models and better characterisation of biomarkers in human patients. The *C9orf72*-HRE is a powerful aid in constructing

these near-human experiments. Studies in presymptomatic *C9orf72*-HRE carriers, designed compassionately and ethically around genetic testing, provide a natural window into early disease (Section 2.4.2).

In this section, I have described the evolution of the ALS disease entity from a clearly defined series of prototypical motor cases to a wider clinical entity united by pathology that spans a multidimensional clinical space - onset, progression rate, UMN/LMN predominance, cognitive involvement, and genetic causation.

1.2 ALS as a brain network disorder

Despite rapid progress in recent decades in understanding the molecular biology of ALS, large mechanistic knowledge gaps remain between cellular toxicity and selective central nervous system degeneration, and from there to clinical manifestations. In-vivo neuroimaging has been powerful in addressing these. I will focus on MRI abnormalities and the resulting hypotheses about the role of structural and functional networks in ALS.

1.2.1 Structural MRI detects grey and white matter damage in ALS

Charcot initially showed the spatial pattern of ALS in both grey and white matter post-mortem[131] - its study in-vivo has been enabled largely by MRI. Grey matter atrophy is detectable using MRI and has rapidly progressed in sophistication. A study published in 1994 used dot-matrix print-outs and manual annotation[132]. ALS patients were studied to validate a pioneering automated whole-brain technique in 2000[133]. The same technique underpins modern machine-learning approaches to subtyping and staging neurodegeneration (in FTD)[134]. Studies describing grey matter atrophy in the brain have shown relationships with UMN/LMN predominance[135], longitudinal change[136], hemispheric asymmetry[137], bulbar-onset[138] and cognitive impairment[139].

White matter changes have also been studied using diffusion-weighted MRI. This is sensitive to reduction in the strong directionality of diffusion exhibited by highly organised white matter tracts. Corticospinal tract integrity is most prominently affected in ALS[140] along with the corpus callosum[141] and wider white matter networks with increasing disease progression[142,143] or cognitive involvement[144–146]. White matter tract integrity has also been specifically studied in *C9orf72* ALS, with widespread tract damage and longitudinal change found[147]. This widespread pattern was similar to a large subset of patients with sporadic ALS, while the remainder showed a more restricted pattern in the corticospinal tract and corpus callosum[148]. Regional callosal involvement has also been more finely correlated with clinical phenotype[149,150]. With ongoing work on multi-site harmonisation, structural MRI of grey and white matter is well on the way to clinical translation in ALS[151].

1.2.2 Spatial patterns of structural degeneration

Beyond simple description of group level differences, the spatial pattern of changes in ALS has also generated hypotheses about disease properties. Even Charcot ventured that spreading pathology could explain the pattern of involvement in the spinal cord, foreshadowing the current zeitgeist and associated debates.

> By what mechanism does the lesion of the grey matter combine with the lesion of the white bundles? Is it a simple propagation by step by step extension through [nervous tissue]? It is much more likely that the spread is through the nerve fibres, which you know normally establish communication between the lateral bundles and the anterior horns.
>
> — Jean-Martin Charcot *p 265, Leçons sur les maladies du système nerveux faites à la Salpêtrière*

In a series of post-mortem studies Braak and colleagues showed distinct spatial patterns for tau (but not $\alpha\beta$-amyloid) in Alzheimer's disease[152,153], α-synuclein in sporadic Parkinson's disease[154], and TDP43 in ALS[155]. The pattern seen in ALS is described as corticofugal. In cases with the most restricted pathology, TDP43 was restricted to the motor cortex and directly connected regions. With greater overall burden, TDP43 pathology was somewhat sequentially seen in a wider cortical and

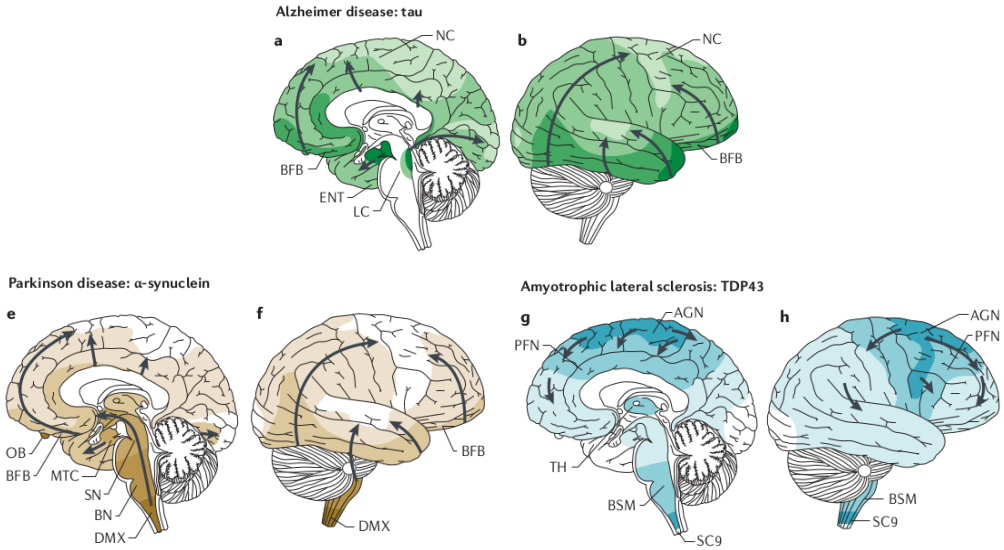

Figure 1.5: Braak staging schematics for $\alpha\beta$-amyloid) in Alzheimer's disease, α-synuclein in sporadic Parkinson's disease, and TDP43 in ALS. Darker shaded regions indicate most restricted pathological findings, while lighter shaded regions show regions affected in brains with more widespread pathological abnormalities.

subcortical distribution (Figure 1.5). Braak staging found a natural counterpart in the theory of prion-like spread in neurodegeneration - that misfolded protein seeds can spread between cells and provoke further cascades of protein misfolding and aggregation[156,157]. Simplified computational models of brain white matter can be made to recapitulate these patterns by varying only the seed region[158].

Challenges to Braak staging and prion-like spread

At its core, Braak staging is the observation of a spatial variability in the frequency of disease markers. A key criticism of this theory is over-reliance on post mortem data - a definitive end point. Staging TDP43 at this end point does not imply that all individuals have progressed through these stages. MRI studies correlating white matter tract damage against disease duration also suffer from this limitation, though some longitudinal data support sequential tract involvement[159–161].

Clinical correlation is also limited. Inspection of cases in large post-mortem series reveals that cases sharing the same neuropathological stage may have widely differing clinical characteristics - for example Stage 1 cases had disease duration ranging from 16 to 156 months[155]. Many Stage 1 patients also had widespread

symptoms, implicating toxicity upstream to TDP43 aggregation. As a result, while the templated spread hypothesis is superficially consistent with clinical mapping of focal onset and spread to contiguous regions in ALS[162–164], direct clinicopathological correlation remains elusive.

Spatially variable vulnerability to disease

Several theories have been proposed as alternatives or elaborations to simple models of prion-like spread of misfolded protein aggregates ALS and other neurodegenerative conditions. In ALS, systematic mutagenesis of the *TARDBP* gene in yeast implicates perinuclear liquid droplets containing TDP43 intermediates as directly toxic while large cytosolic aggregates appear inert[50]. This fits with neuropathological studies in ALS, where soluble intermediate forms of TDP43 are commonly found in post-mortem tissue and TDP43 shows a variety of aggregation morphologies with variable functional properties[165]. Furthermore, where reduced neuron counts suggest more aggressive/advanced disease, ubiquitinated TDP43 aggregates are more frequently found in surviving cells[166]. As with bullet holes in World War II fighters, this suggests a possible interpretation of insoluble TDP43 aggregation as a marker of resistance.

Selective vulnerability and local factors determining toxicity are likely to be relevant across various neurodegenerative disorders. In Parkinson's disease, selective vulnerability based on neuronal morphology and firing properties has been invoked to fill gaps left by simple diffusion models of prion-like spread[167]. In Alzheimer's disease modelling the kinetics of tau spread against local amplification suggest that local amplification of pathology may be more likely to dermine pathological severity in a given brain region[168]. This debate on underlying mechanisms has clear implications for clinical translation. Therapies designed to target and deplete prion-like aggregates or interrupt spread may yield negative results if local factors conferring vulnerability or resistance determine disease severity in-vivo. On the other hand, targeting spreading seeds may be a more viable strategy in targeting pre-symptomatic disease, where disease is likely to be more focal.

1.2.3 Why might the motor cortex be vulnerable in ALS?

Whether ALS begins in the motor cortex and then spreads, or if the spatial pattern simply reflects the probability of a brain region being affected[169], the same follow-up question emerges. Why is the motor cortex vulnerable? Various speculations converge on the idea of specific vulnerabilities in the structure, excitability and network properties of the human motor system.

Evolutionary specialisation for fine top-down motor control

The primate motor system is structurally geared towards finer control of spinal motor neurone pools. In non-primates[170–172], corticospinal projections terminate indirectly on spinal networks (Figure 1.6).

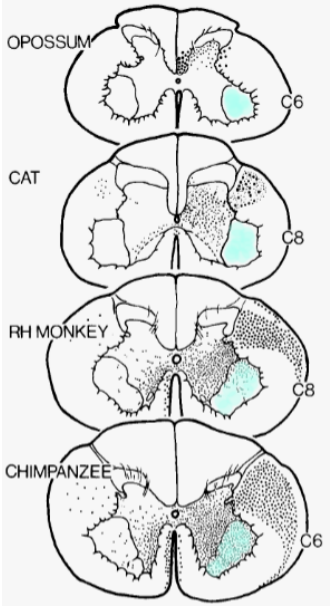

Figure 1.6: Direct corticospinal projections from the left motor cortex in various species. The lateral ventral horn is shaded cyan. Reused with permission from Kuypers, H.G.J.M. (2011). Anatomy of the Descending Pathways. In Comprehensive Physiology, R. Terjung (Ed.).[173]

Humans in particular have many more direct projections to α-motor neurones in the ventral horns - corticomotoneuron (CM) projections. The lateral ventral horn corresponding to the intrinsic muscles of the hand receives particularly dense innervation in humans. This suggests a system that has evolved to expose direct

control of α-motor neurons to the cortex[174], allowing flexible and precise cortical programming of the hands, with clear advantages for tool use[175]. A direct system may however generate points of vulnerability[176].

Spatial selection bias due to clinical diagnosis

Studying selective vulnerability is, however, likely to be influenced by the clinical diagnosis of patients studied. In a cohort selected according to ALS diagnostic criteria, pathology may be more concentrated in motor areas, while in a FTD cohort, frontal or temporal areas may be the most affected. Furthermore, the threshold for clinical detection of pathology may be lower in the motor cortex than in a non-motor region. While motor system involvement remains a cardinal feature and studying this system likely to yield useful biomarkers of disease, the sampling bias driven by clinical diagnosis is an important limitation of this thesis.

Cohorts that include participants on neuropathological or genetic criteria may be less prone to this type of bias. In large genetically stratified cohorts such as GENFI, modelling structural MRI changes in a pseudo-longitudinal manner suggests multiple FTD subtypes with predilection for frontal, temporal, both frontal and temporal, or subcortical regions[134]. While still prone to selection bias favouring cognitive phenotypes, it was notable that the frequency of subtype differed markedly between genotypes (*C9orf72*, *GRN*, and *MAPT*). Future population-based studies may definitively describe the spectrum of pathology associated with TDP43 or *C9orf72* pathology, but some spatial selectivity remains likely.

1.3 Motor network excitability in ALS

1.3.1 Cortical disinhibition is consistently found in ALS

Direct in-vivo evidence of early cortical pathology in ALS patients further solidifies the idea of cortical vulnerability. The development of non-invasive transcranial magnetic stimulation (TMS) in the 1980s[177] allowed in-vivo stimulation of the cortex. Concurrent measurement of the resulting peripheral muscle twitches - motor evoked potentials (MEPs) - reflects overall corticospinal excitability. Overall corticospinal

excitability (minimum stimulation intensity to evoke twitches of a given size) can be paradoxically normal or high in early ALS despite weakness, while accumulating motor neuron loss produces an expected decline in late disease[178]. In paired-pulse experiments, a key physiological inhibitory phenomenon is notably absent in ALS patients[179]. Short-interval cortical inhibition (SICI) in healthy individual consists of a decrement in muscle twitch size when two pulses are applied at intervals of 1-5 milliseconds. In ALS however, this decrement is lost. This finding is more pronounced in early disease and even precedes overt weakness in presymptomatic SOD1 mutation carriers[180]. Cortical disinhibition is also more pronounced over the motor cortex controlling the site of disease onset in patients with very early disease - suggesting a focal origin corresponding to disease onset[181]. It is important to briefly note that other cortical foci may exist, but lack as developed a readout as the motor evoked potential. Sensory cortex[182] and frontal foci of disinhibition[183] require further exploration. For this discussion, however, we will consider motor cortex disinhibition the prototypical pathology in ALS and explore it further.

Underlying mechanisms of cortical disinhibition

Why does SICI occur and what does its loss tell us about ALS? The threshold-tracking TMS data suggest broad loss of SICI across different inter-stimulus intervals, with *average* SICI being the most reliable differentiator between ALS patients and controls[184,185]. However, averaging across intervals blurs together slightly different underlying mechanisms. For 2.5ms SICI, drug-TMS studies implicate signalling via the α-2 or α-3 subunit containing $GABA_A$ receptor, though none of the drugs used is perfectly selective[186–188]. These receptors are most abundant in a parvalbumin-positive interneuron network located in more superficial layers (II/III) in the primary motor cortex[189]. This is corroborated in healthy human MEG studies by the finding that 2.5ms SICI is tightly correlated with the peak activation frequency of the low gamma frequency band[190] - which originates in more superficial layers in the motor cortex[191]. The mechanism underlying 1ms SICI remains controversial - it

may be associated with extracellular GABA concentration as measured by magnetic resonance spectroscopy[192], but reproduction has been challenging[193].

Inhibitory motor cortex microcircuits are disrupted in ALS

Within the motor cortex, excitatory pyramidal cells and inhibitory interneurons form multiple microcircuits incorporating both horizontal (within-layer) and vertical (between-layer) connections[194]. Excitatory inputs to upper layers (2/3) of the motor cortex are processed and amplified within these layers. Disrupted 2.5-3ms SICI strongly suggests dysfunction of this processing. However, this isn't the only site where physiological inhibitory circuitry is damaged in ALS.

The layer II/III interneuron network converges on pyramidal cells' apical dendrites, which carry motor signalling deeper to layer V[195]. There, pyramidal cell bodies are densely innervated by inhibitory connections mediated by the $\alpha 1$ subunit of the $GABA_A$ receptor from parvalbumin-positive (PV+) interneurons in deeper layers. With long horizontal projections and fast-spiking properties that allow ongoing inhibition of multiple pyramidal cells, this interneuronal network produces functional properties such as surround-inhibition, spike-timing synchronisation and tuning to stimulus properties in various cortical regions[196,197].

Within the mouse motor cortex, some PV+ interneurons demonstrate increased firing immediately prior to the onset of voluntary movement, suggesting a role in shaping motor output by gating premature or inappropriate output[198]. The importance of physiological inhibition shaping motor cortex output is demonstrated by pharmacological disinhibition, which results in runaway epileptiform events[195].

Evidence for disruption of this deeper inhibitory filter in ALS comes from neuropathology, where parvalbumin-positive cells are depleted in the primary motor cortex across all layers by $\sim$40%[199]. This proportion remains relatively constant across a marked range of Betz cell loss (down to near complete absence). Layer-specific in-situ hybridisation histopathology also shows decreased $\alpha 1$ subunit

mRNA expression across all layers, with corresponding upregulation of glutamic acid decarboxylase (GAD), the enzyme that produces GABA[200]. Superficially, this evidence of interneuronal damage at various motor cortex sites seems discordant with the observation that TDP43 aggregates are rarely found in interneurons[97]. A potential unifying explanation is that a vulnerable pool of PV+ interneurons is lost in early ALS with no opportunity to sequester TDP43 in inert aggregates. As interneurons demonstrate considerable variability in gene expression, morphology, connectivity and firing frequency[201], highly vulnerable and highly resistant pools may coexist. Disrupted inhibitory signalling might then trigger a cascade of ongoing degeneration in the pyramidal cell (corticomotoneuron), a more structurally and functionally homogeneous population.

Measuring local inhibition and excitation in-vivo

MR spectroscopy has been used to assess overall intracortical excitation and inhibition through total glutamate and GABA respectively in-vivo in ALS - though these are at best proxy measures (Section 4.1.4). GABA was reduced in the left motor cortex in ALS patients[202], together with elevated combined glutamate and glutamine (Glx) when riluzole-naive[203]. Findings on glutamate are conflicting with findings of increase[204], no change[205–207], and decrease in ALS reported[208–210]. Glu/GABA ratio in the supplementary motor cortex was elevated in patients with ALS[211]. Non-invasive measurement of local inhibition and excitation in ALS and presymptomatic disease is one core goal of this thesis. I explore this method further in Section 2.3 describing a novel method to map excitation and inhibition in the motor network. I validate this technique in healthy individuals in Chapter 4, and apply it to established ALS and presymptomatic carriers of the *C9orf72*-HRE in Chapter 5.

1.3.2 Wider motor network excitability and connectivity

Local changes in motor cortex excitability may have knock-on effects in other brain regions, particularly other parts of the motor network. Several functional changes might be expected to result.

Transcallosal projections subtly tune contralateral motor cortex output

Projections across the corpus callosum to contralateral structures may be particularly relevant to motor function and disease[212]. Each motor cortex fine-tunes the outputs from the other through interhemispheric projections that interact with the inhibitory interneuron network in the other motor cortex to produce subtle surround-inhibition effects[213]. Callosal degeneration and resulting motor dysfunction have also been specifically implicated in ALS[141,214].

The supplementary motor area is a close functional neighbour to M1

The primate supplementary motor area (SMA) adjoins the medial primary motor cortex, contributes to ∼10% of the corticospinal tract[215,216], forming direct connections to α motor neurone pools in the contralateral ventral horn of the cervical spinal cord[217]. DWI also shows that the SMA predominantly connects posteriorly to M1 and inferiorly to corticospinal tracts[218], allowing substantial functional overlap with M1. Connectivity between SMA/premotor area and M1 was a significant predictor of better motor outcome in stroke in patients with significant corticospinal tract lesions[219], implying a capacity for motor compensation that could be relevant in ALS.

The thalamus as a connectivity hub in the human brain

In humans, the thalamus has a fan-like structural connectivity pattern to most cortical regions that can be used to subdivide it into regions corresponding to its histological nuclei[220]. The general architecture of a thalamo-cortical loop - with cortical layer 6 and pyramidal tract neurons projecting to the thalamus, while 'core' type thalamo-cortical projections project back to several cortical layers, most prominently layer 4[221]. This canonical brain circuit may have been repurposed extensively for different sensory and motor brain functions. The role of the thalamus in relaying sensory information is best described with visual input through the lateral geniculate nucleus to the primary visual cortex. However, despite lacking a histological granular layer 4, a 'functional' layer 4 is still found to receive inputs from the thalamus and form intra-columnar outputs to layer 2/3[222,223]. Thalamic

atrophy across various nuclei has been reported in both ALS[224] and FTD[225], with pulvinar atrophy uniquely found in *C9orf72* expansion carriers. The consequence of disruption to the thalamo-cortical loop is not well explored in ALS, though abnormal coupling in this circuit has been invoked to explain motor dysfunction in Parkinson's disease models[226].

1.3.3 fMRI measures both local activation and wider network function in ALS

Functional magnetic resonance imaging using blood oxygen level dependent (BOLD) contrast, though strongly affected by vascular properties[227], can be used as a proxy for neuronal activation across the whole brain (Section 2.2). BOLD-fMRI data acquired at rest can be decomposed into resting state networks, showing correlated activity over seconds to minutes[228]. Anatomically similar motor networks can be reproduced when performing motor tasks[229] (Figure 4.1).

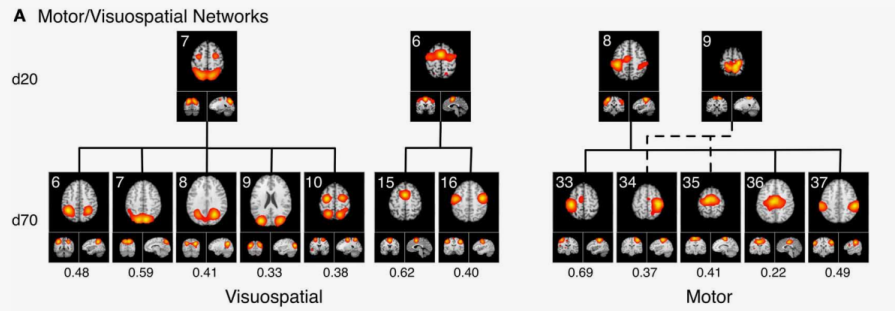

Figure 1.7: Spatial maps derived from independent component analysis that correlate with subjects' metadata from visuospatial and motor tasks. Lower dimensionality (d20) shows brain-wide networks, which become fractionated into constituent nodes at higher dimensionality (d70) - figure reproduced from Ray et. al. Frontiers 2013[230], (CC-BY).

Some consistent findings include spreading cortical activation associated with sustained hand movement[231,232], hyper-activation in early disease[233], and the reorganisation of brain functional networks[234–236] in both task and resting conditions. Brain network connectivity alterations may even predate symptom onset in genetic ALS[237]. Functional connectivity evolves with disease progression[235,238], with developments ongoing to refine this into a clinically useful biomarker[239]. The second overall aim of this thesis is to apply fMRI using a finger movement task to measure local motor

network activation and wider motor network connectivity changes in ALS. I study motor network connectivity changes in established disease in a large multimodal MRI dataset of ALS and PLS patients in Chapter 3.

1.3.4 Unpicking motor network excitability in ALS

By studying individual modalities, I will explore the landscape of motor network excitability along several separate axes that represent a many-to-many correspondence (Section 6.1.1) between modalities (task fMRI, MRSI) and disease properties (local motor cortex excitability, wider motor network dysfunction). In Chapter 6, I integrate multiple noisy measures to generate composite markers reflecting underlying disease properties in a dataset encompassing ALS patients, controls and presymptomatic *C9orf72*-HRE carriers.

My dear Watson, try a little analysis yourself**, said he, with a touch of impatience. **You know my methods. Apply them, and it will be instructive to compare results.

***I cannot conceive anything which will cover the facts**, I answered.*

— The Sign of Four — Sir Arthur Conan Doyle

2 Methods

Contents

I will now discuss the techniques and study design I applied to measure motor

network excitability in ALS.

I focused on non-invasive magnetic resonance imaging techniques in this thesis due to low patient risk, established clinical availability (albeit concentrated in high-income regions[240]), and a high level of technology maturity and standardisation. Several emerging techniques can measure proxies of neural activity and excitability. This section summarises general principles of MRI, and elaborates on the two specific techniques I applied - blood oxygenation level dependent (BOLD) functional MRI and magnetic resonance spectroscopic imaging (MRSI).

2.1 General principles of magnetic resonance imaging

MRI depends on the physical principle of nuclear magnetic resonance (NMR). Many nuclei have a quantum property of 'spin', or angular momentum, around their axis of magnetic polarity. Nuclei in a material have randomly distributed spins when no magnetic field is applied. When surrounded by a strong static magnetic field (denoted B_0) a small proportion of spins become more aligned with its direction - a lower energy state. In a magnetic field, the spin will additionally precess (analogous to the rotation of a tilted spinning top) around the axis of the field. This has a characteristic rotational frequency, the Larmor frequency (ω), proportional to the strength of the static magnetic field and a constant unique to the nucleus in question, the gyromagnetic ratio (γ).

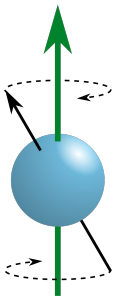

Figure 2.1: Schematic representation of the precessing spin of a proton in a magnetic field. The green arrow indicates the external magnetic field, the black arrow the particle's magnetic dipole moment. CC0, via Wikimedia Commons[241]

2.1.1 Nuclear magnetic resonance

Most clinical MRI considers the special case of **proton** magnetic resonance. As the most common nuclei (^1H) in in the most abundant molecule (H_2O) in the human body, and present in many other biological molecules, techniques targeting the characteristic frequencies of proton magnetic resonance yield highly biologically informative data. If protons in a strong B_0 field are exposed to a weaker oscillating magnetic field (B_1) transmitted into the sample as a radiofrequency (RF) pulse, the precession is perturbed (or 'flipped') - analogous to tilting the top still further away from the vertical.

Once perturbed, the nuclear spin tends to return, or 'relax' from the higher energy misaligned state to lower energy alignment with B_0. As it does so, it emits energy in the form of radiofrequency energy, which can be detected as induced current in a coil of conductive wire (the receive coil) positioned around the sample.

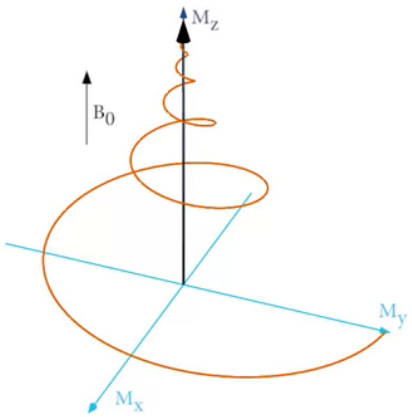

Figure 2.2: The brown line shows the path taken by the vector of a proton's spin when relaxing back into alignment with the B0 magnetic field. CC BY 3.0, via Wikimedia Commons[242]. Link to video

2.1.2 MRI scanner principles

In any given human MRI experiment, the participant is positioned with the region studied (i.e. brain) in the centre of the scanner bore. Immediately surrounding the participant's head is a coil that both transmits the B_1 pulse and receives the

returning signal from the brain. Surrounding the scanner bore is a large cylindrical superconducting magnet (coiled copper wire immersed in liquid helium) generating the B_0 field. Outside this are three sets of coils arranged to generate superimposed gradients in the B_0 field in the x, y and z directions.

2.1.3 Image formation

The returning signal is generally sampled while a gradient is applied (the direction of the gradient is called the 'frequency encode' direction). Depending on a proton's position in the tissue, the field strength it experiences and therefore its Larmor frequency varies according to the gradient applied[243,244]. Therefore the frequency of the signal generated encodes its position (Figure 2.3).

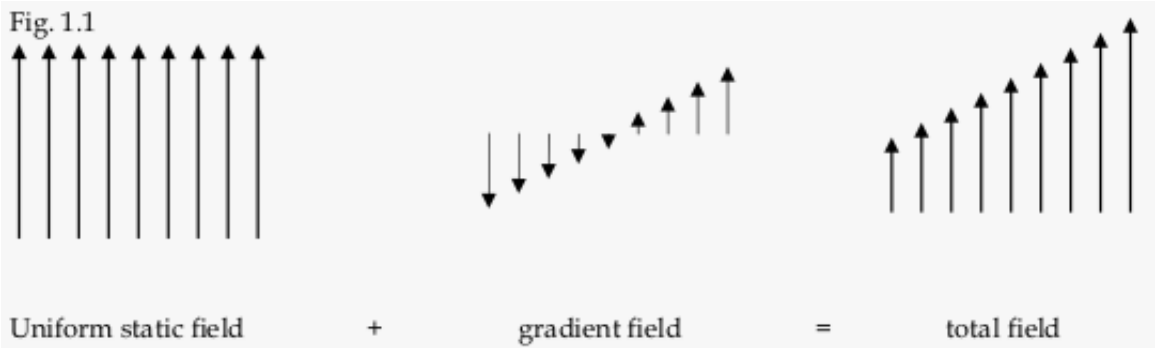

Figure 2.3: Effect of a superimposed gradient field on the static B0 field. Adapted from Bruce Rosen, and Lawrence Wald. HST.584J Magnetic Resonance Analytic, Biochemical, and Imaging Techniques. Spring 2006. Massachusetts Institute of Technology: MIT OpenCourseWare, https://ocw.mit.edu. License: Creative Commons BY-NC-SA.

A new variable, k[245–247], is formulated to represent the possible phase cycles resulting from each gradient application over time. Each time the return signal is sampled its magnitude (or phase) can be plotted according to kx, ky (and kz) forming a k-space image. This signal could originate from protons throughout the sample studied. A subsequent (2d or 3d) Fourier transform of the k-space image recovers position from spatial frequency, generating an map of signal magnitude (or phase) in space (i.e. an image)[248].

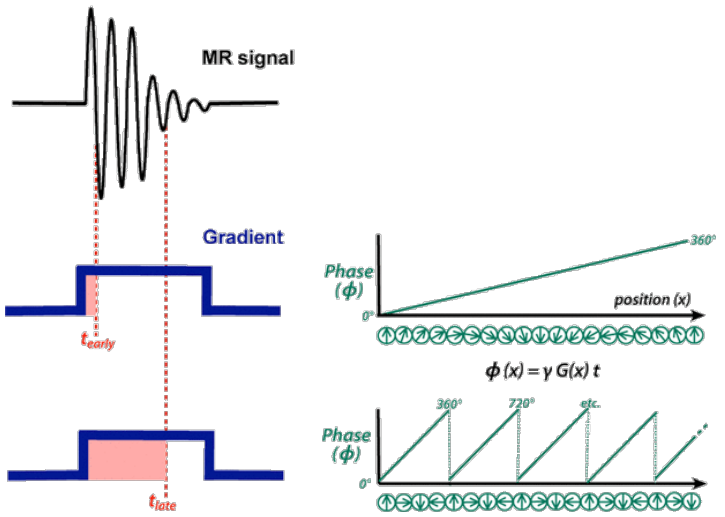

Figure 2.4: Evolution of phase cycles over time as gradients are applied.

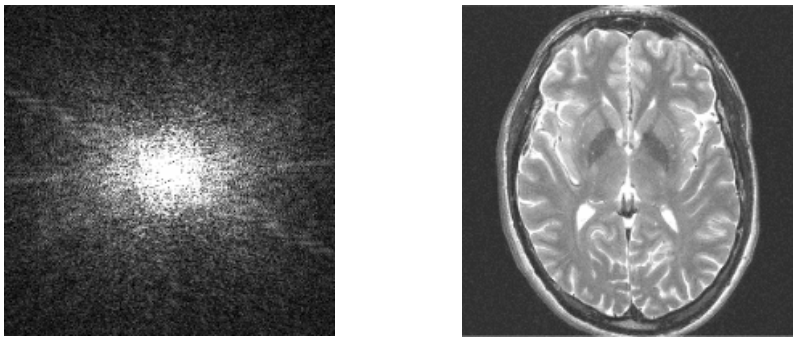

(a) k-space **(b)** image

Figure 2.5: An image of signal magnitude in k-space and the resulting image of signal magnitude in space following 2D Fourier transform. Adapted from Bruce Rosen, and Lawrence Wald. HST.584J Magnetic Resonance Analytic, Biochemical, and Imaging Techniques. Spring 2006. Massachusetts Institute of Technology: MIT OpenCourseWare, https://ocw.mit.edu. License: Creative Commons BY-NC-SA.

The MRI sequences used in research and the clinic result from variations on these basic principles - pulse shape, sequence and gradient field application. In its simplest form, the signal from a region of interest can be read into a spectrum that allows quantification of water and a range of other proton-containing molecules. Sequence design can also target physical processes occurring in the tissue itself e.g. (diffusion of water, iron deposition). Vascular properties and blood flow underpin another set of imaging techniques including functional MRI, arterial spin labelling

and MR angiography. Biophysical models informed by prior knowledge of tissue composition may be applied as in quantitative MRI or MR fingerprinting. Finally, considerations of signal to noise ratio, spatial/temporal resolution and acquisition time cut across all sequence designs. Image acquisition can be accelerated by parallel acquisition using an array of receiver coils[249], and/or sparse k-space sampling with specialised reconstruction[250]. Mathematically informed designs can do more in the same amount of time[251,252]. Finally, data quality has improved over the last 40-50 years as scanner technology has developed, with increasing field strength, gradient field strength/slew speed and field homogeneity.

Scientists wishing to apply MRI are therefore able to acquire more and higher quality data in less time, with a rapid pace of ongoing development. In the following sections, I will discuss the key MR techniques I used, the sequence optimisations involved, and the rationale for their application to ALS - functional MRI and MR spectroscopic imaging.

2.2 BOLD functional MRI - powerful, but imperfect

In this section I will discuss functional magnetic resonance imaging, a technique applied in every experiment described in this thesis. I will discuss the underlying haemodynamic response, its complexities in age and disease, and the importance of the participant's mental state.

2.2.1 Principles of the haemodynamic response function

Seiji Ogawa and colleagues at Bell Labs first demonstrated the contrast between veins and other brain tissues due to the paramagnetic properties of de-oxygenated haemoglobin causing rapid T2 decay (Figure 2.6)[253,254].

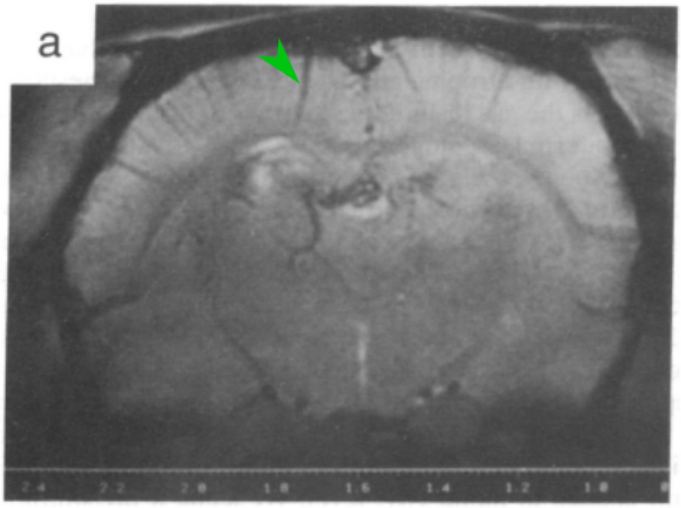

Figure 2.6: Radial dark lines (as indicated by the green arrowhead) show loss of signal in cortical veins in the rat. Adapted from Ogawa et. al. 1990[253]

They showed a dependence on vessel orientation, size, inhaled CO2, and glucose metabolism. They proposed its application for functional human brain imaging in brain parenchyma, and two independent demonstrations soon followed at the Massachusetts General Hospital and at the Center for Magnetic Resonance Research (CMRR), University of Minnesota[255,256].

Why does blood oxygen level dependent (BOLD) contrast vary in the parenchyma? With neural activation, tissue oxygen consumption increases, recruiting increased local blood flow through pre-capillary arterioles. Small veins, which contain most of the tissue blood volume, distend with oxygenated blood, diluting de-oxygenated haemoglobin. This reduces its effect on the magnetic susceptibility of surrounding tissue, causing less rapid signal decay. This "Balloon model" was formulated and described by Buxton and colleagues in 1998[257] (Figure 2.7).

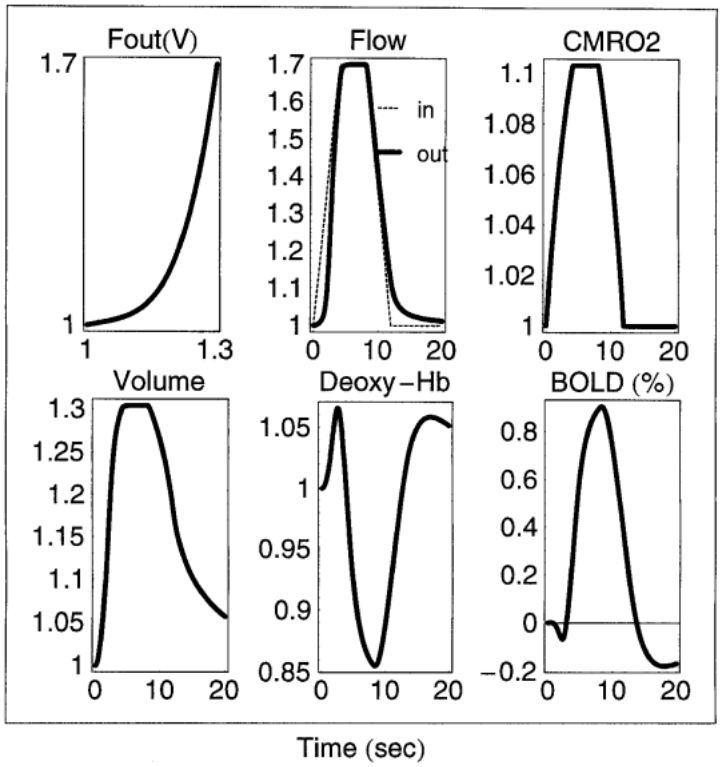

Figure 2.7: The evolution of various components of the Balloon model over time in response to a stimulus. Reproduced with permission from Buxton et. al. 2008.

With a simplified gamma function that mimics the shape of this model, and some elaboration to account for stimuli that occur close enough in time for their haemodynamic responses to be correlated[258,259], this conceptual framework underpins most modern fMRI data analysis. In task fMRI, a canonical haemodynamic response function (Figure 2.8) is generally convolved with an input stimulus time-course, and the data time-course from a given voxel correlated against this, followed by statistical testing on a voxel-wise basis generally with a linear model or permutation inference, from which a 3d map of p-values emerges. Notably, this is not a necessary assumption for data driven approaches, such as independent component analysis in resting state (or task) fMRI[260,261].

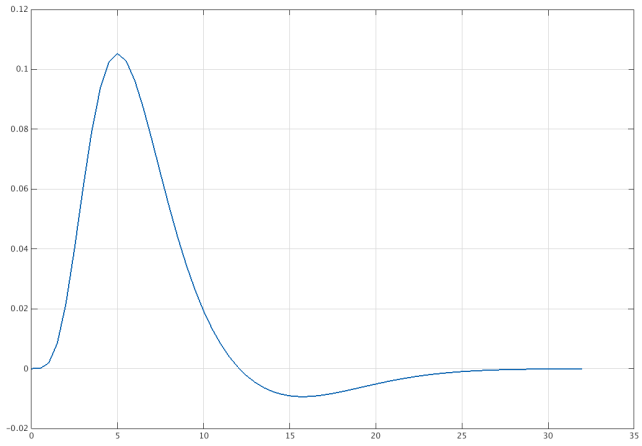

Figure 2.8: The canonical function used to model the haemodynamic response in the SPM toolkit, SPM-wiki, CC BY-SA 3.0, via Wikimedia Commons

The simple HRF models used in modern image analysis toolkits have been applied extensively. More generally, the simple assumption that neural activity produces a haemodynamic response proportional to the duration and intensity of stimulus usually holds[262].

2.2.2 BOLD-fMRI detects brain activation associated with stimuli and at rest

BOLD-fMRI has delivered key advances across a wide range of neuroscience fields. Considering the motor system alone - it has been applied to study motor system physiology (lateralisation[263–265], bimanual control[266], childhood development[267], motor learning[268269], between species differences[270], ageing[271]) as well as in clinical applications (pre-surgical mapping[272], disease characterisation[273–275], clinical trial outcome measures[276]).

BOLD-fMRI is the best available tool for non-invasive measurement of brain activation with sufficient spatial resolution to study different motor system regions and network excitability properties. Thirty years of cumulative refinement in scanner engineering and sequence design have produced major advances in scan duration, spatial resolution and temporal resolution. The current sweet-spot is at 3 Tesla,

with better scanner availability, lower cost, reduced need for specialised institutional expertise, and proximity to clinical translation vs. 7T.

The Human Connectome Project[277] and UK Biobank[278,279] have prepared and published imaging and analysis protocols used to generate datasets with tens of thousands of participants. I selected the UK Biobank 2d-EPI sequence for my data collection (Chapters 4, 5, and 6). This sequence achieves isotropic spatial resolution of 2.4mm, temporal resolution of 0.735s, and whole brain coverage thanks to multiband imaging with 8x acceleration according to the CMRR multiband acquisition[280]. Findings using this sequence would be testable and clinically translatable at multiple centres thanks to openly available sequence/reconstruction code and multi-site harmonisation data. This sequence also represents an improvement over that used in the retrospective dataset analysed in Chapter 3 (Section 3.2.2), which had similar spatial resolution, but much lower temporal resolution (3s).

2.2.3 Elaborating the vascular model

However, BOLD fMRI has several key limitations. First, simple vascular models have been challenged and elaborated. Two-photon microscopy experiments in rodents show that arterioles distend much more than veins with short stimulation[281–283]. Further single-vessel imaging experiments have decomposed the bulk BOLD response into a rapid arterial component driven by volume change and a slightly slower venous component due to changing oxygen saturation[284]. Scaling models up to a vascular network on a cubic millimetre scale further illustrates the contributions from different vascular components[285]. This also predicts substantial variation of BOLD signal dependent on cortical folding since pial veins run parallel to the cortical surface. Venules may drain variable tissue volumes, and drainage patterns differ regionally according to cytoarchitectural profile[227]. In summary, the vascular nature of the BOLD signal makes vascular properties an intrinsic confound.

2.2.4 Neuro-vascular (un)coupling?

Furthermore, the haemodynamic response may not always be tightly coupled to neural activity. The type of neuron activated matters - applying optogenetics to selectively stimulate sub-populations of neurons in the rodent sensory cortex suggests differing roles for inhibitory interneurons and pyramidal neurons[286]. Interneurons may readily recruit blood flow via a nitric oxide mediated mechanism, while pyramidal cell activity is the main driver of oxygen metabolism. The direction of effect may also be inconsistent. In the rodent striatum, paradoxical vasoconstriction and lack of haemodynamic response occurs with noxious stimulation despite increased neural activity[287]. This might plausibly be a regional quirk of the striatum. However, even in the cortex, neurovascular coupling might be stronger in conditions of strong or persistent activation, and less pronounced or absent at rest. For example, BOLD signal is only weakly correlated to neural activity in the awake mouse somatosensory cortex when periods of spontaneous whisker or body movement are excluded[288]. Even during blocked tasks, anticipation and entrainment of vascular changes may confound the link between visual cortex haemodynamic response and neural activity[289].

2.2.5 Generalisability

Finally, simple HRF models may not generalise well to ageing or disease. Healthy older adults are likely to have subclinical comorbidities affecting the brain vasculature, such as diabetes, hypertension and small vessel atherosclerotic disease. The BOLD signal rose more slowly, with a lower peak, in response to a finger tapping task in the sensorimotor cortex of individuals with a previous (distant) subcortical lacunar stroke compared to healthy controls[290]. In otherwise healthy older adults, the BOLD response is prolonged and lower in amplitude with increasing age[291,292], and more noisy than in healthy controls[293].

In ALS, despite a large literature applying BOLD-fMRI, disease effects on the HRF have not been extensively investigated. There is some evidence that the

HRF rise is delayed to visual and auditory stimulation in ALS, and the overall response prolonged to somatosensory stimulation[294].

There is limited work on vascular changes as a result of ALS in the context of the BOLD signal. An unpublished study[295] presented at the 2006 ISMRM conference found both contralateral motor cortex BOLD hyper-activation in ALS and reduced BOLD signal reactivity to breath-holding in the same patient group. This may suggest reduced vascular reactivity in ALS as a contributory mechanism. However, there is substantial interest in alterations of the blood-brain-barrier in ALS[296,297], with evidence of pericyte degeneration and microvascular leakage, with uncertain implications for vascular properties in-vivo.

Various techniques exist to disentangle the contributions of neural and vascular mechanisms to the BOLD signal[298]. Other MR modalities such as arterial spin labelling directly measure brain perfusion and flow. Cerebral blood flow as measured by ASL has been shown to be reduced in small groups of ALS and FTD patients[299,300]. While reduced blood flow would not in itself explain BOLD hyperactivation, altered vascular reactivity might. This can be assessed through CO_2 inhalation or breath hold, though these can be more challenging to perform in ALS patients with some degree of respiratory muscle weakness.

Direct measurement of the neural signal of interest through techniques sensitive to electrical or magnetic fields is possible using techniques such as EEG[301] or MEG[302,303]. In the dataset I collected (Chapters 5 and 6), some MEG data was concurrently collected, though the dataset is incomplete due to a planned MEG scanner replacement. Future directions include comparing the same finger movement task assessed with both BOLD fMRI and MEG.

Completely disentangling the contributions of neural activity, vasculature, and glutamatergic or GABA-ergic signalling may not matter for clinical application, as long as the measured changes contain meaningful clinical information. However, the generally assumed link between the HRF and neural activity should be treated with caution in ALS.

2.2.6 State of mind during fMRI

I will now discuss experimental design to search for fMRI biomarkers of motor network excitability in ALS. The brain's dynamic activity can be measured in a range of differing conditions. In humans, measurement during anaesthesia[304], sleep[305], 'resting' conditions and active task conditions addresses corresponding experimental questions. Even resting conditions vary - standard conditions include awake with eyes closed or fixation cross viewing[306]. More 'naturalistic' conditions such as movie watching or music listening[307,308] have been proposed as alternatives that increase the power to distinguish brain states[309].

Resting state fMRI Decomposing resting state data using independent component analysis yields 'resting state networks'. Each RSN is a statistically independent (maximally non-Gaussian) component of the data, a spatial map of voxels with similar activity over time. This can be due to correlated underlying neuronal activity (functional connectivity) or alternatively to structured noise (e.g. vascular pulsatility).

Regions activated during task fMRI are spatially similar to resting state networks[310] suggesting that they might be functionally related. The high temporal resolution of magnetoencephalography suggests dynamic recruitment of 'resting state' subnetworks for task performance even predicting task responses from features of resting state data[311–313].

As analysis techniques improve, resting state neuroimaging is increasingly appealing in patient groups, promising to map a functional connectome that is reliable (with 500 rs-fMRI timepoints[314]), does not impose differential demands on patients and controls, and is comparable between sites, scanners and studies. BOLD functional MRI (exploratory) end-points are increasingly published in clinical trials for neurodegenerative diseases[276] and registered on clinical trial databases[315].

I have analysed resting state data and the resting state motor network in Chapter 4 in a large consolidated dataset of participants in different studies who

did not do the same motor task. The identical resting state sequence used allowed consolidation of healthy individuals data across multiple studies.

Motor task fMRI In Chapters 3, 5 and 6 I have used data from motor task conditions to increase the motor network signal of interest and to allow data to be directly linked to behaviour that might be meaningful for a patient. Even in healthy controls, the statistical confidence (z-scores) for sensorimotor task activation maps are substantially greater than for sensorimotor networks derived from resting state fMRI[316]. Using motor tasks in the scanner also allows data correlation with detailed behavioural data including response time and accuracy. The ambition for ecologically valid science[317] will undoubtedly make task design more challenging - I tried to balance task difficulty across patient and healthy groups of different ages, and considered in detail the impact of design on experimental power to detect significant differences (Sections 3.2.3, 6.2.3).

2.2.7 Reliability of fMRI measures

Several factors are likely to affect the reliability of the fMRI sequences used in this thesis. Eyes fixated conditions (as used in Chapters 4, 5, and 6) improve the reliability of within-network and intra-session motor network connectivity measures[306]. The reliability of most fMRI measures appears to be proportional to $1/\sqrt{t}$, where t is the scan time[318]. Therefore, while increasing scan time brings diminishing returns, 15-30 minutes of fMRI data would provide a significant increase in reliability over shorter protocols. In practice, however, total scan time is limited by tolerability in patients, and desire to collect data of multiple modalities. In Chapter 3, I worked with a total of 20 minutes of task fMRI data at a temporal resolution of 3 seconds (∼400 averages), while in Chapters 5 and 6, I worked with 6 minutes of task fMRI data at a temporal resolution of 0.735 seconds (∼490 averages).

Nevertheless, BOLD fMRI is intrinsically limited in retest-reliability, with a large systematic review suggesting intra-class correlation coefficient (ICC) ∼0.3 for individual resting state functional connectivity measures[319], and ∼0.4 for motor

task fMRI measures in general[320]. This therefore represents a significant limitation for the use of individual data in correlation with other modalities/clinical data or in making individual level predictions.

While I have applied state-of-the-art neuroimaging approaches for clinical translation in this thesis, in future, emerging techniques such as MEG with optically pumped magnetometers and functional near-infrared spectroscopy may allow more free participant movement[321] and wider scope for both real and virtual reality task design[322], with complex movement tracking enabled by machine learning[323]. The future may include functional neuroimaging of daily tasks such as walking, climbing stairs, food preparation/feeding, writing and phone/computer use. This might eventually open the door to testing therapeutic interventions directly against patient function or rehabilitation.

2.3 MR spectroscopy - direct quantification of neurochemicals

The second key technique I have applied in this thesis is magnetic resonance spectroscopic imaging. I will discuss the general principles of magnetic resonance spectroscopy and rationale for the sequence I have used to achieve mapping of excitatory and inhibitory neurochemicals in the motor system with high spatial resolution.

2.3.1 General principles

The simplest possible nuclear magnetic resonance spectroscopy experiment involves analysis of the frequency content of the return radiofrequency signal from a sample placed in a strong static magnetic field with a radiofrequency pulse applied at right angles. The return signal originates from the sum of the precessing magnetisations of nuclei in the sample. Isidor Isaac Rabi and colleagues demonstrated that characteristic resonance frequencies corresponding to lithium and chloride nuclei could be measured from a sample of LiCl in vacuum in 1938 at Columbia University[324]. Shortly thereafter the same effect was independently demonstrated in paraffin and water respectively by teams headed by Edward Purcell[325] and Felix Bloch[326]. Proton

MR spectroscopy applies the same principle to measure the frequency associated with protons in the human brain, applying a Fourier transform to the return RF signal (or free induction decay [FID] - Figure 2.9a).

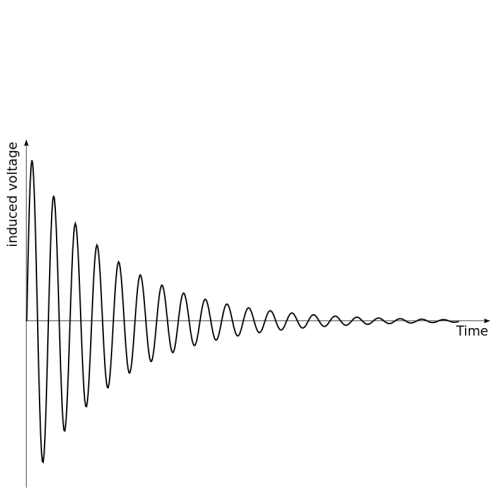

(a) Example return RF signal.

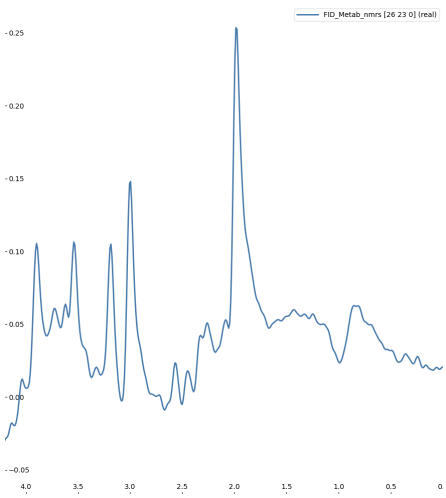

(b) Representative spectrum from a single voxel. The x-axis is conventionally reversed and frequency is expressed as parts per million (ΔHz / MHz)

As the vast majority of protons in the brain are present in water molecules, the corresponding frequency dominates the generated spectrum. Signal corresponding to protons in other molecules in the brain appear as small peaks offset in frequency from the main peak. The water signal is generally suppressed or subtracted. A range of chemical and quantum properties determine the exact number, frequency and splitting properties of the peaks corresponding to a given organic molecule with multiple protons. This results in a signature of peaks corresponding to a given molecule, with peak height proportional to the power at that frequency, or the molecule's abundance (Figure 2.9b).

MR spectroscopy experiments typically involve suppression of the water signal in some form and localisation of the signal from a given region of interest. The resulting spectrum is a composite of all the peaks originating from all the non-water protons in the region of interest. This spectrum can be analysed to measure the peak height and therefore quantify the abundance of the corresponding molecules.

Historically this was done manually, however modern analysis toolkits optimise the fit of a pre-specified set of peaks at known frequencies corresponding to molecules of interest (Figure 2.10).

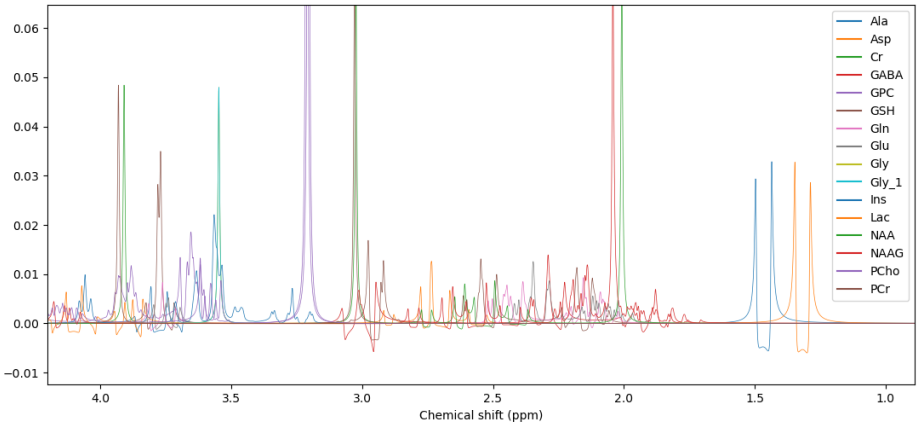

Figure 2.10: Selected metabolite basis spectra for 3T semi-LASER MRSI with 32ms TE.

I applied this technique to directly and non-invasively quantify brain molecules (specifically neurochemicals involved in excitatory and inhibitory signalling) in-vivo.

2.3.2 Limitations of single voxel spectroscopy

MR spectroscopy experiments in humans are commonly performed as **single-voxel** spectroscopy, where localisation pulses dephase signal that does not originate from a volume of interest, typically a 2 × 2 × 2cm cube. This increases the signal-to-noise ratio, making the measurement of low abundance molecules feasible. While single voxel MR spectroscopy (SVS) has been a powerful tool in in-vivo neuroscience, several factors have limited its utility in understanding the neurochemical basis of motor network function.

The large voxel size exacerbates partial-volume effects due to different tissue types contained within the region-of-interest, making quantification potentially challenging. It is also limited to measuring the average value over the entire voxel, with more fine grained analysis not possible.

In addition, SVS typically acquires data from only one region at a time, whereas it is reasonable to assume that functional connectivity between two brain regions would be better characterised if neurochemicals in both regions could be quantified simultaneously. While prior work using interleaved 2 voxel MRS has allowed simultaneous data acquisition from both motor cortices[327], newer techniques allow simultaneous measurement of spectra across a region spanning both motor cortices at higher spatial resolution.

2.3.3 Advancing MR spectroscopy methods

Improving scanner technology and protocol design help address these challenges - since proof-of-principle studies in the 1980s, progressive gains in MRS data quality and acquisition speed have occurred. Specifically, development of 2D and 3D spectroscopic imaging sequences allow collection of spectral data at high spatial resolution from separate voxels within an imaging plane or grid[328]. Historically, the use of magnetic resonance spectroscopic imaging (MRSI) has been limited by extended acquisition time and artefacts associated with subject motion and scanner frequency drift.

I have applied a recently described sequence that mitigates these challenges by combining several sequence design features - metabolite cycling, semi-LASER localisation, and density-weighted concentric rings k-space readout.

Non-water suppressed metabolite cycling This sequence avoids the need for separate water reference and water-suppressed metabolite acquisitions. Prior to localisation, RF pulses invert the spectral range of metabolite signals to either up-field or down-field with respect to water. Addition or subtraction of the two acquisitions therefore produces a pure water spectrum or a pure metabolite spectrum respectively.

semi-LASER localisation This pulse sequence results in data semi-Localised by Adiabatic SElective Refocusing[329]. Similarly to previous approaches to data localisation using PRESS (Point RESolved Spectroscopy), a series of refocusing pulses select signal from within the region of interest to be read out. However, the bandwidth used for these refocusing pulses produces much less chemical shift displacement artefact. This mitigates a major issue when regions near the edge of the brain are studied as signal from the subcutaneous lipid surrounding the skull is mislocalised into the region of interest.

Density weighted concentric rings k-space readout Finally, to achieve faster data readout, a mathematically informed sparse k-space sampling scheme is used consisting of concentric rings spaced progressively more widely (Figure 2.11)[330]. The density-weighting approach also has the side benefit of reducing side lobe artefacts by improving the shape of the spatial response function.

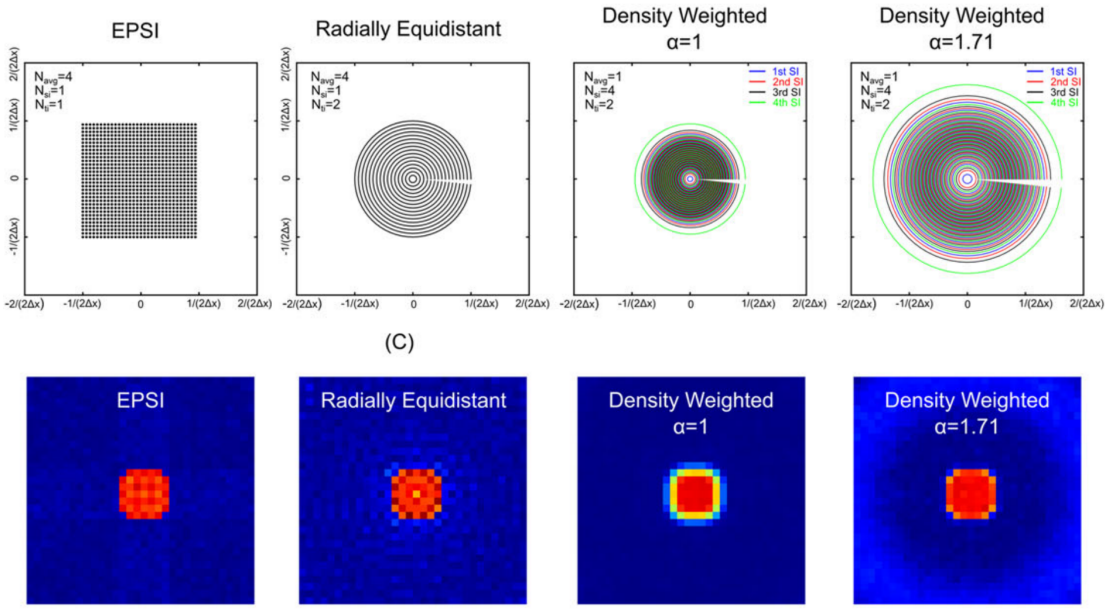

Figure 2.11: Comparison of k-space readout trajectories. With synthetic MRSI data, density weighted concentric rings readout was efficient and mitigated side-lobe artefacts. Adapted under Creative Commons (CC BY 4.0) from Chiew et. al. NMR Biomed 2018[330]

As a result of these design features, this sequence achieves high spatial resolution (5mm × 5mm × 20mm - Figure 2.12) mapping of metabolites across a region

of interest encompassing sensorimotor regions corresponding to both hands[330,331]. This is achieved in a scientifically and clinically feasible time frame (∼15 minutes), allowing spectroscopy to be performed alongside other imaging modalities (structural, functional and diffusion MRI).

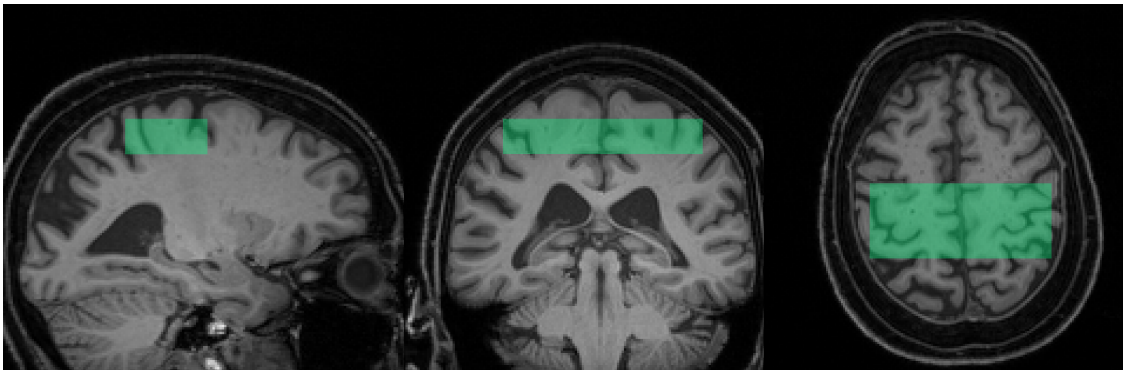

(a) Example volume-of-interest placement

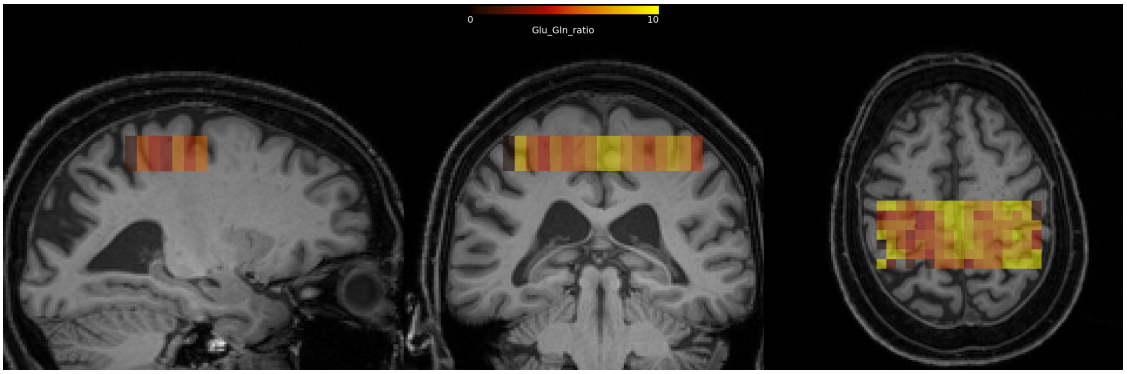

(b) Glutamate+Glutamine concentration (relative to total creatine)

Figure 2.12: Example data from a single healthy control subject. The volume-of-interest is manually placed to encompass both primary motor cortices. The image of metabolite concentration has spatial resolution of 5mm × 5mm × 15mm.

2.3.4 The challenges of quantifying glutamate and GABA

Both GABA and glutamate pose additional technical challenges in quantification. The spectral peaks associated with GABA are small due to its low abundance, multiplet splitting, and overlap with signals from more abundant metabolites[332]. MRS-quantified GABA likely reflects extracellular GABA rather than synaptic GABA in vesicles where protons are shielded from the static magnetic field due to macromolecule binding[333]. Extracellular GABA likely mediates basal inhibitory tone by acting on extra-synaptic $GABA_A$ receptors[334,335]. Tonic inhibitory signalling

dampens the excitability of nearby neurons, perhaps acting alongside local release of inhibition to sharpen/tune excitatory cortical outputs by allowing only preferred stimuli to drive membrane potential above threshold[197].

Glutamate quantification has been shown using both single voxel and 2D spectroscopy[336,337], but linking glutamate concentration to function remains challenging. Glutamate is distributed across multiple pools (neuronal cytoplasm, presynaptic vesicles, and within the synapse). Furthermore, it is closely related to its metabolic precursor glutamine, with rapid astrocytic uptake of extracellular glutamate and conversion to glutamine[338].

Resolving the overlapping peaks of glutamine and glutamate at 3 Tesla is challenging, and total Glu+Gln (or Glx) is often reported. When associated with brain function, glutamate has been more typically associated with wider or more distant brain network connectivity, though few studies have addressed the motor network, and the technical limitations of single voxel spectroscopy remain[339].

To advance this question, I will interrogate the functional significance of finely spatially resolved GABA and glutamate in a multimodal dataset from various studies in healthy physiology. This will test the link between local neurochemical excitability and motor network function. I will also apply this technique in a cohort of patients with ALS, as well as presymptomatic carriers of high-risk genes for ALS, integrating both fMRI and MRSI data to search for disease-related alterations in motor system neurochemical and functional excitability.

2.4 Study design and analysis considerations

2.4.1 Clinical heterogeneity

The presence of a core ALS pathomechanism such as local M1 hyperexcitability in early disease is likely to cut across variable patient populations. However, brain motor networks are likely to differ between individuals[314], and the effect of disease is likely to depend on the body regions affected, rate of progression, duration of disease, and degree of functional impairment. Though the scanner itself imposes

some criteria for patient ability to transfer and lie flat safely, heterogeneity in ALS neuroimaging studies is inevitable and can be mitigated by performing subgroup analyses to isolate early disease[232], or modelling multiple clinical parameters as covariates[340,341]. In Chapter 3 I have used ALSFRS-R, disease duration, and rate of progression as covariates, and collected detailed clinical data including side of onset, cognitive screening, and full neurological examinations.

Examples of subgroup-focused studies include bulbar[342], extrapyramidal[343], and predominantly upper-motor-neuron ALS[344]. In Chapters 5 and 6, I inspect a genetically homogeneous subgroup associated with *C9orf72* repeat expansions.

Single-centre neuroimaging studies are, however, generally underpowered to explain clinical heterogeneity. While combining clustering and modelling disease progression can produce plausible subtypes and staging from cross-sectional data in ALS, this requires hundreds of datasets[134], generally sourced from large multi-centre collaborations. Similar benefits could be obtained without subsuming individual research questions and priorities through preparation of open datasets for collaborative analyses incorporating specific technical expertise[345].

2.4.2 Opening the presymptomatic window

Chapter 6 will focus on the development of integrated multimodal biomarkers of motor network excitability in currently healthy individuals who may carry *C9orf72* expansions. Large multi-centre cohorts 'enriched' for genetic risk to future disease have been constructed in Huntington's disease[346], Alzheimer's dementia[347], and FTD[348] with the aim of discovering early disease biomarkers, modelling their progression to phenoconversion, and guiding therapeutic trial recruitment[349]. In ALS too, various cohorts have been organised nationally (USA - pre-fALS, and France - PREV-DEMALS), with ongoing work on international harmonisation (NiSALS).

Already, a burgeoning literature has highlighted differences in white matter microstructure[350], subcortical structure volume[351], regional metabolism[352] and network functional connectivity[353,354] in asymptomatic *C9orf72*-HRE carriers. These differences span decades before disease onset, and may even extend to developmental differences in the motor system influenced by the mutation. In Chapters 5 and 6, I will test the hypotheses that cortical hyperexcitability is present prior to disease onset in *C9orf72*-HRE carriers in a 'transition' stage. Furthermore, I will investigate the relationship between motor cortex hyperexcitability and wider motor network connectivity in *C9orf72*-HRE carriers.

2.4.3 Power analysis

Given practical considerations such as resource constraint, scanner availability, and access to clinical populations, neuroimaging studies have often been performed as (underpowered) samples of convenience. Power analysis is helpful to guide study design in maximising power to detect a given effect size[355]. Though post-hoc use has been criticised[356], power analysis can also be used to contextualise results, especially negative findings or replication failures. In Chapter 3, I analysed an existing dataset. I have reported a post-hoc power analysis in section 3.4.2. In Chapter 5, I have presented a power analysis for the dataset collected. This dataset is likely to contribute to future consolidated multi-centre datasets of patients with C9orf72-associated disease and presymptomatic individuals.

2.4.4 Analysing and sharing data

The analyses presented in this thesis are generally of large and noisy data types. I have considered how to perform statistical analysis most robustly within my work, as well as how to make the work openly scrutable in future.

Where I have performed statistical analyses of voxel-wise or region-wise data, I have considered type I errors - demonstrated by post-mortem salmon brain 'activity'[357]. I have addressed these concerns by choosing analyses guided by prior

hypotheses and using validated statistical tools that apply multiple comparison correction[358] or mitigate the issue through non-parametric permutation inference[359].

I will also aim to produce open data artefacts from my thesis work[360], including code[361,362], anonymised statistic maps, and analysis pipeline notes/READMEs[363]. As discussed in Chapter 6 and the final conclusions, the clinical translation of neuroimaging findings will increasingly depend on efforts to generalise and validate complex statistical and machine learning techniques.

The hunger of a dragon is slow to wake, but hard to sate.

— The Wizard of Earthsea, Ursula K. Le Guin

3

Motor system excitability and function are remodelled with ALS disease progression

Contents

3.1 Background

3.1.1 Cortical and motor network excitability in ALS

Abnormal cortical excitability is a consistent finding across ALS subtypes. Paired-pulse TMS shows lost physiological short-interval cortical inhibition (SICI) in the motor cortex in early ALS[178,179,181], prior to the onset of lower motor neuron deficit, and shortly before symptom onset in high-risk gene carriers[180]. Reduced extracellular GABA levels in the ALS motor cortex are shown directly through MR spectroscopy[202] and reduced $GABA_A$ receptors through ^{11}C-flumazenil binding[364]. Post-mortem data also point to selective depletion of $GABA_A$-ergic interneuronal signalling[199,200].

While GABA signalling is generally inhibitory at a given synapse, it has an important role in maintaining the synchronous excitability of the motor cortex when the 'inhibitory gate' is lifted for voluntary movement (Section 1.3.1). GABA signalling also mediates complex tuning of motor system output between hemispheres for bimanual and planned tasks (Section 4.1.3).

Glutamatergic excitation induced toxicity is also implicated in ALS. CSF glutamate is elevated in 40% of ALS patients - a subgroup characterised by spinal onset, greater functional impairment and rapid progression[365]. In model systems, hyperexcitability produces motor neuron toxicity through pathways including upregulation of calcium permeable AMPA receptors[366], calcium-dependent endoplasmic reticulum stress, and mitochondrial dysfunction.

Altered excitability may not be limited to the motor cortex, with somatosensory cortex[367] and more widespread excitability alterations reported[368]. In addition to local disinhibition, wider brain dysfunction could occur through disruption of long range, often inhibitory, projections in the motor system[194]. Dynamic compensatory network re-organisation or recruitment may also occur with disease progression[238].

3.1.2 What has fMRI revealed about ALS?

As summarised in Section 1.3.3, work using functional imaging has had a major impact in ALS, demonstrating BOLD hyper-activation in early disease[233], evolution with disease progression[235,238], and working towards integrated clinically useful biomarkers[239]. Both the resting state and a range of hand, bulbar, and cognitive tasks have been studied. As discussed in Section 2.2.6, tasks specifically drive networks of interest, while resting state protocols are feasible in individuals with more functional impairment. Resting state typically has lower signal-to-noise ratio and analysis is more complex. As my focus is on **motor network** excitability, I chose to work with a task fMRI dataset in this chapter.

3.1.3 Choosing an analysis technique - model-based vs. data-driven

Hypotheses relating to the amplitude of activation in relation to finger movement can be relatively simply tested using model-based techniques. In task fMRI data analysis, this is a well validated technique. Voxel-wise analyses generally fit the data in each voxel against a model generated by convolving the assumed haemodynamic response function against the hypothetical timecourse of activation generated by the task. This is a simple and powerful technique that is well suited to localising the activation corresponding to a given function and performing group level comparisons[358]. However, there are advantages to loosening the assumptions made regarding the timecourse of activation. A data-driven technique such as independent component analysis allows multiple statistically independent signal components to be separated without the need for a timecourse to be specified[260,369]. This technique can extract components corresponding to a task, and may in this case be more resilient to between-group haemodynamic function variability[370] - though the probabilistic ICA technique used still builds in some biological assumptions regarding tissue type and haemodynamic response function shape[260]. Applying ICA to decompose the BOLD signal spatially and temporally additionally allows network analysis of fMRI data - specifically of within-motor network connectivity[371].

Defining network nodes in this way may further reduce the risk of bias versus manually specified regions-of-interest. In summary, I applied both model-based and data-driven approaches to address different questions regarding motor activation and motor network connectivity in task fMRI data in ALS.

3.1.4 Hypotheses

In this study we revisit task-fMRI in ALS, analysing a large, well characterised, dataset including patients with ALS, those with PLS, and healthy controls. Studying this large dataset allowed several key outstanding issues in the field to be addressed. Given the challenges in replicability, and previous findings in small, highly selected cohorts, I initially tried to replicate previous findings of spreading activation in ALS. Given the ongoing uncertainty of the status of PLS (a useful model of 'pure' UMN ALS vs. a separate clinical entity), I compared task-related activation in this group too. My key hypotheses were as follows:

1. Cortical disinhibition causes higher overall motor cortex activation and more widespread activation with finger movement in ALS and PLS.

2. Cortical disinhibition causes higher widespread activation in movement inhibition in ALS and PLS.

3. The activation associated with finger movement and movement inhibition are reduced with disease progression and functional decline in ALS and PLS.

4. ALS and PLS are both associated with increased within-motor network functional connectivity in task-fMRI data.

5. The functional connectome derived from motor task-fMRI undergoes reorganisation with disease progression and loss of function in both ALS and PLS.

3.2 Methods

3.2.1 Participants

Study participants were recruited to the Oxford Study for Biomarkers in MND (BioMOx2). ALS and PLS patients were reviewed (MRT and KT) and diagnosed according to consensus criteria (2000 revised El Escorial "definite", "probable" and "possible" ALS) at a tertiary referral centre[21]. Healthy control participants had no history of neurological or psychiatric disease, and no family history of ALS. Demographic and clinical characteristics of all participants are summarised in Table 3.1.

		ALS	**Healthy control**	**PLS**
n		45	19	10
Age, mean (SD)		60.3 (9.9)	61.4 (12.8)	62.5 (14.4)
Sex, n	F	10	11	2
	M	35	8	8
Handedness, n	L	5		
	R	35	19	9
	Missing	5		1
ALSFRS-R mean (SD)		39.2 (5)		38.5 (3.7)
Disease duration (months), mean (SD)		30.7 (23.4)		144.3 (164.3)
Progression rate (Δ ALSFRS-R / month) mean (SD)		0.4 (0.3)		0.2 (0.2)
Site of onset, n	Both legs			3
	Bulbar	10		
	LLL	7		5
	LUL	7		
	RLL	9		1
	RUL	10		
	Right side	1		
	Unknown	1		1

Table 3.1: Demographics table for participants with task-fMRI data from BioMOx2 study.

3.2.2 MRI data acquisition

MRI data was acquired on a single Siemens 3T Magnetom TrioTim scanner at the Oxford Centre for Clinical Magnetic Resonance Research (OCMR), using a

32-channel head coil. A T1-weighted magnetisation prepared rapid gradient echo (MPRAGE) sequence was acquired with 1mm isotropic resolution (TR=3000ms, TE=4.71ms, flip angle=8. Whole-brain blood oxygen level dependent (BOLD) MRI data was acquired during the performance of a motor task using a 2D EPI sequence (TR = 3000ms, TE = 28ms, 3mm isotropic resolution, 10min duration x 2 blocks). A fieldmap was also acquired using a gradient echo imaging sequence (3.5mm $\times$ 3.5mm $\times$ 3mm).

3.2.3 Motor task

Participants were instructed to perform a Go-NoGo motor task designed to investigate motor activity in relation to lateralised motor preparation and execution. An initial lateralisation cue with a shaded indicator pointing towards the side on which to prepare to move was presented for 200ms 3.1. After an interval of either 1 (short wait) or 2 (long wait) seconds, in 80% of trials a Go (green circle) was presented, with NoGo (red target) cues in the remaining 20%. In response to a Go cue, participants were instructed to press a button using the index finger of the hand on that side, and not to move in case of a NoGo cue. A randomised inter-trial interval followed (beta distribution [$\alpha = 2$, $\beta = 5$], interval 2 - 6 seconds). Trials were delivered in a random counterbalanced order of Left/Right directions, and short/long inter-stimulus intervals. Stimuli were presented and cue/response timings recorded using the Psychtoolbox3 MATLAB toolkit[372]. Two blocks of 80 trials each were performed for each participant.

3.3 Analysis

3.3.1 Image preprocessing

Image analysis was performed using the FMRIB software library (FSL)[373]. First, structural T1 images were bias field corrected, brain extracted and registered to MNI152 standard space as part of the *fsl_anat* pipeline. BOLD images were preprocessed using the *FEAT* tool[259]. This included motion-correction, brain extraction, high-pass temporal filtering at 100s full width half maximum (FWHM),

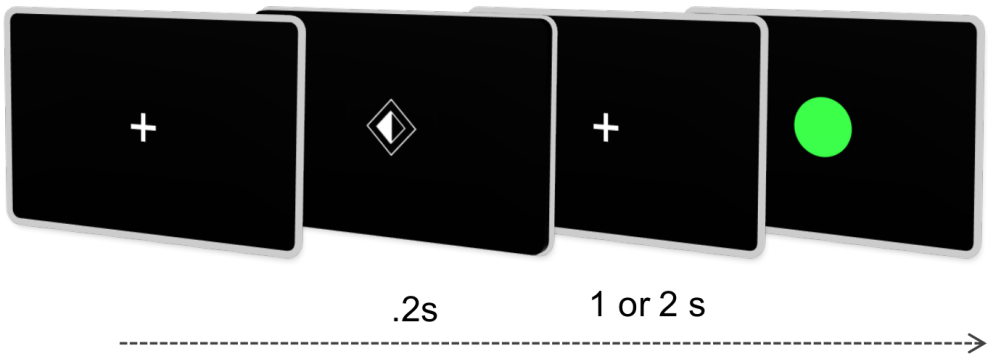

Figure 3.1: On-screen visual cues for the Go/NoGo task. The figure illustrates a trial in which the left hand is cued (inside of diamond is filled) followed by a Go target (NoGo targets coloured red).

unwarping using fieldmap data, and two-step image registration to MNI152 standard space. Diffusion-weighted imaging data used in exploratory analyses was also registered to MNI152 standard space by combining linear registration from native DWI to native structural space using *epi_reg* with the nonlinear registration generated by *fsl_anat*.

3.3.2 Voxel-wise statistics using a general linear model (GLM)

For the FEAT analysis, the task was modelled in the following parts. Separate explanatory variables (EVs) for right and left pointing cues were modelled by convolving the time window between lateralisation cue delivery and the response time (button press) for correct Go trials on that side with the haemodynamic response function. This task model encompassed both movement preparation and execution, which occurred within a short enough timescale for the haemodynamic response to be overlapping. For correct NoGo trials, the EV was modelled using a time period after the NoGo cue was calculated using the mean response time on correct Go trials for that participant. Incorrect trials were modelled as EVs of no interest - i.e. a time-course corresponding to incorrect trials was not included in of subsequent statistical testing.

The contrast parameter estimate (COPE) maps for each lower level contrast were combined across the two task runs using a fixed-effects FEAT analysis.

Group level statistics was then performed using a mixed effects analysis (FLAME 1+2)[358]. This would account for differences in reaction time between participant groups by allowing different group variances. Contrasts for each group mean (ALS, PLS, control), between-group differences, and covariate effects of ALSFRS-R and disease duration within the ALS group were modelled. Where significant findings involved lower level contrasts that subtracted EVs e.g. Go(Right) - Go(Left), the direction of change is ambiguous. Therefore, the mean time-series associated with each EV being subtracted was extracted from the largest significant cluster and plotted.

Z (Gaussianised T/F) statistic images were thresholded using clusters determined by $Z > 3.1$ and a (corrected) cluster significance threshold of $p = 0.05$[374].

3.3.3 Independent component analysis

In this task design, multiple neural processes of interest (movement preparation, execution and response inhibition) are likely to overlap temporally. To address this, I performed a data-driven independent component analysis (ICA). This technique separates mixed data into independently distributed spatial activity patterns without explicitly requiring a time-series model[260]. While typically used with resting-state fMRI data, it can be applied to more complex task designs where explicit time-series specification is challenging or undesirable.

Preprocessing steps prior to ICA were similar to those performed prior to GLM analysis with the exception of image registration - this was not performed at this stage. First, functional data was decomposed using single subject independent component analysis (FSL MELODIC)[375]. This tool decomposes each subject's data (space x time) into a set of maximally statistically independent spatial components (space x components) with associated time-series (components x time). At this stage, the dimensionality is automatically calculated by the tool to maximise explained variance.

Each subject's independent components (ICs) were classified and noise components removed using FMRIB's ICA-based X-noiseifier (FIX)[376,377]. FIX was run with a classification threshold of 20, and removal of motion confounds enabled. Classifier weights used were those derived from training on the Whitehall II imaging study "Standard" dataset. This dataset is similar to ours in both participant characteristics (older adults) and acquisition parameters (TR = 3s, resolution = 3mm isotropic, no spatial smoothing, 100s FWHM highpass temporal filtering). The cleaned output from FIX was then smoothed using a 5mm FWHM Gaussian kernel, and aligned to standard space using the affine matrix and nonlinear warp output by FEAT for the GLM analysis.

Group-level ICA was also run using MELODIC using a temporal concatenation approach. This approach concatenates all subjects cleaned, smoothed functional data in the temporal direction (space x time). The data is decomposed into a set of maximally statistically independent group-level spatial maps. At this stage, dimensionality was set to 100 to allow sufficient separation of large-scale brain networks to allow network analysis without decreasing reliability[378]. Similar dimensionality has been used in previous work, albeit with larger datasets[379]. This value was chosen based on this previous literature in a clinical dataset, and produced plausible splitting of the motor network into sub-components in my analysis. This dimensionality allowed the study hypotheses regarding reorganisation of the functional connectome to be tested. Example IC spatial maps are shown in Figure 3.2. Group ICs were then mapped onto individual subjects' preprocessed and cleaned fMRI data using the first stage of dual-regression[380]. This produces one time-series per group IC per subject, allowing the network of correlations between these time-series to be investigated within and between individuals.

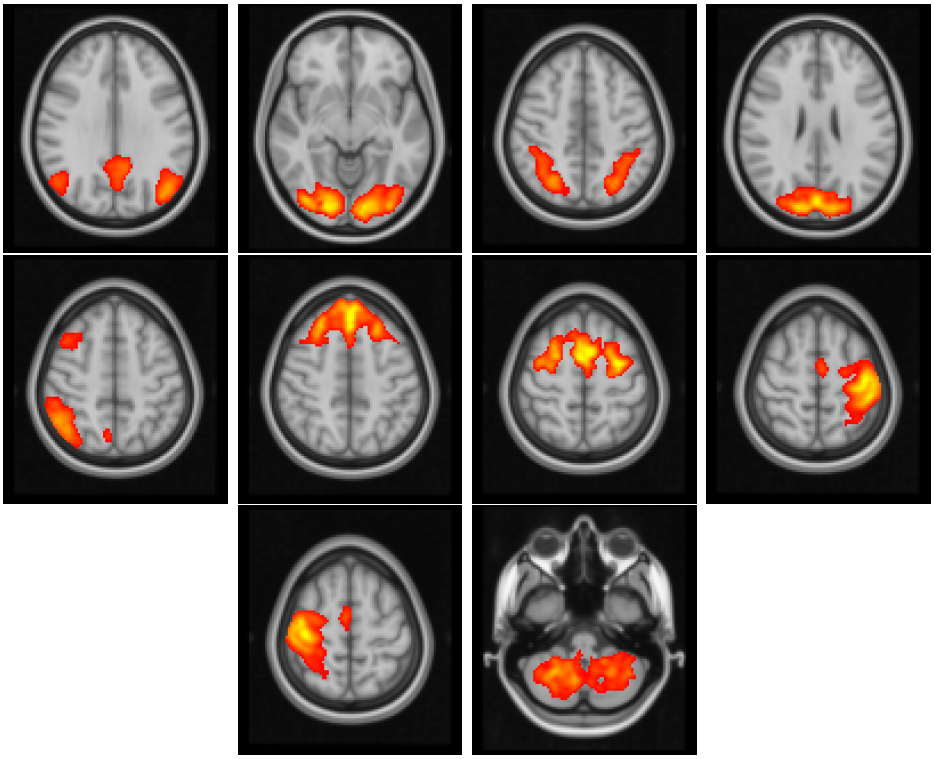

Figure 3.2: Selected independent component spatial maps (z-statistic images) resulting from group ICA.

3.3.4 Network modelling and cross-subject statistics

Generating single-subject and mean functional connectomes

Functional connectivity network analysis was performed using FSLNets (v0.6.3)[381]. Group level ICs were inspected and 72 were manually categorised as noise components based on their spatial distribution (white matter, physiological noise, MRI or movement artefacts) while the remaining 38 ICs were designated nodes in the network matrix (netmat or connectome). The network matrix is a Node x Node correlation matrix, with each element representing the correlation between the corresponding time-series of activity in this pair of nodes. I used partial correlation coefficients to regress out confounding correlations between groups of similar nodes to generate estimates of direct node × node functional connectivity. These partial correlation coefficients are derived through Ridge Regression in FSLNets (rho = 0.01) and converted from Pearson correlation r-values into z-statistics with Fisher's transformation[382]. The 38 nodes were reordered according to a hierarchical clustering

of the group-average full correlation netmat using Ward's method implemented in Matlab to generate the functional connectome.

Between-group statistics and clinical correlation

Using FSLNets, each subject's connectome was unwrapped into a single row with each element representing a network edge between two nodes. Rows for all subjects were stacked to create a Subject × Edges matrix. Each column (i.e. each network edge) in this matrix was tested for between-group differences, and covariate effects of disease duration (from symptom onset), functional score (ALSFRS-R) and disease progression rate (ΔALSFRS-R from onset/time from onset) were tested using a linear regression in FSLNets. As patients with PLS tend to have much longer disease duration than those with ALS, they were not included in the clinical covariate tests. Non-parametric permutation inference using the FSL randomise tool with 5000 permutations was used to correct for multiple comparisons (family-wise error, FWE) across all edges. Results that are significant at FWE-corrected $p < 0.05$ are reported. Followup analyses of cortical thickness and white matter tract integrity corresponding to these findings were performed - these are described in Section 3.6.1.

3.3.5 Exploratory follow-up analyses

After finding motor network nodes underwent changes in connectivity with loss of function in ALS, I performed several exploratory analyses to test the following hypotheses in brain regions corresponding to motor network nodes whose connectivity is remodelled with loss of function in ALS (Selected motor network nodes):

- Selected motor network nodes show reduced cortical thickness (as a marker of disease severity)
- Selected motor network nodes show altered corticospinal tract integrity
- Loss of corticospinal tract integrity is correlated to within-motor-network functional connectivity

Full details of the exploratory analyses performed are summarised in Section 3.6.

3.4 Results

3.4.1 Behavioural outcomes

Mean response time and response accuracy (Button press for Go, no button press for NoGo) were calculated for each trial type. For Go trials, accuracy was high for all three groups (ALS - 97%, Healthy control - 98%, PLS - 97%). NoGo trial accuracy was lower but above 90% for all three groups. Response times were slower in the patient groups for Go trials (ALS - 0.58s, PLS - 0.63s, Healthy control - 0.53s). The results split by trial type are summarised in Figure 3.15.

3.4.2 Task related cortical activation

Go conditions All groups showed a pattern consistent with motor activation (Figure 3.16). Consistent with previous work, I observed that areas activated were qualitatively more widespread in ALS than in healthy controls. However, in the movement (Go) conditions, there were no significant differences between the groups after multiple comparison correction. Representative slices of the group mean activation maps in the Go-Left, Go-Right and NoGo conditions are shown in Figures 3.3, 3.16, and 3.17.

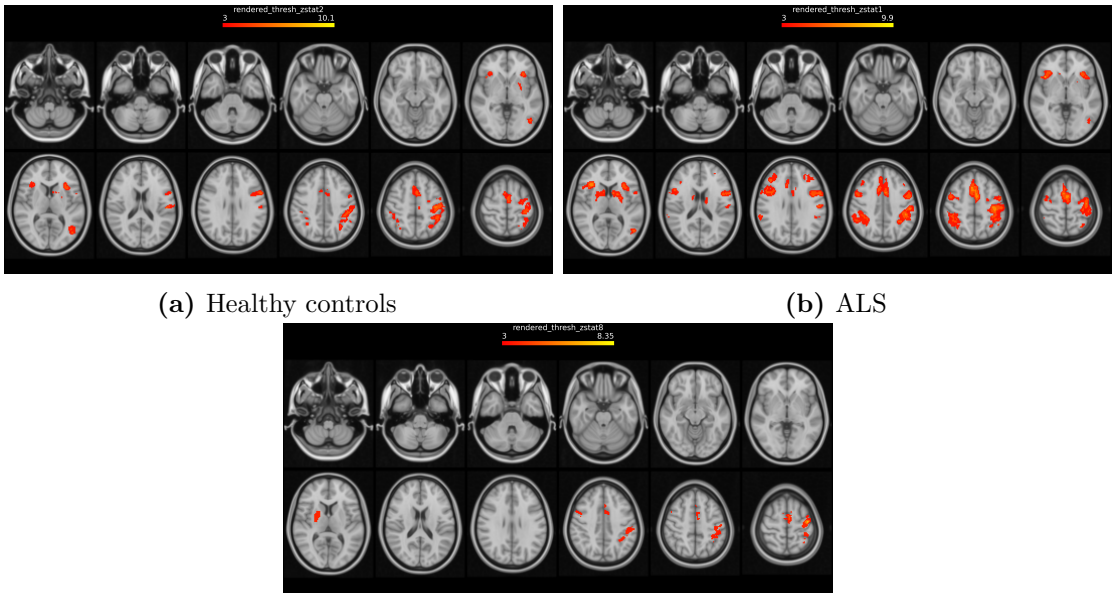

(a) Healthy controls **(b)** ALS

(c) PLS

Figure 3.3: Mean activation in the Go - Right condition.

To contextualise this negative result, I performed a power analysis to compare this result to Mohammadi et. al 2011[232]. They demonstrated an effect size of 16.6% in contralateral motor cortex activation, reporting this as a significant result with uncorrected p-values. I found a similar effect size of 19% (peak voxel t = 14.5 for ALS mean, t = 12.1 for control mean). However, with the group sizes for this comparison (45 ALS, 19 healthy controls), this analysis achieved power of 56% - calculated using G*Power[383] for the t-values reported by Mohammadi et. al., with standard deviation of 0.5.

NoGo conditions

There were significant differences in activation in successful NoGo trials between participants with PLS and the other groups. These are summarised in Figures 3.4a and 3.4b. Participants with PLS showed significantly increased activation in the right insular cortex and left frontal cortex in comparison to controls during the NoGo condition. For this condition, PLS patients also showed significantly increased activation than ALS patients in the insula bilaterally and the left parietal cortex.

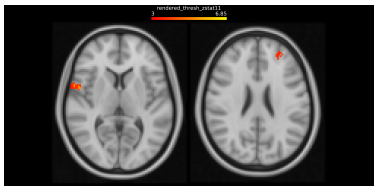

(a) PLS > controls

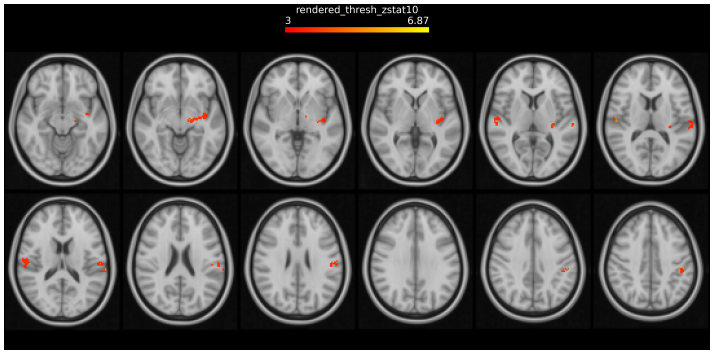

(b) PLS > ALS

Figure 3.4: Significant results for the NoGo condition, thresholded at z>3 and corrected for multiple comparisons at p>0.05.

Clinical correlation

The activation associated with Go(Right) trials was associated with disease progression rate (ΔALSFRS-R / disease duration in months), with significant clusters in the right anterior cingulate cortex/medial frontal cortex and left superior temporal gyrus

($p < 0.05$ after voxel-wise correction for multiple comparisons). These regions were not activated (negative COPE) in slow progressions, but activated in ALS patients with rapid disease progression. Locations of significant clusters and scatterplots of mean contrast parameter estimate (COPE) for right finger movement against progression rate are shown in Figure 3.5

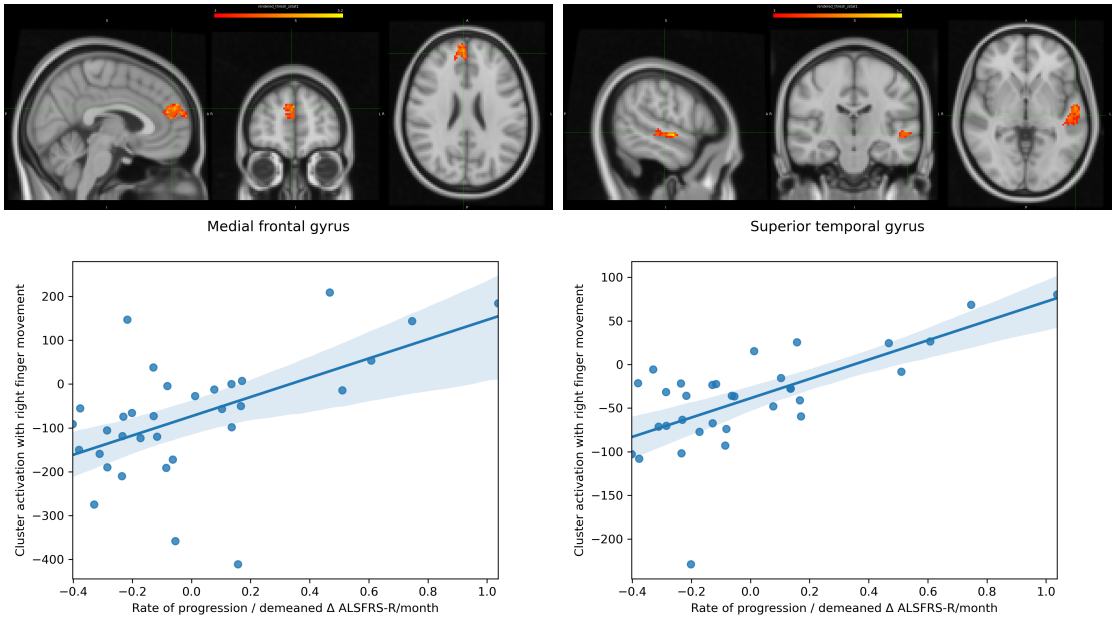

(a) Right medial frontal gyrus **(b)** Left superior temporal gyrus

Figure 3.5: Regions where activation related to right finger movement is correlated with disease progression rate in ALS.

Furthermore, the difference condition Go(Right) > Go(Left) was negatively correlated with disease duration in a region of the left cingulate gyrus (Figure 3.6) ($p < 0.05$ after voxel-wise correction for multiple comparisons). This difference resulted from decreased activation to right finger (contralateral) movement with longer disease duration, while activation of this region to left finger (ipsilateral) movement does not change.

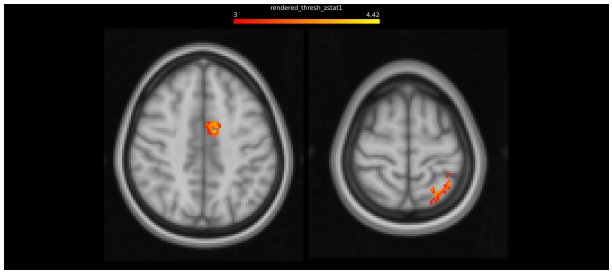

(a) Thresholded statistic map.

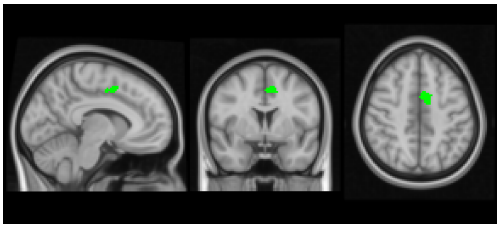

(b) Largest cluster

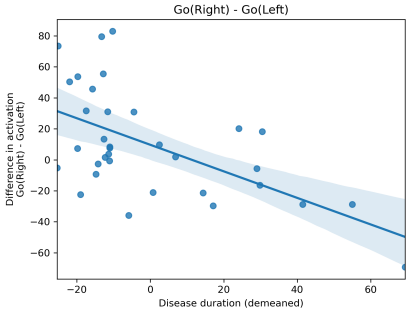

(c) Go(Right) > Go(Left) vs. ALS disease duration.

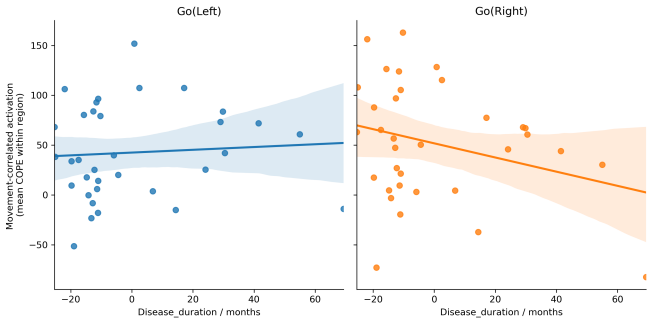

(d) Individual Go(Left) and Go(Right) conditions.

Figure 3.6: Results from voxel-wise correlation of Go(Right) > Go(Left) condition with disease duration in ALS patients, thresholded at z > 3 and corrected for multiple comparisons at p > 0.05. Scatterplots show mean COPE within largest cluster against disease duration.

3.4.3 Between-region network connectivity with ICA/FSLNets

Across all subjects, the network connectivity matrix derived from task-fMRI data showed a distinct clustering pattern to previous work applying the same technique to resting state data[379]. Notably, nodes corresponding to motor areas in both hemispheres were found in different clusters (Figure 3.7), likely reflecting the task design (right and left movement occurred at different time points).

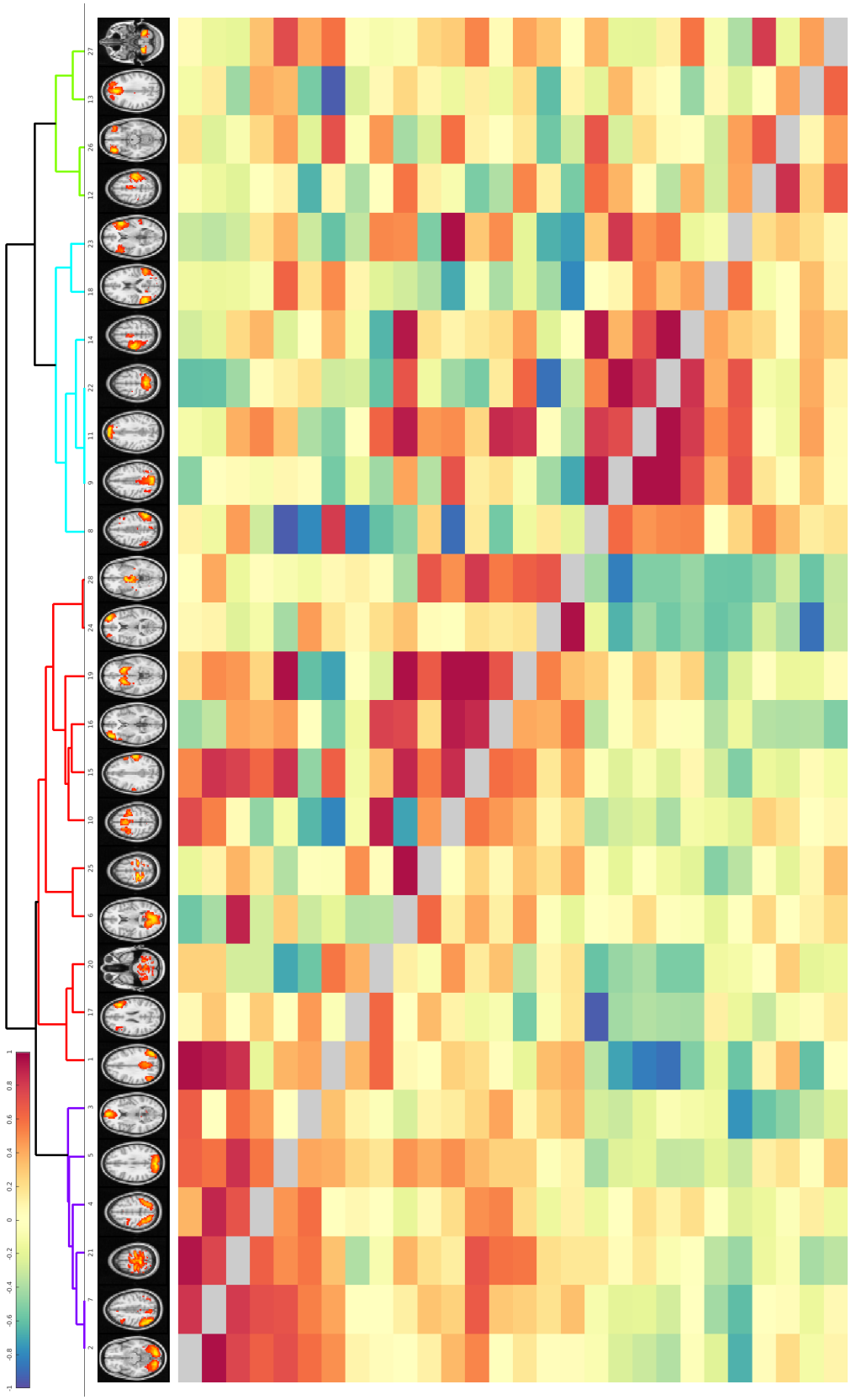

Figure 3.7: The task functional connectome estimated for all participants. Z-statistics for the full correlation (below the diagonal) and partial correlation (above the diagonal) were computed for the nodes derived from ICA. Nodes are ordered according to hierarchical clustering. Node thumbnails are shown above the correlation matrix.

There were no significant differences in network connectivity found between groups after multiple comparison correction. Several network edges were correlated with ALSFRS-R scores ($p < 0.05$ after multiple comparison correction). The spatial details of the significant nodes are summarised in Table 3.2.

Node	Thumbnail	Name	Peak (x/y/z)	Anatomical location
12		Secondary motor	59/62/65	Bilateral medial precentral gyrus
16		Right primary motor	25/52/64	Right pre/postcentral gyri "hand area"
14		Left primary motor	66/53/67	Left pre/postcentral gyri "hand area"
21		Cerebellum	31/35/12	Inferior cerebellum

Table 3.2: Motor network nodes of interest derived from ICA

First, the connection strength between node 12 "Secondary motor" and node 14 "Right primary motor" increased with worse function in ALS patients. This edge was negatively correlated in patients with better functional rating, and positively correlated in those with worse function. Secondly, the connection strength between node 12 "Secondary motor" and node 28 "Cerebellum" decreased in strength with worse function in ALS patients. This edge was positively correlated in those with better function and negatively correlated in those with better function.

Scatterplots of individual patient edge strength vs. ALSFRS-R for these two significant edges are shown in Figure 3.8a and 3.8b along with the corresponding value ranges for healthy controls and those with PLS.

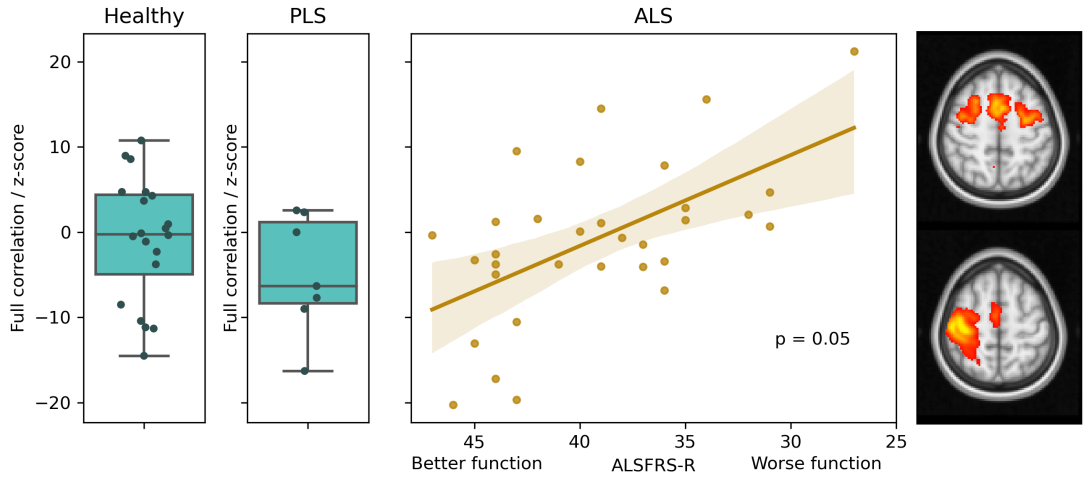

(a) Right primary motor ↔ Secondary motor

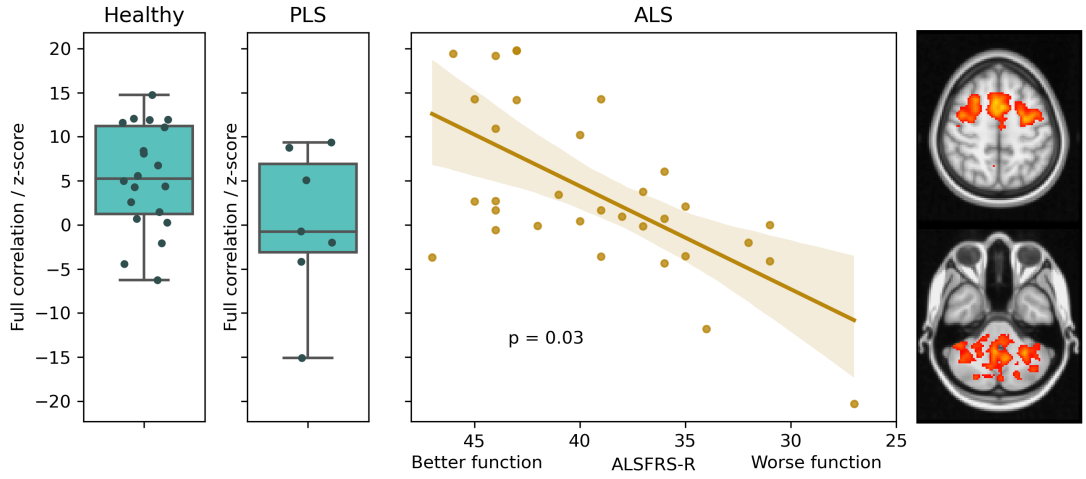

(b) Secondary motor ↔ Cerebellum

Figure 3.8: Scatterplot showing individual edge strength (Full correlation / z score) against functional rating (ALSFRS-R), with a boxplot of healthy control values for the equivalent edge shown for reference. Linear regression has been performed on the scatterplot, with a 95% confidence interval shaded. Multiple comparison correction was performed over all edges using non-parametric permutation inference - p values are corrected.

3.4.4 Followup analyses of regions identified by network analysis

Motor system cortical thickness

I next compared cortical thickness in each node identified by the previous functional connectivity analysis (Table 3.2) between the participant groups (Figure 3.9). Cortical thickness was reduced in the PLS group compared to the healthy controls

in both left hemisphere ROIs as well as in the right hemisphere secondary motor regions. Reduced cortical thickness was found in ALS compared to healthy controls in the left hemisphere primary motor regions but not in the right hemisphere (where the functional connectivity × ALSFRS-R relationship was found previously). No significant correlation was found between cortical thickness in nodes of interest and clinical parameters - ALSFRS-R, disease duration and rate of progression (Figures 3.18, 3.19, 3.20).

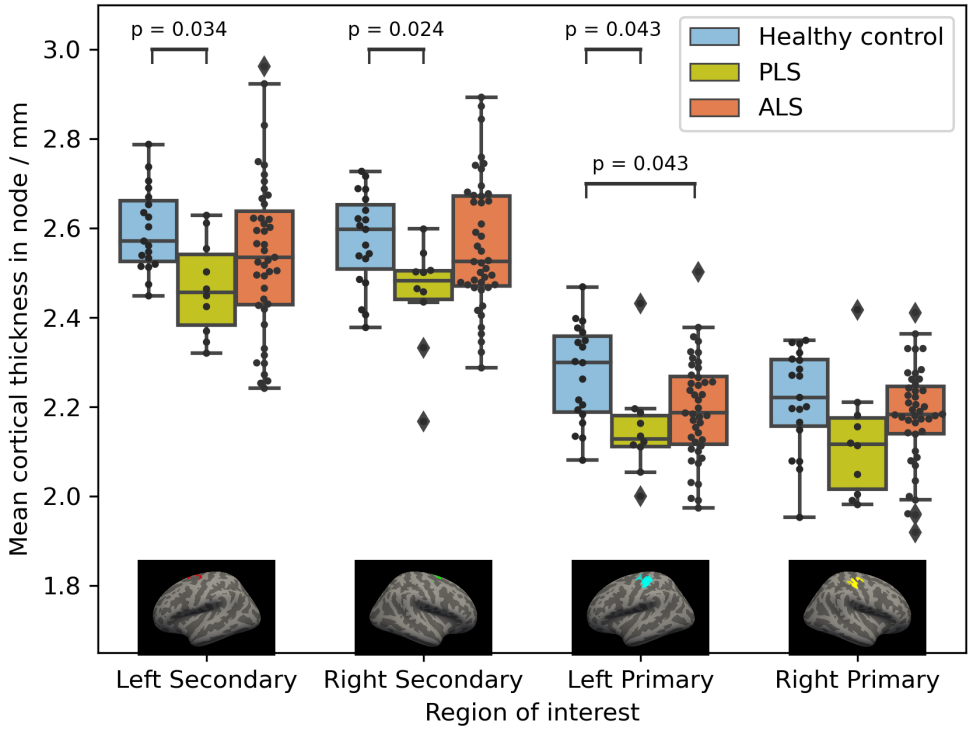

Figure 3.9: Plot illustrating individual observations and spread of FreeSurfer-derived cortical thickness values for each node across the different groups.

Motor system white matter tract integrity

White matter tract integrity (fractional anisotropy [FA]) was reduced in ALS compared to healthy controls in the CST division supplying the Right primary motor node (Figure 3.10). This corresponds to the functional connectivity change previously described involving this node (Figure 3.8a). The integrity of the corpus

callosum connecting the two primary motor nodes was also reduced in ALS compared to healthy controls.

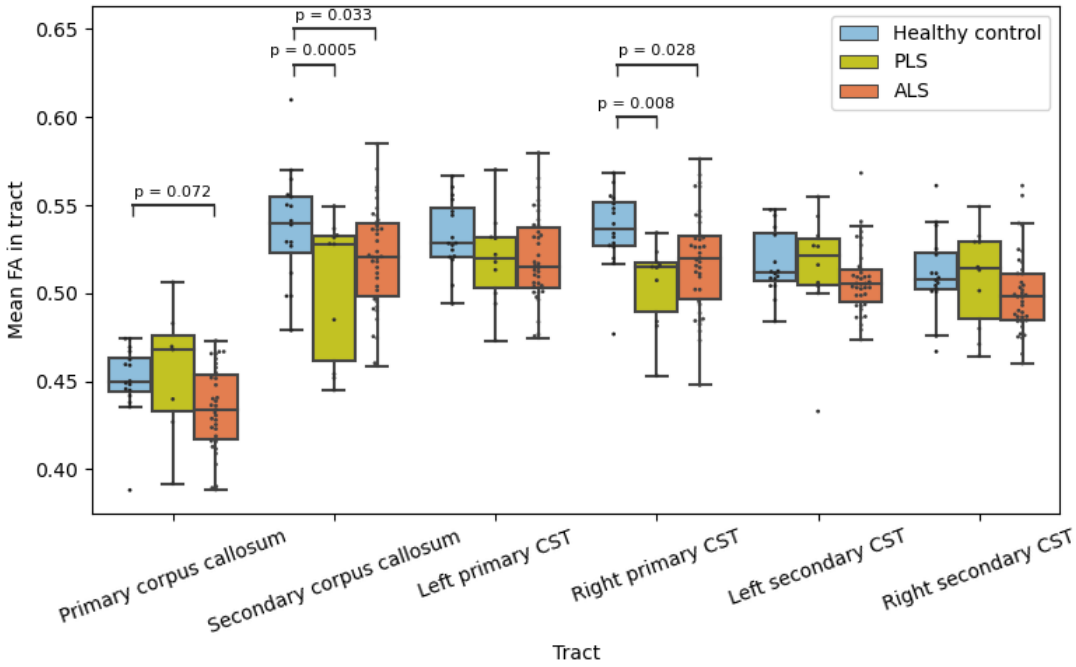

Figure 3.10: FA averaged across entire tract compared between ALS patients and healthy controls.

3.5 Discussion

In this study, I applied task-fMRI to explore disease related cortical disinhibition and brain network remodelling in a large cohort of ALS-spectrum patients.

Motor cortex hyper-activation in ALS may be a task-design dependent phenomenon I first studied the magnitude of BOLD activation on a voxel-wise basis - testing whether this differed between groups and in association with clinical parameters. While I found similar magnitude of increase in peak activation in the contralateral motor cortex in ALS versus healthy controls, this did not survive cluster correction and rigorous correction for multiple comparisons. I performed a power analysis to contextualise this finding in comparison to previous work in the field, finding that even with the larger sample size I studied, power to robustly demonstrate a similar effect size was low (56%). Previous studies demonstrating

task-related hyperactivation have typically employed block designs[232,236,384] with some negative or qualified results[384,385]. Those employing event-based designs have not consistently shown hyperactivation. Stoppel et. al. showed a difference that was not found in a second scanning session (130 trials per session). Mohammadi et. al. found a significant motor cortex cluster for a complex difference contrast (Go trial > successful stop) rather than simply activation[386]. EEG and MEG studies, with finer temporal resolution, demonstrate biphasic differences rather than simply hyper-activation - shallower beta trough with movement but also reduced power in the subsequent rebound[387,388]. Our findings add to the literature, and suggest that future studies on BOLD properties in ALS should consider consolidating datasets to achieve sufficient power, and consider comparing tasks with different temporal profile of activation.

Lateralised hyperactivation in a cingulate motor area in early ALS The voxel-wise analysis demonstrated that a region corresponding to the left posterior cingulate gyrus adjacent to the supplementary motor area activated substantially more to right finger movements than to left finger movements in ALS patients in early disease, but this diminished with disease progression (Figure 3.6). This region's activity was not consistently lateralised in healthy controls. In both monkeys and humans, this region has been implicated in hand movement, with a role for integrating movement and decision making suggested[389,390]. The relationship with disease duration in ALS may point to either pathological hyperexcitability spreading to secondary motor regions in early disease, or an effective compensatory response that is lost with progressive motor system degeneration.

Hyper-activation in non-motor regions in rapidly progressive ALS Activation to right finger movement was higher in several non-motor regions (anterior cingulate, medial frontal, superior temporal cortex) in faster progressing disease (Figure 3.5). The balance of activation between right and left finger movement changed with disease progression within the supplementary and cingulate motor areas. This finding fits with the existing literature suggesting that increased

functional connectivity in ALS is related to disease duration and corticospinal tract integrity[234,302,303]. Our data builds on these findings to suggest that this is most pronounced in aggressive disease - rapid degeneration might break down the inhibitory projections that separate functional networks, with task-related activation breaking through in non-motor regions.

A distinct structural and functional signature in PLS Taken together, the analyses of task-fMRI data, cortical thickness, and white matter tract integrity demonstrate a distinct profile in PLS. There was substantial hyperactivation, particularly in the insulae, in NoGo conditions. This is a novel finding in PLS. While previous studies have demonstrated widespread increased global functional connectivity[391,392], this particular profile of localised hyperactivation has not been reported in PLS. While I did not find significant alterations in the ALS group, a task-EEG study in ALS has also reported hyper-activation of the insula bilaterally with response-inhibition[368]. The precise neural or psychological mechanism assessed by the NoGo condition in Go/NoGo remains controversial. In particular, there is likely a core difference in the cognitive mechanism between Go/NoGo and Stop signal tasks - as demonstrated by the ability of other visual cues to modulate performance[393]. Response inhibition in this context is likely a dynamic executive control process involving choice between several different actions[394]. Interpretation is therefore challenging and may not simply reflect an inhibitory process. I also found evidence for reduced cortical thickness vs. controls in several key motor system nodes in PLS. Taken together, these findings argue for a robust compensatory process that is able to maintain some functions (accuracy of response and response inhibition) in the face of slowly accumulating cortical damage. One notable limitation of this study's findings in PLS is the very long disease course in the participants recruited. Long disease duration has been reported in other neuroimaging work on PLS[344] - this is likely a limitation resulting from the enrichment of slow-progressing disease with extended followup in tertiary services. The resulting survivorship bias is a limitation of this work.

Motor system remodelling correlated to loss of function in ALS Then, I studied the functional connectivity between regions, using data-driven parcellation with ICA. testing whether the functional connectome differed between groups and in association with clinical parameters. I found evidence of reciprocal changes correlated to the functional rating scale in ALS. A node encompassing secondary motor regions is more tightly connected to right hemisphere primary motor regions in patients with worse function, and less connected to a cerebellar node. In the contralateral hemisphere, the corresponding edge strength is associated with integrity of the corticospinal tract division leading to the supplementary motor area. The left primary motor cortex was more affected in ALS in my data, concurrent with previous studies[137,395]. Taken together, these findings suggest a hemisphere-specific pattern of remodelling. The interpretation of this result is limited given the heterogeneity of clinical onset in the included patients (Table 3.1). Future directions include subgrouping patients by side of onset or side more severely affected.

Spread of motor-task related activation to secondary motor regions - premotor, supplementary and cingulate motor regions has been previously reported[231,232,238,396]. My findings dissect this process, identifying a specific remodelling process that, if consistently demonstrated, could be a target for intervention. While non-invasive brain stimulation has thus far been targeted at primary motor areas in ALS[1], novel techniques promise to modulate between-region connectivity[397], a necessary area to explore in ALS.

Overall, my findings further elaborate the heterogeneity of excitability found at different disease stages in time and severity. I applied a task-design that incorporated finger movements under direct monosynaptic cortical control - proposed as the source of a uniquely human vulnerability in ALS. In a large, heterogeneous patient cohort I demonstrated strong clinical correlation of task-fMRI data, implicating non-motor regional activation in rapidly progressing disease, and within motor network remodelling with loss of function. I further contextualised these findings with multimodal imaging data reflecting grey and white matter damage.

3.5.1 Limitations

My analysis is limited in its pseudo-longitudinal design - in a condition where longitudinal imaging data collection is severely limited by progressive respiratory weakness and secretion clearance. As with Braak neuropathological staging, longitudinal trends are being inferred from cross-sectional data. For fMRI to be clinically translated in ALS will require subtyping and staging of degenerative and compensatory processes in large, multi-centre datasets including frequent longitudinal neuroimaging - as done in other neurodegenerative conditions[134,398]. There may be a high degree of inter-individual variability in the specific spatial patterns of compensation that occur in ALS.

Another limitation is the difference in sex distribution between the ALS group and the control group. While activation maps to finger tapping tasks are largely similar in right handed males and females, subtle differences have been reported[399], and future analysis could include sex as a covariate to test for confounding.

Overall, this chapter demonstrates the complexity and variability of task-related fMRI changes in ALS and PLS, adding to the wider process of linking clinical and imaging metrics in fMRI[400].

3.6 Supplemental materials

3.6.1 Cortical thickness and tractography analyses

To follow up the finding of motor network remodelling with functional decline we explored whether this finding could be explained by disease-associated structural damage within the motor system. Neurodegeneration within the nodes identified could result in cortical thinning and altered BOLD properties. Disease associated white matter tract damage might also affect long-range motor projections such as excitatory corticospinal projections or transcallosal projections fine-tuning the output of contralateral nodes. Studies of resting state functional connectivity in ALS have been characterised by difficulty in interpreting findings causally - with equipoise maintained between disease effects and compensatory change. Multimodal MRI data allows this to be unpicked, and multiple lines of causal evidence to be assembled.

Defining nodes of interest

The z-statistic images for the cortical nodes (12, 14, and 16) significantly correlated with ALSFRS-R were thresholded at 80% of the peak value and binarised. As one node (12) encompassed the supplementary motor area and premotor area in both hemispheres, I split this ROI at the midline. The resulting four regions of interest are referred to as **nodes of interest** for the following analyses (Figure 3.11).

Cortical thickness measurement within nodes of interest

First, I assessed grey-matter integrity in the network nodes identified by measuring cortical thickness. Cortical reconstruction and volumetric segmentation was performed from the T1 image with the FreeSurfer image analysis suite (version 7.1.1)[401,402], including brain extraction, registration to standard space, tissue-type segmentation, tessellation of the grey-matter/white-matter boundary and modelling of the surface geometry. The nodes of interest were transformed from MNI standard space into the FreeSurfer standard space (fsaverage) and mapped to the fsaverage grey matter surface (Figure 3.12). For each subject, cortical thickness data was registered to fsaverage space and averaged within each node ROI for each subject.

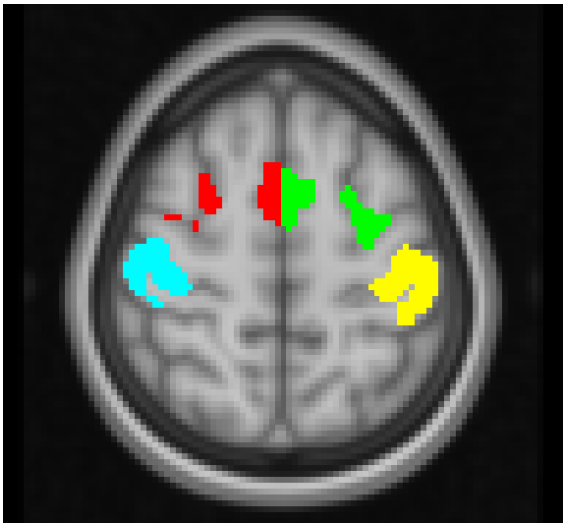

Figure 3.11: Thresholded and binarised masks of regions identified by network connectivity analysis. Cyan - Right motor, Yellow - Left motor, Red - Secondary motor (Right hemisphere), Green - Secondary motor (Left hemisphere).

Tractography using nodes of interest

Then, to assess within motor system tract connectivity, I selected tracts known to be particularly affected in ALS - the corticospinal tract and corpus callosum. The tracts were identified using probabilistic tractography using the XTRACT tool (version 1.4.4) for automating tractography using the probtrackX2 engine from the FSL library. The standard XTRACT protocol for corticospinal tract identification was modified using the cortical network nodes of interest as target masks in separate runs, identifying two divisions of the corticospinal tract (Figure 3.13). The default XTRACT corticospinal tract protocol was otherwise unchanged, including brainstem seed region, exclusion mask and probtrackx2 settings (3000 streamlines, loopback checking, step length 0.5mm, 2000 steps). A representative visualisation of the four divisions of the corticospinal tract generated is shown in Figure 3.14.

The seed, exclusion and target masks are transformed from standard space into each subject's native space using registrations described in section 3.3.1. Tractography is then run in native space as specified. Summary statistics (volume, length, median fractional anisotropy, median mean diffusivity) were generated for each tract using the *xtract_stats* tool with a threshold of 0.02 applied to the tract probability map.

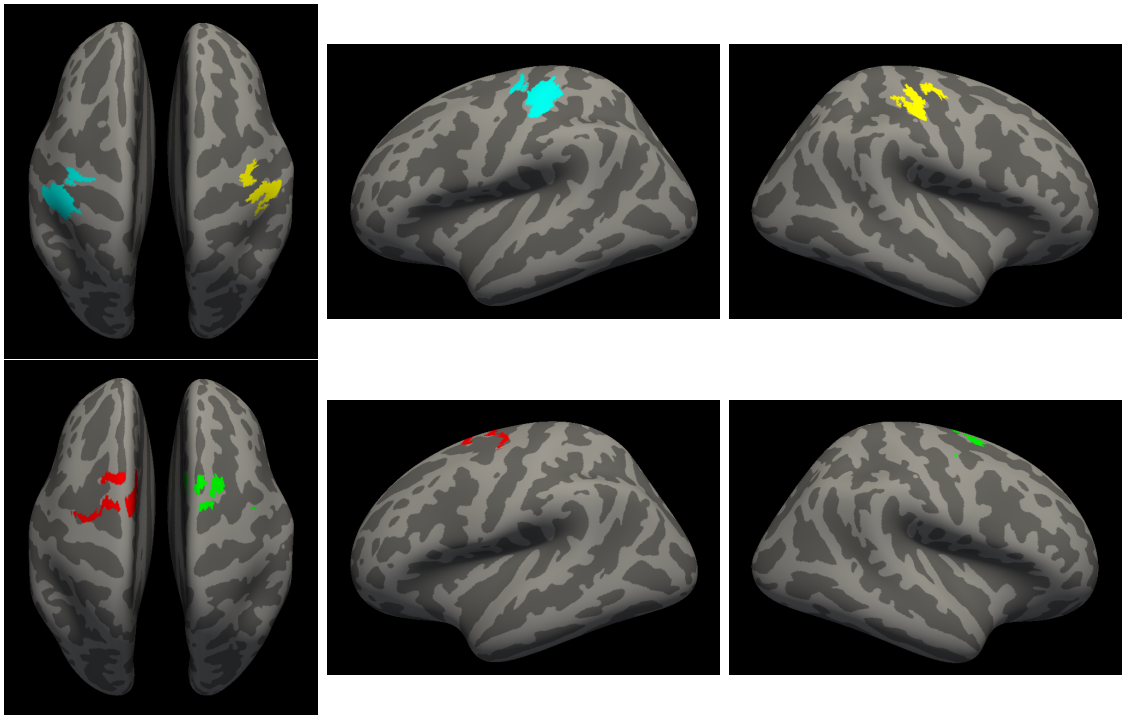

Figure 3.12: Surface ROIs in fsaverage space generated from volume masks in Figure 3.11. Cyan - Left primary motor, Yellow - Right primary motor, Red - Secondary motor (Left hemisphere), Green - Secondary motor (Right hemisphere).

To identify divisions of the corpus callosum corresponding to the nodes of interest, analogous node masks in each hemisphere (e.g. L hemisphere 'motor' node, R hemisphere 'motor' node) were designated as seed and target masks in a custom XTRACT protocol. Exclusion masks were drawn to terminate streamlines travelling down through the internal capsule, as well as across the midline except for a window around the corpus callosum. Tractography was run in both directions (right → left and left → right) and combined. Default probtrackx2 settings were used (5000 streamlines, loopback checking, step length 0.5mm, 2000 steps).

Statistics for exploratory analyses

Statistical analysis was performed using a linear mixed effects model using the *pymer4* Python frontend (version 0.7.6)[403] to the *lme4* R package (version 1.1_21)[404]. Cortical thickness was modelled as the outcome variable. Group, node and their interaction were modelled as fixed effects, while subject was modelled as a random effect.

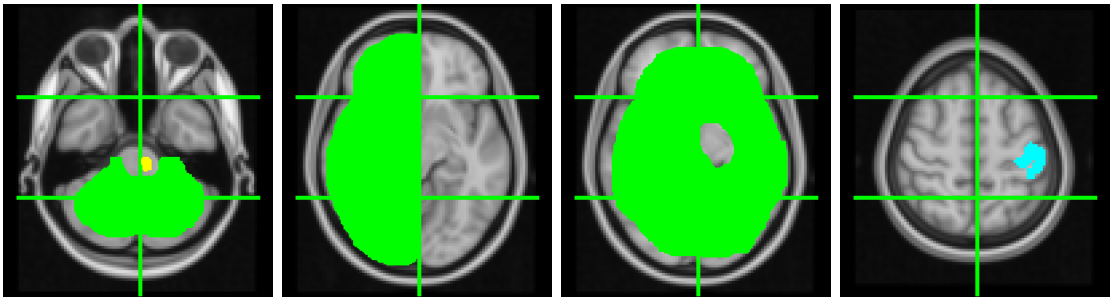

(a) Protocol for left primary motor CST.

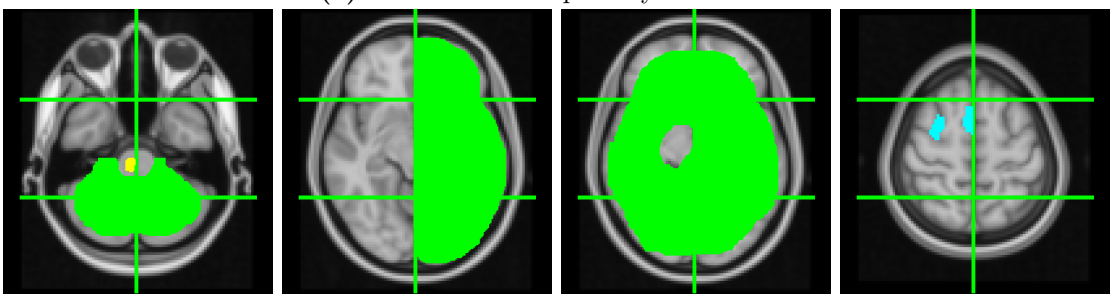

(b) Protocol for right secondary motor CST.

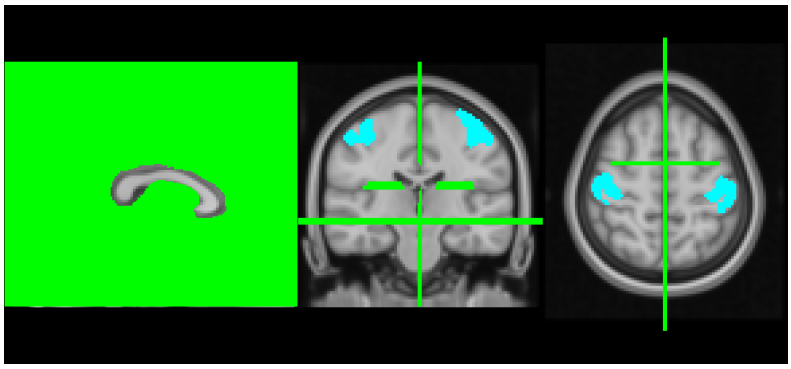

(c) Protocol for primary - primary motor corpus callosum.

Figure 3.13: Standard space masks defining the seed (yellow), exclude (green), and target (cyan) regions for tractography.

$$thickness \sim group * node + (1|subject)$$

For the diffusion data, mean tract FA was modelled as the outcome variable, with fixed effects of group and tract, and random effects of subject.

$$FA_{mean} \sim group * tract + (1|subject)$$

Overall factor effects were estimated using Type III Sums of Squares and Satterthwaite approximated degrees of freedom. For significant effects, post-hoc

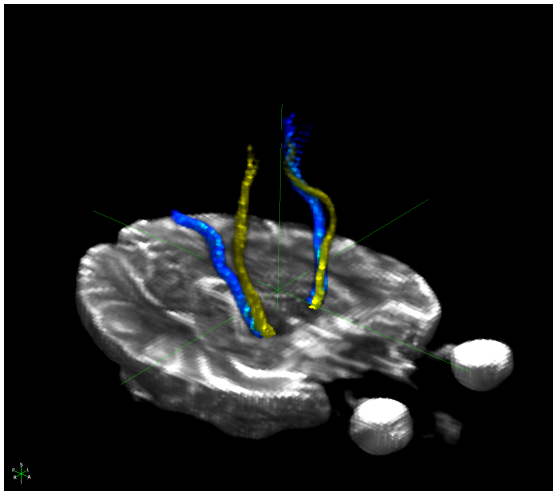

(a) 3d render - oblique

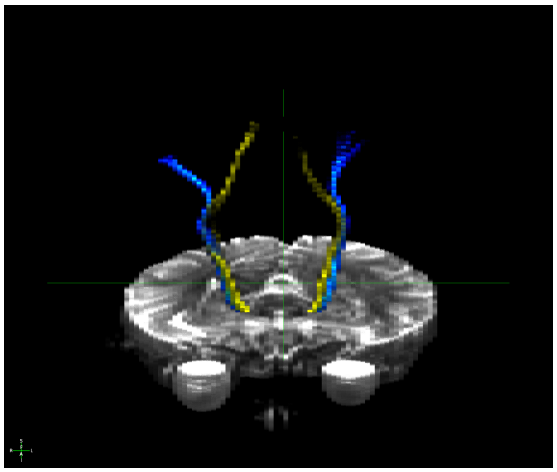

(b) 3d render - front

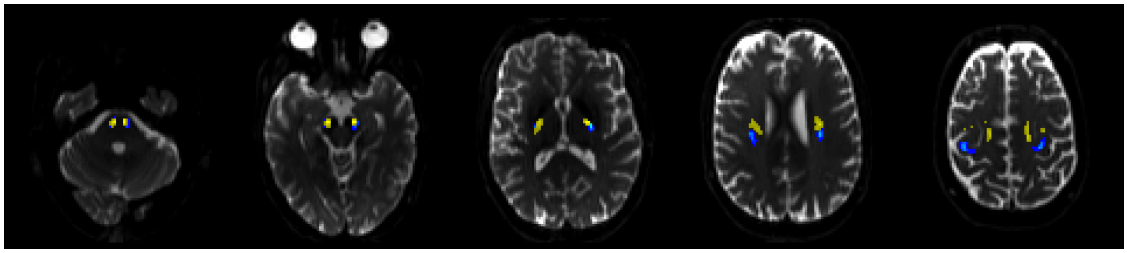

(c) axial views

Figure 3.14: Representative tractography results for corticospinal tracts, colour coded by termination in Primary (Blue) or Secondary (Yellow) motor nodes.

pairwise comparisons were performed using the Tukey HSD method and corrected for multiple comparisons using the FDR method.

3.6.2 Supplemental figures

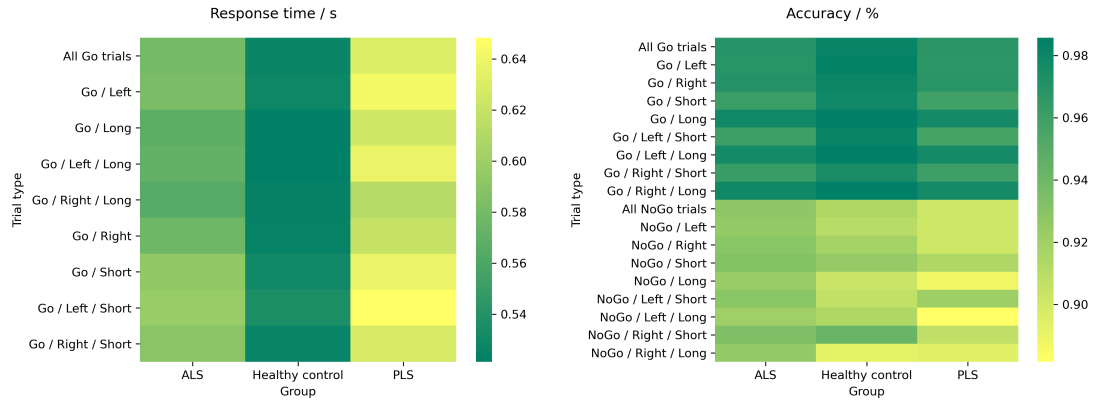

(a) Mean response time / s **(b)** Fraction of correct trials

Figure 3.15: Heatmap of behavioural outcome by group for each trial type.

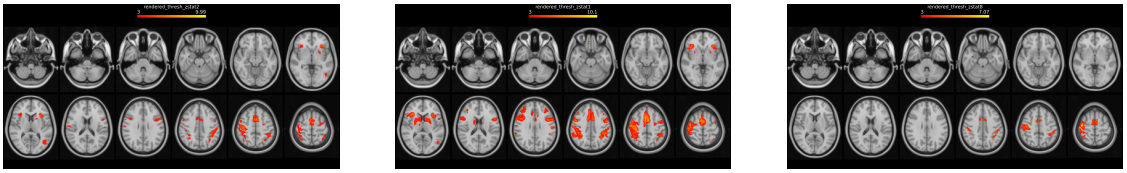

(a) Go - Left - Control **(b)** Go - Left - ALS **(c)** Go - Left - PLS

Figure 3.16: Mean activation in the Go - Left condition for all three groups.

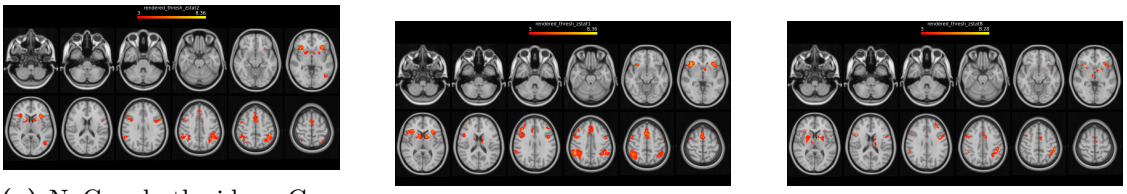

(a) NoGo - both sides - Control **(b)** NoGo - both sides - ALS **(c)** NoGo - both sides - PLS

Figure 3.17: Mean activation in the NoGo condition for all three groups.

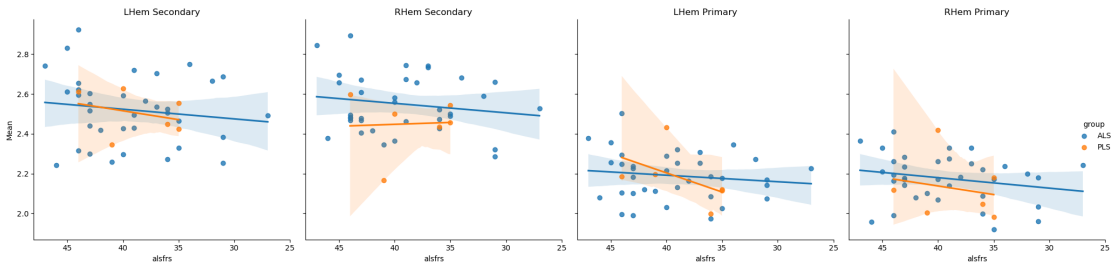

Figure 3.18: Scatterplots of cortical thickness against ALSFRS-R in nodes of interest for ALS patients. Least-squares linear regression and 95% confidence intervals are shown for each plot.

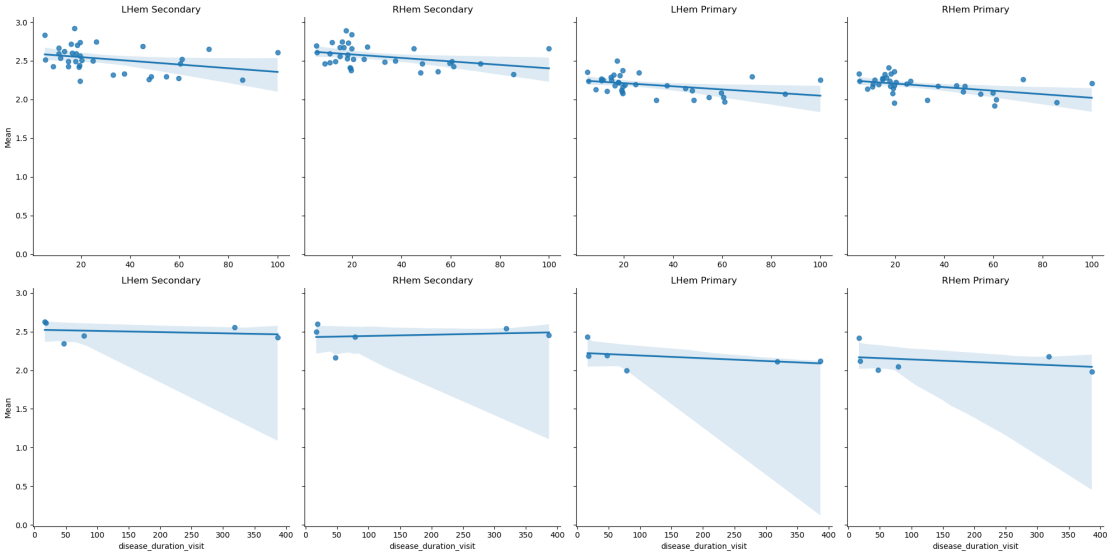

Figure 3.19: Scatterplots of cortical thickness against disease duration in nodes of interest for ALS patients. Least-squares linear regression and 95% confidence intervals are shown for each plot.

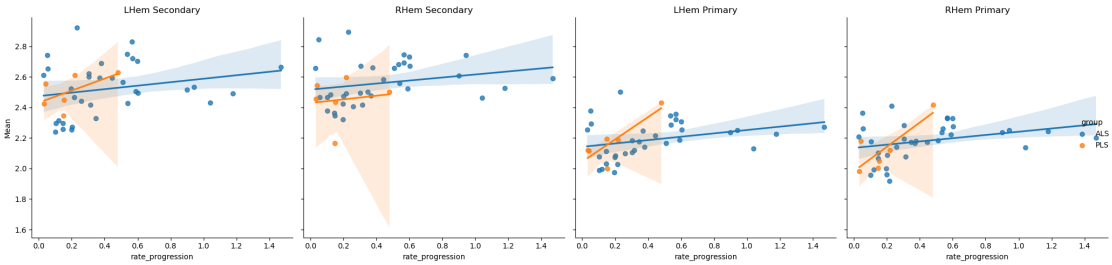

Figure 3.20: Scatterplots of cortical thickness against disease progression rate in nodes of interest for ALS patients. Least-squares linear regression and 95% confidence intervals are shown for each plot.

If you can meet with Triumph and Disaster
And treat those two impostors just the same;

— If, by Rudyard Kipling

4

Mapping physiological motor network excitation, inhibition, and connectivity

Contents

4.1 Background

Almost all human behaviour is controlled by communication within functionally-connected networks of anatomically-disparate brain regions. How connectivity between these regions is controlled, and how this relates to motor function, is incompletely understood. I investigated how local inhibitory and excitatory neurochemical concentrations are distributed spatially across the motor system, and whether this influences motor network connectivity. Of most relevance here are glutamate and γ-aminobutyric acid (GABA), the major excitatory and inhibitory neurotransmitters in the human brain.

4.1.1 Motor function arises from a brain motor network

Functional magnetic resonance imaging using blood oxygen level dependent (BOLD) signal contrast, though strongly affected by vascular properties[227], can be used as a proxy for neuronal activation across the whole brain. BOLD data acquired at rest can be decomposed into resting state networks (RSNs), showing correlated activity over seconds to minutes[228]. Anatomically similar motor networks can be reproduced through motor task functional magnetic resonance imaging (fMRI)[229] (Figure 4.1).

How are these resting networks co-ordinated, and how does network activity relate to motor function? While long range white matter connections define a

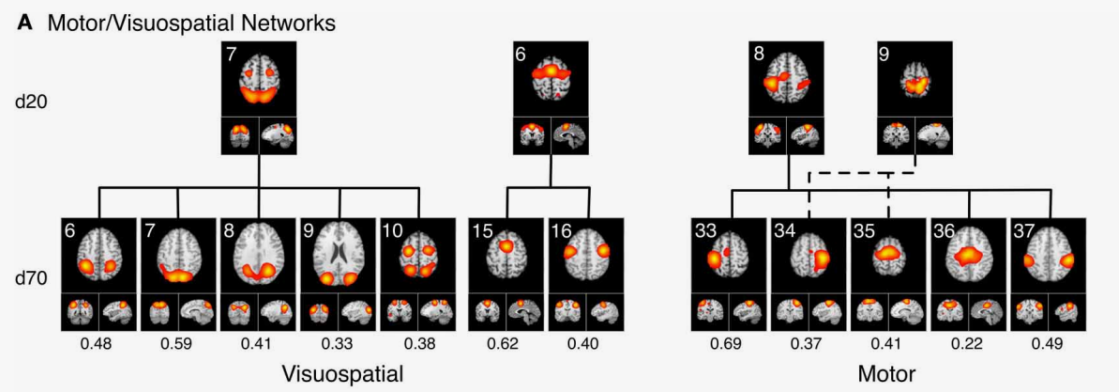

Figure 4.1: Spatial maps derived from independent component analysis that correlate with subjects' metadata from visuospatial and motor tasks. Lower dimensionality (d20) shows brain-wide networks, which become fractionated into constituent nodes at higher dimensionality (d70) - figure reproduced from Ray et. al. Frontiers 2013[230], (CC-BY).

network in space[405], the precise mechanism of functional synchronisation is less well understood. One proposed explanation is that the balance of inhibition and excitation within several key nodes, the primary motor cortices in particular for the motor network, controls wider network function[197]. In this chapter, I will use "node" to refer to a region that is functionally connected to the motor network as a whole. A formal definition of how these regions are derived from a multimodal atlas is given in section 4.3.6.

4.1.2 Inhibition within the motor cortex likely primarily gates excitatory outflow

Within the motor cortex, excitatory pyramidal cells and inhibitory interneurons form multiple microcircuits incorporating both horizontal (within cortical layer) and vertical (between layer) connections[194]. I previously discussed the layer-specific properties and their disruption in ALS in Section 1.3.1. Excitatory inputs to upper layers (2/3) of the motor cortex are processed and amplified within these layers. Excitation descends to deeper layers via pyramidal cells' apical dendrites[195]. Pyramidal cell bodies are densely innervated by inhibitory connections mediated by the $\alpha 1$ subunit of the $GABA_A$ receptor from parvalbumin-positive (PV+) interneurons. With long horizontal projections and fast-spiking properties that allow ongoing inhibition of multiple pyramidal cells, this interneuronal network produces

functional properties such as surround-inhibition, spike-timing synchronisation and tuning to stimulus properties in various cortical regions[196,197]. Some PV+ interneurons demonstrate increased firing immediately prior to the onset of voluntary movement, likely gating premature or inappropriate output[198].

4.1.3 Transcallosal projections tune contralateral motor cortex output

The role of inhibitory signalling in motor function is not confined to the motor cortex, as it both sends and receives information from other motor regions. Specifically, pyramidal cells in the motor cortex project predominantly to the corticospinal tracts, but also to other brain regions. In turn, various motor regions, such as the thalamus, supplementary motor area, premotor cortex, parietal cortex, will send inward projections to influence motor cortex function.

Projections across the corpus callosum to contralateral structures may be particularly relevant to motor function and disease[212]. Each motor cortex fine-tunes the outputs from the other through interhemispheric projections that interact with the inhibitory interneuron network in the other motor cortex[213]. Callosal degeneration and resulting motor dysfunction have also been specifically implicated in neurodegenerative motor system disease[141,214].

4.1.4 Measuring local inhibition and excitation in-vivo

In-vivo, these processes can be non-invasively studied using magnetic resonance spectroscopy. The chemical structure of a molecule influences the interaction between hydrogen nuclei (protons) in the molecule and the static magnetic field of the MRI scanner. This shifts the resonant frequency of these protons, producing characteristic spectral peaks distinct from the main water signal that can be analysed to yield molecular concentration.

MRS allows quantification of **total** concentration of a given neurochemical - across multiple pools including neuronal cytoplasm, pre-synaptic vesicles, within the synaptic cleft, and in the extracellular compartment. This provides a **proxy** measure of inhibitory and excitatory tone (Section 4.1.4).

4.1.5 What is the role of local inhibitory and excitatory tone in the motor network?

These proxy measures of inhibitory and excitatory tone within a given brain region have been shown to be related to behaviours critically dependent on that region. For example, GABA concentration in primary motor cortex (M1) has been correlated to reaction times in healthy controls[192], and decreases in M1 GABA concentration correlate with learning on a subject-by-subject basis[406,407]. Similar relationships have been demonstrated in a number of other brain regions as well[408–410].

Functional MRS studies have demonstrated that excitatory tone as measured by glutamate concentration increases during motor task performance[411,412]. The underlying mechanism remains controversial - changes occurring at timescales greater than several seconds are likely due to altered flux in pathways of energetic metabolism[413]. An alternate explanation for more rapid apparent increase in glutamate is its release from a vesicular compartment where it is less "visible" to MRS due to faster T2* relaxation rate[414]. While this theoretical speculation regarding T2* relaxation rate in humans is not directly correlated with direct quantification in-vivo, some data from guinea pig brain slices may support the idea of "shielded" glutamate[415]. This remains a controversial area in need of more work.

Does inhibitory tone within a brain region influence the connectivity of that region to wider networks?

Local GABA not only relates to behaviour; there is evidence that long-range functional connectivity within networks relates to both GABA and glutamate concentration within key network nodes. For example, functional connectivity within the brain-wide motor resting state network is associated with the degree of

inhibition within the primary motor cortex[416,417]. More generally, local GABA or glutamate concentration within a network node can predict the intrinsic connectivity of associated resting state networks. This has been reported in the default mode network[418], central executive network[419], and in relation to the coupling between networks[420].

In this dataset, I will examine both the baseline spatial distribution of inhibitory tone and its relationship with wider functional network connectivity.

Here, I applied a MRSI sequence that achieves high spatial resolution (5mm × 5mm × 15mm - Figure 4.2) mapping of metabolites across a region of interest encompassing sensorimotor regions corresponding to both hands[330,331] (Section 2.3.3). This is achieved in a scientifically- and clinically-feasible time frame (∼15 minutes), allowing spectroscopy to be performed alongside other multimodal imaging (structural, functional and diffusion MRI).

This rich dataset with spatially-precise neurochemical mapping allows us to better characterise baseline excitability in motor regions of the human brain. More generally, multimodal data allows me to investigate the link between excitability and motor function in normal physiology, ageing and disease (Chapter 5). My specific hypotheses are listed in Section 4.1.6.

Specific design choices and the accompanying rationale are presented in Section 4.2.2.

4.1.6 Hypotheses

As this is a novel approach, I will test a set of basic hypotheses in relation to previously described findings of neurochemical concentration variation by tissue type, brain region, and age to check that my results are plausible. With higher spatial resolution, I will also be able to extend previous analyses into novel domains.

(a) Example volume-of-interest placement

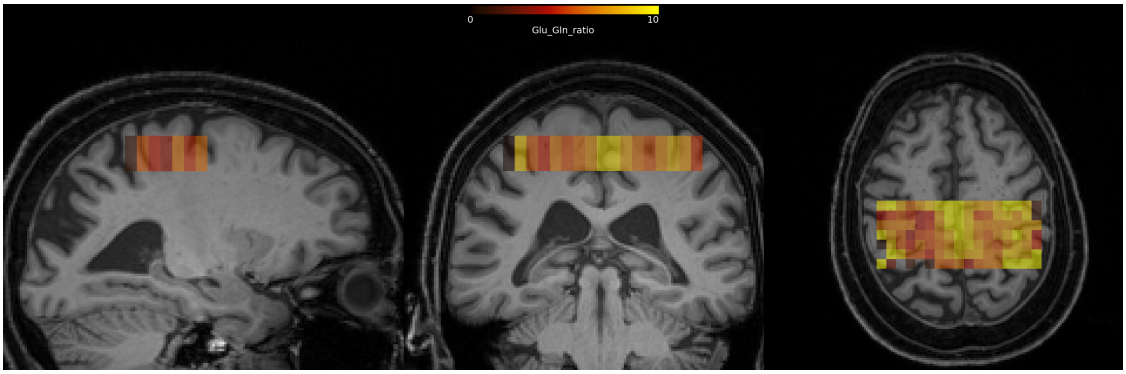

(b) Glutamate+Glutamine concentration (relative to total creatine)

Figure 4.2: Example data from a single healthy control subject. The volume-of-interest is manually placed after structural imaging is acquired to encompass both primary motor cortices. The image of metabolite concentration has spatial resolution of 5mm × 5mm × 15mm.

I will test the following hypotheses in my dataset. Metabolite concentration is analysed in relation to total Creatine ([Metabolite] / [total Creatine]).

Defining the normal range of excitatory and inhibitory neurochemicals in the motor system

Tissue type determines neurochemical profile in the motor system

Differences between grey and white matter have been systematically reviewed for abundant metabolites[421]. NAA, Creatine and myo-Inositol concentrations are higher in grey matter than white, while Choline concentration is higher in white matter. However, these studies have not specifically addressed the motor system. Partial volume effects also produce variability in metabolite quantification that is usually addressed by tissue composition correction[422].

I tested the following hypotheses aiming to replicate previous studies' findings using voxels placed predominantly in grey or white matter. As there is a wide range of tissue fractions covered by the MRSI region of interest, I tested for associations between tissue fraction and neurochemical concentration as follows:

- Grey matter fraction is associated with higher concentrations of NAA, myo-Inositol, glutamate, and GABA than white matter.
- White matter fraction is associated with higher total choline (GPC+PCho) concentration than grey matter.

Neurochemical profile differs between motor network sub-regions

Brain-wide differences in local neurochemical concentration have previously been described using either 2d spectroscopic imaging approaches or placement of multiple single-voxels[421,423–429]. Lateralisation between hemispheres is also of interest in investigating regional functional specialisation in the motor system, though findings have been inconsistent[421,425]. Presumably, cortical dominance explains differences between hemispheres, however as left handed individuals are rarely studied, and under-represented in this dataset too, this remains speculative. I extended this work in the context of the motor network excitation/inhibition balance by testing the following hypotheses:

- Neurochemical profile differs between motor network nodes (primary motor cortex, supplementary motor area, primary somatosensory cortex) and other control regions (cingulate cortex, parietal cortex).
  - NAA concentration is higher in the primary motor cortex than other regions. Based on Tedeschi et. al. 1995, with limited literature found comparing primary motor cortex to other brain regions.
  - Glutamate concentration is higher in the primary motor cortex than other regions. A best estimate based on Tedeschi et. al. 1995, with limited literature found comparing primary motor cortex to other brain regions.

  - GABA concentration is lower in the primary motor cortex than other regions. A best estimate due to limited literature on GABA variation in different brain regions.

- Neurochemical profile in the motor system is lateralised between the hemispheres (higher glutamate and lower GABA concentrations in the left hemisphere than the right hemisphere).

These hypotheses were pre-registered prior to analysis[3].

Exploring the functional role of excitation and inhibition in the motor system

This protocol allows us to correlate neurochemical quantification and functional imaging in the same participants to test the following hypothesis.

- Greater motor network functional connectivity is associated with increased excitatory tone and reduced inhibitory tone on a voxel-wise basis in motor network nodes.

Neurochemical profile changes with age and disease

Changes in neurochemical profile with ageing and neurodegeneration have also been described. With age, NAA decreases and myo-Inositol increases[430–432]. In the neurodegenerative condition amyotrophic lateral sclerosis (ALS), the most consistently reported findings are similar - with reduced NAA and increased myo-Inositol[433]. In the context of this dataset, I tested the following hypotheses related to ageing, and considered ALS and presymptomatic risk-gene carriers in Chapter 5.

- Neurochemical profile in the motor system is correlated with age.
  - Increasing age is correlated with lower NAA, lower glutamate, and higher myo-Inositol concentration in grey matter, white matter, primary motor cortex, and supplementary motor area.
  - Increasing age is correlated with lower NAA, lower glutamate, and higher myo-Inositol concentration on a voxel-wise basis.

4.2 Study participants and MRI protocol

4.2.1 Consolidated MRSI dataset

Data was collected across several study protocols and two Siemens Prisma 3T scanners at the same centre. Individual study aims and study populations are summarised in table 4.1.

Study aim	Condition	Field of view / mm	Sequence time / min	N	Participants
ALS biomarkers	Resting state	85×35×15	13:30	36	18 ALS patients, 18 age matched healthy controls
Drug challenge	Placebo resting state	85×35×15	9:00	15	15 young healthy individuals
Motor task	Pre-task resting state	85×35×15	9:00	15	15 young healthy individuals
Motor task	Pre-task resting state	85×35×15	13:30	16	10 stroke patients, 6 age matched healthy controls

Table 4.1: Individual dataset summary. Healthy control / placebo / pre-task data was used for this analysis.

4.2.2 MRI protocol

MR spectroscopic imaging A novel MRSI protocol was developed to allow rapid acquisition of high resolution MRSI data[331]. Metabolite cycling (incorporating both upfield and downfield signal acquisition) produces simultaneous water and metabolite images. This improves image quality by allowing correction of artefacts due to eddy currents, B0 drift, and subject motion. Fast k-space traversal is achieved through a density-weighted concentric rings sampling trajectory. This also mitigates side lobe artefacts and spatial autocorrelation.

The resulting protocol achieves an in-plane resolution of 5mm × 5mm, sufficiently high spectral quality to quantify low-abundance metabolites (such as glutamate, glutamine), within a feasible time for clinical application. Compared to Steel et. al. 2018, I used a smaller volume-of-interest (VOI) (85mm × 35mm × 15mm) to achieve sufficient signal-noise-ratio for GABA quantification within the acquisition time. Individual voxel dimensions are 5mm × 5mm × 15mm, and the VOI was placed to encompass both primary motor cortices (hand knobs) when scanning. An example of VOI placement is shown in Figure 4.2a. For resting conditions, subjects were instructed to lie still with their eyes open, a visual rest screen was played on the MRI scanner display (landscape scenery in study 1, 2, 4, fixation cross in study 3).

MRSI data was collected along with structural (T1) and resting state BOLD data. Both T1 and fMRI sequence parameters were matched to UK Biobank sequences as follows.

Structural and functional imaging Structural images were acquired using a 3D T1 MPRAGE sequence matched to UK Biobank acquisition parameters[278]. These include 1 × 1 × 1mm spatial resolution, 208 × 256 × 256mm field of view, and in-plane acceleration factor (iPAT) of 2.

Resting state functional MRI was also performed using gradient echo EPI sequences matched to UK Biobank acquisition parameters[278]. These include 2.4 × 2.4 × 2.4mm spatial resolution, 88 × 88 × 64 field of view matrix, 490 timepoints over 6 minutes, TR = 0.735s, TE = 39ms, 8 × multi-slice acceleration, and flip angle 52°.

4.3 Analysis

4.3.1 MRSI processing

The MRSI data analysis pipeline is summarised in Figure 4.3. After reconstruction of the non-Cartesian kt-space data, preprocessing steps of coil combination, phase-frequency alignment, averaging and residual water removal were performed. These

preprocessing steps utilise a custom binary for this MRSI protocol. NIfTI images incorporating preprocessed spectra are generated, allowing fitting and quantification to be performed separately. Then, using the open source FSL-MRS spectroscopy analysis toolbox[434], a linear combination of basis spectra was fitted to the data using Markov chain Monte Carlo (MCMC) optimisation.

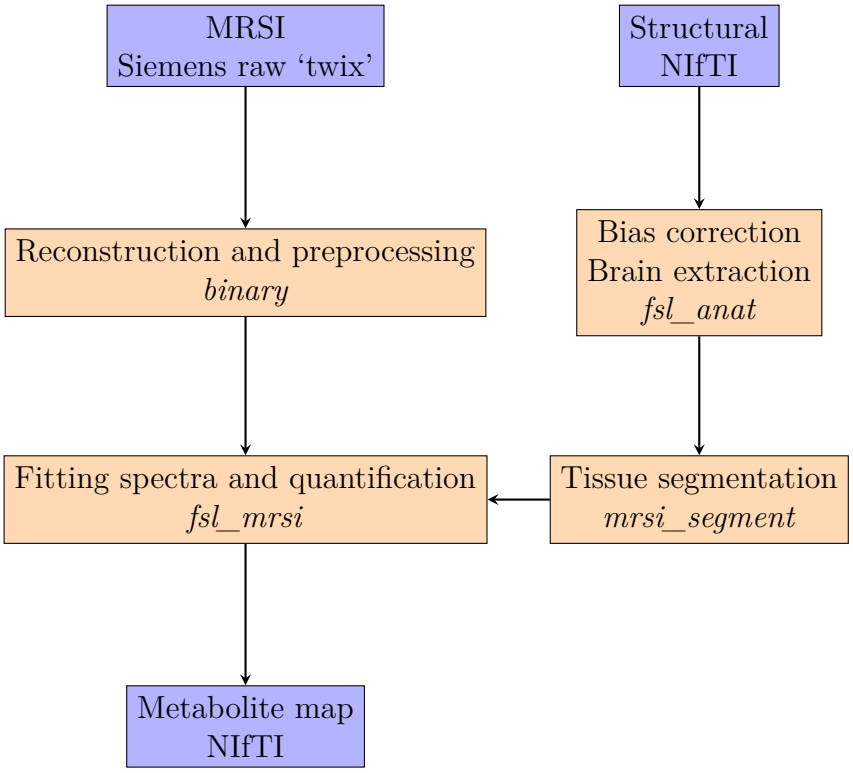

Figure 4.3: Flowchart of MRSI preprocessing and fitting steps

Quality control

Quality control metrics (signal-to-noise ratio, Cramér-Rao lower bound (CRLB) and full-width half-maximum) derived from the FSL-MRS toolkit were reviewed for each metabolite globally. Metabolite quantification was performed using relative referencing (to total Creatine) in FSL-MRS. Best-practice guidance in this field[435] highlights caveats with both relative and 'absolute' or tissue water referencing. Relative referencing may not be appropriate in clinical populations and limits comparison between studies. However, referencing to tissue water is also limited

Name	Brodmann areas	Atlas values	Atlas labels
Motor	4	8	4
Somatosensory	3, 1, 2	9, 51, 52	3b, 1, 2
Parietal	5	36, 37, 39	5m, 5mv, 5L
Cingulate	4	38, 40, 41	23c, 24dd, 24dv
Premotor	6	54, 55, 56, 96	6d, 6mp, 6v, 6a

Table 4.2: Summary of atlas regions selected for subsequent ROI-based analyses

by wide confidence intervals in estimating tissue relaxation time parameters. As such I chose relative water referencing for this thesis analysis.

4.3.2 Structural MRI processing

Structural images were analysed using the *mrsi_segment* tool built into the FSL-MRS package. This applies the *fsl_anat* structural processing pipeline in the FMRIB software library (FSL) to perform pre-processing steps including bias correction, brain extraction[436], registration to standard space[437,438] and tissue segmentation[439]. The resulting tissue composition estimates are used to correct for tissue partial volume effects within the MRSI VOI.

4.3.3 Atlas derived regions of interest

I derived the following regions of interest from the volumetric HCP-MMP1 atlas in MNI space[440,441] by combining the specified labels in Table 4.2. This atlas was chosen for ROIs that are tightly circumscribed to cortical grey matter. In results figures, the regions of interest are labelled as follows - Motor, Premotor, Somatosensory and Parietal in each hemisphere.

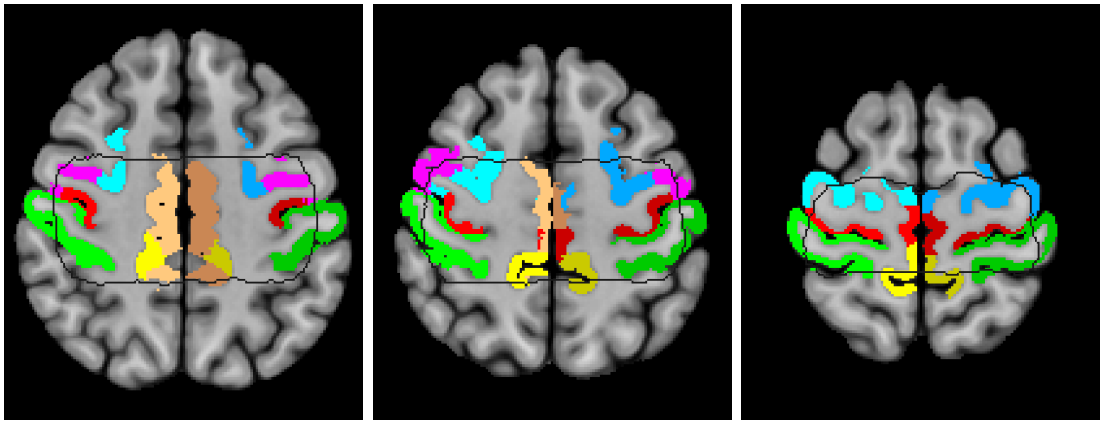

Figure 4.4: Representative slices of standard space ROIs used. Red - Motor, Green - Somatosensory, Yellow - Parietal, Beige - Cingulate, Blue - Premotor. The left hemisphere ROIs are slightly darker than right hemisphere ROIs. The black lines show a region with coverage of at least 10 participants.

4.3.4 Registration technique comparison

Both the native space resolution of the MRSI data (5mm × 5mm × 15mm) and partial-volume effects make inferring differences between tissue types or structures challenging. Furthermore, as discussed above, an atlas with tightly defined cortical grey-matter ROIs was chosen. Imprecise registration could therefore dilute the power of my standard space analyses. I tested registration from native to standard space using the following techniques:

- FNIRT (both default and optimised UK Biobank configurations)
- ANTs (SyN) (default python configuration)
- AFNI @SSwarper pipeline
  - default settings (wsinc5 interpolation algorithm)
  - linear interpolation

To compare the techniques in a practical manner for this dataset, a semi-automated analysis was performed. Grey matter regions of interest corresponding to both hand areas (hand knobs) were drawn manually on a single representative axial slice of each subject's T1 image. These masks were then transformed to

standard space using each technique. The techniques were compared using an overlap heatmap generated by summing the standard space masks. The same process was done with a mask of the MRSI volume-of-interest to visually assess the degree of deformation. For this dataset, the AFNI @SSwarper tool with default settings performed best, and so is used for further analyses.

4.3.5 Resting state fMRI processing

Resting state fMRI was analysed using the FMRIB software library (FSL). Pre-processing steps including brain extraction, motion correction and fieldmap unwarping were performed through FEAT. Independent component analysis of the single subject data was performed and components classified as noise were removed (MELODIC, FIX)[376,377]. Resting state fMRI data was co-registered through two steps - linear registration of subject functional data to the subject structural image (*align_epi_anat*), followed by non-linear registration from subject structural space to MNI152 standard space (3dNwarpApply using the AFNI @SSwarper output warp). Smoothing was performed with a 5mm full-width-half-maximum (FWHM). Group level resting state networks (spatial independent component maps) were generated through independent component analysis of concatenated subject data (MELODIC). Subject specific RSNs were produced using dual regression[380,442]. This two stage process regresses the group spatial maps into each subject's 4d data to give a subject time-course for each RSN (stage 1). Then those time-courses are regressed into the same 4d dataset to get a subject-specific spatial map of correlation with each RSN (stage 2).

4.3.6 Statistical analysis

Defining the normal range of excitatory and inhibitory neurochemicals in the motor system

Neurochemical concentrations differ globally between grey matter and white matter To display the global trends in neurochemical I plotted neurochemical concentration against tissue fraction for all voxels passing quality control. Tissue fraction was derived from the *fsl_anat* pipeline used in section 4.3.1. I then fit a

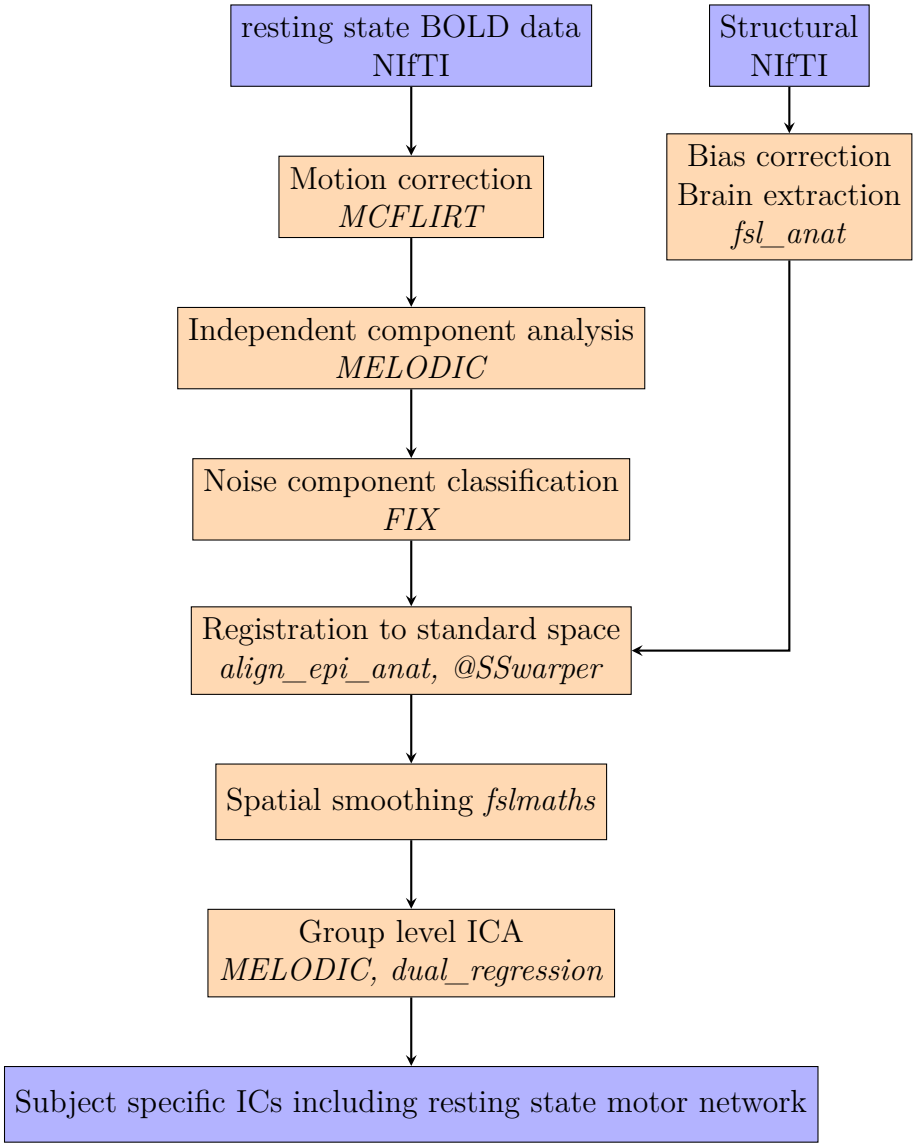

Figure 4.5: Flowchart of rs-fMRI processing

linear mixed effects model with metabolite concentration as the outcome variable, fixed effect of metabolite, metabolite * white matter fraction and metabolite * grey matter fraction interactions, and nested random effects of participant and voxel location in MRSI region of interest. I reported significant effect sizes for the interactions tested where relevant to specified hypotheses.

Neurochemical concentrations differ between motor network nodes The ROIs were compared using a linear mixed effects model, with metabolite concentration as the outcome variable, fixed effect of 'metabolite', random effect of

'node', and a node * metabolite interaction. I performed post-hoc *t*-tests using the Satterthwaite approximations to degrees of freedom if significant to identify the specific metabolites contributing to differences and the direction of effect.

Neurochemical profile changes with age I tested for a correlation between metabolite concentration and age on a voxel-wise basis for metabolites meeting quality control criteria using non-parametric permutation inference with the FSL tool PALM, treating multiple metabolites as different modalities[359]. This produced per-metabolite probability maps of those brain regions showing correlation with age.

Investigating lateralisation of neurochemical profile in the motor system

I tested for lateralisation of the neurochemical profile by comparing ROIs across both hemispheres using a linear mixed effects model, with metabolite concentration as the outcome variable, fixed effect of "hemisphere", fixed effect of "metabolite", random effect of "node", hemisphere * node and node * metabolite interactions. I performed post-hoc *t*-tests using the Satterthwaite approximations to degrees of freedom if significant to identify the specific metabolites contributing to differences and the direction of effect.

Exploring the functional role of excitatory and inhibitory tone in the motor system

Glutamate and GABA were quantified on a voxel-wise basis for each MRSI dataset. These maps, representing voxel-wise excitatory and inhibitory neurotransmitter tone, were analysed along with the corresponding motor resting state network using the FSL tool PALM[359]. Using non-parametric permutation inference, this tool tests for significant correlation between the input glutamate and GABA maps and motor network connectivity represented as a voxel-wise EV. This analysis is performed at 2mm resolution due to the standard space and reference chosen for group ICA.

4.4 Results

4.4.1 Registration technique comparison

The standard space overlap obtained after warping native space hand-labelled ROIs is shown by technique in Figure 4.6. While all techniques tended to produce good overlap in the standard space hand area, the best result (qualitatively - tightest overlap or quantitatively - largest value at peak) was obtained using the default @SSwarper tool.

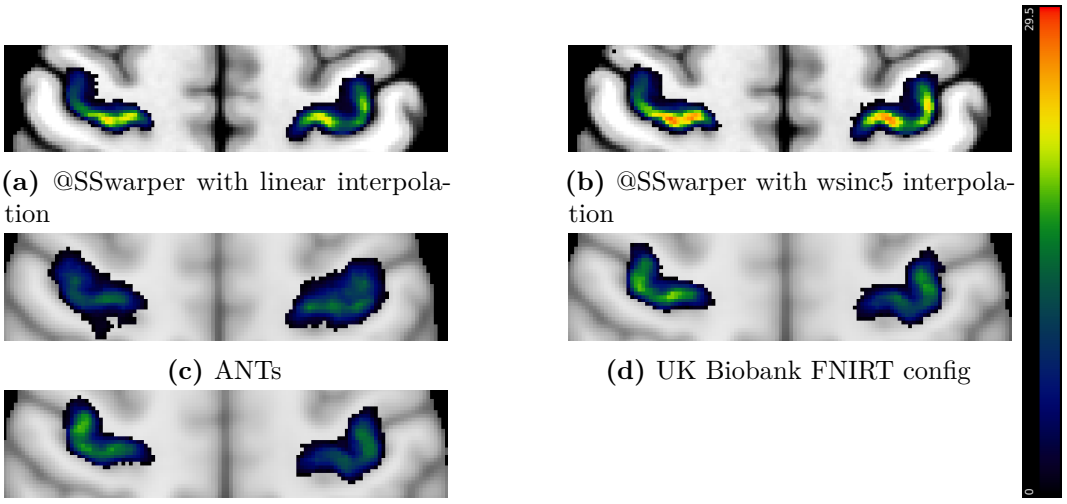

(a) @SSwarper with linear interpolation

(b) @SSwarper with wsinc5 interpolation

(c) ANTs

(d) UK Biobank FNIRT config

(e) Default FNIRT config

Figure 4.6: Comparison of registration techniques. A manually masked hand knob slice in each hemisphere was transformed to standard space for each structural scan. The number of masks overlapping is represented by colour. Panels using @SSwarper are overlaid on the AFNI MNI152 standard space.

Similarly, the standard space overlap of the entire MRSI volume is shown in Supplemental Figure 4.22. This shows qualitatively the degree to which different techniques deform the region of interest. ANTs is the least aggressively deforming, @SSwarper the most, with FNIRT intermediate. While there are tradeoffs between these techniques in performance between cortical and subcortical regions[443], I chose @SSwarper for this dataset going forward due to its better performance (both in terms of peak overlap and qualitatively) in the motor system hand area.

4.4.2 Quality control

Selecting metabolites with good data quality

To select the metabolites with sufficiently good data quality for further analysis, I first derived the mean relative Cramér-Rao lower bound (CRLB) for each metabolite across the entire dataset (Table 4.3). Metabolites with a 75th percentile relative CRLB greater than or equal to 25% were excluded from further analysis. Metabolites surviving this step are highlighted in the table.

	relative Cramér-Rao lower bound (CRLB)			
	mean	50th percentile	75th percentile	90th percentile
Ala	470.26	174.61	999.00	999.00
Asc	133.44	27.03	53.28	452.31
Asp	29.05	13.22	17.08	25.95
Cr	32.56	10.40	13.67	21.83
Cr+PCr	8.06	3.52	4.36	5.75
GABA	42.54	16.30	23.66	42.68
GPC	19.26	6.26	8.21	15.54
GSH	31.47	10.25	13.36	22.47
Glc	88.91	23.11	39.75	106.27
Glc+Tau	38.27	13.94	20.48	34.84
Gln	58.46	16.77	24.67	53.40
Glu	31.58	7.30	9.92	15.45
Glu+Gln	23.15	5.81	7.46	10.68
Gly_1	408.58	105.45	999.00	999.00
Ins	12.69	5.98	7.37	11.35
Lac	419.60	138.38	999.00	999.00
MM09	22.06	12.75	17.12	28.68
MM12	236.30	69.03	183.29	999.00
MM14	203.35	62.31	149.45	999.00
MM17	105.97	33.87	59.05	143.78
MM21	297.26	60.50	529.33	999.00
NAA	13.08	4.24	5.11	6.92
NAA+NAAG	13.65	3.95	5.03	6.70
NAAG	173.21	26.89	67.88	999.00
PCho	817.48	999.00	999.00	999.00
PCho+GPC	8.31	4.73	5.82	8.97
PCr	42.19	11.55	15.70	27.19
PE	282.61	51.70	357.14	999.00
Scyllo	39.89	13.37	19.34	35.08
Tau	574.42	999.00	999.00	999.00

Table 4.3: Table showing mean and 50th/75th/90th percentiles of relative Cramér-Rao lower bounds for each metabolite fitted by default in FSL-MRS with this basis set. Those highlighted in green meet my overall quality control criterion (75th percentile CRLB $<$ 25%) and are kept for further analyses.

Filtering individual voxel data

Then, I proceeded to check data quality at the level of the individual voxel. Absolute CRLB was chosen for voxel-wise filtering as the overall dataset including Chapter 5 includes a clinical subgroup as well as a wide age range. Filtering using a relative CRLB threshold has been criticised due to the potential of both introducing between-group biases, and obscuring true between-group differences[444]. I plotted a histogram for each metabolite of absolute CRLB values from each voxel across the entire dataset (Figure 4.7 shows selected metabolites, with all metabolites in Supplemental figure 4.23). As expected, the distribution of absolute CRLB was skewed for all

metabolites, with high confidence in fitting for most voxels and a long tail indicating voxels with lower confidence. Due to the skewness of these distributions, I selected a threshold of the 90th percentile of the absolute CRLB for each metabolite and excluded voxels with a CRLB greater than or equal to this from further analyses.

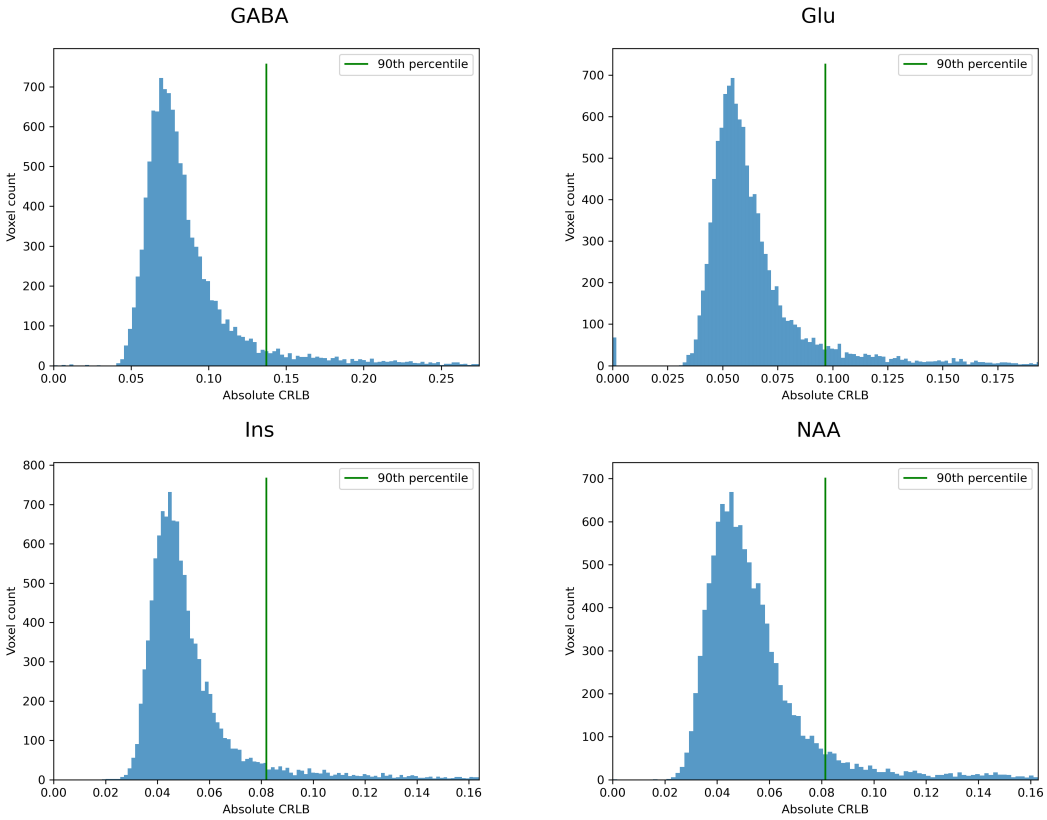

Figure 4.7: Histogram of absolute CRLB (concentration relative to total creatine multiplied by relative CRLB%) for all voxels in the dataset - separated by metabolite. Within each graph the vertical green line shows the 90th percentile value.

Spatial variation in data quality

To test whether there was any systematic spatial variation in data quality, a standard-space heatmap of voxels failing quality control using absolute CRLB (Section 4.4.2) was generated. Results for two selected metabolites on either side of the central frequency (NAA and PCho+GPC) are shown in Figure 4.8. This consistently showed lower data quality in voxels on the right-most edge of the MRSI region of interest.

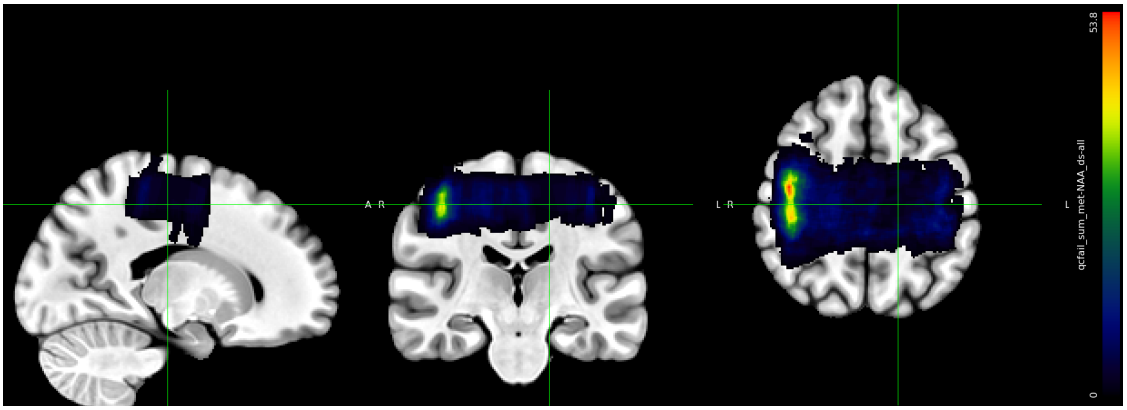

(a) NAA

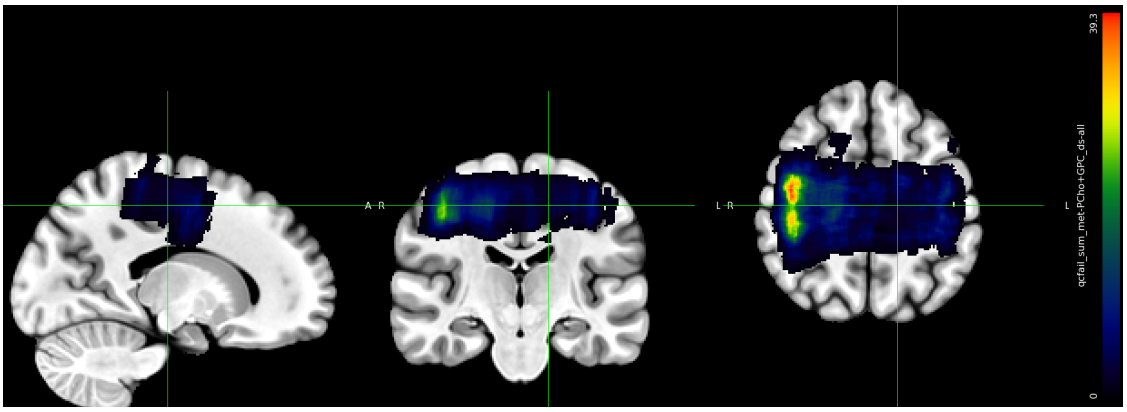

(b) PCho+GPC

Figure 4.8: Heatmap of voxels failing quality control for two representative metabolites on either side of the central frequency.

On visual inspection of the MRSI data, the spectra in voxels failing QC showed characteristic spectral abnormalities for lipid-related chemical shift displacement artefacts (Figure 4.9). In collaboration with the institutional spectroscopists, work is in progress to review the reconstruction tool and add lipid-correction post-processing. However in the interim, I have proceeded with further analysis using the voxels passing quality control. This could introduce a bias in the ROI based analysis by sampling ROIs on the right side of the brain less than on the left, as a result I performed follow-up analyses of the occupancy (total number of voxels with QC passing data per subject per ROI) to test this.

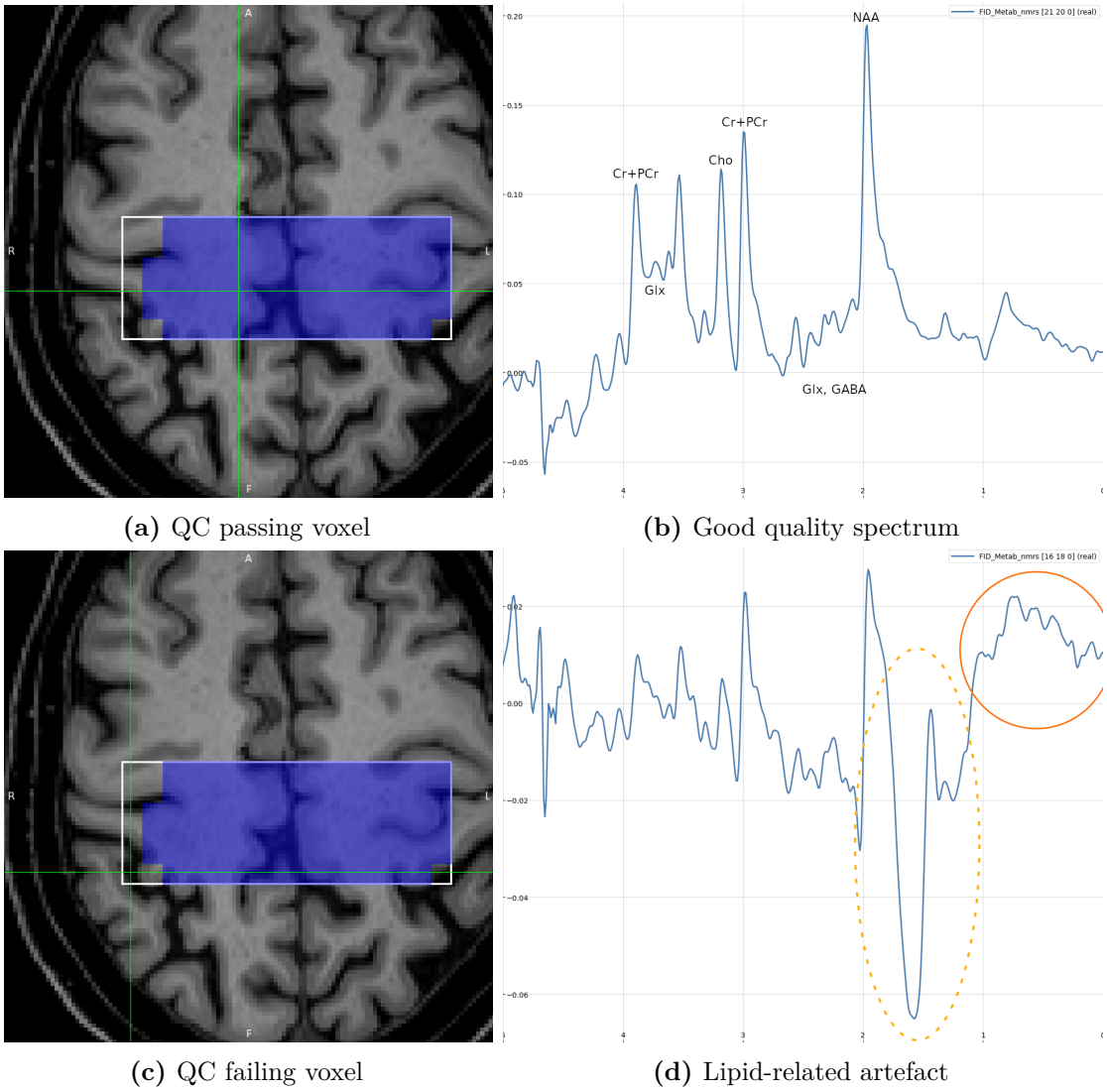

(a) QC passing voxel

(b) Good quality spectrum

(c) QC failing voxel

(d) Lipid-related artefact

Figure 4.9: Example spectrum associated with low data quality in the voxels on the rightmost edge of the region of interest.

4.4.3 Neurochemical profile variation by tissue type

Here I have summarised significant findings in selected metabolites from the linear mixed effects model specified in Section 4.3.6. As the region of interest was deliberately placed within the brain parenchyma, the range of CSF tissue fraction is low, and therefore general conclusions about CSF cannot be drawn from this analysis.

NAA

I predicted that NAA would be higher in grey matter than white matter. However, there were significant interactions between NAA concentration and both white

matter (estimate 0.2, $p < 0.001$) and grey matter tissue fraction (estimate 0.1, $p < 0.001$). Both effect sizes were positive and small, suggesting that NAA is positively correlated with both grey matter and white matter fraction. This relationship is plotted in Figure 4.10 where NAA was present at similar concentration in both grey matter and white matter voxels.

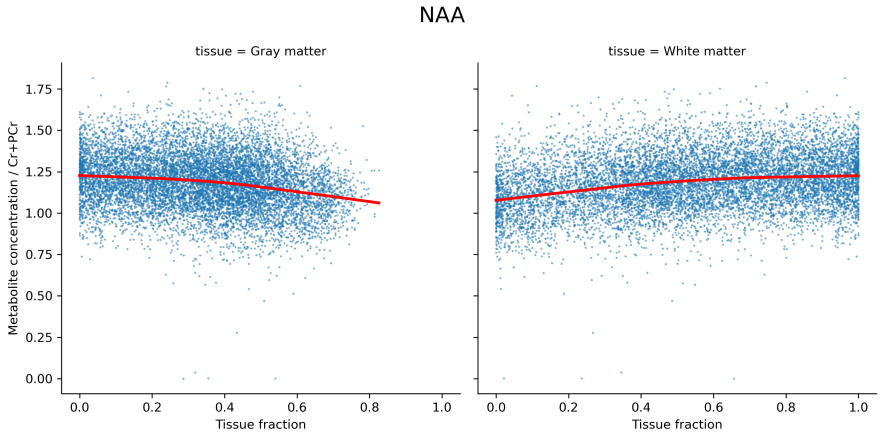

Figure 4.10: Scatterplot of NAA concentration against tissue fraction for all voxels. The red trendline shows locally weighted linear regression (lowess).

Glutamate and glutamine

I predicted that glutamate would be higher in grey matter than white matter. There were significant interactions between glutamate (Figure 4.11), glutamine and total glutamate+glutamine (Supplemental figure 4.24) with both grey matter (Glu - estimate 0.17, $p < 0.001$, Gln - -0.08, $p < 0.001$, Glu+Gln - estimate 0.08, $p < 0.001$) and white matter fraction (Glu - estimate -0.29, $p < 0.001$, Gln - -0.12, $p < 0.001$, Glu+Gln - estimate -0.43, $p < 0.001$). The effect size was greatest for glutamate, which was higher in grey matter predominant voxels and lower in white matter voxels. Glutamine levels were lower with smaller effect sizes for the interactions with both grey and white matter fraction.

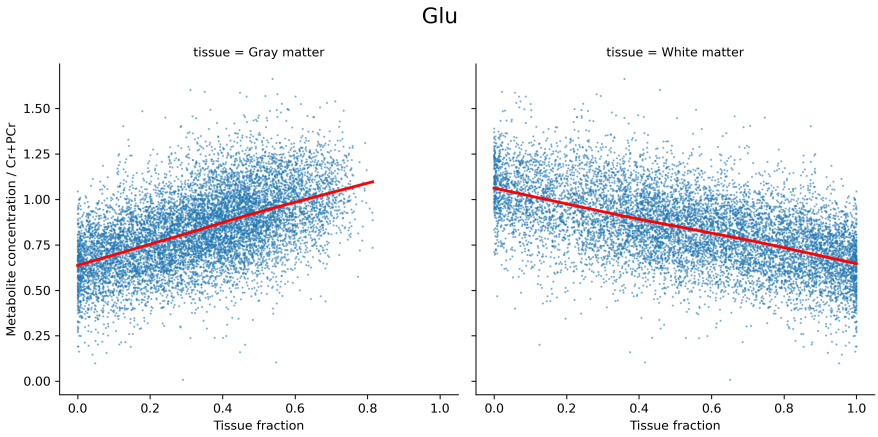

Figure 4.11: Scatterplot of Glutamate concentration against tissue fraction for all voxels. The red trendline shows locally weighted linear regression (lowess).

GABA

I expected that GABA would be higher in grey matter than white matter. However, I found higher GABA levels in white matter predominant voxels than in grey matter voxels. There were significant interactions between GABA (Figure 4.12) and both grey matter (estimate 0.05, $p = 0.02$) and white matter fraction (estimate 0.199, $p < 0.001$).

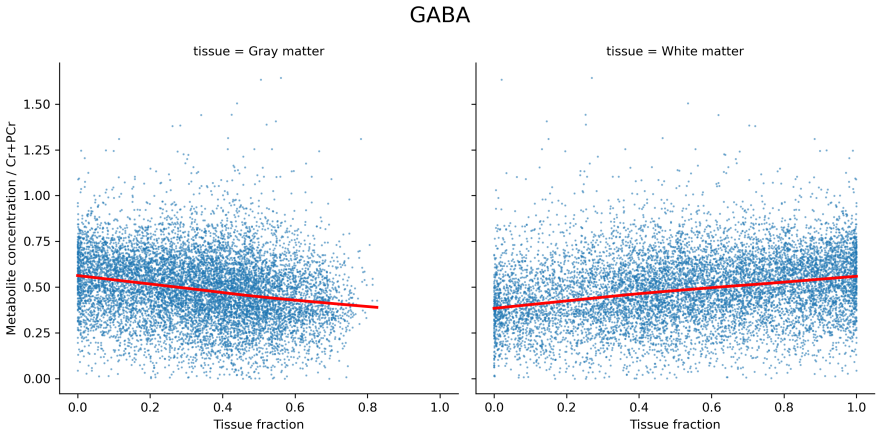

Figure 4.12: Scatterplot of GABA concentration against tissue fraction for all voxels. The red trendline shows locally weighted linear regression (lowess).

myo-Inositol

I expected that myo-Inositol would be higher in grey matter than white matter. However, myo-Inositol was higher in white matter predominant voxels and lower in

grey matter predominant voxels (Figure 4.13). There were significant interactions between the glial marker myo-Inositol and both grey (estimate -0.07, $p < 0.01$) and white matter fraction (estimate 0.13, $p < 0.001$).

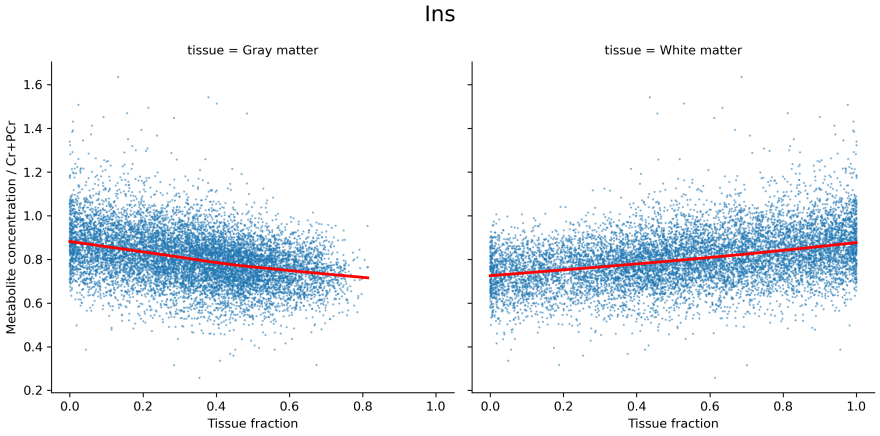

Figure 4.13: Scatterplot of myo-Inositol concentration against tissue fraction for all voxels. The red trendline shows locally weighted linear regression (lowess).

total Choline

I predicted that total Choline would be higher in white matter than grey matter. There were significant interactions between total choline concentration and white matter fraction (estimate 0.09, $p < 0.001$) but not grey matter fraction. There was a nonlinear relationship between total choline and grey/white matter fraction, suggesting lower levels in grey matter but a floor level in predominantly grey matter voxels (Figure 4.14).

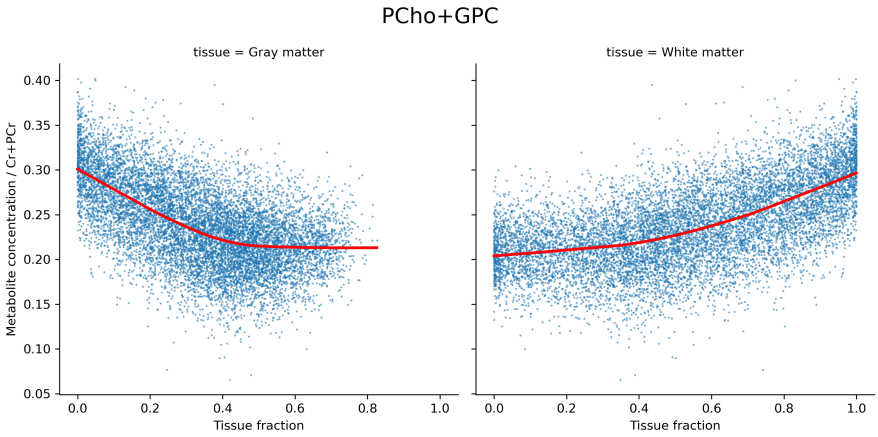

Figure 4.14: Scatterplot of total Choline concentration against tissue fraction for all voxels. The red trendline shows locally weighted linear regression (lowess).

4.4.4 Neurochemical profile of motor network nodes

I went on to address my hypotheses relating to neurochemical differences between motor network nodes (Section 4.1.6). The linear mixed effects model showed a significant main effect of metabolite ($F = 5039$, $p < 0.001$) and the metabolite * hemisphere * node interaction ($F = 11.13$, $p < 0.001$). The results of post-hoc pairwise testing are shown in the boxplots below for selected metabolites. All p-values were corrected for multiple comparisons for the total number of post-hoc tests conducted using the Holm-Bonferroni method.

Glutamate and total Glu+Gln I predicted that glutamate concentration was higher in the primary motor cortex than other regions, and higher in the dominant hemisphere. However, this was not the case for glutamate (Figure 4.15) or total Glu+Gln (Figure 4.16). Pooled across both hemispheres, glutamate and total Glu+Gln were lower in the Premotor region than in other regions. When split by hemisphere, glutamate and Glu+Gln concentration was greater in the right hemisphere for Motor and Somatosensory regions, but greater in the left hemisphere in Parietal and Cingulate regions.

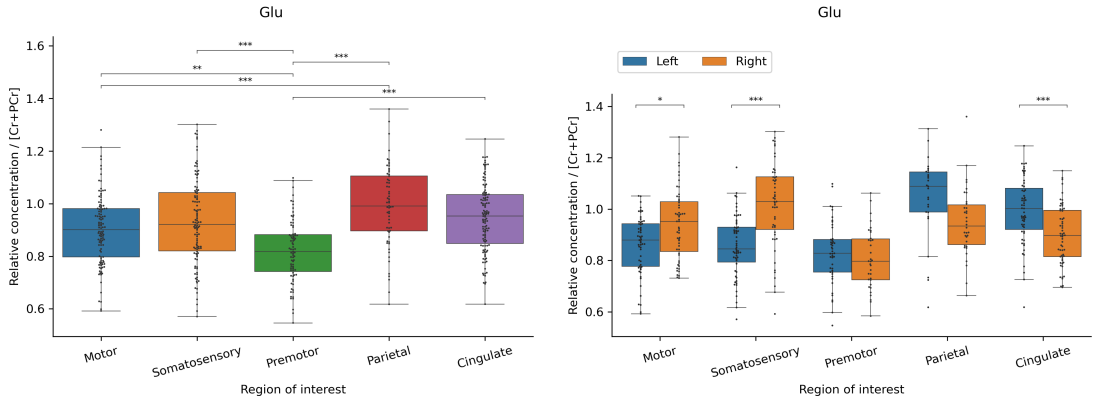

(a) Pooled across both hemispheres. **(b)** Separated by hemisphere.

Figure 4.15: Glutamate quantified across regions. *** $p < 0.001$, ** $p < 0.01$, * $p < 0.05$.

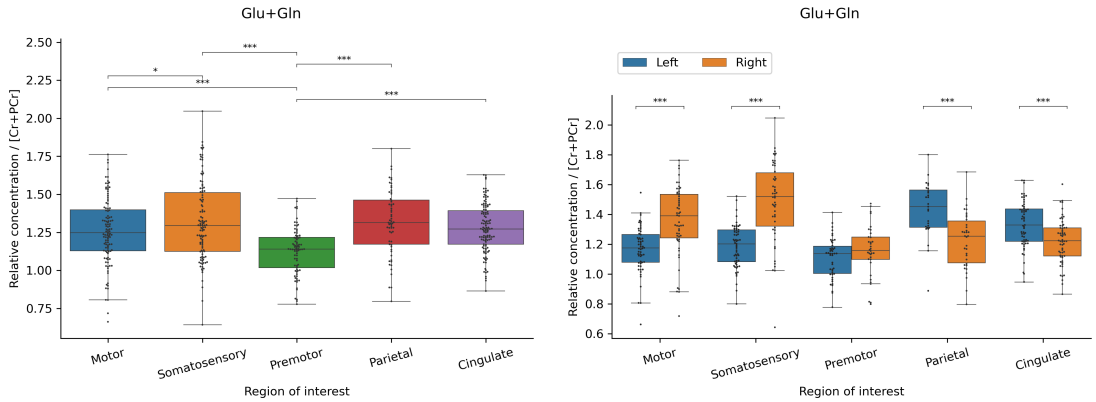

(a) Pooled across both hemispheres. **(b)** Separated by hemisphere.

Figure 4.16: Total glutamine + glutamate quantified across regions. *** $p < 0.001$, ** $p < 0.01$, * $p < 0.05$.

GABA I predicted that GABA concentration would be lower in the primary motor cortex than other regions, and lower in the left hemisphere than the right. I did not find lower GABA in the primary motor cortex, however I did find the expected lateralisation between hemispheres. GABA concentration was lower in the Parietal region than in all other regions, and lower in the Cingulate region than the Motor region. GABA concentration was not lateralised in the other regions.

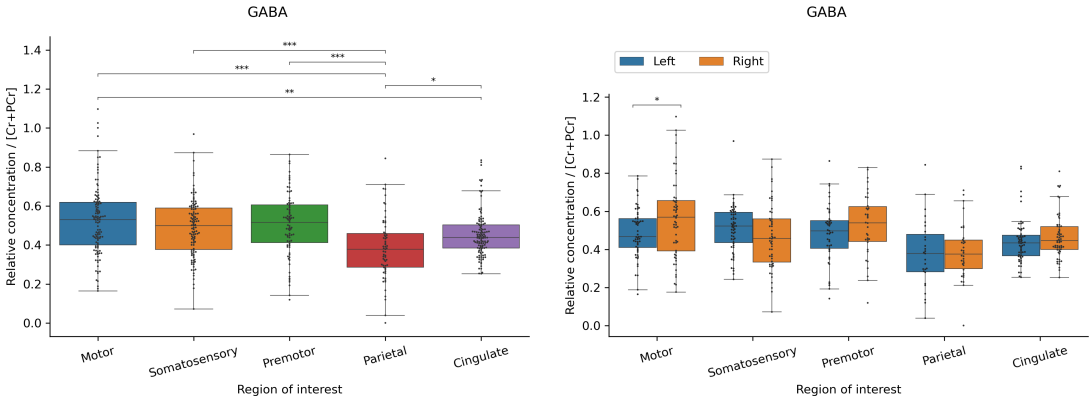

(a) Pooled across both hemispheres. **(b)** Separated by hemisphere.

Figure 4.17: GABA quantified across regions. *** $p < 0.001$, ** $p < 0.01$, * $p < 0.05$.

NAA I predicted that NAA would be higher in the primary motor cortex than all other regions. The highest levels of NAA were found in the primary motor, primary somatosensory and parietal cortices. NAA concentration was lower in the Cingulate region than all other regions. It was also lower in the Premotor region than in the Somatosensory region. NAA was not found to be lateralised between hemispheres.

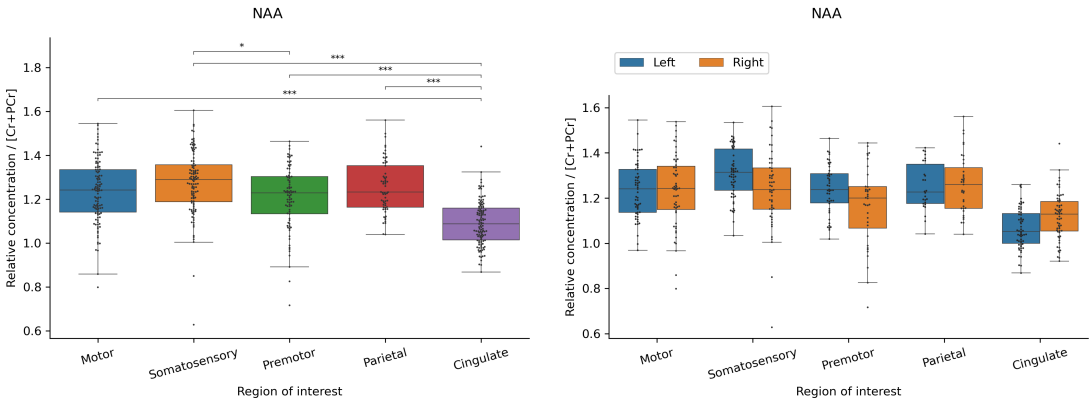

(a) Pooled across both hemispheres. **(b)** Separated by hemisphere.

Figure 4.18: NAA quantified across regions. *** $p < 0.001$, ** $p < 0.01$, * $p < 0.05$.

4.4.5 Voxel-wise correlation with age

I predicted that increasing age would be associated with lower NAA, lower glutamate and higher myo-Inositol on a voxel-wise basis. I found reduced NAA with increasing age in the cingulate cortex and in adjacent white matter in the left hemisphere

(Figure 4.19). Glutamate concentration in a similar region was also lower with increasing age. Lower glutamate with age was also found in the right hand knob and adjacent somatosensory cortex.

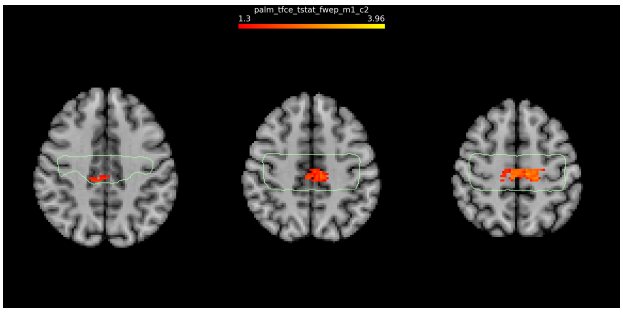

(a) NAA

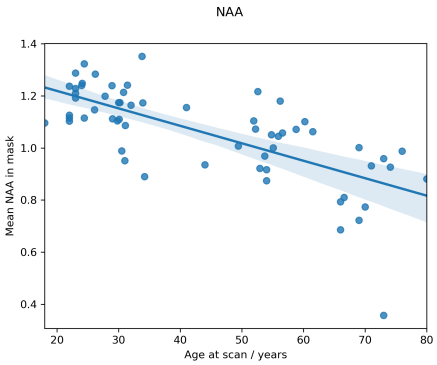

(b) NAA

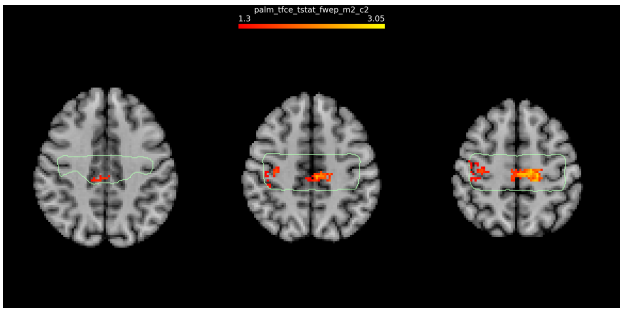

(c) Glu

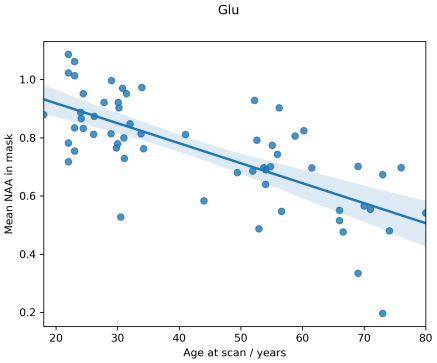

(d) Glu

Figure 4.19: Spatial maps of statistically significant voxels ($p < 0.05$) for correlation with age. p-values are given as $-log(p)$ so a threshold of > 1.30 corresponds to $p < 0.05$. p-values are corrected for family-wise error and spatial maps are corrected using threshold-free cluster enhancement.

4.4.6 Voxel-wise correlation with motor resting state network

Group ICA of all subjects resting state data was performed with dimensionality 25. This dimensionality was chosen in order to avoid splitting the motor network into sub-components. The aim of this analysis was to test the correlation of local neurochemical excitatory and inhibitory tone with within-motor-network connectivity on a voxelwise basis. Previous work using this dimensionality forms the basis of whole-network resting state fMRI data analysis in the UK Biobank

dataset[279]. Selected IC spatial maps are shown in Figure 4.20. Of these, IC 3 was selected as the representative sensorimotor network due to greatest similarity with sensorimotor resting state network derived from large datasets[369].

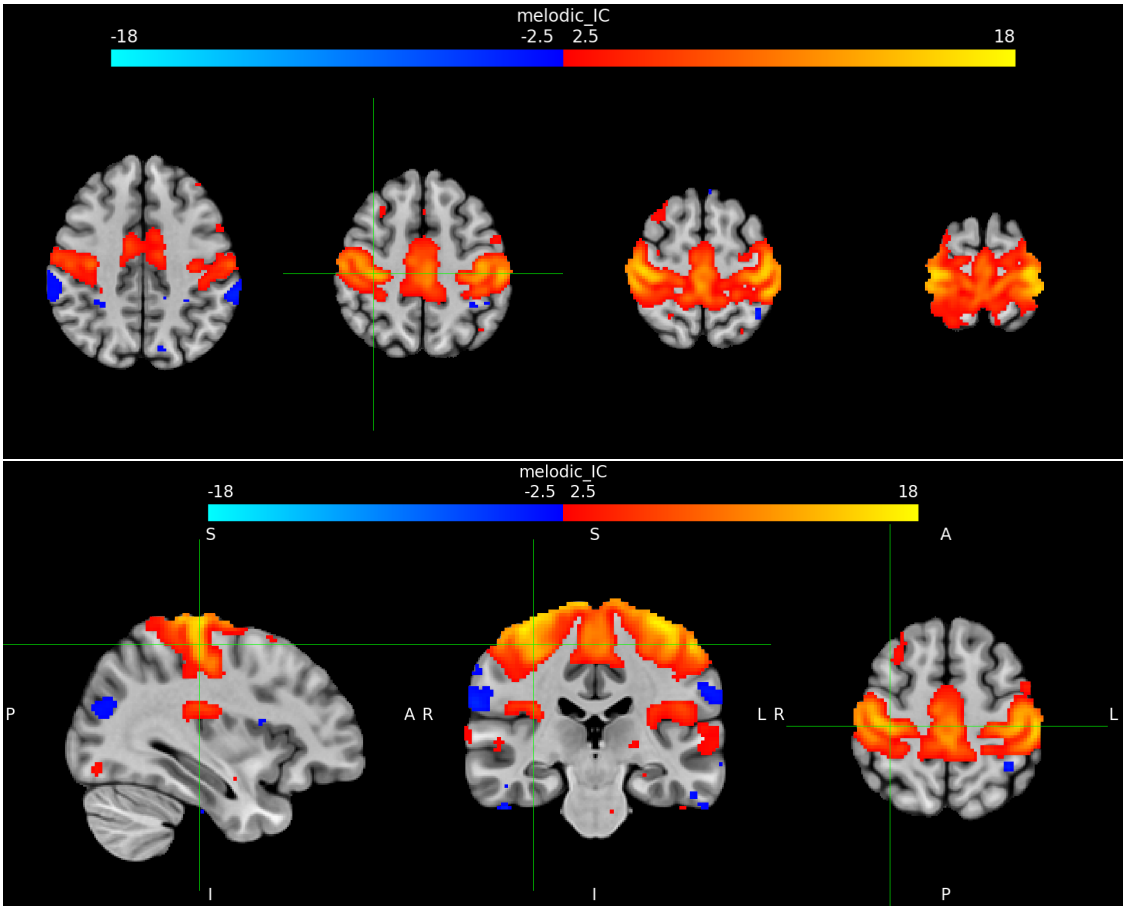

Figure 4.20: Representative axial and orthogonal slices of the thresholded spatial map of IC 3.

Subject specific spatial maps of connectivity to the group motor IC were generated using dual regression (stage 2 outputs). To test the hypotheses that local inhibitory and excitatory neurotransmitter tone are associated with motor-network connectivity on a voxel-wise basis, a PALM analysis was performed with GABA and Glu spatial maps as inputs, and the subject specific motor connectivity maps as a voxel-wise explanatory variable. Statistical testing is done using non-parametric combination to perform joint inference across multiple inputs. For each input metabolite, an parametric distribution of the test statistic is generated through permutation. This allows z-score transformation of the input, and spatial

statistics to be performed. In this analysis, correction using threshold-free cluster enhancement was performed.

The resulting spatial maps (uncorrected for family-wise error) showed that voxel-wise glutamate concentration was correlated to motor network connectivity in the left motor hand area, adjacent somatosensory cortex, and in the left posterior cingulate cortex. This relationship was also found in the right hemisphere motor hand area, with a smaller cluster (Figure 4.21a).

GABA concentration was correlated to motor network connectivity in the left motor and sensory hand area alone (Figure 4.21c).

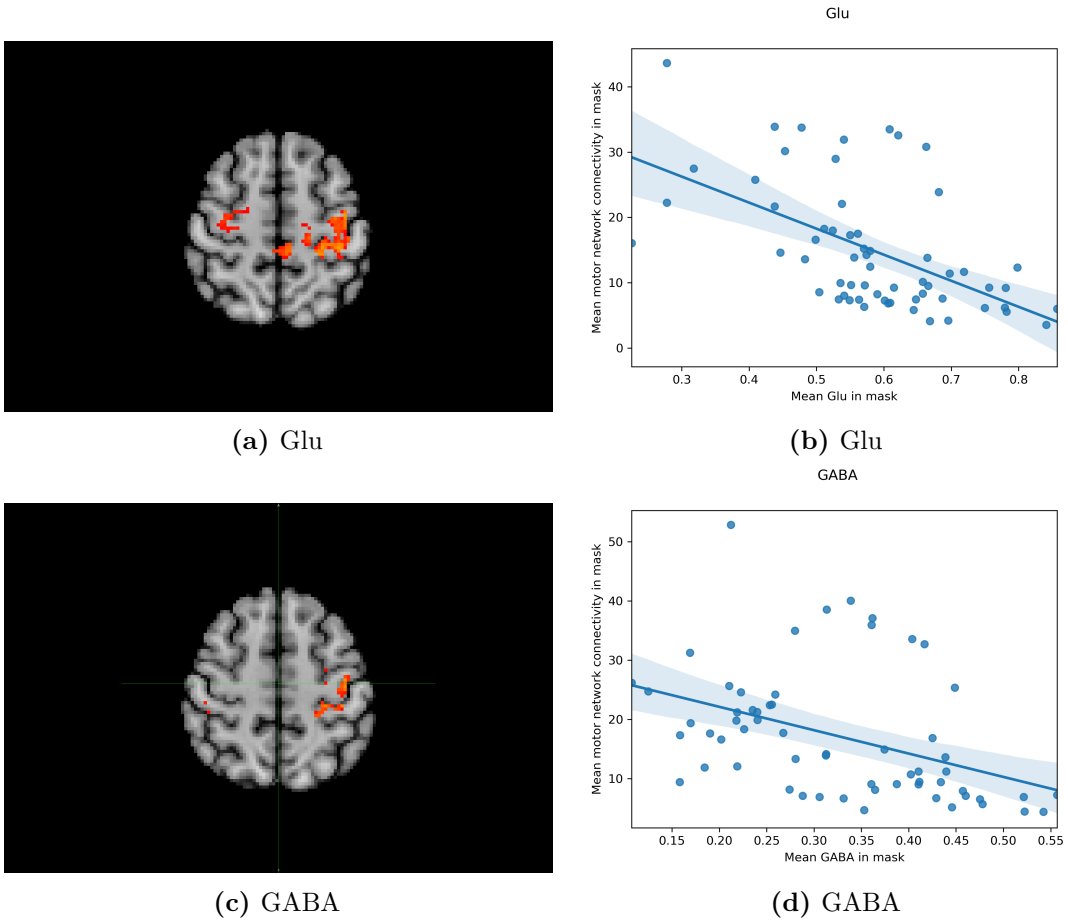

(a) Glu **(b)** Glu

(c) GABA **(d)** GABA

Figure 4.21: Spatial maps of significant voxels (uncorrected $p < 0.05$) for correlation with motor network connectivity. Spatial maps are corrected using threshold-free cluster enhancement.

4.5 Discussion

In this chapter I have applied a novel neurochemical imaging technique to a healthy population to characterise excitatory and inhibitory tone in the resting motor network. I have checked the underlying data quality and performed quality control filtering on a voxel-wise basis. I have compared registration techniques to maximise the power of this technique in exploring local variation in neurochemical concentration. I tested the hypotheses set out earlier, with the following key findings.

4.5.1 Neurochemical concentration varies by tissue type

Various metabolites concentration varied with tissue fraction, prominently glutamate, GABA, myo-Inositol and total choline. As expected from previous work, Glu was concentrated in grey matter. However, the finding of higher GABA concentration in white matter predominant voxels was counterintuitive, as was the finding of similar NAA concentration in both white and grey matter. Furthermore, the relationship between tissue fraction and metabolite concentration was not necessarily linear. These findings could reflect protocol-specific variation in reconstruction and fitting. Reconstruction is technically challenging to review - this work is ongoing with institutional spectroscopists. I chose to fit the reconstructed spectra using FSL-MRS for this analysis. While the fitting techniques used are analogous to other widely used toolkits in the field, refitting the data with a tool such as LCModel could be considered in future work to test the role of fitting in generating this particular finding. This is a significant limitation to be considered in the interpretation of further results in this thesis relating to GABA. However, given previous studies have generally utilised smaller numbers and single-voxel techniques, this suggests that avenues still remain for MRSI studies establishing region and tissue-type specific baseline values.

4.5.2 Excitatory neurochemical tone is regionally lateralised in the healthy human brain

My region-of-interest analysis demonstrated regional variation the excitatory neurotransmitter glutamate, as well as the glutamate+glutamine metabolite pool. I found lower glutamate in the premotor cortex without hemispheric lateralisation. It is challenging to align this data to previous glutamate MRS literature[338] - large single voxels were generally placed encompassing mixed tissues, with standard space alignment generally not attempted.

Glutamate has not previously been shown to be lateralised across multiple human brain regions. Previous work involving sequential placement of single voxels in both motor cortices involved small numbers of participants, with between-hemisphere differences not reported[445]. A study of glutamate transporter expression in mice showed lateralisation in the cingulate cortex (L>R), but not in premotor or motor regions[446]. In more obviously lateralised systems such as the language system, both post-mortem[447] and population genetics[448] studies suggest that glutamate-system genes are lateralised, and that their lateralisation contributes to brain function.

4.5.3 Reduced excitatory neurochemical tone in the right sensorimotor hand area is associated with increasing age

Lower glutamate has been reported in adults aged 45-55 in the motor leg area at 4T using single voxel MR spectroscopy compared to younger adults (age ∼25)[449]. Lower glutamate levels in older adults than young adults have also been reported in the hippocampus, occipital, cingulate cortex, and deep brain structures[337,450–453]. Some uncertainty remains, and the magnitude of difference may differ across brain regions, and between men and women[451,454]. My findings elaborate the understanding of glutamate change with age, showing with fine spatial resolution that this relationship is particularly strong in the posterior cingulate cortex and right sensorimotor hand area. The absence of a significant relationship with age in the left hand area in this dataset may be due to a smaller effect size in the dominant hemisphere, or

may suggest resilience or compensatory changes on that side. Findings such as these further underscore the need for reliability and validation studies in older populations to place positive findings in clinical populations in context, and allow meaningful clinical translation.

4.5.4 Excitatory and inhibitory neurochemical tone in the sensorimotor hand areas is associated with resting motor network connectivity

Higher resting state glutamate and lower GABA has been linked to default mode network activity in the in the anterior and posterior cingulate cortex[418,455,456]. A common mechanism has been proposed - that the balance between local neural/neurochemical excitation and inhibition in a given network node drives its long range connectivity[197]. In the motor system, the literature is inconsistent. Lower hand motor area GABA concentration has been associated with both wider motor network and M1-M1 connectivity, while glutamate was not[416]. In relation to long term motor tasks, this relationship may be modulated by the intensity of practice, with left hand area GABA levels and motor network connectivity inversely related[269]. I found lower GABA in association with increased resting motor network connectivity in the left sensorimotor hand area, but not the right. However, I also found that lower glutamate was correlated with increased motor network connectivity in both hand areas, with greater cluster extent in the left hemisphere.

Lower glutamate (but not GABA) in the posterior cingulate cortex was also associated with higher motor system connectivity. Taken together, this supports the theory that GABA-ergic tone in the motor cortex normally gates motor output, and suggests that baseline differences in total GABA may be related to motor network function. However my findings suggest that motor cortex glutamate is also functionally relevant. Lower levels of glutamate in the right hemisphere, distant motor cortex regions, and adjacent default mode network nodes compared to the left hemisphere could reflect reduced excitatory tone (noise) within the motor network and competition from other networks, allowing the physiological release of inhibition in the left motor cortex (signal) to proceed cleanly.

Could this relationship be mediated by age? The literature on motor network connectivity changes with aging is conflicting. While the left prefrontal and right cingulate areas may show reduced within-motor-network resting state motor network connectivity in older adults[457], a more complex picture of compensatory increases of within-motor-network connectivity in age 50-60, followed by a precipitous decline, has also been reported[458]. To address this limitation, future work will include age as a covariate in this analysis.

4.5.5 Limitations

Several technical and methodological limitations are important to consider alongside these findings. The z-resolution of the imaging region of interest remains coarse (15mm). This necessary tradeoff to maintain SNR results in significant volume averaging in the z-direction. The resulting voxel-wise correlation of low-resolution input data (2.4mm isotropic functional data and $5 \times 5 \times 15$mm MRSI data) makes balancing power to detect spatial variation and performing robust multiple comparison correction challenging.

Harmonising data across multiple datasets in an opportunistically performed study is challenging. In this combined dataset, all data was collected with an identical pulse sequence, but on two Siemens Prisma 3T scanners on different sites. As discussed in the Methods section there were also differences in study design and participant characteristics. This is a significant limitation of this work, which could be addressed in future work by including study as a regressor in the statistical modelling.

To summarise, in one of the largest MR spectroscopic imaging datasets to date, I found significant baseline variation the landscape of excitation in key motor network nodes in health and ageing. The high spatial resolution offered by this novel technique illustrates an interplay between both neurochemicals and functional connectivity that implicates both excitatory and inhibitory influences in determining motor network connectivity. In subsequent thesis chapters I will explore whether this neurochemical landscape differs in ALS and carriers of ALS-risk genes, and

whether integrated neurochemical and functional motor network data may yield biomarkers of early disease activity.

4.6 Supplemental materials

Registration method comparison

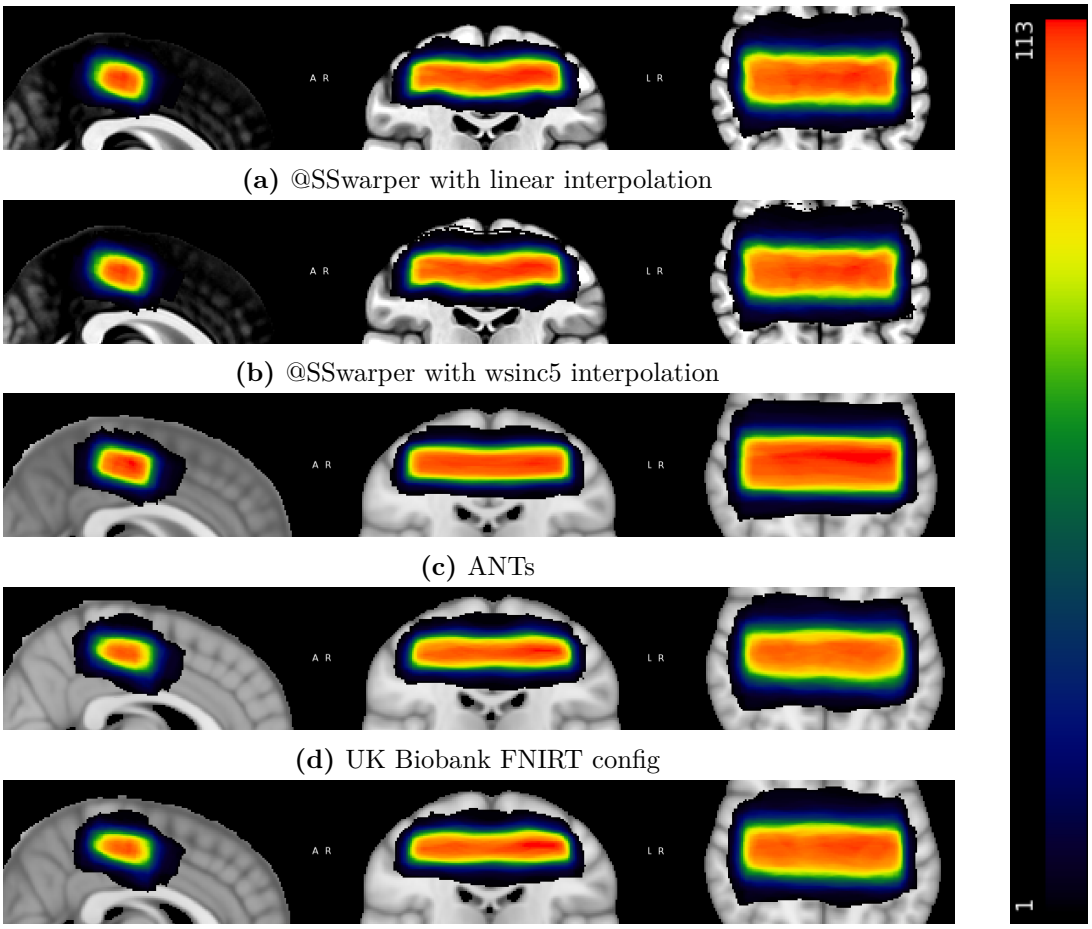

(a) @SSwarper with linear interpolation

(b) @SSwarper with wsinc5 interpolation

(c) ANTs

(d) UK Biobank FNIRT config

(e) Default FNIRT config

Figure 4.22: Comparison of registration techniques. The native space MRSI region of interest mask was transformed to standard space. The number of subjects overlapping at each voxel is represented by colour. Panels using @SSwarper are shown overlaid on the AFNI version of the MNI152 standard space.

Quality control - filtering by absolute CRLB

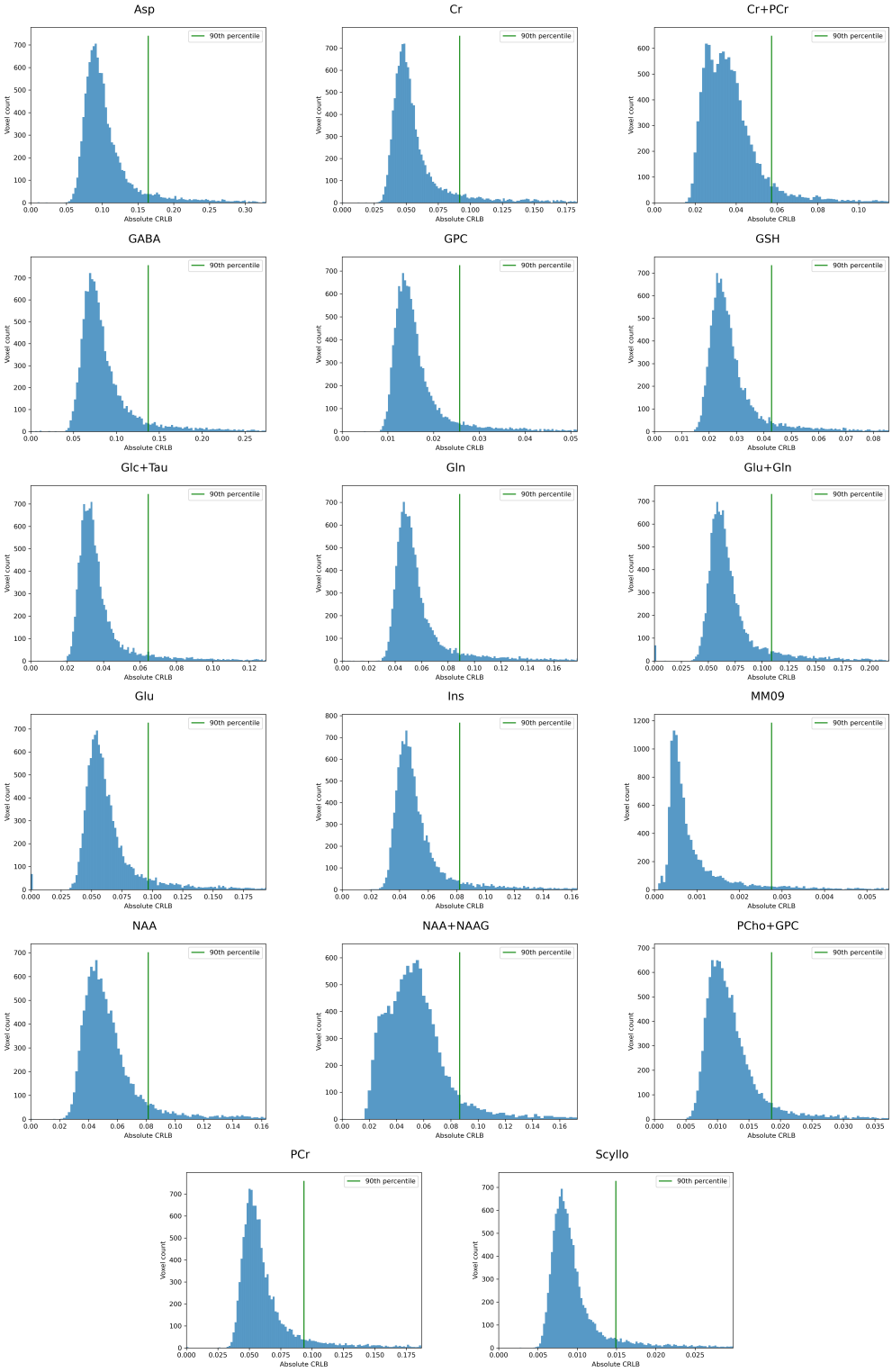

Figure 4.23: Histogram of absolute CRLB (concentration relative to total creatine multiplied by relative CRLB%) for all voxels in the dataset - separated by metabolite. Within each graph the vertical green line shows the 90th percentile value.

Tissue fraction relationship to metabolite concentration

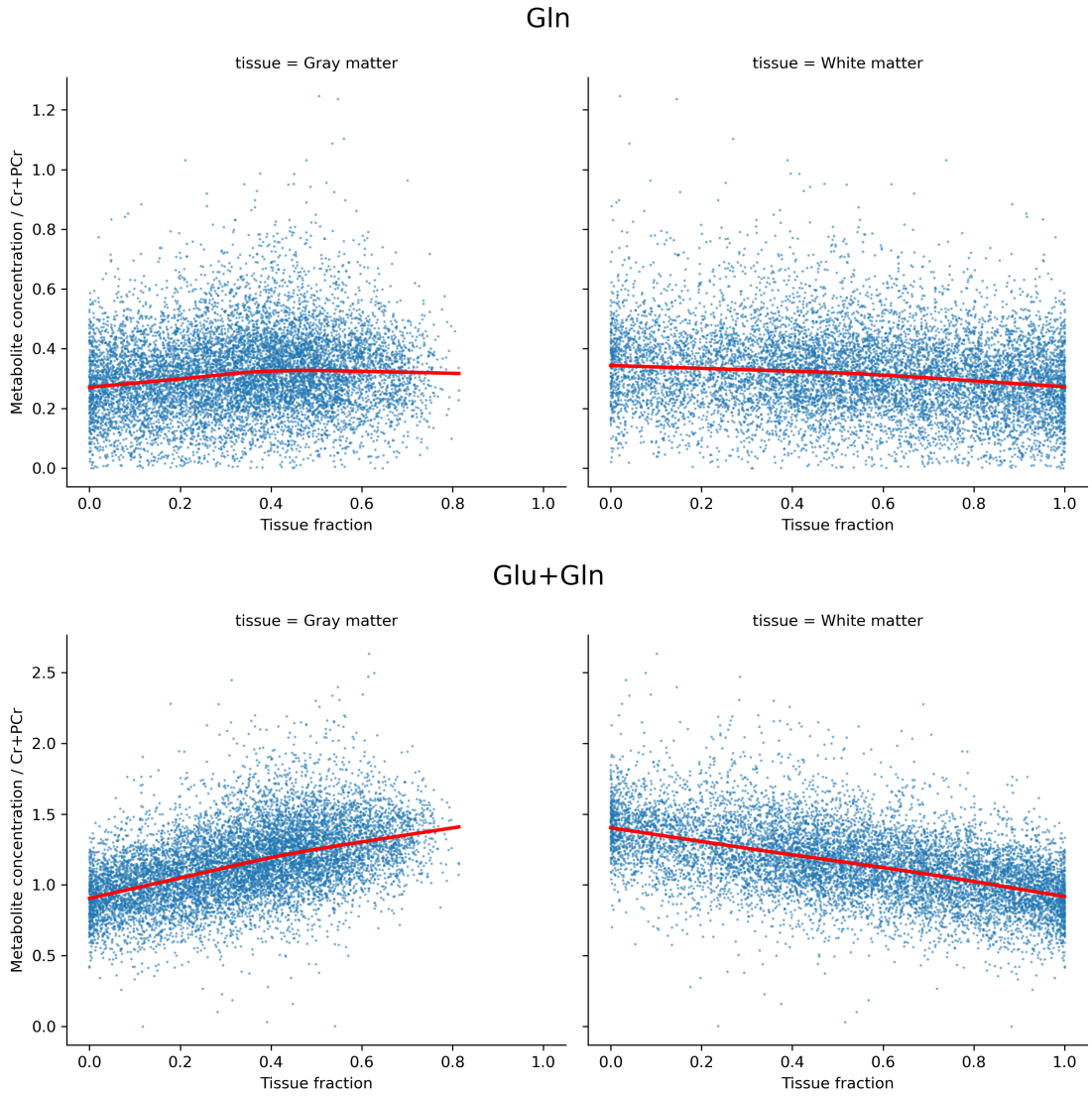

Figure 4.24: Tissue fraction relationship with metabolite concentration for total Glu+Gln and Gln.

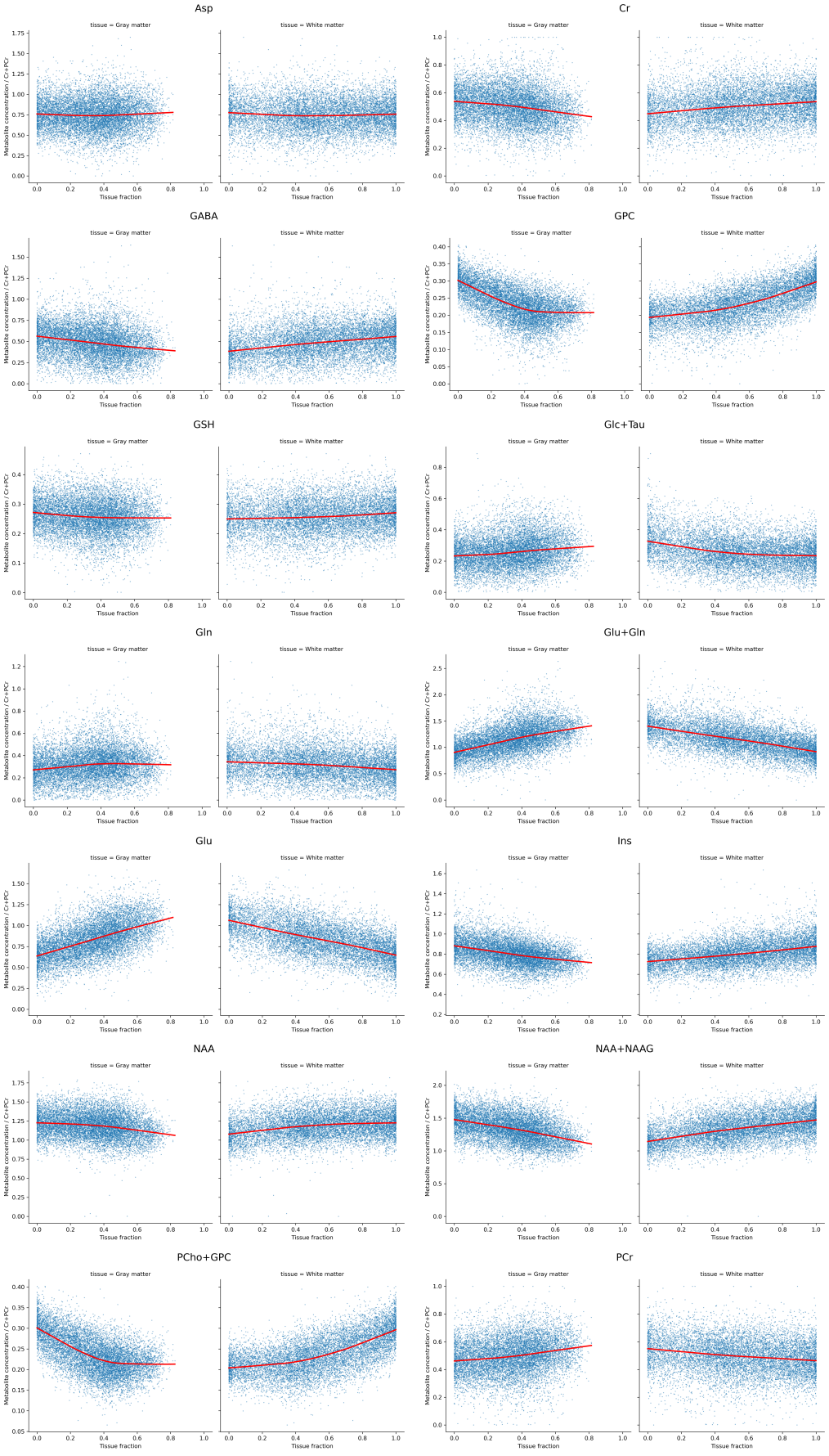

Figure 4.25: Tissue fraction relationship with metabolite concentration for all metabolites passing quality control.

With the right computer algorithms, I can hack you back in time...

— Hackerman, Kung Fury (2015)

5

Neurochemical mapping in established and presymptomatic ALS

Contents

5.1 Introduction

In the previous chapter I described the normal variation in local neurochemical tone as measured using magnetic resonance spectroscopic imaging. I described the effect of tissue type, brain region, associations with age, and the interaction with the resting state motor network. In this chapter, I will apply the same MRSI technique to describe cortical excitability in relation to neurochemical tone in both established ALS and presymptomatic disease.

5.1.1 MRS provides promising biomarkers of neurodegeneration in ALS

Unlike functional MRI, MR spectroscopy has an established history of clinical application in brain tumour diagnosis and physiological characterisation[459]. The application of single voxel MR spectroscopy in ALS research began in the late 1990s with the demonstration of reduced n-acetylaspartate (NAA) in the motor cortex and other brain regions[460–463]. NAA is required for neuronal mitochondrial function, and therefore is non-specifically localised throughout neurons[464]. This highly abundant, neuron-specific metabolite was therefore the most suited to exploration in initial studies at 1.5 Tesla. NAA loss has been further shown to be correlated with upper motor neuron disease burden and progression rate in ALS[465,466]. Through multi-centre imaging consortia, this is one promising avenue for clinical translation of MRS in ALS[433].

5.1.2 MRSI in ALS - localisation of a spatially varying disease process?

I have previously discussed the potential benefits from MR spectroscopic imaging at higher spatial resolution (Section 2.3.3). MRSI has provided key insights into ALS, a disease process characterised by selective vulnerability of different brain regions.

At 1.5T, imaging several brain slices allowed demonstration of NAA reduction in both M1 and the corticospinal tract in the same patients, allowing a comparison between hemispheres[467]. MRSI studies at higher field strength have demonstrated

that NAA reduction is asymmetric[468], tracks widespread grey and white matter damage[469,470], can be correlated in the corticospinal tract to loss of function[471], and responds variably to riluzole treatment between regions[472]. Other markers such as GSH, a marker of oxidative stress and glial damage, have also been studied with MRSI. GSH is reduced in the left motor cortex and corticospinal tract, correlated with disease duration[473].

5.1.3 Applying MRS to investigate cortical excitability

MRS and MRSI could also be applied to investigate cortical hyper-excitabilityin ALS. However, metabolites classically associated with neural signalling and excitability such as glutamate and GABA are much less abundant than NAA in the human brain. While GABA and glutamate pools as quantified by MRS are proxy measures at best (Section 4.1.4), they are functionally relevant and non-invasively assessable. With compounding advances in field strength, scanner capabilities and sequence design, these have also been studied in ALS. The application of spectral editing techniques suggested diminished GABA in the left motor cortex in ALS patients[202], together with elevated combined glutamate and glutamine (Glx) when riluzole-naïve[203]. Data on glutamate in the left motor hand area are conflicting, with findings of increase[204], no change[205–207], and decrease all reported in ALS[208–210]. Glu/GABA ratio has been described as an index of cortical excitability - and was found to be elevated in the supplementary motor cortex of patients with ALS[211].

5.1.4 Measuring neurochemical cortical excitability in established ALS and presymptomatic disease

Cortical hyperexcitability/disinhibition has been demonstrated in ALS using TMS[474], activation-PET[364], and in the context of some task fMRI designs[232]. This even extends to a disinhibited 'hot-spot' in the earliest phase after symptom onset[181], and loss of physiological inhibition in presymptomatic gene carriers just prior to symptom onset[180]. However, neurochemical alteration in presymptomatic disease is

less well studied. Spinal cord NAA is lower in *SOD1* mutation carriers[475], however published work and openly available data is lacking for *C9orf72*[476].

In this chapter, I have applied a novel MRSI technique designed to measure glutamate and GABA as measures of cortical excitability in ALS. I recruited a cohort including ALS patients (both sporadic and *C9orf72*-HRE carriers), healthy controls, and a large (for a single study) number of first degree relatives of individuals with *C9orf72*-HRE associated disease. I have tested the following in this MRSI dataset:

- NAA, glutamate and glutamine are reduced in ALS vs. healthy controls across various motor network regions (Left/Right Motor, Premotor and Somatosensory regions as defined in Chapter 4).
- NAA, glutamate and glutamine are reduced in *C9orf72*-HRE positive vs. *C9orf72*-HRE negative relatives across Left/Right Motor, Premotor and Somatosensory regions.
- The hemispheric lateralisation of these metabolites described in Chapter 4 is disrupted in ALS and *C9orf72*-HRE+ relatives.
- The relationship between local neurochemical excitatory and inhibitory tone and resting state motor network connectivity described in Chapter 4 is disrupted in ALS and *C9orf72*-HRE+ relatives.

5.2 Methods

5.2.1 Study participants and recruitment

ALS patients were recruited from a single neurology tertiary referral centre between 2019 and 2021. All patients had a diagnosis of ALS made according to consensus criteria (2008 Awaji guidelines)[22]by an experienced sub-specialist neurologist (KT or MRT). The study was advertised to families where a patient had received a positive test for the *C9orf72* hexanucleotide repeat expansion (with patient consent), or where a family was aware of a positive test in a deceased patient. Healthy first and second-degree relatives of the *C9orf72*-HRE carrier were eligible to take part. An

initial screening interview was performed to ascertain study eligibility, review study procedures, and confirm MRI safety. Participant demographics are summarised in Table 5.1 - prepared with the tableone[477] Python package.

5.2.2 Power calculation

Power calculation for this dataset was challenging given the variety of imaging data collected, including structural, functional, and neurochemical MRI data. For MRSI data, the power also varies between different metabolites. To illustrate this, I performed two power calculations[383] with two metabolites with differing confidence levels in quantification - glutamate and GABA. I estimated the following based on normative data and previous publications using single voxel MRS in ALS[202,203]. For Glu, assuming group means of 1 in controls, 0.9 in ALS, and standard deviation of 0.1, 80% power would be achieved with a sample size of 14 ALS patients and 14 healthy controls. In contrast, for GABA, assuming group mean of 1 in controls, 0.9 in ALS, and standard deviation of 0.2, 80% power would require a sample size of 32 participants in each group. This dataset is therefore well powered to find group level differences in metabolites where higher quality data is available. In contrast, for metabolites with noisier data, power is a significant limitation.

Genetic testing

All healthy family members were consented to genetic testing under a double blind protocol. Blood samples were taken for DNA isolation and Southern blot analysis for the *C9orf72*-HRE. The genetic test results were stored with a third party genetic data guardian. On analysis of the dataset, group level analyses were performed using a double-key system to allow statistical analysis while not revealing individual subject genetic status to either researchers or study participants.

5.2.3 Imaging methods

The novel MRSI sequence, design considerations, and technical parameters were as discussed in Section 4.2.2. In summary, spectra were acquired in a region-of-interest measuring 85mm × 35mm × 15mm placed to encompass both primary

		ALS	*C9orf72*-HRE+ relative	*C9orf72*-HRE– relative	Healthy control
n		17	18	20	20
sex, n	F	6	11	11	8
	M	11	7	9	12
age, mean (SD)		56.6 (13.0)	48.5 (15.5)	40.7 (15.8)	55.0 (10.0)
Disease duration (months), mean (SD)		20.0 (13.6)			
Site of onset, n	LLL	6			
	LUL	2			
	RLL	3			
	RUL	3			
	bulbar	3			

Table 5.1: Demographics for Oxford *C9orf72* cohort study participants with completed MRI scans.

motor cortex hand knobs. Individual voxel dimensions are 5mm × 5mm × 15mm. Subjects were instructed to lie still in the MRI scanner with their eyes open, while landscape scenery images were displayed.

Structural and functional imaging Structural images were acquired using a 3d T1 MPRAGE sequence matched to UK Biobank acquisition parameters[278]. These include 1 × 1 × 1mm spatial resolution, 208 × 256 × 256mm field of view, and in-plane acceleration factor iPAT=2.

Resting state functional MRI was also performed using gradient echo EPI sequences matched to UK Biobank acquisition parameters[278]. These include 2.4 × 2.4 × 2.4mm spatial resolution, 88 × 88 × 64 field of view matrix, 490 timepoints over

6 minutes, TR = 0.735s, TE = 39ms, 8 × multi-slice acceleration, and flip angle 52°.

Structural image preprocessing, segmentation and registration to standard space were performed as described in Chapter 4. Functional image preprocessing, denoising with single subject ICA, and resting state network derivation with independent component analysis and dual regression were performed as described in Chapter 4.

5.2.4 MRSI processing

MRSI data reconstruction, preprocessing (coil combination, phase-frequency alignment, averaging, and residual water removal) were performed using the same pipeline described in Chapter 4, utilising a custom binary developed for this protocol. The output NIfTI images incorporating preprocessed spectra were then processed using the open source FSL-MRS toolkit, with a linear combination of basis spectra fitted using Markov chain Monte Carlo (MCMC) optimisation.

5.2.5 Atlas derived regions of interest

As in Chapter 4 I derived the following regions of interest from the volumetric HCP-MMP1 atlas in MNI space[440,441] by combining the specified labels in Table 4.2. In results figures, the regions of interest are labelled as follows - Motor, Pre-motor, Somatosensory and Parietal in each hemisphere.

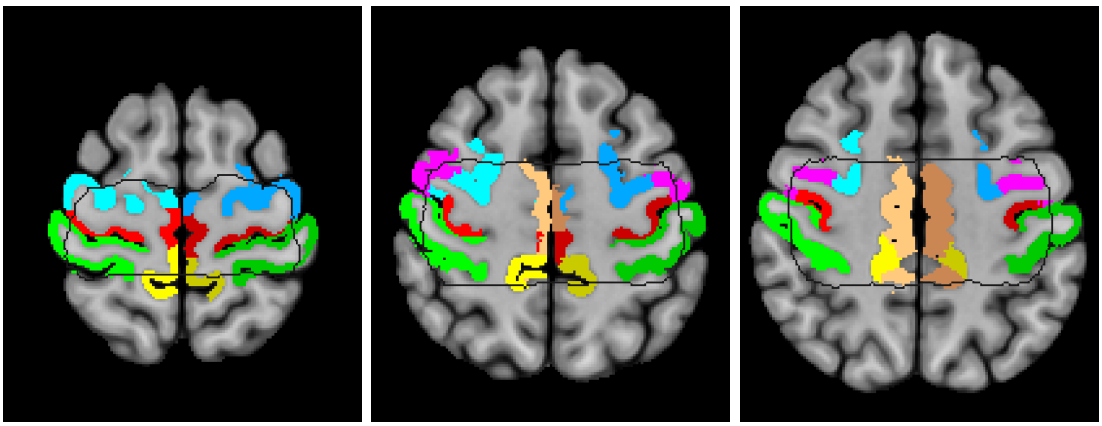

Figure 5.1: Representative slices of standard space ROIs used. Red - Motor, Green - Somatosensory, Yellow - Parietal, Beige - Cingulate, Blue - Premotor. The left hemisphere ROIs are slightly darker than right hemisphere ROIs. The black lines show a region with coverage of at least 10 participants.

5.2.6 Statistical analysis

Group level differences in neurochemical concentration and symmetry - ROI based

Regions of interest as specified above were compared using a linear mixed effects model, with metabolite concentration as the outcome variable, fixed effect of "metabolite", fixed effect of “group”, random effect of “node”, and a node * metabolite interaction. I calculated estimated effects of “node”, “group”, “metabolite” and node * metabolite interaction, followed by post-hoc t-tests using the Satterthwaite approximations to degrees of freedom if significant to identify the specific metabolites contributing to differences and the direction of effect.

Combining control groups As region-of-interest analyses were prepared as inputs to the work on dimensionality reduction and application of statistical classifiers in Chapter 6, the two healthy groups (unrelated healthy controls and *C9orf72*-HRE– family members were combined into a single control group). This was done because the distinction between two healthy groups is not directly relevant to the overall aim to find disease biomarkers, and would dilute the power of group classification to demonstrate validity. This is a future avenue for enquiry - while *C9orf72*-HRE– family members are not known to have a greater than population risk for ALS, if there were significant differences from unrelated healthy controls this would be unexpected and interesting. As such the use of these individuals as controls, though not unprecedented in this literature[478], is a limitation of the analyses in this Chapter and Chapter 6.

Group level differences in neurochemical concentration - voxel-wise

Group level differences in NAA, Glu, and GABA were tested on a voxel-wise basis using the FSL tool PALM[359] for the following comparisons - ALS patients vs. healthy controls, and *C9orf72*-HRE+ vs. *C9orf72*-HRE– family members. Each metabolite was treated as a separate input modality. Non-parametric inference and combination were performed. Cluster correction was performed using threshold-free cluster enhancement.

Relationship between local neurochemical measures of excitability and motor network connectivity

Glutamate and GABA maps in standard space, representing voxel-wise excitatory and inhibitory neurochemical tone, were analysed along with the corresponding motor resting state network using the FSL tool PALM[359]. Using non-parametric permutation inference, this tool allows testing for significant correlation between neurochemical data and functional connectivity data on a voxel-wise basis.

5.3 Results

5.3.1 Region of interest results

NAA

NAA/Cr was reduced in the Motor, Premotor, Somatosensory, and Cingulate regions in ALS compared to healthy controls. NAA/Cr was reduced in the Motor and Somatosensory regions in *C9orf72*-HRE+ individuals compared to healthy controls. Finally, in the Motor region, NAA/Cr was lower in ALS than in *C9orf72*-HRE+ individuals (Figure 5.2). These findings were symmetrical between hemispheres (Supplemental Figure 5.13).

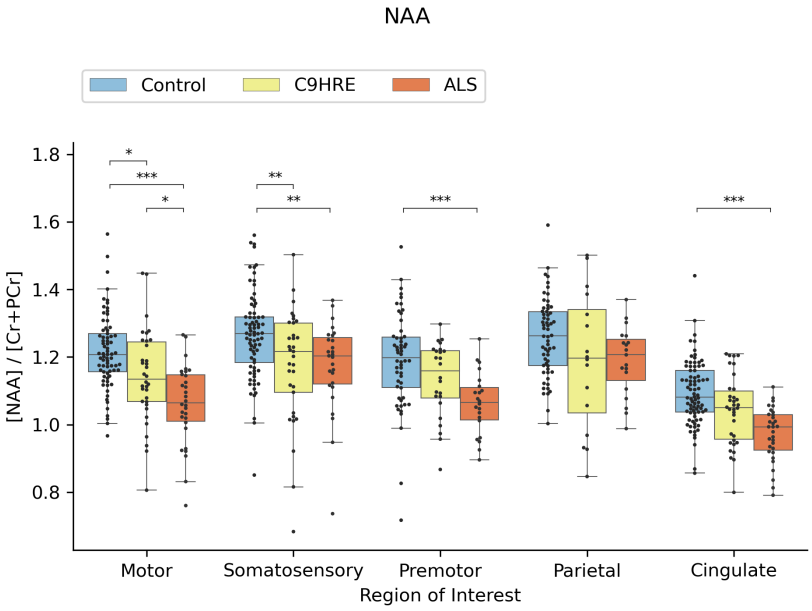

Figure 5.2: NAA variation across regions, separated by group.

Glu+Gln, Glu and Gln

Total Glu+Gln was reduced in Motor, Somatosensory regions in ALS patients compared to both healthy controls and *C9orf72*-HRE+ individuals (Figure 5.3). Glu+Gln was also lower in the Parietal and Cingulate regions in ALS patients compared to healthy controls.

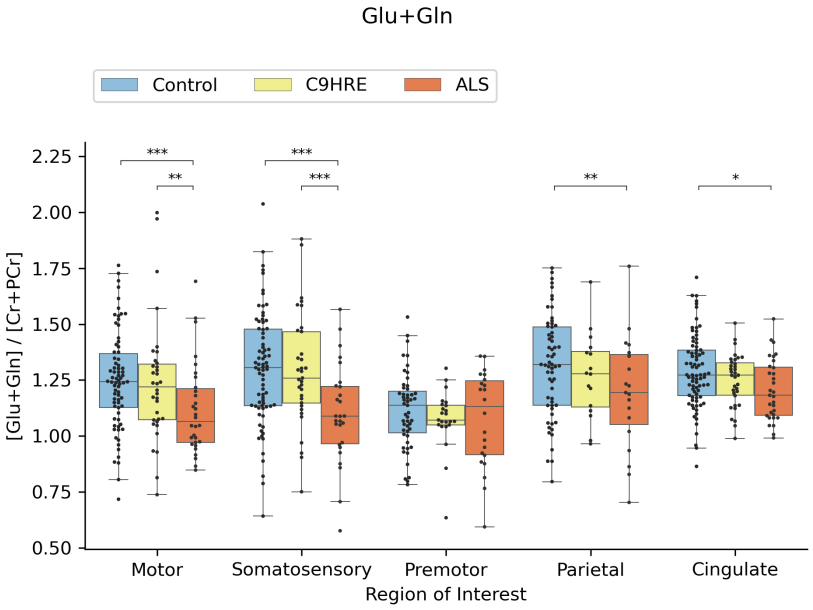

Figure 5.3: Glu+Gln variation across regions, separated by group.

These findings were related to hemispheric lateralisation. In healthy controls, in the previous chapter I demonstrated that Glu and Glu+Gln were higher in the right Motor region than the left. The reduction in ALS was seen in the right Motor region but not the left, while the size of reduction was greater in the right Somatosensory region than the left (Figure 5.4).

When Glu and Gln were considered alone, reductions in ALS were seen in the right Somatosensory region but not the left (Supplemental figure 5.14a).

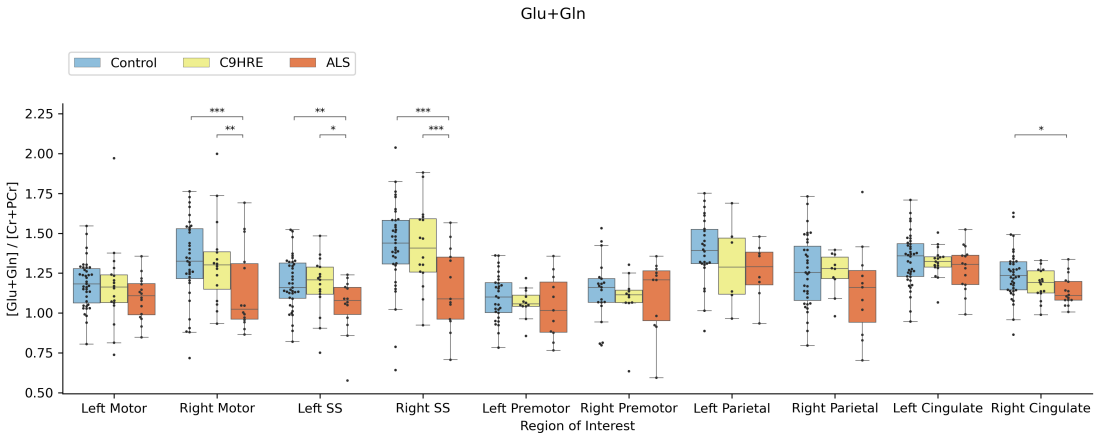

Figure 5.4: Glu+Gln variation across regions, split by hemisphere, separated by group.

GABA

GABA was reduced in the Motor region in ALS compared to healthy controls (Figure 5.5). When split by hemisphere this reduction appears to be more prominent in the left Motor region than the right (Supplemental figure 5.15).

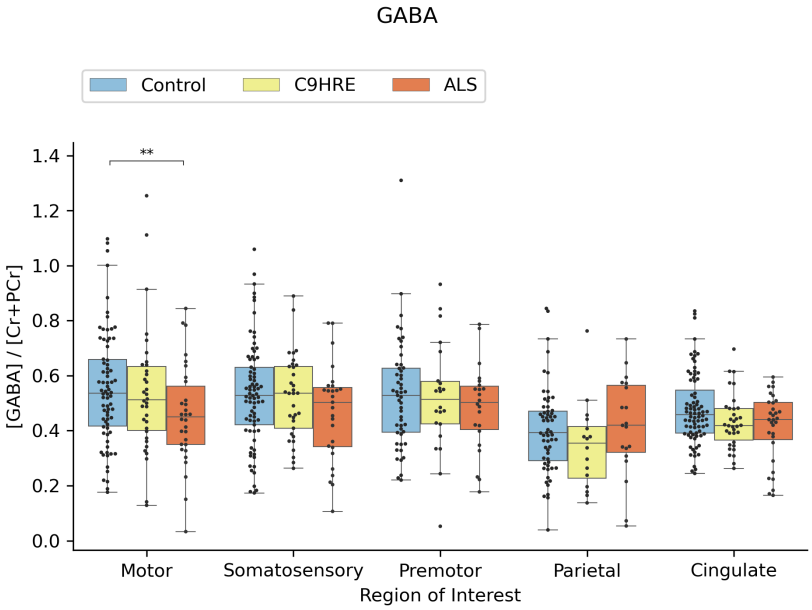

Figure 5.5: GABA variation across regions, separated by group.

5.3.2 Voxel-wise results

Group level differences - ALS patients vs. controls

NAA There was a widespread reduction in voxel-wise NAA between patients and controls. This was more concentrated towards the posterior part of the region of interest. There was no clear white or grey matter predominance of this result.

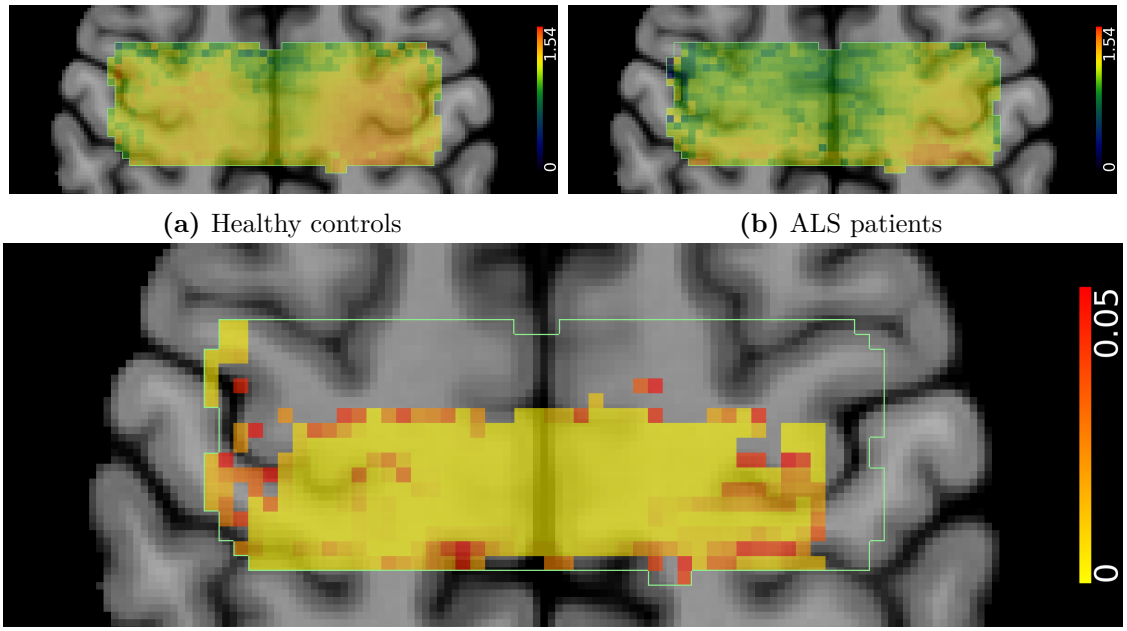

(a) Healthy controls **(b)** ALS patients

Figure 5.6: Control NAA/Cr > ALS NAA/Cr. Significant regions $p < 0.05$. Spatial maps cluster corrected using threshold-free cluster enhancement.

Glu Glu was lower in ALS patients in the right hemisphere motor hand area but not the left. Glu reductions were also seen bilaterally in the postcentral gyrus, and medial parts of the precentral gyrus.

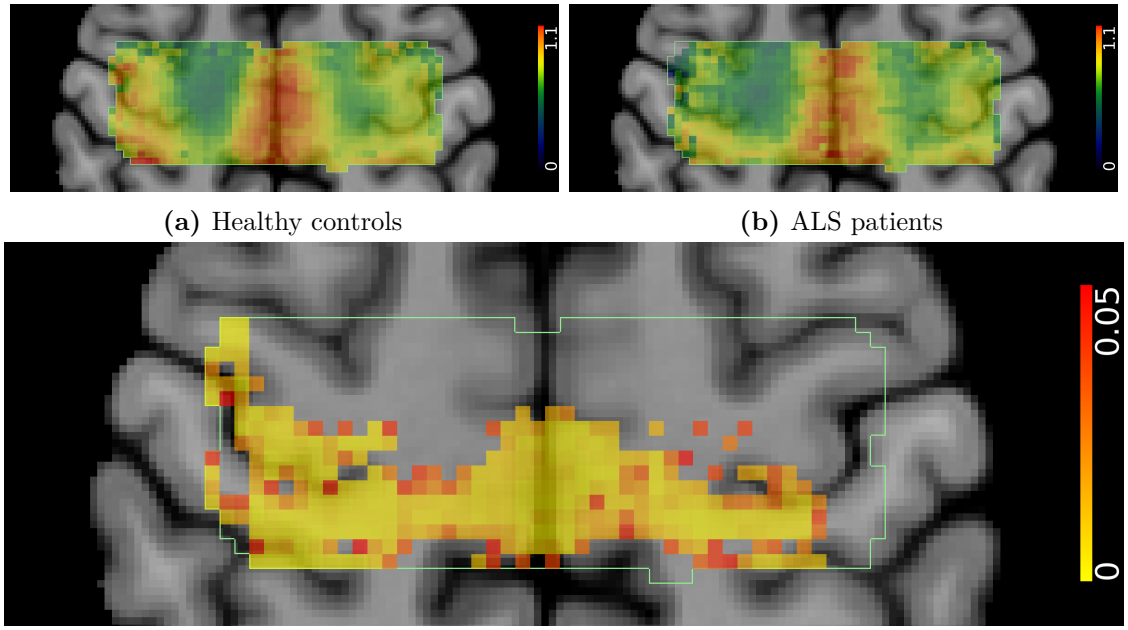

(a) Healthy controls **(b)** ALS patients

Figure 5.7: Control Glu/Cr > ALS Glu/Cr. Significant regions $p < 0.05$. Spatial maps cluster corrected using threshold-free cluster enhancement.

GABA GABA was lower in ALS patients in the left hemisphere motor hand area but not the right. GABA was also reduced in the left precentral gyrus, and both postcentral gyri. Significant regions were more extensive on the left side than the right.

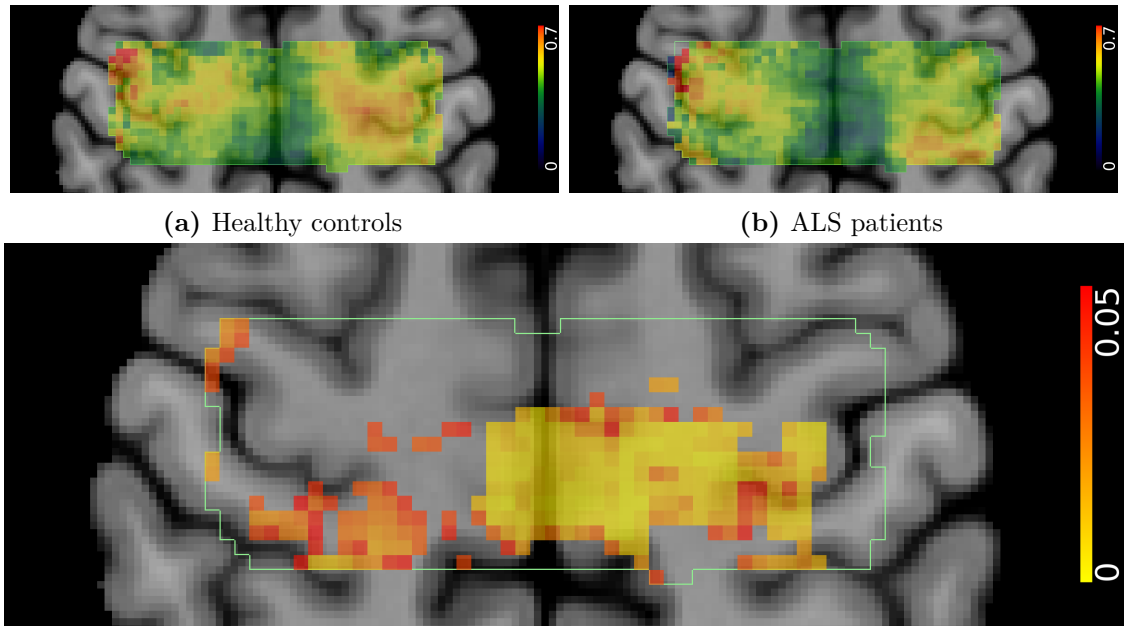

(a) Healthy controls **(b)** ALS patients

Figure 5.8: Control GABA/Cr > ALS GABA/Cr. Significant regions $p < 0.05$. Spatial maps cluster corrected using threshold-free cluster enhancement.

Group level differences - *C9of72*-HRE+ vs. *C9orf72*-HRE– healthy relatives

NAA Figures 5.9a and 5.9b show the group mean standard space NAA/Cr map for presymptomatic *C9orf72*-HRE+ and *C9orf72*-HRE– individuals. However, there was no significant difference after voxel-wise multiple comparison correction.

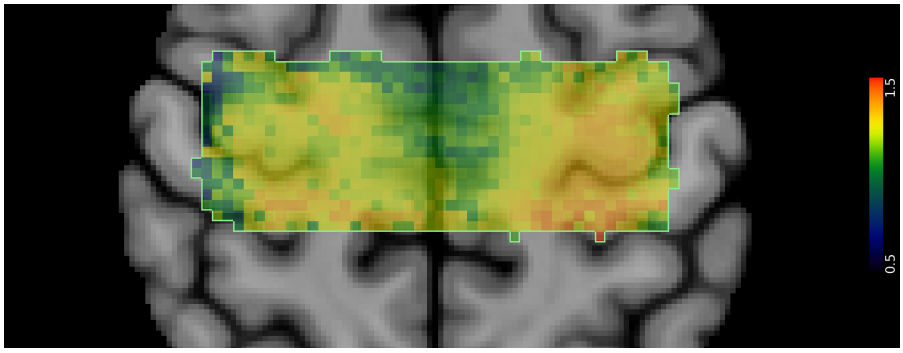

(a) *C9orf72*-HRE negative relatives

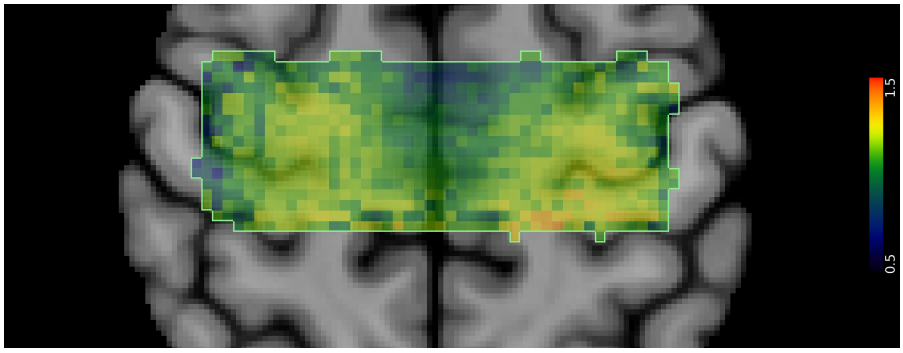

(b) *C9orf72*-HRE positive relatives

GABA

GABA was lower in the left motor hand area in the *C9orf72*-HRE+ group than in the *C9orf72*-HRE– group. GABA level was not significantly correlated with participant age - this data is not plotted with identifiable data points to maintain blinding of individual research participants' to genetic status.

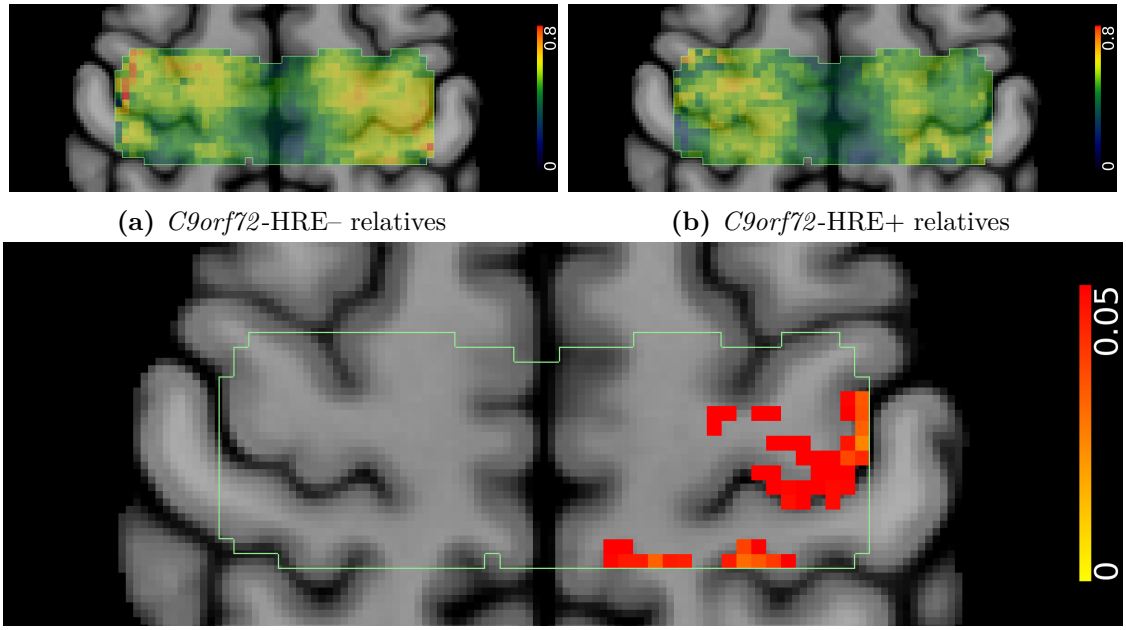

(a) *C9orf72*-HRE– relatives **(b)** *C9orf72*-HRE+ relatives

Figure 5.10: *C9orf72*-HRE+ vs. *C9orf72*-HRE– groups. GABA/Cr. Significant regions $p < 0.05$. Spatial maps cluster corrected using threshold-free cluster enhancement.

Glu There was no significant voxel-wise difference in Glu/Cr between *C9orf72*-HRE+ and-HRE– relatives.

Voxel-wise correlation with motor network connectivity

Glu x motor network The voxel-wise correlation between local glutamate and motor network connectivity showed a similar pattern in the healthy controls as in the previous Chapter's results (Figure 5.11). Glutamate was negatively correlated to motor network connectivity in both motor hand areas. In ALS patients however, this pattern was disrupted, with widespread positive correlations between local glutamate and motor network connectivity in the postcentral gyrus and left medial precentral gyrus. In *C9orf72*-HRE positive individuals, a mixed picture of both positive and negatively correlated clusters was observed. In this group, glutamate in the left hand area and cingulate gyrus was positively correlated with motor network connectivity, while there were negatively correlated clusters in the left premotor cortex and right medial motor cortex (Figure 5.11). Interpretation of statistical comparisons between the correlation maps in these four groups is challenging as

this is a difference condition (correlation in Group A > correlation in Group B) - further voxelwise stats and interpretation are avenues for future work.

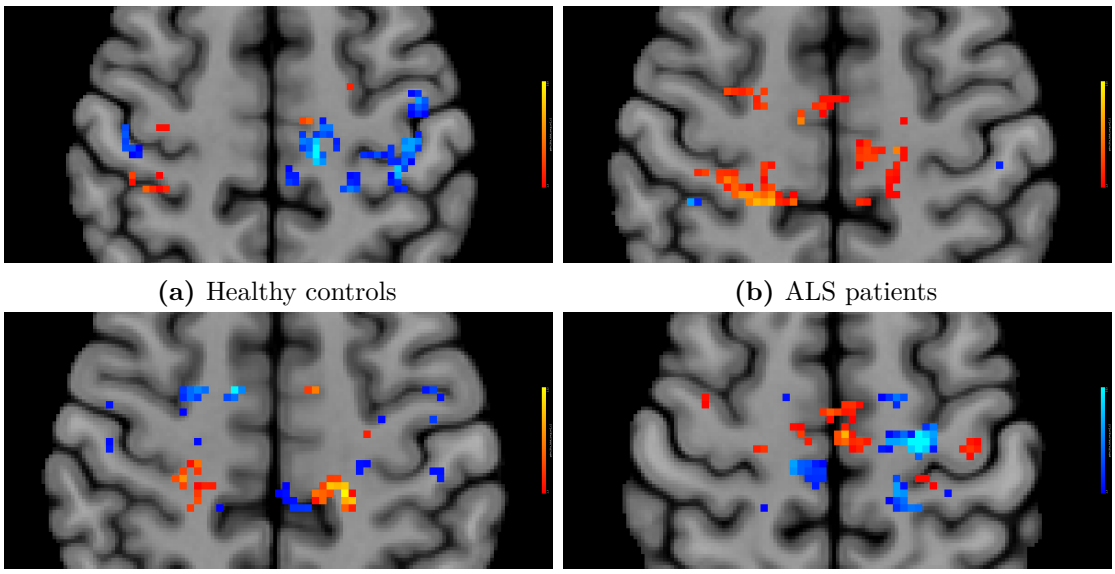

(a) Healthy controls **(b)** ALS patients

(c) *C9orf72*-HRE negative relatives **(d)** *C9orf72*-HRE carrier relatives

Figure 5.11: Voxel-wise correlation of Glu/Cr with subject resting state motor network connectivity.

GABA x motor network In healthy controls, local GABA was negatively associated with motor network connectivity in the left hand area, with a small cluster in the right sensory hand area. In the medial motor cortex and cingulate cortex bilaterally, there were positively correlated clusters (Figure 5.12). In ALS patients, there were no significant clusters in the motor hand regions, and no clear pattern. In *C9orf72*-HRE– individuals these medial structures were negatively correlated with motor network connectivity. In *C9orf72* HRE+ individuals, local GABA was positively correlated with motor network connectivity in the left sensory hand area and left cingulate cortex, and negatively correlated in the left premotor area. Interpretation of statistical comparisons between the correlation maps in these four groups is challenging as this is a difference condition (correlation in Group A > correlation in Group B) - further voxelwise stats and interpretation are avenues for future work.

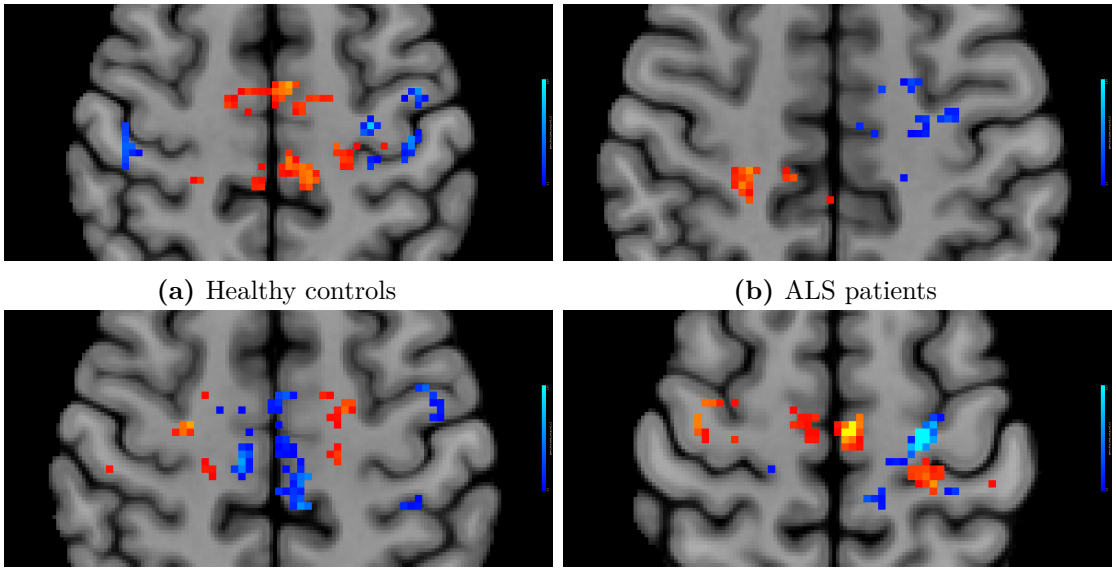

(a) Healthy controls **(b)** ALS patients

(c) *C9orf72*-HRE negative relatives **(d)** *C9orf72*-HRE carrier relatives

Figure 5.12: Voxel-wise correlation of GABA/Cr with subject resting state motor network connectivity.

5.4 Discussion

In this chapter I have performed a novel multimodal analysis of neurochemical markers of regional excitation and inhibition in both established and presymptomatic ALS. The combination of high-resolution spectroscopic imaging of excitability markers along with a genetically characterised presymptomatic cohort is novel in the ALS literature.

ALS is a neurochemically asymmetrical disease I found reduced NAA in widespread motor regions in ALS, consistent with previous work. There was also widespread reduction of glutamate in both the precentral and postcentral gyrus in ALS, with notable sparing of the left hemisphere hand area. GABA was also reduced in ALS in primary motor and somatosensory regions, with notable sparing of the opposite (right) hemisphere hand area. These findings add weight to the view that ALS is a (slightly) asymmetric disease process, as suggested by cortical thickness data[137,395], and my earlier network functional connectivity changes (Chapter 3). The greater depletion of GABA in the left hemisphere may

therefore be a marker of degeneration, while the maintenance of glutamate may be a marker of compensation. Future MRS studies of glutamate or GABA in ALS, along with clinical translation projects, may need to account for differing neurochemical profile in the right and left hand areas.

As discussed in Chapter 3, the interpretation of this result is limited given the heterogeneity of the site of onset in the included patients (Table 5.1). Future directions include subgrouping patients by side of onset or side more severely affected.

A disinhibited hot-spot in the left motor hand area in *C9orf72*-HRE+ individuals I found a region of reduced GABA in the left motor hand area in *C9orf72* HRE+ individuals. This is a novel imaging finding in this patient group, and in presymptomatic ALS as a whole. This would concur with previous neurophysiological findings of a disinhibited hot-spot in early disease, but could widen the window for early detection. As there is no increasing trend with age, however, it is unclear whether this marker reflects a different initial state of the motor system in *C9orf72*-HRE+ individuals, or a marker/driver of neurodegeneration.

Disrupted patterns of motor network connectivity in ALS There was a clear change in the link between local Glu, GABA and motor network function in ALS. The relationship with glutamate changed direction across various parts of the motor system, while the relationship with GABA was lost. This might support the view of GABA change as a marker of direct damage by disinhibition to motor network function, while the glutamate changes are secondary. The fMRI network connectivity field has been divided on whether network alterations show direct degenerative processes or compensation[234,396,479]. This adds evidence to that debate and suggests that neurochemical interactions may elucidate whether a change is damaging or compensatory.

Higher spatial resolution MRS data increases interpretability of findings The fine spatial resolution of this technique allowed the disruption of physiological asymmetry and network connectivity relationships of inhibitory and excitatory

tone to be studied. While tissue volume averaging remains a problem, and new challenges with multiple comparison correction are created by this technique, it enabled powerful voxel-wise inference showing previously unknown spatial trends.

Can GABA be reliably quantified using MRSI at 3T? GABA quantification has been consistently challenging, and its quantification at 3T without using spectral editing or short echo time imaging remains controversial. In this dataset, individual GABA measurements had greater uncertainty (relative CRLB) than more abundant metabolites (Table 4.3), however, this is comparable to previous MEGA-PRESS or SPECIAL MRS datasets[210]. Previous analyses with this technique support its validity for quantifying GABA[480].

As previously noted in Section 4.1.4, caution is advisable in treating GABA and Glu measurements as markers of inhibitory or excitatory neurotransmission, rather they may reflect a more generalised excitability "tone".

Possible confounds in *C9orf72*-HRE carriers There are also several variables that could affect my findings in *C9orf72*-HRE carriers. Variable penetrance and age of onset[481] have been consistently described, as well as within-family variation in clinical manifestation[482]. The pathology may also be shaped by protective genetic variants[483]. These factors are likely to contribute to variation in which brain regions abnormalities could be first detected. With larger datasets, high spatial resolution MRSI may allow sub-stratification of presymptomatic changes in different brain regions.

In summary, high resolution excitatory and inhibitory neurochemical mapping generates a range of novel insights into the ALS disease process and a candidate presymptomatic signature. In the following chapter I will integrate these measures with previously discussed functional imaging measures to derive a composite multimodal imaging biomarker of cortical excitability in ALS.

5.5 Supplemental Figures

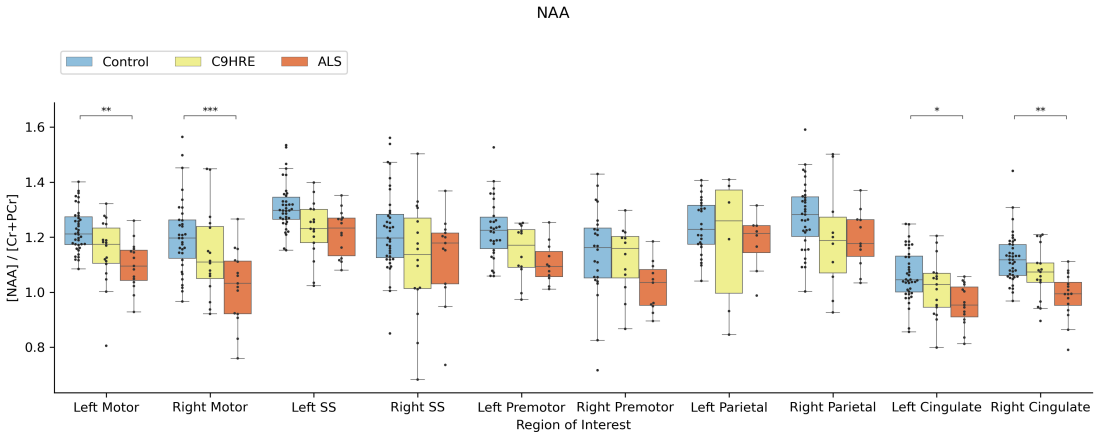

Figure 5.13: NAA variation across regions split by hemisphere, separated by group. Somatosensory is abbreviated to SS.

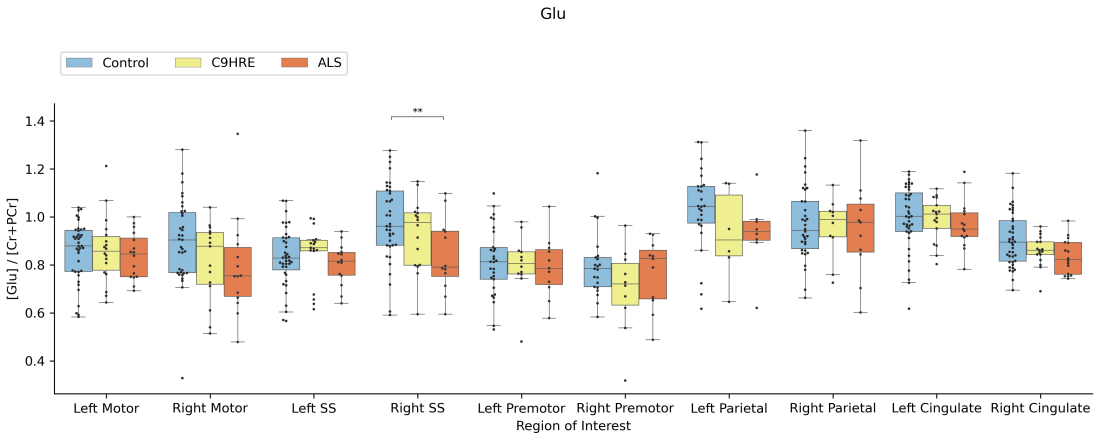

(a) Glu

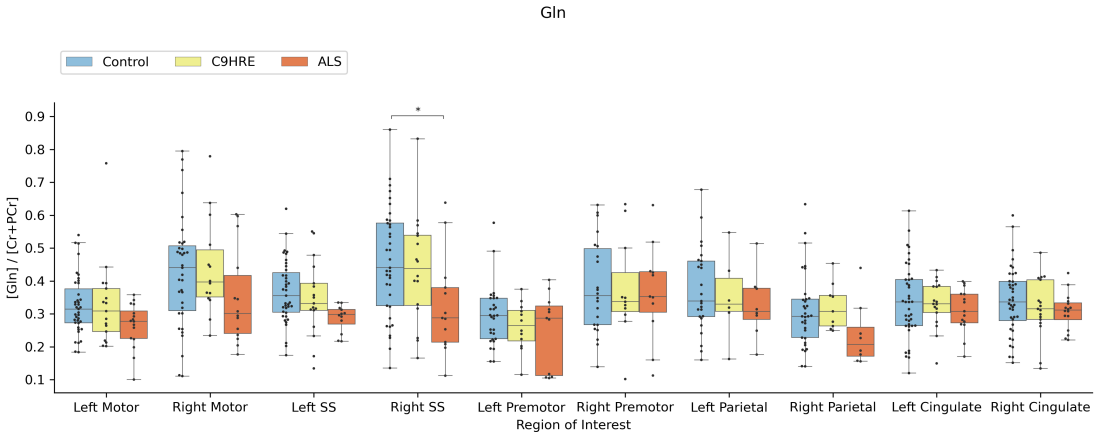

(b) Gln

Figure 5.14: Separate plots for Glu and Gln variation across regions, split by hemisphere, separated by group.

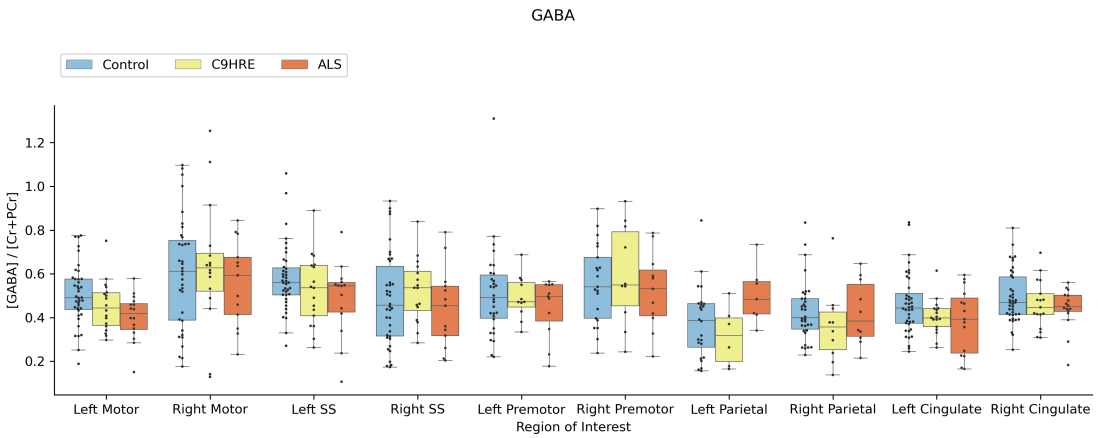

Figure 5.15: GABA variation across regions, separated by group.

On two occasions I have been asked, ***"Pray, Mr. Babbage, if you put into the machine wrong figures, will the right answers come out?"*** *In one case a member of the Upper, and in the other a member of the Lower, House put this question. I am not able rightly to apprehend the kind of confusion of ideas that could provoke such a question.*

— p.67, Passages from the Life of a Philosopher, Charles Babbage

6

Integrating multimodal measures of cortical excitability in ALS and presymptomatic disease

Contents

6.1 Introduction

6.1.1 A many-to-many correspondence between imaging modalities and disease properties

Cortical hyperexcitability is a key pathophysiological theme in ALS (Section 1.3.1). In previous chapters I have described group level differences between ALS, healthy controls and presymptomatic *C9orf72*-HRE carriers in motor system excitability as measured using functional MRI and MR spectroscopic imaging.

Task-related BOLD fMRI activation was higher with lower ALS disease duration in a cingulate/SMA motor region while increased between-region connectivity of primary and secondary motor areas was correlated in the right hemisphere with loss of function (Chapter 3). This builds on previous literature on fMRI trajectories in ALS, suggesting increased/more diffuse activation as an early disease on a background of ongoing compensatory connectivity changes.

MR spectroscopic imaging shows lateralisation of inhibitory (GABA) and excitatory (Glu) tone in the healthy motor system (Chapter 4) - both GABA and glutamate levels are lower at rest in the left primary motor cortex than the right - suggesting that the right and left motor cortices are physiologically tuned to different excitability levels.

In ALS, glutamate reduction was widespread in the motor and somatosensory cortices and maintained in the left motor hand area (Chapter 5). On the other hand GABA reduction was more concentrated in the left hemisphere and motor hand area in ALS, and focal GABA reduction in the left motor hand knob was found in *C9orf72*-HRE carriers. These findings suggest that selective GABA depletion may be present before disease onset, and that these findings may be highly focal. Ongoing neurodegeneration produces an abnormal pattern of excitability that may have toxic pathogenic implications as well as reflecting compensatory mechanisms.

Thus far, I have linked data from several modalities (rs-fMRI, t-fMRI, MRSI) to several facets of motor system excitability individually - baseline inhibitory/excitatory

"tone", task-related activation, and between-region connectivity - with the aim of breaking down the umbrella concept of cortical hyperexcitability. I have shown that this is a **many-to-many** correspondence with multiple modalities allowing fuller characterisation of multiple pathologies. Integration of multiple noisy individual modalities and data reduction to specific measures of underlying disease properties may facilitate successful generalisation in research and translation to the clinic.

6.1.2 Why integrate multiple modalities?

Many studies in ALS consider data derived from a single modality to represent a single pathogenic process (e.g. cortical thickness reduction cell body death, DTI FA reduction axonal loss in long tracts), however the value of combining modalities has been shown extensively. The literature on combining modalities in ALS reflects wider themes in neuroimaging - hypothesis falsification with spatial statistics, granular description with multiple modalities, and harnessing multiple modalities using machine learning for making predictions[484].

6.1.3 Hypothesis driven disease mechanism exploration

Between-modality correlation typically tests the interaction between two different features in relation to an underlying disease process - usually phrased with a null hypothesis of no correlation between the pair. For example, studying resting state fMRI and DTI together links structural and functional network damage supporting a pathological role for network excitability[485]. TMS and resting state fMRI together illustrate the functional consequences of abnormal cortical excitability[486]. Other studies have applied multiple techniques concurrently in ALS to study the Papez circuit[487], cerebellar dentate nucleus[488], and model local vs distant network excitability[489].

6.1.4 Granular description of cohorts using multiple modalities

Some multimodal studies are descriptive, seeking imaging correlates of ALS subgroups or clinical properties - for example along the ALS-FTD spectrum[341] or

according to *C9orf72*-HRE status[351] without necessarily applying the findings to an underlying hypothesis or desired outcome. A variant on this theme is the description of change over time in ALS using multiple modalities[490].

6.1.5 Harnessing multiple modalities for better predictions

Finally, many studies begin with a desired outcome, and harness multimodal data in a more agnostic manner, aiming to optimise performance. Most simply this can be head to head comparison of modalities in detecting abnormality[491,492]. Many studies have compared classification accuracy between ALS and healthy controls using a range of statistical tools - linear models, support vector machines, and multi-layer perceptrons[493–497]. In addition to classification, this class of tools can make quantitative estimates through regression of measures such as survival in ALS[498,499] or response to therapy in clinical trials[500].

Exploring multimodal data reflecting cortical excitability

In this chapter, I will synthesise my findings to explore the disease theme of cortical excitability. I will select features according to the work previously presented in this thesis, and perform dimensionality reduction using linear discriminant analysis to compare and consolidate features. Finally, I will use the task of participant classification as a test-bed for the validity of this approach, aiming to draw insight into the role of different cortical excitability properties in presymptomatic and established ALS.

6.2 Methods

6.2.1 Study participants

Details of study participants, recruitment, inclusion criteria and demographics are summarised in Section 5.2.1.

6.2.2 MRI imaging

In addition to the T1 weighted and MR spectroscopic sequences discussed in Section 5.2.3, I analysed the task-fMRI data collected during the same scanning session. Task functional MRI was performed using gradient echo EPI sequences matched to UK Biobank acquisition parameters[278]. These include 2.4 × 2.4 × 2.4mm spatial resolution, 88 × 88 × 64 field of view matrix, 490 timepoints over 6 minutes, TR = 0.735s, TE = 39ms, 8× multi-slice acceleration, and flip angle 52°.

6.2.3 Task design and analysis

Participants were instructed to perform a cued motor task designed to investigate motor activity in relation to lateralised motor preparation and execution (schematic in Figure 6.1). An initial lateralisation cue with a letter L or R indicating the side on which to prepare to move was presented for 200ms (Figure 3.1). After a random interval evenly distributed between 0.8 and 1.2 seconds a Go cue (filled circle) was presented for 200ms. In response to the Go cue, participants were instructed to make a single movement of the index finger of the hand on the cued side towards the thumb, but not touching it, followed by a return to the starting position. A random inter-stimulus interval evenly distributed between 3 and 5 seconds followed. Trials were delivered in a random counterbalanced order of Left/Right directions. Stimuli were presented and stimulus and response timestamps recorded using the Psychtoolbox3 MATLAB toolkit[372]. Stimuli were presented centrally on a dark grey 32 inch TV screen with height × width of approximately 100 pixels (screen height 1080 pixels). One block of 60 trials was performed for each participant.

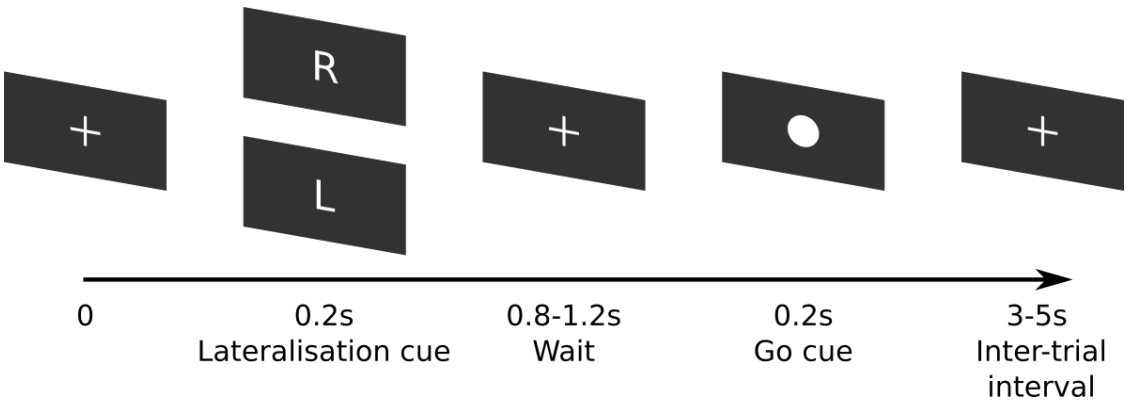

Figure 6.1: Schematic of task stimuli and timings.

6.2.4 Functional connectivity analysis

As in Section 3.3.3, I performed a data-driven independent component analysis (ICA).

Data was preprocessed for motion correction (MCFLIRT) and highpass filtering (FWHM 100s). Then, functional data was decomposed using single subject independent component analysis (FSL MELODIC)[375] with dimensionality automatically calculated by the tool to maximise explained variance.

Each subject's independent components (ICs) were classified and noise components removed using FMRIB's ICA-based X-noiseifier (FIX)[376,377]. FIX was run with a classification threshold of 20, and removal of motion confounds enabled. Classifier weights used were those derived from training on the UK Biobank imaging study dataset. This dataset is similar to mine in participant characteristics (older adults) and has identical acquisition parameters. The cleaned output from FIX was then smoothed using a 5mm FWHM Gaussian kernel, and aligned to standard space using the affine matrix and nonlinear warp generated using the AFNI @SSwarper tool.

Group-level ICA was also run using MELODIC using a temporal concatenation approach. At this stage, dimensionality was set to 75 to allow sufficient separation of large-scale brain networks to allow network analysis without decreasing reliability[378]. Similar dimensionality settings have been used in previous work, albeit with larger datasets[379]. Example IC spatial maps are shown in Figure 3.2. Group ICs were then mapped onto individual subjects' preprocessed and cleaned fMRI data using the

first stage of dual-regression[380]. Following on from the findings of Chapter 3, three nodes were selected for further functional connectivity analysis based on spatial location over the primary and secondary motor regions respectively (Figure 6.2).

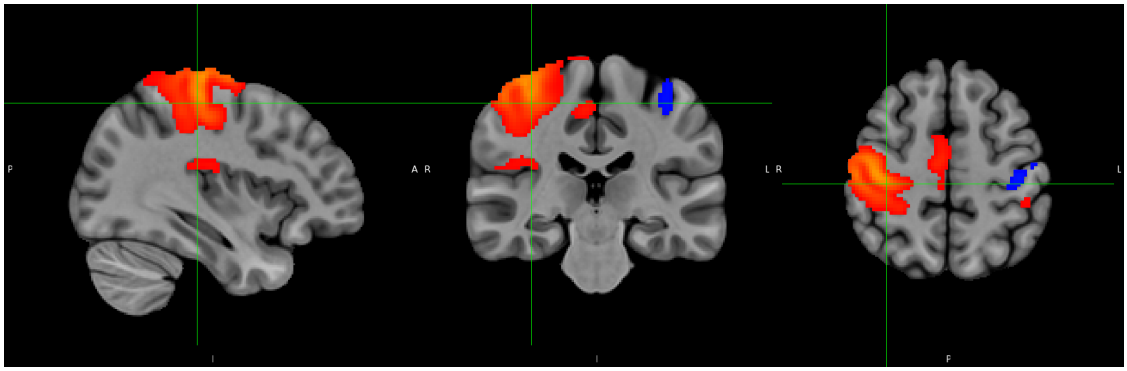

(a) Right Primary motor

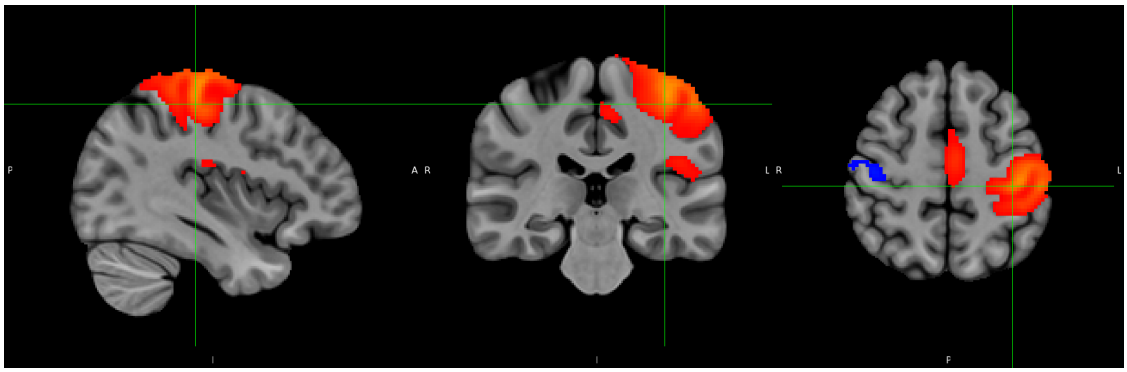

(b) Left Primary motor

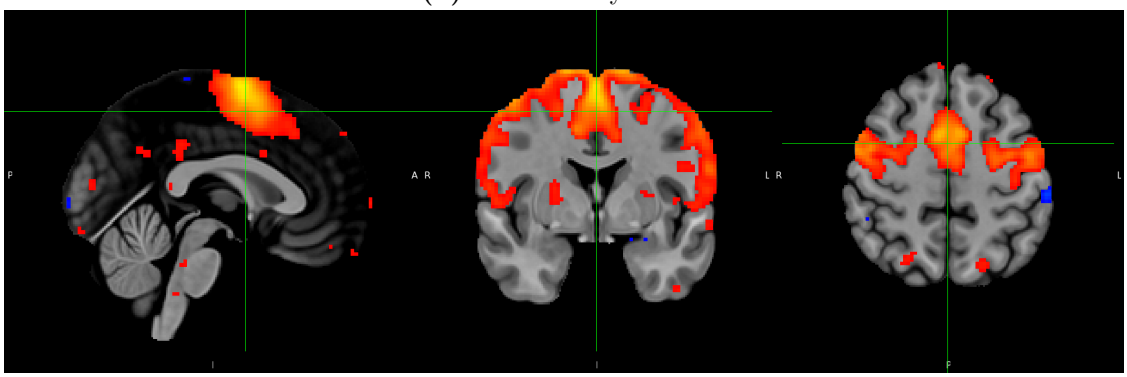

(c) Secondary motor

Figure 6.2: Selected independent component spatial maps (z-statistic images) resulting from group ICA and assigned labels.

6.2.5 Feature selection

Having found clinically correlated functional connectivity involving primary motor secondary motor edges, the right and left hemisphere "Primary motor" ×

"Secondary motor" functional connectivity were extracted from dual regression stage 2 outputs, as was between-hemisphere "Primary motor" × "Primary motor" functional connectivity.

Given previous findings in the literature of increased motor cortex activation with movement, I selected the mean COPE for right and finger movement in the region of the right and left primary motor area respectively.

Finally, I selected the mean concentration (relative to total creatine) of NAA, GABA, Glu and Ins in the right and left primary motor area. In total, 8 MRSI features and 7 task fMRI features were selected.

6.2.6 Data preprocessing and dimensionality reduction

Under certain conditions, the incorporation of multiple noisy inputs, even if partially redundant, can be expected to yield an information gain[501], and therefore improved understanding of the underlying process or group difference. Non-redundant inputs would be expected to yield insight into multiple different meaningful patterns. To avoid the pitfalls of over-fitting, non-generalisability however, feature selection should aggressively minimise the number of features studied in small datasets[502].

From selected features, I subtracted the mean and scaled to unit variance - zero centering and standardisation is required for subsequent analyses. I then applied linear discriminant analysis using the scikit-learn Python package (version 1.0.2)[503]. This is a supervised technique for dimensionality reduction that projects the raw data in a way as to maximise group separation using known labels. I selected this technique because my dataset has known groups stratified by disease status and genetic vulnerability.

6.2.7 Group separation - Linear support vector classifier

I tested the performance of the combined features generated by LDA using a linear support vector machine classifier (SVC). I used the default implementation of LinearSVC[504] in the scikit-learn Python toolkit (version 1.0.2)[503] [linear kernel, default regularisation parameter (1.0), and default loss function ('squared hinge')].

To compare the performance of different initial feature sets I tested this using MRSI-derived features only, tfMRI-derived features only, and both. Classification performance is reported in terms of class-wise and average positive-predictive-value and sensitivity.

6.2.8 Validation

To validate this classification technique I first performed leave-one-out cross validation using scikit-learn. This involves removing one (or more) participants from the training data, re-training the classifier, and predicting the group label of the held-out participant(s). This technique robustly estimates mean prediction error and is computationally feasible in our dataset[505]. I additionally performed stratified K-fold (K = 5) cross validation using scikit-learn - this trains the classifier on smaller subsets of the data, which estimates generalisability to other datasets with corresponding features.

6.3 Results

Dimensionality reduction The participants were plotted - colour coded according to group - according to linear discriminants in Figure 6.3, for each set of input features (MRSI only, task-fMRI only, and both). Group separation was qualitatively best when both sets of input features were used.

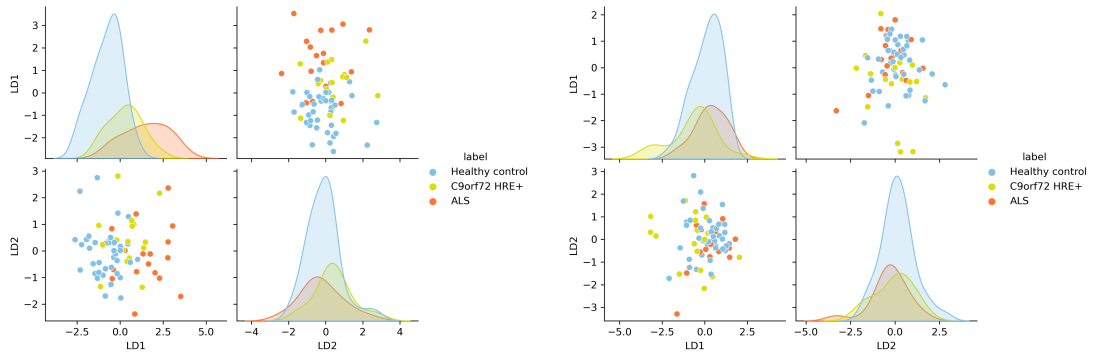

(a) MRSI features

(b) task fMRI features

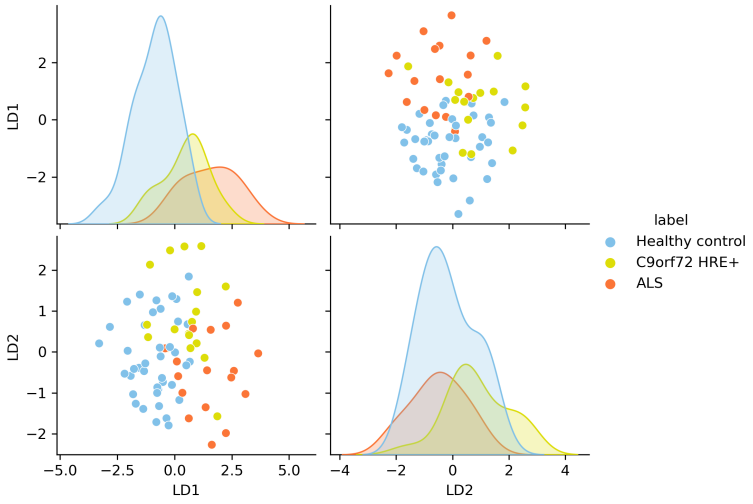

(c) Both

Figure 6.3: Pairwise plots of linear discriminants when using MRSI and task-fMRI features alone and when combined.

The scaling factors for input features are shown in Supplemental figure 6.6 for individual modalities and Figure 6.4 for both combined. The first linear discriminant was formed from a range of different inputs - NAA/Cr from bilateral hemispheres, right hemisphere GABA, right hemisphere Gln, left hemisphere Ins, and left hemisphere COPE for right hand movements. The second linear discriminant was heavily loaded onto the left motor cortex COPE associated with movements of either hand.

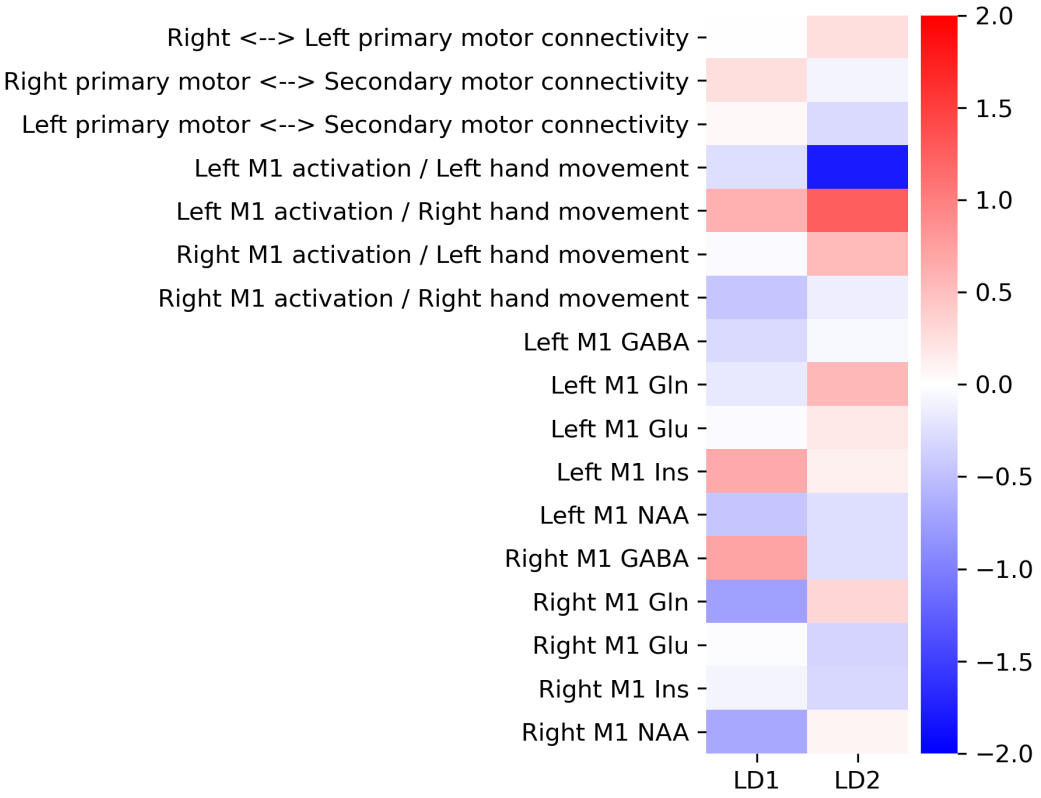

Figure 6.4: Scaling factors applied to input data features in the generation of linear discriminants plotted as a colour bar.

Support vector machine classifier Classification results when MRSI features, tfMRI features, and both are included are shown in Figure ??. Notably, MRSI features alone offer intermediate performance in classification between ALS patients and other groups. However, classification performance improves when features from both modalities are used. Task fMRI features alone do not perform well at classification between ALS and controls. However, they do separate a subset of the *C9orf72*-HRE carrying relatives. The overall performance of the classifier is summarised in Table 6.1.

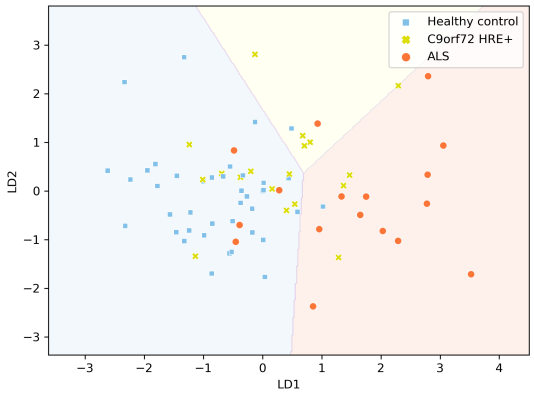

(a) MRSI features

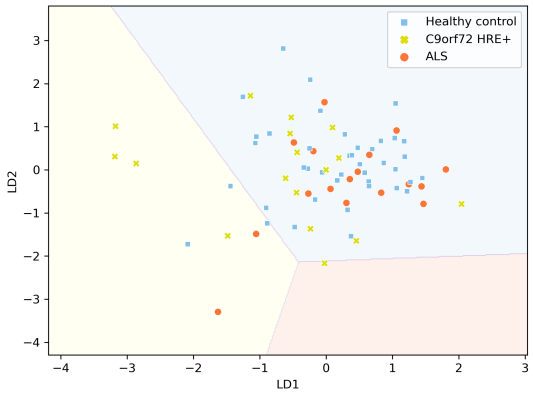

(b) task fMRI features

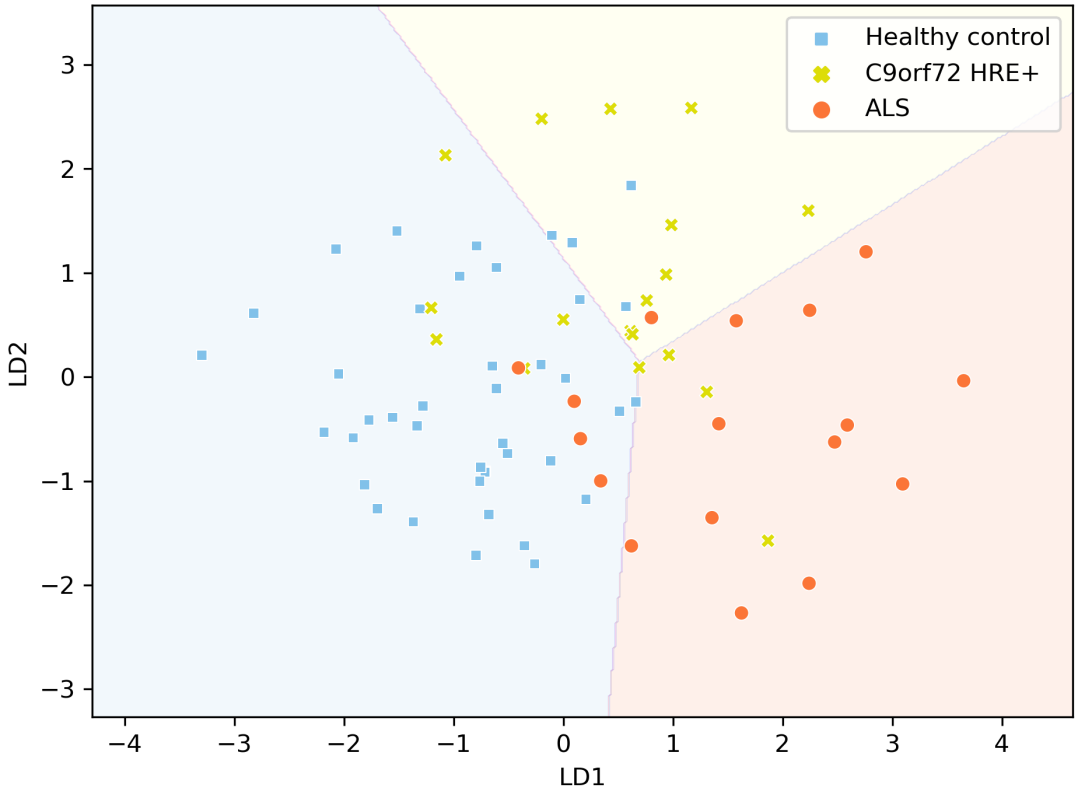

(c) Both

Figure 6.5: Group separation using LinearSVC using MRSI and task-fMRI features alone and when combined. Each point represents an individual subject, with the first and second linear discriminants plotted on the x and y axes respectively. The colour/style of a point indicates its true group membership, while the shaded background segments show the decision boundaries for the classifier.

Group	Performance metric	Input modalities		
		tfMRI only	MRSI only	both
ALS	PPV	0.0	0.71	0.71
	sensitivity	0.0	0.71	0.71
C9orf72-HRE	PPV	0.44	0.67	0.64
	sensitivity	0.58	0.22	0.50
Control	PPV	0.58	0.74	0.80
	sensitivity	0.93	0.95	0.88
Overall	Leave-one-out accuracy	0.54	0.71	0.72
	Stratified k-fold accuracy	0.53	0.69	0.72

Table 6.1: Summary of classification performance when using both MRSI and task fMRI input features. Random chance would be expected to produce 3-group classification accuracy of 0.33.

6.4 Discussion

In this chapter, I explored cortical excitability through integrating data derived from multiple modalities. While in previous chapters I assessed individual techniques in high spatial resolution using voxel-wise or region-wise statistics, here I aimed to distil the features of cortical excitability that perform well at differentiating groups with established ALS as well as presymptomatic disease. I trained a classifier to test these features, with the aim of better understanding which features perform best in this dataset, as well as extracting and validating generalisable principles regarding MRSI and tfMRI changes in ALS.

6.4.1 A robust composite measure of pathology

MRSI alone allowed good separation of ALS patients from controls, with *C9orf72*-HRE+ individuals occupying an intermediate place on this axis (LD1) (Figure 6.5a). This was not solely due to the inclusion of motor cortex NAA - typically seen as a marker of neurodegeneration, but also reflective of mitochondrial energetics - shown

by the spread of scalings across multiple inputs in Figure 6.6a. The composite marker most successful at separating ALS patients (LD1, Figure 6.4) included NAA in both motor cortices as well as GABA and Gln in the right motor cortex, as well as left motor cortex activation to right hand movement. One possible explanation for this is the accumulation of neurochemical and functional pathology with disease progression - which might be sub-clinical in *C9orf72*-HRE+ individuals.

6.4.2 Marked left M1 hyper-activation in a subset of *C9orf72*-HRE+ individuals

Differentiating *C9orf72*-HRE carriers from other groups was more challenging, with lower positive predictive value and sensitivity in classification. However, a notable subset were separated according to predominantly fMRI changes, in particular left motor cortex activation to finger movement on either side, as well as right motor cortex activation to left index finger movement - LD2, Figure (6.4). This suggests marked BOLD hyper-activation in the left motor cortex, perhaps reflective of a transient period of hyper-excitability that is no longer seen in established disease.

One possible confound is greater attention, effort or anxiety from gene carriers who are aware of the familial risks. In a previous finger movement task-MEG study the SOD1 and *C9orf72* mutation carrier groups had the fastest response time, but higher error rate on NoGo trials[388]. However, this would not sufficiently explain why this effect may be seen in the left primary motor cortex but not the right in a task that involved both hands.

This work presents a novel combination of techniques, in a large, genetically characterised cohort with individuals representing normal physiology, established disease, and the presymptomatic stage. I chose to apply powerful and flexible data science tools to explore cortical excitability further in this context, while making conservative choices to avoid the "curse of dimensionality", over-fitting, and non-generalisability. Feature selection was curated based on prior work, and aggressive dimensionality reduction performed. A simple classifier (linear support vector machine) was chosen to facilitate interpretation and introspection.

However, this dataset remains small in the context of the literature on classification according to neuroimaging parameters in neurodegeneration. Validation is therefore challenging - within this dataset, I have shown that classifier performance is not clearly driven by outliers, or overfit to data subsets. Validation on a completely new dataset was not possible - as no other dataset combining task fMRI and high resolution spectroscopy in these patient groups exists.

Our findings argue strongly for the value of including spectroscopy, and in particular, spectroscopic imaging, in MRI studies of ALS going forward. The spatial resolution enables focused analyses in the most abnormal regions. Future directions for validating these findings and advancing towards clinical application for diagnosis and assessing disease progression might include performing multimodal imaging as part of the diagnostic process in ALS, to demonstrate utility in a real-world classification scenario. Higher field strength (7T) imaging as well as longitudinal followup may better characterise the functional activation changes in *C9orf72*-HRE+ individuals and their implications for risk stratification and recruitment to gene therapy clinical trials.

6.5 Supplemental Figures

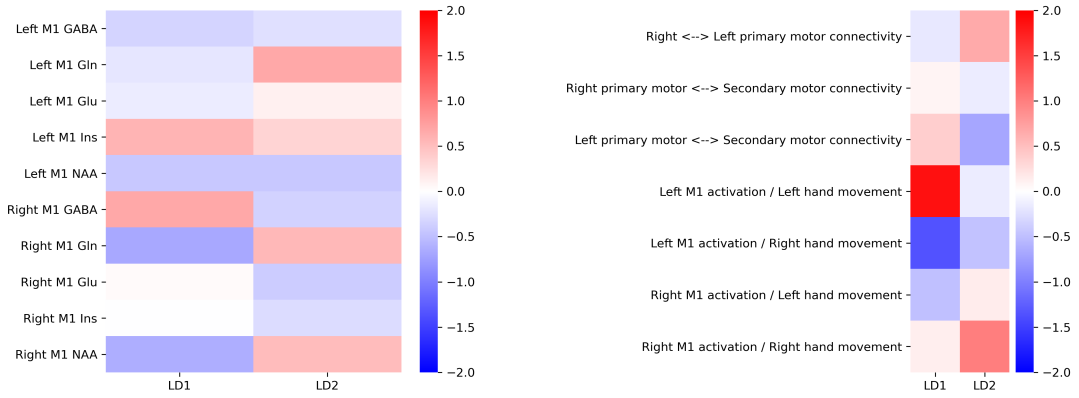

(a) MRSI features **(b)** task fMRI features

Figure 6.6: Scaling factors applied to inputs in generation of linear discriminants.

The whole of life is just like watching a film.
Only it's as though you always get in ten minutes after the big picture has started, and no one will tell you the plot, so you have to work it out all yourself from the clues.

— Thud! by Terry Pratchett

7 Conclusions

Contents

This thesis makes several contributions to the study of motor network excitability in healthy individuals, established ALS and presymptomatic disease. I extended the known characterisation of task-fMRI activation changes in ALS in Chapter 3. Then, in Chapter 4 I applied and validated a novel MRSI technique to describe variation in excitation and inhibition across the motor system in normal physiology, and its correlation with age and functional connectivity. In Chapter 5 I extended this technique to study the change in this motor inhibition/excitation landscape

in established and presymptomatic disease. Finally, I explored how integrated biomarkers of cortical excitability might be interesting and useful.

Finally, I will consider the limitations of my cross-sectional work and possible future directions in understanding biomarker trajectories for diagnosis, prognosis and therapy trials. I will refer to the BEST framework[506] published by the NIH and FDA to describe candidate biomarkers and potential applications in this chapter.

7.1 Motor network excitability in ALS is dependent on disease stage and functional impairment

In Chapter 3 I investigated task fMRI in a large multimodal imaging dataset with patients with ALS, PLS and healthy controls. There were several key findings. First, I found abnormal extra-motor hyperactivation in ALS in rapidly progressive disease. Together with a negative finding for previously reported findings of motor cortex hyperactivation in ALS, this suggests that simple cortical hyperactivation may occur primarily alongside early disease symptoms, and may diminish in more advanced disease. This could be due to degeneration of the physiological inhibitory synaptic plasticity that may segregate function[507].

I also found between-region connectivity changes strongly correlated with ALSFRS-R of a network node comprising "Secondary" motor regions (supplementary and premotor areas). There were reciprocal changes in the connectivity of this node with a cerebellar node (higher connectivity in better function) and the right primary motor area node (higher connectivity in worse function).

Taken together, these findings indicated different axes to motor system connectivity changes in ALS, with some changes confined to important subgroups (rapid progressors) and clinical correlation with disease progression (though inference of longitudinal trends from cross-sectional data must be done with caution).

7.2 Neurochemical excitability is lateralised in the healthy motor network

To extend the evaluation of motor network excitability beyond fMRI, I hypothesised that measurement of local neurochemical indicators by magnetic resonance spectroscopic imaging would yield additional insight into this core ALS pathology. I demonstrated a novel analysis pipeline including data quality validation and comparison of registration technique in a large pooled dataset of healthy controls.

I demonstrated good data quality for metabolites of interest (NAA, Glu, Glu+Gln, GABA, Ins) in the dataset, and found clear associations in their concentration with both tissue type and age. Notably, I found clear interhemispheric differences in metabolite concentration. Glu and Glu+Gln were lower in the left primary motor and somatosensory cortices, but higher in the left parietal and cingulate regions, while GABA was lower in the left primary motor region.

I further demonstrated that Glu concentration was negatively correlated with resting state motor network connectivity in both motor hand areas, while this relationship was only found in the left motor hand area for GABA. Finally, I demonstrated age-associated reduction in local NAA concentration in the midline motor regions, and reduction in Glu in the right hemisphere motor hand area.

This study, through fine grained neurochemical mapping, yields multiple novel insights into motor system excitation and inhibition. The motor hand areas appear to have different "set-points" for excitation and inhibition, which are relevant to their functional connectivity, and differentially affected by healthy ageing. These changes may be associated with hemispheric dominance, however this conclusion is limited by inclusion criteria for right-handed study participants in most included datasets.

7.3 Lateralised changes in local excitation and inhibition occur in ALS and presymptomatic individuals

Having characterised normal motor inhibition and excitation, I extended this technique in a study including both patients with established ALS and healthy individuals carrying a genetic mutation (*C9orf72*-HRE) conferring a high risk for ALS/FTD.

In this dataset, I found robust neurochemical evidence for neurodegeneration (loss of NAA) with presymptomatic individuals lying in between healthy controls and ALS patients. I found widespread loss of glutamate in the pre and post central gyri in ALS vs. controls, but relative preservation of glutamate levels in the left hand area. GABA was also widely depleted in motor regions, but with relative preservation in the right motor hand area. Finally, in presymptomatic individuals, there was lower GABA in a region tightly corresponding to left primary motor cortex hand area grey matter.

In the context of our previous findings, this could represent further evidence implicating early selective loss of physiological inhibition in ALS. TMS studies have shown left motor cortex disinhibition shortly prior to disease onset in individuals at risk of *SOD1* ALS, and evidence of greater motor hand area disinhibition contralateral to the side of disease onset in early disease. This, however, is the first neurochemical quantification of a disinhibited "hot spot" in presymptomatic ALS. Greater degeneration of inhibitory interneurons in the left hemisphere would concur with previous findings that ALS is an asymmetric disease in cortical thickness loss - and biased towards the dominant hemisphere. Disinhibition in the left hemisphere could explain the preservation of glutamate levels in the face of more widespread degeneration in ALS. Longitudinal studies are essential to test this hypothesis.

7.4 Composite biomarkers may better detect established disease and changes prior to symptom onset

Both fMRI and MRSI yield noisy and imperfect individual measures that are ill-suited to prediction on an individual level, and have been challenging to translate across the field of neurodegeneration. I applied linear discriminant analysis using data features selected to represent motor cortex excitability and network connectivity to address this challenge by combining biomarkers. I used the task of group classification to test the value of these composite measures. This approach allows the information content of the input features to be compared - i.e. noisy features with large overlap between groups will be weighted much lower than those that differ between groups. These may be useful as *diagnostic biomarkers*[506] as they detect or confirm the presence of disease. Another advantage is to generate composite markers that might reflect characteristics of different stages of the disease process - i.e. established or late disease vs. presymptomatic disease/vulnerability to future disease. With repeated longitudinal measurement, these would be considered *monitoring biomarkers.*[506]

I found that the composite markers produced performed well at the task of 3-group classification, and were robust to perturbation of the input data by splitting the dataset into test-train subsets, and leaving out subjects. The resulting measures were indeed composites, reflecting the value of combining multiple noisy inputs for noise reduction and maximising information content.

Composite features (particularly metabolites) perform well to detect established disease The first composite measure performed best at separating ALS patients from the other groups in the study, and was weighted more towards MRSI inputs (notably across multiple metabolites). Notably, when splitting the inputs by modality, MRSI-derived features alone performed much better at characterising ALS than task fMRI-derived features alone. Presymptomatic carriers

were intermediate between normal controls and ALS, supporting the view that this measure detects degenerative processes which may be subclinical in this group.

Marked differences in left motor cortex task related BOLD activation in a subset of *C9orf72*-HRE carriers The second composite measure was heavily loaded onto the metrics derived from task fMRI, much more in the left motor cortex than the right. Incorporating both MRSI and tfMRI measures yielded much better performance at identifying presymptomatic gene carriers than either alone. Several presymptomatic gene carriers are significant outliers by task fMRI metrics, suggesting a separate axis to the composite marker of degeneration described above. This might reflect a pre-existing vulnerability to disease or a hyper-excitable risk/transformation state, with confounds such as task-related attention or anxiety possibly contributing.

7.5 Limitations and future directions

7.5.1 Cortical excitability is noisy and varies with space and time

All of the individual candidate markers described in this thesis are individually noisy metrics. To some extent this could be explained by the limitations of non-invasive experimental techniques. However, previous work suggests that excitability/inhibition related to motor activity is intrinsically variable across conditions of preparation, learning, and adaptation, and has roles in reducing interference, and refining outputs[508–510]. Physiological variability in cortical excitability is likely to be highly relevant to attempts to harness cortical excitability in the study of ALS. The underlying landscape of cortical excitability between different brain areas in different individuals (Chapters 4 and 5) must be considered to minimise confounding in clinical studies.

Longitudinal studies - an ongoing challenge My thesis work is limited in its cross-sectional design - while I have assembled an initial cohort of *C9orf72*-HRE carriers, longitudinal study is outside the scope of this thesis. Longitudinal MR imaging in ALS is inherently challenging due to development of respiratory and bulbar weakness. The COVID-19 pandemic has disrupted clinical trials globally[511]. My findings argue strongly for the inclusion of MR spectroscopy and fMRI in the design of these longitudinal studies. With enough data cortical excitability could be described in relation to pre-existing vulnerability, disease progression, and functional compensation.

In other neurodegenerative conditions, the assembly of large consortium datasets and longitudinal study has allowed biomarkers to be compared and their trajectories described. While theoretical frameworks often focus on an idealised sigmoid or linear trajectory (Figure 7.1a), a variety of trajectories have been observed in practice(Figure 7.1b)[512].

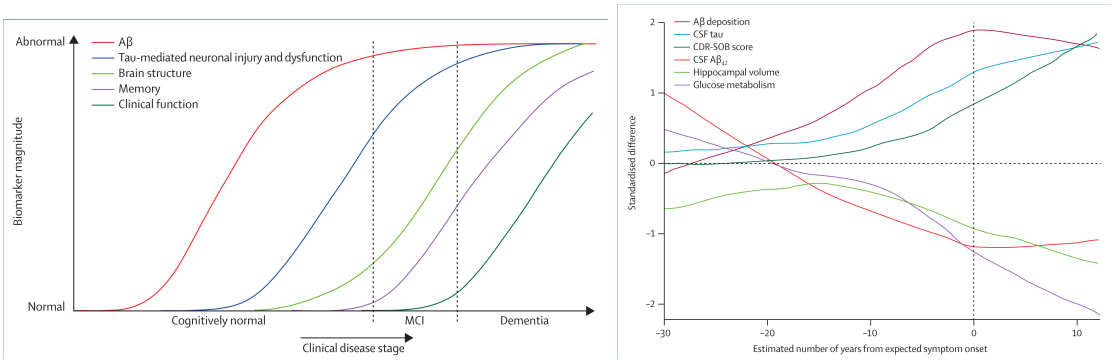

(a) Idealised **(b)** Observed

Figure 7.1: Idealised and observed disease progression in Alzheimer's disease. Reused with permission from Jack 2013, Lancet Neurology[512].

I will conclude by briefly discussing how this could impact the application of composite biomarkers of cortical excitability.

7.5.2 Applying composite biomarkers of neurodegeneration

Composite markers of neurodegeneration have several potential applications. For diagnosis, the value of such markers depends on their noisiness, and the strength

of segregation against disease mimics or healthy controls. My findings suggest that there is an underlying composite marker of cortical excitability alterations and neurodegeneration in ALS. However, prospective data in a diagnostic clinic for ALS may be required to test whether these changes are valuable in informing the diagnostic process for individuals where there is clinical doubt. Longitudinal or pseudolongitudinal analyses of larger datasets may clarify the trajectory of these changes. A sigmoid transition around or before the time of disease onset would facilitate diagnosis and be more robust to noise (Figure 7.2b), while a linear trajectory may characterise the underlying process better for application to disease staging and prognostication (Figure 7.2c), with potential improvement in diagnostic performance with technological improvement (Figure 7.2a).

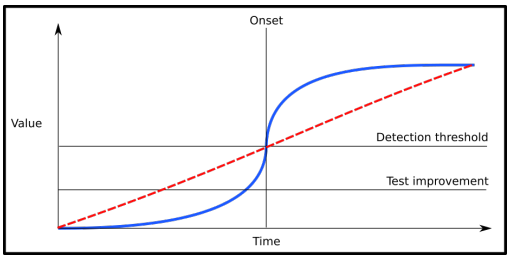

(a) Diagnosis - Detection threshold.

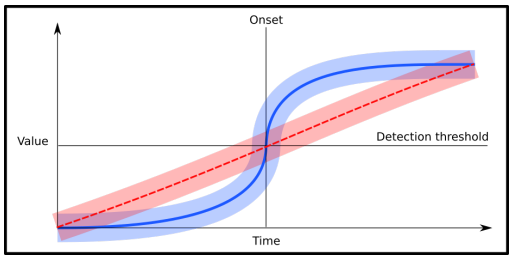

(b) Diagnosis - Noise.

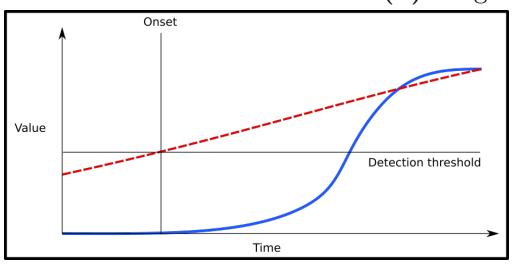

(c) Disease staging and prognosis.

Figure 7.2: Biomarker trajectory (red - linear, blue - sigmoid) and its effect for clinical applications.

Another possible application is in sub-stratification or clinical trial selection. For clinical trials aimed at modulating cortical excitability, whether pharmacological or through non-invasive brain stimulation[1], it may be reasonable to select patients in whom cortical excitability is abnormal at baseline.

7.5.3 Applying presymptomatic disease biomarkers

Group-level differences between presymptomatic carriers of the *C9orf72*-HRE mutation and healthy controls may reflect several different biomarker trajectories (Figure 7.3). One possibility is that the difference long predates disease, perhaps even originating in development (dashed green line). These sorts of differences could explain how the stage is set for future neurodegeneration. Neurodevelopment has been increasingly implicated in Huntington's disease, another repeat-expansion neurodegenerative disorder[513].

Alternatively, there could be a detectable change during an individual's adult lifetime before disease onset. While this could be a unidirectional change (dotted blue line), it might also be only transiently observable (red continuous line). Understanding these trajectories will be necessary to apply these biomarkers in presymptomatic disease to identify novel disease processes and target intervention[514]. These could qualify as *prognostic biomarkers*[506] if they were reliably able to identify a clinical event (i.e. motor system decompensation or neuronal damage) to guide the initiation or escalation of treatment.

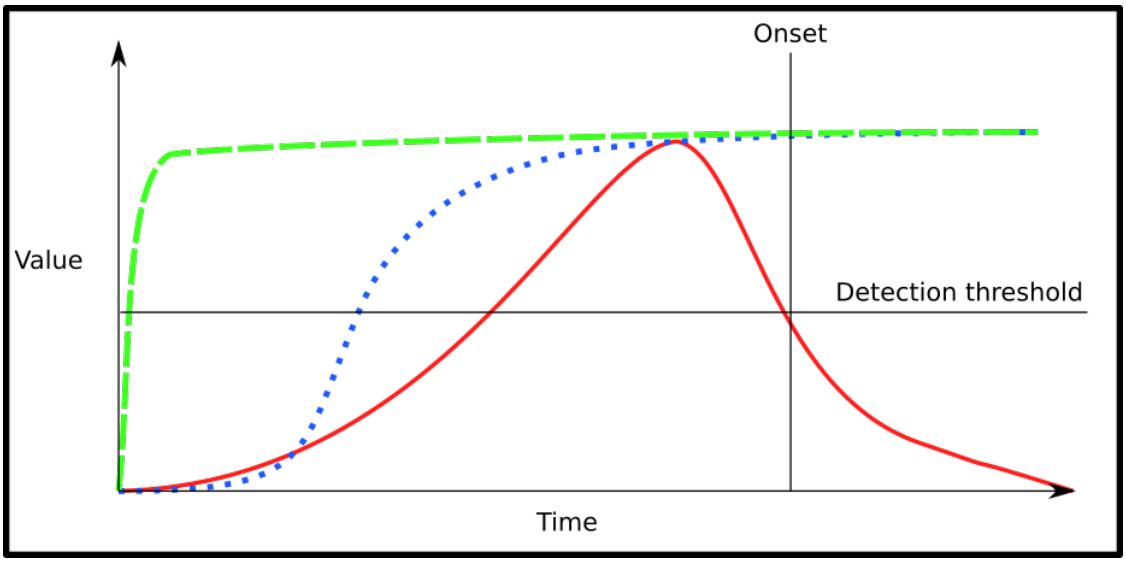

Figure 7.3: Several possible presymptomatic biomarker trajectories.

Ongoing refinement of disease markers might allow disease related changes to be detected, and therapeutic intervention planned. Some of these presymptomatic

findings might also apply to sporadic ALS, where the presymptomatic phase is not generally tractable to study apart from large population datasets[515].

7.5.4 Identifying and treating early disease

With recognition of the pathogenic potential of ALS-causing mutations, pre-implantation genetic diagnosis, in-utero genetic screening, and gene-editing may lead to many fewer individuals being born with these risk factors. This is unlikely to become universal, however. A range of other conceptual strategies have been described for treating or preventing ALS at early stages[516].

In principle, therapy aimed at the genetic target could be started at any point, and be expected to reduce the risk of future disease conversion. Gene therapy delivered using viral vectors have demonstrated this promise in spinal muscular atrophy[517]. However, because the precise molecular genetic mechanisms of disease are uncertain, the conceptual design of gene therapy interventions remains challenging, and the therapeutic benefit uncertain. Gene therapy trials using antisense oligonucleotides (ASO) delivered through lumbar puncture have begun in individuals with ALS. The first Phase 1 trial in *C9orf72*-associated ALS has met safety and tolerability endpoints, but no evidence of clinical benefit or secondary endpoint improvement[518,519]. There remain significant ethical concerns about extending trials to presymptomatic individuals given the morbidity associated with repeat lumbar puncture and adverse effects associated with early generation ASOs. FDA approval has been granted for a phase 3 trial of a *SOD1*-targeted antisense oligonucleotide (tofersen) in presymptomatic individuals with elevation in plasma neurofilament light chain triggering treatment initiation[520]. Neurofilament light chain levels in plasma and CSF serve as *response biomarkers*[506] potentially indicating a biological response in individuals exposed to treatment.

Further study of cortical excitability in presymptomatic disease could identify non-gene therapeutic targets. A disinhibited left hemisphere motor “hot-spot” and primary secondary motor connectivity are two candidates that could be modulated using a wide range of pharmacological[521] or brain stimulation techniques[522].

References

1. Edmond, E. C., Stagg, C. J. & Turner, M. R. Therapeutic Non-Invasive Brain Stimulation in Amyotrophic Lateral Sclerosis: Rationale, Methods and Experience. *Journal of Neurology, Neurosurgery & Psychiatry* **90,** 1131–1138. doi:10.1136/jnnp-2018-320213. pmid: 31072957 (Oct. 1, 2019).
2. Dharmadasa, T. *et al.* Genetic Testing in Motor Neurone Disease. *Practical Neurology,* practneurol-2021–002989. doi:10.1136/practneurol-2021-002989. pmid: 35027459 (Jan. 13, 2022).
3. Edmond, E. C. *et al.* Magnetic Resonance Spectroscopic Imaging Markers of Inhibitory and Excitatory Motor Cortical Function in Healthy Individuals and Those with Amyotrophic Lateral Sclerosis. *OSF.io.* doi:10.17605/OSF.IO/5APBJ (July 7, 2020).
4. Edmond, E. C. *et al.* Magnetic Resonance Spectroscopic Imaging Markers of Inhibitory and Excitatory Motor Cortical Function in Healthy Individuals and Those with Amyotrophic Lateral Sclerosis. *OSF.io.* doi:10.17605/OSF.IO/MXHDJ (Mar. 11, 2021).
5. Andrushko, J. W. *et al. Fatigue Induces Behavioural Improvements in the Unfatigued Hand via Altered Functional Connectivity and Neurochemicals in Cortical Motor Areas* Oct. 24, 2021. doi:10.1101/2021.10.23.464569.
6. Charcot, J. Amyotrophies Spinales Deuteropathiques Sclérose Latérale Amyotrophique & Sclérose Latérale Amyotrophique. *Bureaux du Progrès Médical* **2,** 234–66 (Oeuvres Complétes) 1874).
7. Bell, C. Case of Partial Wasting of the Muscles of the Upper Extremities. *The nervous system of the human body. London: Longmans,* 432–4 (1836).
8. Cruveilhier, M. Sur La Paralysie Musculaire Atrophique. *Arch Gen Med* **1,** 561–603 (1853).
9. Aran, F. *et al.* Recherches Sur Une Maladie Non Encore Décrite Du Système Musculaire (Atrophie Musculaire Progressive). *Arch Gen Med* **24,** 172 (1850).
10. Turner, M. R., Swash, M. & Ebers, G. C. Lockhart Clarke's Contribution to the Description of Amyotrophic Lateral Sclerosis. *Brain* **133,** 3470–3479 (2010).
11. Clarke, J. L. & Jackson, J. H. On a Case of Muscular Atrophy, with Disease of the Spinal Cord and Medulla Oblongata. *Medico-chirurgical transactions* **50,** 489 (1867).
12. Ravits, J., Paul, P. & Jorg, C. Focality of Upper and Lower Motor Neuron Degeneration at the Clinical Onset of ALS. *Neurology* **68,** 1571–1575. doi:10.1212/01.wnl.0000260965.20021.47 (May 8, 2007).

13. Fujimura-Kiyono, C. *et al.* Onset and Spreading Patterns of Lower Motor Neuron Involvements Predict Survival in Sporadic Amyotrophic Lateral Sclerosis. *Journal of Neurology, Neurosurgery & Psychiatry* **82,** 1244–1249. doi:10.1136/jnnp-2011-300141 (Nov. 1, 2011).

14. Atassi, N. *et al.* The PRO-ACT Database: Design, Initial Analyses, and Predictive Features. *Neurology* **83,** 1719–1725. doi:10.1212/WNL.0000000000000951 (Nov. 4, 2014).

15. Turner, M. R. *et al.* Concordance between Site of Onset and Limb Dominance in Amyotrophic Lateral Sclerosis. *Journal of Neurology, Neurosurgery & Psychiatry* **82,** 853–854. doi:10.1136/jnnp.2010.208413. pmid: 20562391 (Aug. 1, 2011).

16. Shoesmith, C. L., Findlater, K., Rowe, A. & Strong, M. J. Prognosis of Amyotrophic Lateral Sclerosis with Respiratory Onset. *Journal of Neurology, Neurosurgery & Psychiatry* **78,** 629–631. doi:10.1136/jnnp.2006.103564. pmid: 17088331 (June 1, 2007).

17. Swinnen, B. & Robberecht, W. The Phenotypic Variability of Amyotrophic Lateral Sclerosis. *Nature Reviews Neurology* **10,** 661 (2014).

18. Proudfoot, M., Jones, A., Talbot, K., Al-Chalabi, A. & Turner, M. R. The ALSFRS as an Outcome Measure in Therapeutic Trials and Its Relationship to Symptom Onset. *Amyotrophic Lateral Sclerosis and Frontotemporal Degeneration* **17,** 414–425. doi:10.3109/21678421.2016.1140786 (Aug. 17, 2016).

19. Shefner, J. M. *et al.* A Proposal for New Diagnostic Criteria for ALS. *Clinical Neurophysiology* **131,** 1975–1978. doi:10.1016/j.clinph.2020.04.005 (Aug. 2020).

20. Brooks, B. R. El Escorial World Federation of Neurology Criteria for the Diagnosis of Amyotrophic Lateral Sclerosis. Subcommittee on Motor Neuron Diseases/Amyotrophic Lateral Sclerosis of the World Federation of Neurology Research Group on Neuromuscular Diseases and the El Escorial "Clinical Limits of Amyotrophic Lateral Sclerosis" Workshop Contributors. *Journal of the Neurological Sciences* **124 Suppl,** 96–107. doi:10.1016/0022-510x(94)90191-0. pmid: 7807156 (July 1994).

21. Brooks, B. R., Miller, R. G., Swash, M. & Munsat, T. L. El Escorial Revisited: Revised Criteria for the Diagnosis of Amyotrophic Lateral Sclerosis. *Amyotrophic lateral sclerosis and other motor neuron disorders* **1,** 293–299 (2000).

22. De Carvalho, M. *et al.* Electrodiagnostic Criteria for Diagnosis of ALS. *Clinical Neurophysiology* **119,** 497–503. doi:10.1016/j.clinph.2007.09.143 (Mar. 2008).

23. Gordon, P. H. *et al.* Efficacy of Minocycline in Patients with Amyotrophic Lateral Sclerosis: A Phase III Randomised Trial. *The Lancet. Neurology* **6,** 1045–1053. doi:10.1016/S1474-4422(07)70270-3. pmid: 17980667 (Dec. 2007).

24. Miller, R. G. *et al.* Phase III Randomized Trial of Gabapentin in Patients with Amyotrophic Lateral Sclerosis. *Neurology* **56,** 843–848. doi:10.1212/WNL.56.7.843. pmid: 11294919 (Apr. 10, 2001).

25. Geevasinga, N. *et al.* Diagnostic Criteria in Amyotrophic Lateral Sclerosis: A Multicenter Prospective Study. *Neurology* **87,** 684–690. doi:10.1212/WNL.0000000000002988. pmid: 27440148 (Aug. 16, 2016).

26. Pugdahl, K. *et al.* Gold Coast Diagnostic Criteria Increase Sensitivity in Amyotrophic Lateral Sclerosis. *Clinical Neurophysiology* **132,** 3183–3189 (2021).

27. Belsh, J. M. ALS Diagnostic Criteria of El Escorial Revisited: Do They Meet the Needs of Clinicians as Well as Researchers? *Amyotrophic Lateral Sclerosis and Other Motor Neuron Disorders* **1,** S57–S60. doi:10.1080/14660820052415925. pmid: 11464928 (sup1 Mar. 2000).

28. Arai, T. *et al.* TDP-43 Is a Component of Ubiquitin-Positive Tau-Negative Inclusions in Frontotemporal Lobar Degeneration and Amyotrophic Lateral Sclerosis. *Biochemical and Biophysical Research Communications* **351,** 602–611. doi:10.1016/j.bbrc.2006.10.093. pmid: 17084815 (Dec. 22, 2006).

29. Neumann, M. *et al.* Ubiquitinated TDP-43 in Frontotemporal Lobar Degeneration and Amyotrophic Lateral Sclerosis. *Science (New York, N.Y.)* **314,** 130–133. doi:10.1126/science.1134108. pmid: 17023659 (Oct. 6, 2006).

30. Ou, S. H., Wu, F., Harrich, D., García-Martínez, L. F. & Gaynor, R. B. Cloning and Characterization of a Novel Cellular Protein, TDP-43, That Binds to Human Immunodeficiency Virus Type 1 TAR DNA Sequence Motifs. *Journal of Virology* **69,** 3584–3596. doi:10.1128/jvi.69.6.3584-3596.1995 (June 1995).

31. Ayala, Y. M. *et al.* TDP-43 Regulates Its mRNA Levels through a Negative Feedback Loop. *The EMBO Journal* **30,** 277–288. doi:10.1038/emboj.2010.310 (Jan. 19, 2011).

32. Polymenidou, M. *et al.* Long Pre-mRNA Depletion and RNA Missplicing Contribute to Neuronal Vulnerability from Loss of TDP-43. *Nature Neuroscience* **14,** 459–468. doi:10.1038/nn.2779 (4 Apr. 2011).

33. Avendaño-Vázquez, S. E. *et al.* Autoregulation of TDP-43 mRNA Levels Involves Interplay between Transcription, Splicing, and Alternative polyA Site Selection. *Genes & Development* **26,** 1679–1684. doi:10.1101/gad.194829.112. pmid: 22855830 (Jan. 8, 2012).

34. Bembich, S. *et al.* Predominance of Spliceosomal Complex Formation over Polyadenylation Site Selection in TDP-43 Autoregulation. *Nucleic Acids Research* **42,** 3362–3371. doi:10.1093/nar/gkt1343 (Mar. 1, 2014).

35. Sugai, A. *et al.* Non-Genetically Modified Models Exhibit TARDBP mRNA Increase Due to Perturbed TDP-43 Autoregulation. *Neurobiology of Disease* **130,** 104534. doi:10.1016/j.nbd.2019.104534 (Oct. 1, 2019).

36. Weskamp, K. *et al.* Shortened TDP43 Isoforms Upregulated by Neuronal Hyperactivity Drive TDP43 Pathology in ALS. *Journal of Clinical Investigation* **130,** 1139–1155. doi:10.1172/JCI130988 (Jan. 27, 2020).

37. Gitcho, M. A. *et al.* TARDBP 3-UTR Variant in Autopsy-Confirmed Frontotemporal Lobar Degeneration with TDP-43 Proteinopathy. *Acta Neuropathologica* **118,** 633–645. doi:10.1007/s00401-009-0571-7 (Nov. 2009).

38. Chook, Y. Karyopherins and Nuclear Import. *Current Opinion in Structural Biology* **11,** 703–715. doi:10.1016/S0959-440X(01)00264-0 (Dec. 1, 2001).

39. Winton, M. J. *et al.* Disturbance of Nuclear and Cytoplasmic TAR DNA-binding Protein (TDP-43) Induces Disease-like Redistribution, Sequestration, and Aggregate Formation. *Journal of Biological Chemistry* **283,** 13302–13309. doi:10.1074/jbc.M800342200 (May 2008).

40. Walker, A. K. *et al.* Functional Recovery in New Mouse Models of ALS/FTLD after Clearance of Pathological Cytoplasmic TDP-43. *Acta Neuropathologica* **130,** 643–660. doi:10.1007/s00401-015-1460-x (Nov. 2015).

41. Nishimura, A. L. *et al.* Nuclear Import Impairment Causes Cytoplasmic Trans-Activation Response DNA-binding Protein Accumulation and Is Associated with Frontotemporal Lobar Degeneration. *Brain* **133,** 1763–1771. doi:10.1093/brain/awq111 (June 2010).

42. Freibaum, B. D. *et al.* GGGGCC Repeat Expansion in C9orf72 Compromises Nucleocytoplasmic Transport. *Nature* **525,** 129–133. doi:10.1038/nature14974. pmid: 26308899 (7567 Sept. 2015).

43. Jovičić, A. *et al.* Modifiers of C9orf72 Dipeptide Repeat Toxicity Connect Nucleocytoplasmic Transport Defects to FTD/ALS. *Nature Neuroscience* **18,** 1226–1229. doi:10.1038/nn.4085 (9 Sept. 2015).

44. Lee, K.-H. *et al.* C9orf72 Dipeptide Repeats Impair the Assembly, Dynamics, and Function of Membrane-Less Organelles. *Cell* **167,** 774–788.e17. doi:10.1016/j.cell.2016.10.002. pmid: 27768896 (Oct. 20, 2016).

45. Zhang, K. *et al.* The C9orf72 Repeat Expansion Disrupts Nucleocytoplasmic Transport. *Nature* **525,** 56–61. doi:10.1038/nature14973 (7567 Sept. 2015).

46. Solomon, D. A. *et al.* A Feedback Loop between Dipeptide-Repeat Protein, TDP-43 and Karyopherin- Mediates C9orf72-related Neurodegeneration. *Brain* **141,** 2908–2924. doi:10.1093/brain/awy241 (Oct. 1, 2018).

47. Budini, M. *et al.* Cellular Model of TAR DNA-binding Protein 43 (TDP-43) Aggregation Based on Its C-terminal Gln/Asn-rich Region. *Journal of Biological Chemistry* **287,** 7512–7525. doi:10.1074/jbc.M111.288720 (Mar. 2012).

48. Fuentealba, R. A. *et al.* Interaction with Polyglutamine Aggregates Reveals a Q/N-rich Domain in TDP-43. *Journal of Biological Chemistry* **285,** 26304–26314. doi:10.1074/jbc.M110.125039 (Aug. 2010).

49. Jiang, L.-L. *et al.* Two Mutations G335D and Q343R within the Amyloidogenic Core Region of TDP-43 Influence Its Aggregation and Inclusion Formation. *Scientific Reports* **6,** 23928. doi:10.1038/srep23928 (1 Mar. 31, 2016).

50. Bolognesi, B. *et al.* The Mutational Landscape of a Prion-like Domain. *bioRxiv,* 592121 (2019).

51. Guenther, E. L. *et al.* Atomic Structures of TDP-43 LCD Segments and Insights into Reversible or Pathogenic Aggregation. *Nature Structural & Molecular Biology* **25,** 463–471. doi:10.1038/s41594-018-0064-2 (6 June 2018).

52. Nelson, P. T. *et al.* Limbic-Predominant Age-Related TDP-43 Encephalopathy (LATE): Consensus Working Group Report. *Brain* **142,** 1503–1527. doi:10.1093/brain/awz099 (June 1, 2019).

53. David, A. S. & Gillham, R. A. Neuropsychological Study of Motor Neuron Disease. *Psychosomatics* **27,** 441–445 (1986).

54. Gallassi, R. *et al.* Cognitive Impairment in Motor Neuron Disease. *Acta neurologica scandinavica* **71,** 480–484 (1985).

55. Gallassi, R. *et al.* Neuropsychological, Electroencephalogram and Brain Computed Tomography Findings in Motor Neuron Disease. *European neurology* **29,** 115–120 (1989).

56. Hartikainen, P., Helkala, E.-L., Soininen, H. & Riekkinen, P. Cognitive and Memory Deficits in Untreated Parkinson's Disease and Amyotrophic Lateral Sclerosis Patients: A Comparative Study. *Journal of neural transmission-Parkinson's disease and dementia section* **6,** 127–137 (1993).

57. Iwasaki, Y., Kinoshita, M., Ikeda, K., Takamiya, K. & Shiojima, T. Cognitive Impairment in Amyotrophic Lateral Sclerosis and Its Relation to Motor Disabilities. *Acta neurologica scandinavica* **81,** 141–143 (1990).

58. Iwasaki, Y., Kinoshita, M., Ikeda, K., Takamiya, K. & Shiojima, T. Neuropsychological Dysfunctions in Amyotrophic Lateral Sclerosis: Relation to Motor Disabilities. *International journal of neuroscience* **54,** 191–195 (1990).

59. Kew, J. *et al.* The Relationship between Abnormalities of Cognitive Function and Cerebral Activation in Amyotrophic Lateral Sclerosis: A Neuropsychological and Positron Emission Tomography Study. *Brain* **116,** 1399–1423 (1993).

60. Poloni, M., Capitani, E., Mazzini, L. & Ceroni, M. Neuropsychological Measures in Amyotrophic Lateral Sclerosis and Their Relationship with CT Scan-Assessed Cerebral Atrophy. *Acta neurologica scandinavica* **74,** 257–260 (1986).

61. Strong, M. J. *et al.* Consensus Criteria for the Diagnosis of Frontotemporal Cognitive and Behavioural Syndromes in Amyotrophic Lateral Sclerosis. *Amyotrophic Lateral Sclerosis* **10,** 131–146 (2009).

62. Abrahams, S. & Bak, T. Edinburgh Cognitive and Behavioural ALS Screen-Ecas English Version 2013 (2013).

63. Niven, E. *et al.* Validation of the Edinburgh Cognitive and Behavioural Amyotrophic Lateral Sclerosis Screen (ECAS): A Cognitive Tool for Motor Disorders. *Amyotrophic Lateral Sclerosis and Frontotemporal Degeneration* **16,** 172–179 (2015).

64. Chiò, A. *et al.* Neurobehavioral Dysfunction in ALS Has a Negative Effect on Outcome and Use of PEG and NIV. *Neurology* **78,** 1085–1089 (2012).

65. Bock, M. *et al.* Cognitive-Behavioral Changes in Amyotrophic Lateral Sclerosis: Screening Prevalence and Impact on Patients and Caregivers. *Amyotrophic Lateral Sclerosis and Frontotemporal Degeneration* **17,** 366–373 (2016).

66. Tremolizzo, L. *et al.* Behavioural but Not Cognitive Impairment Is a Determinant of Caregiver Burden in Amyotrophic Lateral Sclerosis. *European neurology* **75,** 191–194 (2016).

67. Crockford, C. *et al.* ALS-specific Cognitive and Behavior Changes Associated with Advancing Disease Stage in ALS. *Neurology* **91,** e1370–e1380 (2018).

68. Schreiber, H. *et al.* Cognitive Function in Bulbar–and Spinal–Onset Amyotrophic Lateral Sclerosis. *Journal of neurology* **252,** 772–781 (2005).

69. Bock, M. *et al.* Progression and Effect of Cognitive-Behavioral Changes in Patients with Amyotrophic Lateral Sclerosis. *Neurology: Clinical Practice* **7,** 488–498 (2017).

70. Gregory, J. M. *et al.* Executive, Language and Fluency Dysfunction Are Markers of Localised TDP-43 Cerebral Pathology in Non-Demented ALS. *Journal of Neurology, Neurosurgery & Psychiatry,* jnnp–2019 (2019).

71. Byrne, S. *et al.* Rate of Familial Amyotrophic Lateral Sclerosis: A Systematic Review and Meta-Analysis. *Journal of Neurology, Neurosurgery & Psychiatry* **82,** 623–627 (2011).

72. Cooper-Knock, J. *et al.* Clinico-Pathological Features in Amyotrophic Lateral Sclerosis with Expansions in C9ORF72. *Brain* **135,** 751–764. doi:10.1093/brain/awr365. pmid: 22366792 (Mar. 2012).

73. Renton, A. E., Chiò, A. & Traynor, B. J. State of Play in Amyotrophic Lateral Sclerosis Genetics. *Nature neuroscience* **17,** 17. pmid: 24369373 (2014).

74. Chiò, A. *et al.* Extensive Genetics of ALS. *Neurology* **79,** 1983–1989. doi:10.1212/WNL.0b013e3182735d36. pmid: 23100398 (Nov. 6, 2012).

75. Kenna, K. P. *et al.* Delineating the Genetic Heterogeneity of ALS Using Targeted High-Throughput Sequencing. *Journal of Medical Genetics* **50,** 776–783. doi:10.1136/jmedgenet-2013-101795. pmid: 23881933 (Nov. 1, 2013).

76. Van Blitterswijk, M. *et al.* Evidence for an Oligogenic Basis of Amyotrophic Lateral Sclerosis. *Human Molecular Genetics* **21,** 3776–3784. doi:10.1093/hmg/dds199 (Sept. 1, 2012).

77. Al-Chalabi, A. *et al.* An Estimate of Amyotrophic Lateral Sclerosis Heritability Using Twin Data. *Journal of Neurology, Neurosurgery, and Psychiatry* **81,** 1324–1326. doi:10.1136/jnnp.2010.207464. pmid: 20861059 (Dec. 2010).

78. Ryan, M., Heverin, M., McLaughlin, R. L. & Hardiman, O. Lifetime Risk and Heritability of Amyotrophic Lateral Sclerosis. *JAMA Neurology* **76,** 1367–1374. doi:10.1001/jamaneurol.2019.2044. pmid: 31329211 (Nov. 2019).

79. *Amyotrophic Lateral Sclerosis/Motor Neuron Disease (Version 1.59)* https://panelapp.genomicsengland.co.uk/panels/263/ (2022).

80. Shepheard, S. R. *et al.* Value of Systematic Genetic Screening of Patients with Amyotrophic Lateral Sclerosis. *Journal of Neurology, Neurosurgery & Psychiatry* **92,** 510–518. doi:10.1136/jnnp-2020-325014. pmid: 33589474 (May 1, 2021).

81. Rosen, D. R. *et al.* Mutations in Cu/Zn Superoxide Dismutase Gene Are Associated with Familial Amyotrophic Lateral Sclerosis. *Nature* **362,** 59–62 (1993).

82. Miller, T. *et al.* Phase 1–2 Trial of Antisense Oligonucleotide Tofersen for SOD1 ALS. *New England Journal of Medicine* **383,** 109–119 (2020).

83. Bravo-Hernandez, M. *et al.* Spinal Subpial Delivery of AAV9 Enables Widespread Gene Silencing and Blocks Motoneuron Degeneration in ALS. *Nature Medicine* (Dec. 2019).

84. Benatar, M. Lost in Translation: Treatment Trials in the SOD1 Mouse and in Human ALS. *Neurobiology of disease* **26,** 1–13 (2007).

85. Collaborative Medicinal Development Pty Limited. *A Multicenter, Randomized, Double-Blind, Placebo-Controlled Phase 2 Study of Cu(II)ATSM in Patients With Amyotrophic Lateral Sclerosis/Motor Neuron Disease* Clinical trial registration NCT04082832 (clinicaltrials.gov, Nov. 4, 2019).

86. Morita, M. *et al.* A Locus on Chromosome 9p Confers Susceptibility to ALS and Frontotemporal Dementia. *Neurology* **66,** 839–844 (2006).

87. Valdmanis, P. N. *et al.* Three Families with Amyotrophic Lateral Sclerosis and Frontotemporal Dementia with Evidence of Linkage to Chromosome 9p. *Archives of neurology* **64,** 240–245 (2007).

88. Vance, C. *et al.* Familial Amyotrophic Lateral Sclerosis with Frontotemporal Dementia Is Linked to a Locus on Chromosome 9p13. 2–21.3. *Brain* **129,** 868–876 (2006).

89. Van Es, M. A. *et al.* Genome-Wide Association Study Identifies 19p13. 3 (UNC13A) and 9p21. 2 as Susceptibility Loci for Sporadic Amyotrophic Lateral Sclerosis. *Nature genetics* **41,** 1083–1087 (2009).

90. Zou, Z.-Y., Liu, M.-S., Li, X.-G. & Cui, L.-Y. The Distinctive Genetic Architecture of ALS in Mainland China. *Journal of Neurology, Neurosurgery & Psychiatry* **87,** 906–907. doi:10.1136/jnnp-2015-311654. pmid: 26519472 (Aug. 1, 2016).

91. Zou, Z.-Y. *et al.* Genetic Epidemiology of Amyotrophic Lateral Sclerosis: A Systematic Review and Meta-Analysis. *Journal of Neurology, Neurosurgery & Psychiatry* **88,** 540–549. doi:10.1136/jnnp-2016-315018. pmid: 28057713 (July 1, 2017).

92. Chadi, G. *et al.* Genetic Analysis of Patients with Familial and Sporadic Amyotrophic Lateral Sclerosis in a Brazilian Research Center. *Amyotrophic Lateral Sclerosis and Frontotemporal Degeneration* **18,** 249–255. doi:10.1080/21678421.2016.1254245. pmid: 27978769 (Apr. 3, 2017).

93. Nel, M. *et al.* C9orf72 Repeat Expansions in South Africans with Amyotrophic Lateral Sclerosis. *Journal of the Neurological Sciences* **401,** 51–54. doi:10.1016/j.jns.2019.04.026 (June 15, 2019).

94. Shamim, U. *et al.* C9orf72 Hexanucleotide Repeat Expansion in Indian Patients with ALS: A Common Founder and Its Geographical Predilection. *Neurobiology of Aging* **88,** 156.e1–156.e9. doi:10.1016/j.neurobiolaging.2019.12.024 (Apr. 2020).

95. DeJesus-Hernandez, M. *et al.* Expanded GGGGCC Hexanucleotide Repeat in Noncoding Region of C9ORF72 Causes Chromosome 9p-Linked FTD and ALS. *Neuron* **72,** 245–256 (2011).

96. Renton, A. E. *et al.* A Hexanucleotide Repeat Expansion in C9ORF72 Is the Cause of Chromosome 9p21-Linked ALS-FTD. *Neuron* **72,** 257–268 (2011).

97. Nolan, M. *et al.* Quantitative Patterns of Motor Cortex Proteinopathy across ALS Genotypes. *Acta Neuropathologica Communications* **8,** 98. doi:10.1186/s40478-020-00961-2 (July 2, 2020).

98. Levine, T. P., Daniels, R. D., Gatta, A. T., Wong, L. H. & Hayes, M. J. The Product of C9orf72, a Gene Strongly Implicated in Neurodegeneration, Is Structurally Related to DENN Rab-GEFs. *Bioinformatics* **29,** 499–503 (2013).

99. Sellier, C. *et al.* Loss of C9 ORF 72 Impairs Autophagy and Synergizes with polyQ Ataxin-2 to Induce Motor Neuron Dysfunction and Cell Death. *The EMBO journal* **35,** 1276–1297 (2016).

100. Freischmidt, A. *et al.* Haploinsufficiency of TBK1 Causes Familial ALS and Fronto-Temporal Dementia. *Nature neuroscience* **18,** 631–636 (2015).

101. Sullivan, P. M. *et al.* The ALS/FTLD Associated Protein C9orf72 Associates with SMCR8 and WDR41 to Regulate the Autophagy-Lysosome Pathway. *Acta neuropathologica communications* **4,** 1–16 (2016).

102. Shi, Y. *et al.* Haploinsufficiency Leads to Neurodegeneration in C9ORF72 ALS/FTD Human Induced Motor Neurons. *Nature medicine* **24,** 313–325 (2018).

103. Al-Chalabi, A. *et al.* Analysis of Amyotrophic Lateral Sclerosis as a Multistep Process: A Population-Based Modelling Study. *The Lancet Neurology* **13,** 1108–1113 (2014).

104. Ash, P. E. *et al.* Unconventional Translation of C9ORF72 GGGGCC Expansion Generates Insoluble Polypeptides Specific to c9FTD/ALS. *Neuron* **77,** 639–646 (2013).

105. Mori, K. *et al.* The C9orf72 GGGGCC Repeat Is Translated into Aggregating Dipeptide-Repeat Proteins in FTLD/ALS. *Science* **339,** 1335–1338 (2013).

106. Haeusler, A. R., Donnelly, C. J. & Rothstein, J. D. The Expanding Biology of the C9orf72 Nucleotide Repeat Expansion in Neurodegenerative Disease. *Nature Reviews Neuroscience* **17,** 383–395 (2016).

107. Lee, Y.-B. *et al.* Hexanucleotide Repeats in ALS/FTD Form Length-Dependent RNA Foci, Sequester RNA Binding Proteins, and Are Neurotoxic. *Cell reports* **5,** 1178–1186 (2013).

108. Xu, Z. *et al.* Expanded GGGGCC Repeat RNA Associated with Amyotrophic Lateral Sclerosis and Frontotemporal Dementia Causes Neurodegeneration. *Proceedings of the National Academy of Sciences* **110,** 7778–7783 (2013).

109. Donnelly, C. J. *et al.* RNA Toxicity from the ALS/FTD C9ORF72 Expansion Is Mitigated by Antisense Intervention. *Neuron* **80,** 415–428 (2013).

110. Sareen, D. *et al.* Targeting RNA Foci in iPSC-derived Motor Neurons from ALS Patients with a C9ORF72 Repeat Expansion. *Sci. Transl. Med.* **5,** 208ra149. doi:10.1126/scitranslmed.3007529 (Oct. 2013).

111. Wen, X. *et al.* Antisense Proline-Arginine RAN Dipeptides Linked to C9ORF72-ALS/FTD Form Toxic Nuclear Aggregates That Initiate in Vitro and in Vivo Neuronal Death. *Neuron* **84,** 1213–1225 (2014).

112. Zhang, Y.-J. *et al.* Aggregation-Prone c9FTD/ALS Poly (GA) RAN-translated Proteins Cause Neurotoxicity by Inducing ER Stress. *Acta neuropathologica* **128,** 505–524. pmid: 25173361 (2014).

113. Boeynaems, S. *et al.* Drosophila Screen Connects Nuclear Transport Genes to DPR Pathology in c9ALS/FTD. *Scientific Reports* **6,** 20877. doi:10.1038/srep20877. pmid: 26869068 (Feb. 12, 2016).

114. Chang, Y.-J., Jeng, U.-S., Chiang, Y.-L., Hwang, I.-S. & Chen, Y.-R. The Glycine-Alanine Dipeptide Repeat from C9orf72 Hexanucleotide Expansions Forms Toxic Amyloids Possessing Cell-to-Cell Transmission Properties. *The Journal of Biological Chemistry* **291,** 4903–4911. doi:10.1074/jbc.M115.694273. pmid: 26769963 (Mar. 4, 2016).

115. Kanekura, K. *et al.* Poly-Dipeptides Encoded by the C9ORF72 Repeats Block Global Protein Translation. *Human molecular genetics* **25,** 1803–1813. pmid: 26931465 (2016).

116. May, S. *et al.* C9orf72 FTLD/ALS-associated Gly-Ala Dipeptide Repeat Proteins Cause Neuronal Toxicity and Unc119 Sequestration. *Acta Neuropathologica* **128,** 485–503. doi:10.1007/s00401-014-1329-4. pmid: 25120191 (Oct. 2014).

117. Mizielinska, S. *et al.* C9orf72 Repeat Expansions Cause Neurodegeneration in Drosophila through Arginine-Rich Proteins. *Science (New York, N.Y.)* **345,** 1192–1194. doi:10.1126/science.1256800. pmid: 25103406 (Sept. 5, 2014).

118. Ohki, Y. *et al.* Glycine-Alanine Dipeptide Repeat Protein Contributes to Toxicity in a Zebrafish Model of C9orf72 Associated Neurodegeneration. *Molecular Neurodegeneration* **12,** 6. doi:10.1186/s13024-016-0146-8. pmid: 28088213 (Jan. 14, 2017).

119. Schludi, M. H. *et al.* Spinal Poly-GA Inclusions in a C9orf72 Mouse Model Trigger Motor Deficits and Inflammation without Neuron Loss. *Acta Neuropathologica* **134,** 241–254. doi:10.1007/s00401-017-1711-0. pmid: 28409281 (Aug. 2017).

120. Swaminathan, A. *et al.* Expression of C9orf72-related Dipeptides Impairs Motor Function in a Vertebrate Model. *Human Molecular Genetics* **27,** 1754–1762. doi:10.1093/hmg/ddy083. pmid: 29528390 (May 15, 2018).

121. Yamakawa, M. *et al.* Characterization of the Dipeptide Repeat Protein in the Molecular Pathogenesis of c9FTD/ALS. *Human molecular genetics* **24,** 1630–1645. pmid: 25398948 (2015).

122. Zhang, Y.-J. *et al.* C9ORF72 Poly(GA) Aggregates Sequester and Impair HR23 and Nucleocytoplasmic Transport Proteins. *Nature Neuroscience* **19,** 668–677. doi:10.1038/nn.4272. pmid: 26998601 (May 2016).

123. Esanov, R. *et al.* A C9ORF72 BAC Mouse Model Recapitulates Key Epigenetic Perturbations of ALS/FTD. *Molecular Neurodegeneration* **12,** 46. doi:10.1186/s13024-017-0185-9 (June 12, 2017).

124. Jiang, J. *et al.* Gain of Toxicity from ALS/FTD-Linked Repeat Expansions in C9ORF72 Is Alleviated by Antisense Oligonucleotides Targeting GGGGCC-Containing RNAs. *Neuron* **90,** 535–550. doi:10.1016/j.neuron.2016.04.006. pmid: 27112497 (May 4, 2016).

125. Jury, N. *et al.* Widespread Loss of the Silencing Epigenetic Mark H3K9me3 in Astrocytes and Neurons along with Hippocampal-Dependent Cognitive Impairment in C9orf72 BAC Transgenic Mice. *Clinical Epigenetics* **12,** 32. doi:10.1186/s13148-020-0816-9 (Feb. 18, 2020).

126. O'Rourke, J. G. *et al.* C9orf72 BAC Transgenic Mice Display Typical Pathologic Features of ALS/FTD. *Neuron* **88,** 892–901. doi:10.1016/j.neuron.2015.10.027. pmid: 26637796 (Dec. 2, 2015).

127. Peters, O. M. *et al.* Human C9ORF72 Hexanucleotide Expansion Reproduces RNA Foci and Dipeptide Repeat Proteins but Not Neurodegeneration in BAC Transgenic Mice. *Neuron* **88,** 902–909. doi:10.1016/j.neuron.2015.11.018. pmid: 26637797 (Dec. 2, 2015).

128. Liu, Y. *et al.* C9orf72 BAC Mouse Model with Motor Deficits and Neurodegenerative Features of ALS/FTD. *Neuron* **90,** 521–534. doi:10.1016/j.neuron.2016.04.005. pmid: 27112499 (May 4, 2016).

129. Le Bras, A. Modeling ALS/FTD in Mice: Updates on the C9orf72 BAC Transgenic Mice. *Lab Animal* **50,** 13–13. doi:10.1038/s41684-020-00693-9 (1 Jan. 2021).

130. Mordes, D. A. *et al.* Absence of Survival and Motor Deficits in 500 Repeat C9ORF72 BAC Mice. *Neuron* **108,** 775–783.e4. doi:10.1016/j.neuron.2020.08.009 (Nov. 25, 2020).

131. Charcot, J. M. *Leçons Sur Les Maladies Du Système Nerveux Faites à La Salpêtrière* (V. Adrien Delahaye, 1877).

132. Kiernan, J. A. & Hudson, J. Frontal Lobe Atrophy in Motor Neuron Diseases. *Brain* **117,** 747–757. doi:10.1093/brain/117.4.747 (Aug. 1, 1994).

133. Fischl, B. & Dale, A. M. Measuring the Thickness of the Human Cerebral Cortex from Magnetic Resonance Images. *Proceedings of the National Academy of Sciences* **97,** 11050–11055. doi:10.1073/pnas.200033797 (Sept. 26, 2000).

134. Young, A. L. *et al.* Uncovering the Heterogeneity and Temporal Complexity of Neurodegenerative Diseases with Subtype and Stage Inference. *Nature Communications* **9,** 4273. doi:10.1038/s41467-018-05892-0 (1 Oct. 15, 2018).

135. Kwan, J. Y., Meoded, A., Danielian, L. E., Wu, T. & Floeter, M. K. Structural Imaging Differences and Longitudinal Changes in Primary Lateral Sclerosis and Amyotrophic Lateral Sclerosis. *NeuroImage: Clinical* **2,** 151–160. doi:10.1016/j.nicl.2012.12.003 (Jan. 1, 2013).

136. Schuster, C. *et al.* Longitudinal Course of Cortical Thickness Decline in Amyotrophic Lateral Sclerosis. *Journal of Neurology* **261,** 1871–1880. doi:10.1007/s00415-014-7426-4 (Oct. 1, 2014).

137. Devine, M. S., Kiernan, M. C., Heggie, S., McCombe, P. A. & Henderson, R. D. Study of Motor Asymmetry in ALS Indicates an Effect of Limb Dominance on Onset and Spread of Weakness, and an Important Role for Upper Motor Neurons. *Amyotrophic Lateral Sclerosis & Frontotemporal Degeneration* **15,** 481–487. doi:10.3109/21678421.2014.906617. pmid: 24809721 (Dec. 2014).

138. Steinbach, R. *et al.* Patterns of Grey and White Matter Changes Differ between Bulbar and Limb Onset Amyotrophic Lateral Sclerosis. *NeuroImage: Clinical* **30,** 102674. doi:10.1016/j.nicl.2021.102674. pmid: 33901988 (Jan. 1, 2021).

139. Chang, J. L. *et al.* A Voxel-Based Morphometry Study of Patterns of Brain Atrophy in ALS and ALS/FTLD. *Neurology* **65,** 75–80. doi:10.1212/01.wnl.0000167602.38643.29. pmid: 16009889 (July 12, 2005).

140. Ellis, C. M. *et al.* Diffusion Tensor MRI Assesses Corticospinal Tract Damage in ALS. *Neurology* **53,** 1051–1051. doi:10.1212/WNL.53.5.1051. pmid: 10496265 (Sept. 1, 1999).

141. Filippini, N. *et al.* Corpus Callosum Involvement Is a Consistent Feature of Amyotrophic Lateral Sclerosis. *Neurology* **75,** 1645–1652. doi:10.1212/WNL.0b013e3181fb84d1. pmid: 21041787 (Nov. 2, 2010).

142. Bede, P. & Hardiman, O. Longitudinal Structural Changes in ALS: A Three Time-Point Imaging Study of White and Gray Matter Degeneration. *Amyotrophic Lateral Sclerosis and Frontotemporal Degeneration* **19,** 232–241. doi:10.1080/21678421.2017.1407795. pmid: 29214883 (Apr. 3, 2018).

143. Senda, J. *et al.* Structural MRI Correlates of Amyotrophic Lateral Sclerosis Progression. *Journal of Neurology, Neurosurgery & Psychiatry* **88,** 901–907. doi:10.1136/jnnp-2016-314337. pmid: 28501822 (Nov. 1, 2017).

144. Femiano, C. *et al.* Apathy Is Correlated with Widespread Diffusion Tensor Imaging (DTI) Impairment in Amyotrophic Lateral Sclerosis. *Behavioural Neurology* **2018.** doi:10.1155/2018/2635202 (2018).

145. Kasper, E. *et al.* Microstructural White Matter Changes Underlying Cognitive and Behavioural Impairment in ALS – An In Vivo Study Using DTI. *PLOS ONE* **9,** e114543. doi:10.1371/journal.pone.0114543 (Dec. 11, 2014).

146. Lulé, D. *et al.* Cognitive Phenotypes of Sequential Staging in Amyotrophic Lateral Sclerosis. *Cortex* **101,** 163–171. doi:10.1016/j.cortex.2018.01.004 (Apr. 1, 2018).

147. Müller, H.-P. *et al.* In Vivo Histopathological Staging in C9orf72-associated ALS: A Tract of Interest DTI Study. *NeuroImage: Clinical* **27,** 102298. doi:10.1016/j.nicl.2020.102298 (Jan. 1, 2020).

148. Westeneng, H.-J. *et al.* Widespread Structural Brain Involvement in ALS Is Not Limited to the C9orf72 Repeat Expansion. *Journal of Neurology, Neurosurgery & Psychiatry* **87,** 1354–1360. doi:10.1136/jnnp-2016-313959. pmid: 27756805 (Dec. 1, 2016).

149. Müller, H.-P. *et al.* Segmental Involvement of the Corpus Callosum in C9orf72-associated ALS: A Tract of Interest-Based DTI Study. *Therapeutic Advances in Chronic Disease* **12,** 20406223211002969. doi:10.1177/20406223211002969. pmid: 33815737 (Jan. 1, 2021).

150. Tu, S. *et al.* Regional Callosal Integrity and Bilaterality of Limb Weakness in Amyotrophic Lateral Sclerosis. *Amyotrophic Lateral Sclerosis and Frontotemporal Degeneration,* 1–7. doi:10.1080/21678421.2020.1733020. pmid: 32106716 (Feb. 28, 2020).

151. Kalra, S. *et al.* A Prospective Harmonized Multicenter DTI Study of Cerebral White Matter Degeneration in ALS. *Neurology* **95,** e943–e952. doi:10.1212/WNL.0000000000010235. pmid: 32646955 (Aug. 25, 2020).

152. Braak, H. & Braak, E. Neuropathological Stageing of Alzheimer-related Changes. *Acta Neuropathologica* **82,** 239–259. doi:10.1007/BF00308809 (Sept. 1, 1991).

153. Braak, H. & Braak, E. Staging of Alzheimer's Disease-Related Neurofibrillary Changes. *Neurobiology of Aging. The Schmitt Symposium: The Cytoskeleton and Alzheimer's Disease* **16,** 271–278. doi:10.1016/0197-4580(95)00021-6 (May 1, 1995).

154. Braak, H. *et al.* Staging of Brain Pathology Related to Sporadic Parkinson's Disease. *Neurobiology of Aging* **24,** 197–211. doi:10.1016/S0197-4580(02)00065-9 (Mar. 1, 2003).

155. Brettschneider, J. *et al.* Stages of pTDP-43 Pathology in Amyotrophic Lateral Sclerosis. *Annals of Neurology* **74,** 20–38. doi:10.1002/ana.23937 (2013).

156. Aguzzi, A. & Rajendran, L. The Transcellular Spread of Cytosolic Amyloids, Prions, and Prionoids. *Neuron* **64,** 783–790. doi:10.1016/j.neuron.2009.12.016. pmid: 20064386 (Dec. 24, 2009).

157. Brettschneider, J., Tredici, K. D., Lee, V. M.-Y. & Trojanowski, J. Q. Spreading of Pathology in Neurodegenerative Diseases: A Focus on Human Studies. *Nature Reviews Neuroscience* **16,** 109–120. doi:10.1038/nrn3887 (2 Feb. 2015).

158. Weickenmeier, J., Jucker, M., Goriely, A. & Kuhl, E. A Physics-Based Model Explains the Prion-like Features of Neurodegeneration in Alzheimer's Disease, Parkinson's Disease, and Amyotrophic Lateral Sclerosis. *Journal of the Mechanics and Physics of Solids* **124,** 264–281. doi:10.1016/j.jmps.2018.10.013 (Mar. 1, 2019).

159. Gorges, M. *et al.* Corticoefferent Pathology Distribution in Amyotrophic Lateral Sclerosis: In Vivo Evidence from a Meta-Analysis of Diffusion Tensor Imaging Data. *Scientific reports* **8,** 15389 (2018).

160. Kassubek, J. *et al.* Diffusion Tensor Imaging Analysis of Sequential Spreading of Disease in Amyotrophic Lateral Sclerosis Confirms Patterns of TDP-43 Pathology. *Brain* **137,** 1733–1740. doi:10.1093/brain/awu090 (June 1, 2014).

161. Kassubek, J. *et al.* Imaging the Pathoanatomy of Amyotrophic Lateral Sclerosis in Vivo: Targeting a Propagation-Based Biological Marker. *J Neurol Neurosurg Psychiatry* **89,** 374–381 (2018).

162. Ravits, J., Laurie, P., Fan, Y. & Moore, D. H. Implications of ALS Focality: Rostral–Caudal Distribution of Lower Motor Neuron Loss Postmortem. *Neurology* **68,** 1576–1582. doi:10.1212/01.wnl.0000261045.57095.56. pmid: 17485644 (May 8, 2007).

163. Ravits, J. M. & La Spada, A. R. ALS Motor Phenotype Heterogeneity, Focality, and Spread: Deconstructing Motor Neuron Degeneration. *Neurology* **73,** 805–811. doi:10.1212/WNL.0b013e3181b6bbbd. pmid: 19738176 (Sept. 8, 2009).

164. Sekiguchi, T. *et al.* Spreading of Amyotrophic Lateral Sclerosis Lesions—Multifocal Hits and Local Propagation? *Journal of Neurology, Neurosurgery & Psychiatry* **85,** 85–91. doi:10.1136/jnnp-2013-305617. pmid: 24027298 (Jan. 1, 2014).

165. Camilus, N., Quintero Arias, C. & Martic, S. Role of Triggers on the Structural and Functional Facets of TAR DNA-binding Protein 43. *Neuroscience.* doi:10.1016/j.neuroscience.2022.11.027 (Nov. 25, 2022).

166. Giordana, M. T. *et al.* TDP-43 Redistribution Is an Early Event in Sporadic Amyotrophic Lateral Sclerosis. *Brain Pathology* **20,** 351–360. doi:10.1111/j.1750-3639.2009.00284.x (2010).

167. Surmeier, D. J., Obeso, J. A. & Halliday, G. M. Parkinson's Disease Is Not Simply a Prion Disorder. *Journal of Neuroscience* **37,** 9799–9807. doi:10.1523/JNEUROSCI.1787-16.2017. pmid: 29021297 (Oct. 11, 2017).

168. Meisl, G. *et al.* In Vivo Rate-Determining Steps of Tau Seed Accumulation in Alzheimer's Disease. *Science Advances* **7,** eabh1448. doi:10.1126/sciadv.abh1448. pmid: 34714685 (Oct. 29, 2021).

169. Burke, R. E., Dauer, W. T. & Vonsattel, J. P. G. A Critical Evaluation of the Braak Staging Scheme for Parkinson's Disease. *Annals of Neurology* **64,** 485–491. doi:10.1002/ana.21541 (2008).

170. Alstermark, B., Isa, T. & Tantisira, B. Integration in Descending Motor Pathways Controlling the Forelimb in the Cat. *Experimental Brain Research* **84,** 561–568 (1991).

171. Yang, H.-W. & Lemon, R. An Electron Microscopic Examination of the Corticospinal Projection to the Cervical Spinal Cord in the Rat: Lack of Evidence for Cortico-Motoneuronal Synapses. *Experimental brain research* **149,** 458–469 (2003).

172. Alstermark, B. & Ogawa, J. In Vivo Recordings of Bulbospinal Excitation in Adult Mouse Forelimb Motoneurons. *Journal of Neurophysiology* **92,** 1958–1962. doi:10.1152/jn.00092.2004 (Sept. 1, 2004).

173. Kuypers, H. G. J. M. in *Comprehensive Physiology* 597–666 (John Wiley & Sons, Ltd, 2011). doi:10.1002/cphy.cp010213. eprint: https://onlinelibrary.wiley.com/doi/pdf/10.1002/cphy.cp010213.

174. Quallo, M. M., Kraskov, A. & Lemon, R. N. The Activity of Primary Motor Cortex Corticospinal Neurons during Tool Use by Macaque Monkeys. *The Journal of Neuroscience: The Official Journal of the Society for Neuroscience* **32,** 17351–17364. doi:10.1523/JNEUROSCI.1009-12.2012. pmid: 23197726 (Nov. 28, 2012).

175. Lemon, R. N. & Griffiths, J. Comparing the Function of the Corticospinal System in Different Species: Organizational Differences for Motor Specialization? *Muscle & Nerve* **32,** 261–279. doi:10.1002/mus.20333. pmid: 15806550 (Sept. 2005).

176. Eisen, A., Turner, M. R. & Lemon, R. Tools and Talk: An Evolutionary Perspective on the Functional Deficits Associated with Amyotrophic Lateral Sclerosis. *Muscle & Nerve* **49,** 469–477. doi:10.1002/mus.24132 (2014).

177. Barker, A. T., Jalinous, R. & Freeston, I. L. NON-INVASIVE MAGNETIC STIMULATION OF HUMAN MOTOR CORTEX. *The Lancet* **325,** 1106–1107. doi:10.1016/S0140-6736(85)92413-4 (May 11, 1985).

178. Eisen, A., Pant, B. & Stewart, H. Cortical Excitability in Amyotrophic Lateral Sclerosis: A Clue to Pathogenesis. *Canadian Journal of Neurological Sciences* **20,** 11–16. doi:10.1017/S031716710004734X (Feb. 1993).

179. Vucic, S. & Kiernan, M. C. Novel Threshold Tracking Techniques Suggest That Cortical Hyperexcitability Is an Early Feature of Motor Neuron Disease. *Brain* **129,** 2436–2446. doi:10.1093/brain/awl172 (Sept. 1, 2006).

180. Vucic, S., Nicholson, G. A. & Kiernan, M. C. Cortical Hyperexcitability May Precede the Onset of Familial Amyotrophic Lateral Sclerosis. *Brain: A Journal of Neurology* **131,** 1540–1550. doi:10.1093/brain/awn071. pmid: 18469020 (Pt 6 June 2008).

181. Dharmadasa, T., Matamala, J. M., Howells, J., Vucic, S. & Kiernan, M. C. Early Focality and Spread of Cortical Dysfunction in Amyotrophic Lateral Sclerosis: A Regional Study across the Motor Cortices. *Clinical Neurophysiology* **131,** 958–966. doi:10.1016/j.clinph.2019.11.057 (Apr. 1, 2020).

182. Nardone, R. *et al.* Disinhibition of Sensory Cortex in Patients with Amyotrophic Lateral Sclerosis. *Neuroscience Letters* **722,** 134860. doi:10.1016/j.neulet.2020.134860 (Mar. 2020).

183. McMackin, R. *et al.* Cognitive Network Hyperactivation and Motor Cortex Decline Correlate with ALS Prognosis. *Neurobiology of Aging.* doi:10.1016/j.neurobiolaging.2021.03.002. pmid: 33964609 (Mar. 10, 2021).

184. Matamala, J. M. *et al.* Inter-Session Reliability of Short-Interval Intracortical Inhibition Measured by Threshold Tracking TMS. *Neuroscience Letters* **674,** 18–23. doi:10.1016/j.neulet.2018.02.065 (May 1, 2018).

185. Vucic, S., Cheah, B. C., Yiannikas, C. & Kiernan, M. C. Cortical Excitability Distinguishes ALS from Mimic Disorders. *Clinical Neurophysiology* **122,** 1860–1866. doi:10.1016/j.clinph.2010.12.062 (Sept. 1, 2011).

186. Ziemann, U., Lönnecker, S., Steinhoff, B. J. & Paulus, W. The Effect of Lorazepam on the Motor Cortical Excitability in Man. *Experimental brain research* **109,** 127–135 (1996).

187. Ilić, T. V. *et al.* Short-Interval Paired-Pulse Inhibition and Facilitation of Human Motor Cortex: The Dimension of Stimulus Intensity. *The Journal of Physiology* **545,** 153–167. doi:10.1113/jphysiol.2002.030122 (2002).

188. Lazzaro, V. D. *et al.* GABAA Receptor Subtype Specific Enhancement of Inhibition in Human Motor Cortex. *The Journal of Physiology* **575,** 721–726. doi:10.1113/jphysiol.2006.114694 (2006).

189. Huntsman, M. M., Woods, T. M. & Jones, E. G. Laminar Patterns of Expression of GABAA Receptor Subunit mRNAs in Monkey Sensory Motor Cortex. *Journal of Comparative Neurology* **362,** 565–582. doi:10.1002/cne.903620410 (1995).

190. Zich, C. *et al.* Human Motor Cortical Gamma Activity Relates to GABAergic Signalling and to Behaviour. *bioRxiv,* 2021.06.16.448658. doi:10.1101/2021.06.16.448658 (June 16, 2021).

191. Bonaiuto, J. J. *et al.* Lamina-Specific Cortical Dynamics in Human Visual and Sensorimotor Cortices. *eLife* **7,** e33977. doi:10.7554/eLife.33977 (Oct. 22, 2018).

192. Stagg, C. J., Bachtiar, V. & Johansen-Berg, H. The Role of GABA in Human Motor Learning. *Current Biology* **21,** 480–484. doi:10.1016/j.cub.2011.01.069 (Mar. 2011).

193. Dyke, K. *et al.* Comparing GABA-dependent Physiological Measures of Inhibition with Proton Magnetic Resonance Spectroscopy Measurement of GABA Using Ultra-High-Field MRI. *NeuroImage* **152,** 360–370. doi:10.1016/j.neuroimage.2017.03.011 (May 15, 2017).

194. McColgan, P., Joubert, J., Tabrizi, S. J. & Rees, G. The Human Motor Cortex Microcircuit: Insights for Neurodegenerative Disease. *Nature Reviews Neuroscience* **21,** 401–415. doi:10.1038/s41583-020-0315-1 (8 Aug. 2020).

195. Weiler, N., Wood, L., Yu, J., Solla, S. A. & Shepherd, G. M. G. Top-down Laminar Organization of the Excitatory Network in Motor Cortex. *Nature Neuroscience* **11,** 360–366. doi:10.1038/nn2049 (3 Mar. 2008).

196. Hensch, T. K. Critical Period Plasticity in Local Cortical Circuits. *Nature Reviews Neuroscience* **6,** 877–888. doi:10.1038/nrn1787 (Nov. 2005).

197. Isaacson, J. S. & Scanziani, M. How Inhibition Shapes Cortical Activity. *Neuron* **72,** 231–243. doi:10.1016/j.neuron.2011.09.027 (Oct. 2011).

198. Estebanez, L., Hoffmann, D., Voigt, B. C. & Poulet, J. F. Parvalbumin-Expressing GABAergic Neurons in Primary Motor Cortex Signal Reaching. *Cell Reports* **20,** 308–318. doi:10.1016/j.celrep.2017.06.044 (July 2017).

199. Nihei, K., McKee, A. C. & Kowall, N. W. Patterns of Neuronal Degeneration in the Motor Cortex of Amyotrophic Lateral Sclerosis Patients. *Acta neuropathologica* **86,** 55–64 (1993).

200. Petri, S. *et al.* GABAA-receptor mRNA Expression in the Prefrontal and Temporal Cortex of ALS Patients. *Journal of the neurological sciences* **250,** 124–132. pmid: 17011586 (2006).

201. Wamsley, B. & Fishell, G. Genetic and Activity-Dependent Mechanisms Underlying Interneuron Diversity. *Nature Reviews Neuroscience* **18,** 299–309. doi:10.1038/nrn.2017.30 (5 May 2017).

202. Foerster, B. R. *et al.* Decreased Motor Cortex -Aminobutyric Acid in Amyotrophic Lateral Sclerosis. *Neurology* **78,** 1596–1600. doi:10.1212/WNL.0b013e3182563b57. pmid: 22517106 (Aug. 2011).

203. Foerster, B. R. *et al.* An Imbalance between Excitatory and Inhibitory Neurotransmitters in Amyotrophic Lateral Sclerosis Revealed by Use of 3-T Proton Magnetic Resonance Spectroscopy. *JAMA Neurol.* **70,** 1009–1016. doi:10.1001/jamaneurol.2013.234 (Aug. 2013).

204. Han, J. & Ma, L. Study of the Features of Proton MR Spectroscopy ((1)H-MRS) on Amyotrophic Lateral Sclerosis. *Journal of magnetic resonance imaging: JMRI* **31,** 305–308. doi:10.1002/jmri.22053. pmid: 20099342 (Feb. 2010).

205. Bradley, W. G., Bowen, B. C., Pattany, P. M. & Rotta, F. 1H-magnetic Resonance Spectroscopy in Amyotrophic Lateral Sclerosis. *Journal of the Neurological Sciences* **169,** 84–86. doi:10.1016/s0022-510x(99)00221-x. pmid: 10540013 (Oct. 31, 1999).

206. Van der Graaff, M. M. *et al.* MR Spectroscopy Findings in Early Stages of Motor Neuron Disease. *AJNR. American journal of neuroradiology* **31,** 1799–1806. doi:10.3174/ajnr.A2217. pmid: 20801763 (Nov. 2010).

207. Cheong, I. *et al.* Ultra-High Field Proton MR Spectroscopy in Early-Stage Amyotrophic Lateral Sclerosis. *Neurochemical Research* **42,** 1833–1844. doi:10.1007/s11064-017-2248-2. pmid: 28367604 (June 2017).

208. Bowen, B. C. *et al.* MR Imaging and Localized Proton Spectroscopy of the Precentral Gyrus in Amyotrophic Lateral Sclerosis. *AJNR. American journal of neuroradiology* **21,** 647–658. pmid: 10782773 (Apr. 2000).

209. Atassi, N. *et al.* Ultra High-Field (7tesla) Magnetic Resonance Spectroscopy in Amyotrophic Lateral Sclerosis. *PloS One* **12,** e0177680. doi:10.1371/journal.pone.0177680. pmid: 28498852 (2017).

210. Blicher, J. U. *et al.* Short Echo-Time Magnetic Resonance Spectroscopy in ALS, Simultaneous Quantification of Glutamate and GABA at 3 T. *Scientific Reports* **9,** 17593. doi:10.1038/s41598-019-53009-4 (Dec. 2019).

211. Sako, W. *et al.* MR Spectroscopy and Imaging-Derived Measurements in the Supplementary Motor Area for Biomarkers of Amyotrophic Lateral Sclerosis. *Neurological Sciences: Official Journal of the Italian Neurological Society and of the Italian Society of Clinical Neurophysiology* **42,** 4257–4263. doi:10.1007/s10072-021-05107-3. pmid: 33594539 (Oct. 2021).

212. Harris, K. D. & Shepherd, G. M. G. The Neocortical Circuit: Themes and Variations. *Nature Neuroscience* **18,** 170–181. doi:10.1038/nn.3917 (2 Feb. 2015).

213. Carson, R. G. Inter-Hemispheric Inhibition Sculpts the Output of Neural Circuits by Co-Opting the Two Cerebral Hemispheres. *The Journal of Physiology* **n/a.** doi:10.1113/JP279793.

214. Proudfoot, M. *et al.* Impaired Corticomuscular and Interhemispheric Cortical Beta Oscillation Coupling in Amyotrophic Lateral Sclerosis. *Clinical Neurophysiology* **129,** 1479–1489. pmid: 29678369 (2018).

215. He, S. Q., Dum, R. P. & Strick, P. L. Topographic Organization of Corticospinal Projections from the Frontal Lobe: Motor Areas on the Medial Surface of the Hemisphere. *Journal of Neuroscience* **15,** 3284–3306. doi:10.1523/JNEUROSCI.15-05-03284.1995. pmid: 7538558 (May 1, 1995).

216. Dum, R. P. & Strick, P. L. The Origin of Corticospinal Projections from the Premotor Areas in the Frontal Lobe. *The Journal of Neuroscience: The Official Journal of the Society for Neuroscience* **11,** 667–689. pmid: 1705965 (Mar. 1991).

217. Dum, R. P. & Strick, P. L. Spinal Cord Terminations of the Medial Wall Motor Areas in Macaque Monkeys. *Journal of Neuroscience* **16,** 6513–6525. doi:10.1523/JNEUROSCI.16-20-06513.1996. pmid: 8815929 (Oct. 15, 1996).

218. Johansen-Berg, H. *et al.* Changes in Connectivity Profiles Define Functionally Distinct Regions in Human Medial Frontal Cortex. *Proceedings of the National Academy of Sciences* **101,** 13335–13340. doi:10.1073/pnas.0403743101. pmid: 15340158 (Sept. 7, 2004).

219. Schulz, R. *et al.* Interactions Between the Corticospinal Tract and Premotor–Motor Pathways for Residual Motor Output After Stroke. *Stroke* **48,** 2805–2811. doi:10.1161/STROKEAHA.117.016834 (Oct. 1, 2017).

220. Johansen-Berg, H. *et al.* Functional–Anatomical Validation and Individual Variation of Diffusion Tractography-based Segmentation of the Human Thalamus. *Cerebral Cortex* **15,** 31–39. doi:10.1093/cercor/bhh105 (Jan. 1, 2005).

221. Shepherd, G. M. G. & Yamawaki, N. Untangling the Cortico-Thalamo-Cortical Loop: Cellular Pieces of a Knotty Circuit Puzzle. *Nature Reviews Neuroscience,* 1–18. doi:10.1038/s41583-021-00459-3 (May 6, 2021).

222. Barbas, H. & García-Cabezas, M. Á. Motor Cortex Layer 4: Less Is More. *Trends in Neurosciences* **38,** 259–261. doi:10.1016/j.tins.2015.03.005 (May 1, 2015).

223. Bopp, R., Holler-Rickauer, S., Martin, K. A. C. & Schuhknecht, G. F. P. An Ultrastructural Study of the Thalamic Input to Layer 4 of Primary Motor and Primary Somatosensory Cortex in the Mouse. *Journal of Neuroscience* **37,** 2435–2448. doi:10.1523/JNEUROSCI.2557-16.2017. pmid: 28137974 (Mar. 1, 2017).

224. Chipika, R. H. *et al.* MRI Data Confirm the Selective Involvement of Thalamic and Amygdalar Nuclei in Amyotrophic Lateral Sclerosis and Primary Lateral Sclerosis. *Data in Brief* **32,** 106246. doi:10.1016/j.dib.2020.106246. pmid: 32944601 (Oct. 2020).

225. Bocchetta, M. *et al.* Thalamic Nuclei in Frontotemporal Dementia: Mediodorsal Nucleus Involvement Is Universal but Pulvinar Atrophy Is Unique to *C9orf72*. *Human Brain Mapping* **41,** 1006–1016. doi:10.1002/hbm.24856 (Mar. 2020).

226. Reis, C. *et al.* Thalamocortical Dynamics Underlying Spontaneous Transitions in Beta Power in Parkinsonism. *NeuroImage* **193,** 103–114. doi:10.1016/j.neuroimage.2019.03.009 (June 1, 2019).

227. Turner, R. How Much Cortex Can a Vein Drain? Downstream Dilution of Activation-Related Cerebral Blood Oxygenation Changes. *NeuroImage* **16,** 1062–1067. doi:10.1006/nimg.2002.1082 (Aug. 2002).

228. Biswal, B., Zerrin Yetkin, F., Haughton, V. M. & Hyde, J. S. Functional Connectivity in the Motor Cortex of Resting Human Brain Using Echo-Planar MRI. *Magnetic resonance in medicine* **34,** 537–541 (1995).

229. Kristo, G. *et al.* Task and Task-Free FMRI Reproducibility Comparison for Motor Network Identification: Task and Task-Free fMRI Reproducibility Comparison for Motor Network Identification. *Human Brain Mapping* **35,** 340–352. doi:10.1002/hbm.22180 (Jan. 2014).

230. Ray, K. L. *et al.* ICA Model Order Selection of Task Co-Activation Networks. *Frontiers in Neuroscience* **7.** doi:10.3389/fnins.2013.00237 (2013).

231. Kollewe, K. *et al.* Patterns of Cortical Activity Differ in ALS Patients with Limb and/or Bulbar Involvement Depending on Motor Tasks. *Journal of Neurology* **258,** 804–810. doi:10.1007/s00415-010-5842-7 (May 1, 2011).

232. Mohammadi, B., Kollewe, K., Samii, A., Dengler, R. & Mıfmmode \ ddotu \ else ü\ finte, T. F. Functional Neuroimaging at Different Disease Stages Reveals Distinct Phases of Neuroplastic Changes in Amyotrophic Lateral Sclerosis. *Hum. Brain Mapp.* **32,** 750–758. doi:10.1002/hbm.21064. pmid: 20836159 (May 2011).

233. Mohammadi, B. *et al.* Changes of Resting State Brain Networks in Amyotrophic Lateral Sclerosis. *Experimental Neurology* **217,** 147–153. doi:10.1016/j.expneurol.2009.01.025 (May 1, 2009).

234. Agosta, F. *et al.* Sensorimotor Functional Connectivity Changes in Amyotrophic Lateral Sclerosis. *Cerebral Cortex (New York, N.Y.: 1991)* **21,** 2291–2298. doi:10.1093/cercor/bhr002. pmid: 21368084 (Oct. 2011).

235. Menke, R. A. L., Proudfoot, M., Talbot, K. & Turner, M. R. The Two-Year Progression of Structural and Functional Cerebral MRI in Amyotrophic Lateral Sclerosis. *NeuroImage: Clinical* **17,** 953–961. doi:10.1016/j.nicl.2017.12.025 (Jan. 1, 2018).

236. Poujois, A. *et al.* Brain Plasticity in the Motor Network Is Correlated with Disease Progression in Amyotrophic Lateral Sclerosis. *Human Brain Mapping* **34,** 2391–2401. doi:10.1002/hbm.22070 (2013).

237. Lee, S. E. *et al.* Network Degeneration and Dysfunction in Presymptomatic C9ORF72 Expansion Carriers. *NeuroImage: Clinical* **14,** 286–297. doi:10.1016/j.nicl.2016.12.006 (Jan. 1, 2017).

238. Stoppel, C. M. *et al.* Structural and Functional Hallmarks of Amyotrophic Lateral Sclerosis Progression in Motor- and Memory-Related Brain Regions. *NeuroImage: Clinical* **5,** 277–290. doi:10.1016/j.nicl.2014.07.007 (Jan. 1, 2014).

239. Querin, G., Biferi, M. G. & Pradat, P.-F. Biomarkers for C9orf7-ALS in Symptomatic and Pre-symptomatic Patients: State-of-the-art in the New Era of Clinical Trials. *Journal of Neuromuscular Diseases* **9,** 25–37. doi:10.3233/JND-210754 (Jan. 1, 2022).

240. Geethanath, S. & Vaughan Jr., J. T. Accessible Magnetic Resonance Imaging: A Review. *Journal of Magnetic Resonance Imaging* **49,** e65–e77. doi:10.1002/jmri.26638 (2019).

241. FbrG. *English: The Magnetic Moment of a Nucleus Precesses around the Direction of an External Magnetic Field (Green). The Direction of the Precession Depends on the Sign of the Gyromagnetic Ratio, . Here the Precession Is Depicted for Nuclei with > 0 (e.g. Protons).* Jan. 7, 2021.

242. Pannini. *Français : Représentation Visuelle Du Spin d'un Proton Dans à Un Champ Magnétique Constant B0 Puis Soumis à Une Onde Magnétique B1.* 8 December 2013, 23:11:21.

243. Lauterbur, P. C. Image Formation by Induced Local Interactions: Examples Employing Nuclear Magnetic Resonance. *Nature* **242,** 190–191. doi:10.1038/242190a0 (5394 Mar. 1973).

244. Carr, H. Y. Field Gradients in Early MRI. *Physics Today* **57,** 83–83. doi:10.1063/1.1784322 (July 2004).

245. Likes, R. S. *US Patent* 4307343A (1981).

246. Ljunggren, S. A Simple Graphical Representation of Fourier-Based Imaging Methods. *Journal of Magnetic Resonance (1969)* **54,** 338–343. doi:10.1016/0022-2364(83)90060-4 (Sept. 1, 1983).

247. Twieg, D. B. The K-Trajectory Formulation of the NMR Imaging Process with Applications in Analysis and Synthesis of Imaging Methods. *Medical Physics* **10,** 610–621. doi:10.1118/1.595331. pmid: 6646065 (1983 Sep-Oct).

248. Kumar, A., Welti, D. & Ernst, R. R. NMR Fourier Zeugmatography. *Journal of Magnetic Resonance (1969)* **18,** 69–83. doi:10.1016/0022-2364(75)90224-3 (Apr. 1, 1975).

249. Deshmane, A., Gulani, V., Griswold, M. A. & Seiberlich, N. Parallel MR Imaging. *Journal of magnetic resonance imaging : JMRI* **36,** 55–72. doi:10.1002/jmri.23639. pmid: 22696125 (July 2012).

250. Yang, A. C.-Y., Kretzler, M., Sudarski, S., Gulani, V. & Seiberlich, N. Sparse Reconstruction Techniques in MRI: Methods, Applications, and Challenges to Clinical Adoption. *Investigative radiology* **51,** 349–364. doi:10.1097/RLI.0000000000000274. pmid: 27003227 (June 2016).

251. Wong, E. C. Vessel-Encoded Arterial Spin-Labeling Using Pseudocontinuous Tagging. *Magnetic Resonance in Medicine* **58,** 1086–1091. doi:10.1002/mrm.21293. pmid: 17969084 (Dec. 2007).

252. Zimine, I., Petersen, E. T. & Golay, X. Dual Vessel Arterial Spin Labeling Scheme for Regional Perfusion Imaging. *Magnetic Resonance in Medicine* **56,** 1140–1144. doi:10.1002/mrm.21049. pmid: 16986112 (Nov. 2006).

253. Ogawa, S., Lee, T. M., Kay, A. R. & Tank, D. W. Brain Magnetic Resonance Imaging with Contrast Dependent on Blood Oxygenation. *Proceedings of the National Academy of Sciences of the United States of America* **87,** 9868–9872. doi:10.1073/pnas.87.24.9868. pmid: 2124706 (Dec. 1990).

254. Ogawa, S. & Lee, T. M. Magnetic Resonance Imaging of Blood Vessels at High Fields: In Vivo and in Vitro Measurements and Image Simulation. *Magnetic Resonance in Medicine* **16,** 9–18. doi:10.1002/mrm.1910160103. pmid: 2255240 (Oct. 1990).

255. Ogawa, S. *et al.* Intrinsic Signal Changes Accompanying Sensory Stimulation: Functional Brain Mapping with Magnetic Resonance Imaging. *Proceedings of the National Academy of Sciences* **89,** 5951–5955. doi:10.1073/pnas.89.13.5951. pmid: 1631079 (July 1, 1992).

256. Kwong, K. K. *et al.* Dynamic Magnetic Resonance Imaging of Human Brain Activity during Primary Sensory Stimulation. *Proceedings of the National Academy of Sciences of the United States of America* **89,** 5675–5679. pmid: 1608978 (June 15, 1992).

257. Buxton, R. B., Wong, E. C. & Frank, L. R. Dynamics of Blood Flow and Oxygenation Changes during Brain Activation: The Balloon Model. *Magnetic Resonance in Medicine* **39,** 855–864. doi:10.1002/mrm.1910390602. pmid: 9621908 (June 1998).

258. Friston, K. J., Mechelli, A., Turner, R. & Price, C. J. Nonlinear Responses in fMRI: The Balloon Model, Volterra Kernels, and Other Hemodynamics. *NeuroImage* **12,** 466–477. doi:10.1006/nimg.2000.0630. pmid: 10988040 (Oct. 2000).

259. Woolrich, M. W., Ripley, B. D., Brady, M. & Smith, S. M. Temporal Autocorrelation in Univariate Linear Modeling of FMRI Data. *NeuroImage* **14,** 1370–1386. doi:10.1006/nimg.2001.0931 (Dec. 1, 2001).

260. Beckmann, C. F. & Smith, S. M. Probabilistic Independent Component Analysis for Functional Magnetic Resonance Imaging. *IEEE Transactions on Medical Imaging* **23,** 137–152. doi:10.1109/TMI.2003.822821 (Feb. 2004).

261. Hu, D. *et al.* Unified SPM-ICA for fMRI Analysis. *NeuroImage* **25,** 746–755. doi:10.1016/j.neuroimage.2004.12.031. pmid: 15808976 (Apr. 15, 2005).

262. Heeger, D. J. & Ress, D. What Does fMRI Tell Us about Neuronal Activity? *Nature Reviews Neuroscience* **3,** 142–151. doi:10.1038/nrn730 (2 Feb. 2002).

263. Mattay, V. S. *et al.* Hemispheric Control of Motor Function: A Whole Brain Echo Planar fMRI Study. *Psychiatry Research* **83,** 7–22. doi:10.1016/s0925-4927(98)00023-7. pmid: 9754701 (July 15, 1998).

264. Rao, S. M. *et al.* Functional Magnetic Resonance Imaging of Complex Human Movements. *Neurology* **43,** 2311–2318. doi:10.1212/wnl.43.11.2311. pmid: 8232948 (Nov. 1993).

265. Allison, J. D., Meador, K. J., Loring, D. W., Figueroa, R. E. & Wright, J. C. Functional MRI Cerebral Activation and Deactivation during Finger Movement. *Neurology* **54,** 135–135. doi:10.1212/WNL.54.1.135. pmid: 10636139 (Jan. 11, 2000).

266. Jäncke, L. *et al.* fMRI Study of Bimanual Coordination. *Neuropsychologia* **38,** 164–174. doi:10.1016/S0028-3932(99)00062-7 (Feb. 1, 2000).

267. Mall, V. *et al.* Recruitment of the Sensorimotor Cortex - A Developmental fMRI Study. *Neuropediatrics* **36,** 373–379. doi:10.1055/s-2005-873077 (Dec. 2005).

268. Berlot, E., Popp, N. J. & Diedrichsen, J. A Critical Re-Evaluation of fMRI Signatures of Motor Sequence Learning. *eLife* **9,** e55241. doi:10.7554/eLife.55241. pmid: 32401193 (May 13, 2020).

269. Sampaio-Baptista, C. *et al.* Changes in Functional Connectivity and GABA Levels with Long-Term Motor Learning. *NeuroImage* **106,** 15–20. doi:10.1016/j.neuroimage.2014.11.032. pmid: 25463472 (Feb. 1, 2015).

270. Orban, G. A. *et al.* Similarities and Differences in Motion Processing between the Human and Macaque Brain: Evidence from fMRI. *Neuropsychologia. The Neuropsychology of Motion Perception* **41,** 1757–1768. doi:10.1016/S0028-3932(03)00177-5 (Jan. 1, 2003).

271. Burianová, H. *et al.* Motor Neuroplasticity: A MEG-fMRI Study of Motor Imagery and Execution in Healthy Ageing. *Neuropsychologia* **146,** 107539. doi:10.1016/j.neuropsychologia.2020.107539 (Sept. 1, 2020).

272. Matthews, P. M. & Jezzard, P. Functional Magnetic Resonance Imaging. *Journal of Neurology, Neurosurgery & Psychiatry* **75,** 6–12. pmid: 14707297 (Jan. 1, 2004).

273. Lenzi, D. *et al.* Effect of Corpus Callosum Damage on Ipsilateral Motor Activation in Patients with Multiple Sclerosis: A Functional and Anatomical Study. *Human Brain Mapping* **28,** 636–644. doi:10.1002/hbm.20305 (2007).

274. Mallol, R. *et al.* Compensatory Cortical Mechanisms in Parkinson's Disease Evidenced with fMRI during the Performance of Pre-Learned Sequential Movements. *Brain Research* **1147,** 265–271. doi:10.1016/j.brainres.2007.02.046 (May 25, 2007).

275. Ward, N. S., Brown, M. M., Thompson, A. J. & Frackowiak, R. S. J. Neural Correlates of Motor Recovery after Stroke: A Longitudinal fMRI Study. *Brain* **126,** 2476–2496. doi:10.1093/brain/awg245 (Nov. 1, 2003).

276. Sha, S. J. *et al.* Safety, Tolerability, and Feasibility of Young Plasma Infusion in the Plasma for Alzheimer Symptom Amelioration Study: A Randomized Clinical Trial. *JAMA Neurology* **76,** 35. doi:10.1001/jamaneurol.2018.3288 (Jan. 1, 2019).

277. Glasser, M. F. *et al.* The Minimal Preprocessing Pipelines for the Human Connectome Project. *NeuroImage* **80,** 105–124. doi:10.1016/j.neuroimage.2013.04.127. pmid: 23668970 (Oct. 15, 2013).

278. *UK Biobank Brain Imaging - Acquisition Protocol* https://www.fmrib.ox.ac.uk/ukbiobank/protocol/ (2020).

279. Alfaro-Almagro, F. *et al.* Image Processing and Quality Control for the First 10,000 Brain Imaging Datasets from UK Biobank. *NeuroImage* **166,** 400–424. doi:10.1016/j.neuroimage.2017.10.034 (Feb. 1, 2018).

280. Uğurbil, K. *et al.* Pushing Spatial and Temporal Resolution for Functional and Diffusion MRI in the Human Connectome Project. *NeuroImage* **80,** 80–104. doi:10.1016/j.neuroimage.2013.05.012. pmid: 23702417 (Oct. 15, 2013).

281. Drew, P. J., Shih, A. Y. & Kleinfeld, D. Fluctuating and Sensory-Induced Vasodynamics in Rodent Cortex Extend Arteriole Capacity. *Proceedings of the National Academy of Sciences* **108,** 8473–8478. doi:10.1073/pnas.1100428108. pmid: 21536897 (May 17, 2011).

282. Fernández-Klett, F., Offenhauser, N., Dirnagl, U., Priller, J. & Lindauer, U. Pericytes in Capillaries Are Contractile in Vivo, but Arterioles Mediate Functional Hyperemia in the Mouse Brain. *Proceedings of the National Academy of Sciences* **107,** 22290–22295. doi:10.1073/pnas.1011321108. pmid: 21135230 (Dec. 21, 2010).

283. Hillman, E. M. C. *et al.* Depth-Resolved Optical Imaging and Microscopy of Vascular Compartment Dynamics during Somatosensory Stimulation. *NeuroImage* **35,** 89–104. doi:10.1016/j.neuroimage.2006.11.032 (Mar. 1, 2007).

284. Yu, X. *et al.* Sensory and Optogenetically Driven Single-Vessel fMRI. *Nature Methods* **13,** 337–340. doi:10.1038/nmeth.3765 (4 Apr. 2016).

285. Gagnon, L. *et al.* Quantifying the Microvascular Origin of BOLD-fMRI from First Principles with Two-Photon Microscopy and an Oxygen-Sensitive Nanoprobe. *Journal of Neuroscience* **35,** 3663–3675 (2015).

286. Vazquez, A. L., Fukuda, M. & Kim, S.-G. Inhibitory Neuron Activity Contributions to Hemodynamic Responses and Metabolic Load Examined Using an Inhibitory Optogenetic Mouse Model. *Cerebral Cortex* **28,** 4105–4119. doi:10.1093/cercor/bhy225 (Nov. 1, 2018).

287. Shih, Y.-Y. I., Wey, H.-Y., De La Garza, B. H. & Duong, T. Q. Striatal and Cortical BOLD, Blood Flow, Blood Volume, Oxygen Consumption, and Glucose Consumption Changes in Noxious Forepaw Electrical Stimulation. *Journal of Cerebral Blood Flow & Metabolism* **31,** 832–841. doi:10.1038/jcbfm.2010.173 (Mar. 1, 2011).

288. Winder, A. T., Echagarruga, C., Zhang, Q. & Drew, P. J. Weak Correlations between Hemodynamic Signals and Ongoing Neural Activity during the Resting State. *Nature Neuroscience* **20,** 1761–1769. doi:10.1038/s41593-017-0007-y (12 Dec. 2017).

289. Sirotin, Y. B. & Das, A. Anticipatory Haemodynamic Signals in Sensory Cortex Not Predicted by Local Neuronal Activity. *Nature* **457,** 475–479. doi:10.1038/nature07664 (7228 Jan. 2009).

290. Pineiro, R., Pendlebury, S., Johansen-Berg, H. & Matthews, P. M. Altered Hemodynamic Responses in Patients after Subcortical Stroke Measured by Functional MRI. *Stroke* **33,** 103–109. doi:10.1161/hs0102.100482. pmid: 11779897 (Jan. 2002).

291. Taoka, T. *et al.* Age Correlation of the Time Lag in Signal Change on EPI-fMRI. *Journal of Computer Assisted Tomography* **22,** 514–517 (July–Aug. 1998).

292. Hesselmann, V. *et al.* Age Related Signal Decrease in Functional Magnetic Resonance Imaging during Motor Stimulation in Humans. *Neuroscience Letters* **308,** 141–144. doi:10.1016/S0304-3940(01)01920-6 (Aug. 10, 2001).

293. D'Esposito, M., Zarahn, E., Aguirre, G. K. & Rypma, B. The Effect of Normal Aging on the Coupling of Neural Activity to the Bold Hemodynamic Response. *NeuroImage* **10,** 6–14. doi:10.1006/nimg.1999.0444 (July 1, 1999).

294. Lulé, D. *et al.* Neuroimaging of Multimodal Sensory Stimulation in Amyotrophic Lateral Sclerosis. *Journal of Neurology, Neurosurgery, and Psychiatry* **81,** 899–906. doi:10.1136/jnnp.2009.192260. pmid: 20543183 (Aug. 2010).

295. Sage, C., Peeters, R., Robberecht, W. & Sunaert, S. Vascular versus Neuronal Defects in Amyotrophic Lateral Sclerosis: An fMRI Study. *Proceedings of ISMRM.*

296. Garbuzova-Davis, S. *et al.* Amyotrophic Lateral Sclerosis: A Neurovascular Disease. *Brain Research* **1398,** 113–125. doi:10.1016/j.brainres.2011.04.049 (June 29, 2011).

297. Garbuzova-Davis, S. *et al.* Impaired Blood–Brain/Spinal Cord Barrier in ALS Patients. *Brain Research* **1469,** 114–128. doi:10.1016/j.brainres.2012.05.056 (Aug. 21, 2012).

298. Tsvetanov, K. A., Henson, R. N. & Rowe, J. B. Separating Vascular and Neuronal Effects of Age on fMRI BOLD Signals. *Philosophical Transactions of the Royal Society B* **376,** 20190631 (2021).

299. Wang, Y. *et al.* Brain Structural and Perfusion Changes in Amyotrophic Lateral Sclerosis-Frontotemporal Dementia Patients with Cognitive and Motor Onset: A Preliminary Study. *Brain Imaging and Behavior* **16,** 2164–2174. doi:10.1007/s11682-022-00686-x (Oct. 1, 2022).

300. *(ISMRM 2011) Assessment of Cerebral Blood Flow in Amyotrophic Lateral Sclerosis Using Arterial Spin Labeling MR Imaging* https://archive.ismrm.org/2011/2217.html (2023).

301. Deligani, R. J. *et al.* Electrical and Hemodynamic Neural Functions in People with ALS: An EEG-fNIRS Resting-State Study. *IEEE Transactions on Neural Systems and Rehabilitation Engineering* **28,** 3129–3139. doi:10.1109/TNSRE.2020.3031495 (2020).

302. Proudfoot, M. *et al.* Increased Cerebral Functional Connectivity in ALS: A Resting-State Magnetoencephalography Study. *Neurology,* 10–1212. pmid: 29661904 (2018).

303. Sorrentino, P. *et al.* Brain Functional Networks Become More Connected as Amyotrophic Lateral Sclerosis Progresses: A Source Level Magnetoencephalographic Study. *NeuroImage Clinical* **20,** 564–571. doi:10.1016/j.nicl.2018.08.001. pmid: 30186760 (Jan. 1, 2018).

304. Warren, A. E. L. *et al.* Combined Isoflurane-Remifentanil Anaesthesia Permits Resting-State fMRI in Children with Severe Epilepsy and Intellectual Disability. *Brain Topography* **33,** 618–635. doi:10.1007/s10548-020-00782-5 (Sept. 1, 2020).

305. Picchioni, D., Duyn, J. H. & Horovitz, S. G. Sleep and the Functional Connectome. *NeuroImage. Mapping the Connectome* **80,** 387–396. doi:10.1016/j.neuroimage.2013.05.067 (Oct. 15, 2013).

306. Patriat, R. *et al.* The Effect of Resting Condition on Resting-State fMRI Reliability and Consistency: A Comparison between Resting with Eyes Open, Closed, and Fixated. *NeuroImage* **78,** 463–473. doi:10.1016/j.neuroimage.2013.04.013 (Sept. 1, 2013).

307. Hasson, U. & Honey, C. J. Future Trends in Neuroimaging: Neural Processes as Expressed within Real-Life Contexts. *NeuroImage. 20 YEARS OF fMRI* **62,** 1272–1278. doi:10.1016/j.neuroimage.2012.02.004 (Aug. 15, 2012).

308. Spiers, H. J. & Maguire, E. A. Decoding Human Brain Activity during Real-World Experiences. *Trends in Cognitive Sciences* **11,** 356–365. doi:10.1016/j.tics.2007.06.002 (Aug. 1, 2007).

309. Van der Meer, J. N., Breakspear, M., Chang, L. J., Sonkusare, S. & Cocchi, L. Movie Viewing Elicits Rich and Reliable Brain State Dynamics. *Nature Communications* **11,** 5004. doi:10.1038/s41467-020-18717-w. pmid: 33020473 (Oct. 5, 2020).

310. Cole, M. W., Ito, T., Bassett, D. S. & Schultz, D. H. Activity Flow over Resting-State Networks Shapes Cognitive Task Activations. *Nature Neuroscience* **19,** 1718–1726. doi:10.1038/nn.4406 (12 Dec. 2016).

311. Baker, A. P. *et al.* Fast Transient Networks in Spontaneous Human Brain Activity. *eLife* **3,** e01867. doi:10.7554/eLife.01867. pmid: 24668169 (Mar. 25, 2014).

312. O'Neill, G. C. *et al.* Dynamic Recruitment of Resting State Sub-Networks. *NeuroImage* **115,** 85–95. doi:10.1016/j.neuroimage.2015.04.030 (July 15, 2015).

313. Becker, R. *et al.* Transient Spectral Events in Resting State MEG Predict Individual Task Responses. *NeuroImage* **215,** 116818. doi:10.1016/j.neuroimage.2020.116818 (July 15, 2020).

314. Gordon, E. M. *et al.* Precision Functional Mapping of Individual Human Brains. *Neuron* **95,** 791–807.e7. doi:10.1016/j.neuron.2017.07.011 (Aug. 16, 2017).

315. Sadraee, A., Paulus, M. & Ekhtiari, H. fMRI as an Outcome Measure in Clinical Trials: A Systematic Review in Clinicaltrials.Gov. *Brain and Behavior* **11,** e02089. doi:10.1002/brb3.2089 (2021).

316. Molloy, E. K., Meyerand, M. E. & Birn, R. M. The Influence of Spatial Resolution and Smoothing on the Detectability of Resting-State and Task fMRI. *NeuroImage* **86,** 221–230. doi:10.1016/j.neuroimage.2013.09.001 (Feb. 1, 2014).

317. Nastase, S. A., Goldstein, A. & Hasson, U. Keep It Real: Rethinking the Primacy of Experimental Control in Cognitive Neuroscience. *NeuroImage* **222,** 117254. doi:10.1016/j.neuroimage.2020.117254 (Nov. 15, 2020).

318. Shah, L. M., Cramer, J. A., Ferguson, M. A., Birn, R. M. & Anderson, J. S. Reliability and Reproducibility of Individual Differences in Functional Connectivity Acquired during Task and Resting State. *Brain and behavior* **6,** e00456 (2016).

319. Noble, S., Scheinost, D. & Constable, R. T. A Decade of Test-Retest Reliability of Functional Connectivity: A Systematic Review and Meta-Analysis. *Neuroimage* **203,** 116157 (2019).

320. Elliott, M. L. *et al.* What Is the Test-Retest Reliability of Common Task-Functional MRI Measures? New Empirical Evidence and a Meta-Analysis. *Psychological Science* **31,** 792–806 (2020).

321. Boto, E. *et al.* Moving Magnetoencephalography towards Real-World Applications with a Wearable System. *Nature* **555,** 657–661. doi:10.1038/nature26147 (7698 Mar. 2018).

322. Roberts, G. *et al.* Towards OPM-MEG in a Virtual Reality Environment. *NeuroImage* **199,** 408–417. doi:10.1016/j.neuroimage.2019.06.010 (Oct. 1, 2019).

323. Mathis, A. *et al.* DeepLabCut: Markerless Pose Estimation of User-Defined Body Parts with Deep Learning. *Nature Neuroscience* **21,** 1281–1289. doi:10.1038/s41593-018-0209-y (9 Sept. 2018).

324. Rabi, I. I., Zacharias, J. R., Millman, S. & Kusch, P. A New Method of Measuring Nuclear Magnetic Moment. *Physical review* **53,** 318 (1938).

325. Purcell, E. M., Torrey, H. C. & Pound, R. V. Resonance Absorption by Nuclear Magnetic Moments in a Solid. *Physical review* **69,** 37 (1946).

326. Bloch, F. Nuclear Induction. *Physical review* **70,** 460 (1946).

327. Bachtiar, V. *et al.* Modulating Regional Motor Cortical Excitability with Noninvasive Brain Stimulation Results in Neurochemical Changes in Bilateral Motor Cortices. *The Journal of Neuroscience* **38,** 7327–7336. doi:10.1523/JNEUROSCI.2853-17.2018 (Aug. 15, 2018).

328. Bogner, W., Hangel, G., Esmaeili, M. & Andronesi, O. C. 1D-spectral Editing and 2D Multispectral in Vivo 1 H-MRS and 1 H-MRSI - Methods and Applications. *Analytical Biochemistry* **529,** 48–64. doi:10.1016/j.ab.2016.12.020 (July 2017).

329. Scheenen, T. W. J., Klomp, D. W. J., Wijnen, J. P. & Heerschap, A. Short Echo Time 1H-MRSI of the Human Brain at 3T with Minimal Chemical Shift Displacement Errors Using Adiabatic Refocusing Pulses. *Magnetic Resonance in Medicine* **59,** 1–6. doi:10.1002/mrm.21302 (2008).

330. Chiew, M. *et al.* Density-Weighted Concentric Rings k-Space Trajectory for 1H Magnetic Resonance Spectroscopic Imaging at 7 T. *NMR in Biomedicine* **31,** e3838. doi:10.1002/nbm.3838 (2018).

331. Steel, A. *et al.* Metabolite-Cycled Density-Weighted Concentric Rings k-Space Trajectory (DW-CRT) Enables High-Resolution 1 H Magnetic Resonance Spectroscopic Imaging at 3-Tesla. *Scientific Reports* **8,** 7792. doi:10.1038/s41598-018-26096-y (Dec. 2018).

332. Puts, N. A. & Edden, R. A. In Vivo Magnetic Resonance Spectroscopy of GABA: A Methodological Review. *Progress in Nuclear Magnetic Resonance Spectroscopy* **60,** 29–41. doi:10.1016/j.pnmrs.2011.06.001 (Jan. 2012).

333. Stagg, C. J., Bachtiar, V. & Johansen-Berg, H. What Are We Measuring with GABA Magnetic Resonance Spectroscopy? *Communicative & Integrative Biology* **4,** 573–575. doi:10.4161/cib.16213. pmid: 22046466 (Sept. 1, 2011).

334. Semyanov, A., Walker, M. C., Kullmann, D. M. & Silver, R. A. Tonically Active GABAA Receptors: Modulating Gain and Maintaining the Tone. *Trends in Neurosciences* **27,** 262–269. doi:10.1016/j.tins.2004.03.005 (May 1, 2004).

335. Glykys, J. & Mody, I. Activation of GABAA Receptors: Views from Outside the Synaptic Cleft. *Neuron* **56,** 763–770. doi:10.1016/j.neuron.2007.11.002 (Dec. 6, 2007).

336. Hurd, R. *et al.* Measurement of Brain Glutamate Using TE-averaged PRESS at 3T. *Magnetic Resonance in Medicine* **51,** 435–440. doi:10.1002/mrm.20007. pmid: 15004781 (Mar. 2004).

337. Schubert, F., Gallinat, J., Seifert, F. & Rinneberg, H. Glutamate Concentrations in Human Brain Using Single Voxel Proton Magnetic Resonance Spectroscopy at 3 Tesla. *NeuroImage* **21,** 1762–1771. doi:10.1016/j.neuroimage.2003.11.014. pmid: 15050596 (Apr. 2004).

338. Ramadan, S., Lin, A. & Stanwell, P. Glutamate and Glutamine: A Review of in Vivo MRS in the Human Brain. *NMR in Biomedicine* **26,** 1630–1646. doi:10.1002/nbm.3045 (2013).

339. Duncan, N. W., Wiebking, C. & Northoff, G. Associations of Regional GABA and Glutamate with Intrinsic and Extrinsic Neural Activity in Humans—A Review of Multimodal Imaging Studies. *Neuroscience & Biobehavioral Reviews* **47,** 36–52. doi:10.1016/j.neubiorev.2014.07.016 (Nov. 1, 2014).

340. Bede, P. *et al.* Grey Matter Correlates of Clinical Variables in Amyotrophic Lateral Sclerosis (ALS): A Neuroimaging Study of ALS Motor Phenotype Heterogeneity and Cortical Focality. *Journal of Neurology, Neurosurgery & Psychiatry* **84,** 766–773. doi:10.1136/jnnp-2012-302674. pmid: 23085933 (July 1, 2013).

341. Omer, T. *et al.* Neuroimaging Patterns along the ALS-FTD Spectrum: A Multiparametric Imaging Study. *Amyotrophic Lateral Sclerosis and Frontotemporal Degeneration* **18,** 611–623. doi:10.1080/21678421.2017.1332077. pmid: 28562080 (Oct. 2, 2017).

342. Shellikeri, S. *et al.* Speech Network Regional Involvement in Bulbar ALS: A Multimodal Structural MRI Study. *Amyotrophic Lateral Sclerosis and Frontotemporal Degeneration* **20,** 385–395. doi:10.1080/21678421.2019.1612920. pmid: 31088163 (July 3, 2019).

343. Feron, M. *et al.* Extrapyramidal Deficits in ALS: A Combined Biomechanical and Neuroimaging Study. *Journal of Neurology* **265,** 2125–2136. doi:10.1007/s00415-018-8964-y (Sept. 1, 2018).

344. Finegan, E. *et al.* The Clinical and Radiological Profile of Primary Lateral Sclerosis: A Population-Based Study. *Journal of Neurology* **266,** 2718–2733. doi:10.1007/s00415-019-09473-z (Nov. 1, 2019).

345. Frisoni, G. B. *et al.* Virtual Imaging Laboratories for Marker Discovery in Neurodegenerative Diseases. *Nature Reviews Neurology* **7,** 429–438. doi:10.1038/nrneurol.2011.99 (8 Aug. 2011).

346. Tabrizi, S. J. *et al.* Biological and Clinical Manifestations of Huntington's Disease in the Longitudinal TRACK-HD Study: Cross-Sectional Analysis of Baseline Data. *The Lancet Neurology* **8,** 791–801 (2009).

347. Bateman, R. J. *et al.* Clinical and Biomarker Changes in Dominantly Inherited Alzheimer's Disease. *New England Journal of Medicine* **367,** 795–804 (2012).

348. Rohrer, J., Warren, J., Fox, N. & Rossor, M. Presymptomatic Studies in Genetic Frontotemporal Dementia. *Revue neurologique* **169,** 820–824 (2013).

349. Schuster, C., Elamin, M., Hardiman, O. & Bede, P. Presymptomatic and Longitudinal Neuroimaging in Neurodegeneration—from Snapshots to Motion Picture: A Systematic Review. *Journal of Neurology, Neurosurgery & Psychiatry* **86,** 1089–1096. doi:10.1136/jnnp-2014-309888. pmid: 25632156 (Oct. 1, 2015).

350. Wen, J. *et al.* Neurite Density Is Reduced in the Presymptomatic Phase of C9orf72 Disease. *J Neurol Neurosurg Psychiatry,* jnnp–2018 (2018).

351. De Vocht, J. *et al.* Use of Multimodal Imaging and Clinical Biomarkers in Presymptomatic Carriers of *C9orf72* Repeat Expansion. *JAMA Neurology.* doi:10.1001/jamaneurol.2020.1087. pmid: 32421156 (May 18, 2020).

352. Popuri, K. *et al.* FDG-PET in Presymptomatic C9orf72 Mutation Carriers. *NeuroImage: Clinical* **31,** 102687. doi:10.1016/j.nicl.2021.102687 (Jan. 1, 2021).

353. Shoukry, R. S., Waugh, R., Bartlett, D., Raitcheva, D. & Floeter, M. K. Longitudinal Changes in Resting State Networks in Early Presymptomatic Carriers of C9orf72 Expansions. *NeuroImage. Clinical* **28,** 102354. doi:10.1016/j.nicl.2020.102354. pmid: 32769055 (July 20, 2020).

354. Waugh, R. E., Danielian, L. E., Shoukry, R. F. S. & Floeter, M. K. Longitudinal Changes in Network Homogeneity in Presymptomatic C9orf72 Mutation Carriers. *Neurobiology of Aging* **99,** 1–10. doi:10.1016/j.neurobiolaging.2020.11.014. pmid: 33421737 (Mar. 1, 2021).

355. Desmond, J. E. & Glover, G. H. Estimating Sample Size in Functional MRI (fMRI) Neuroimaging Studies: Statistical Power Analyses. *Journal of Neuroscience Methods* **118,** 115–128. doi:10.1016/S0165-0270(02)00121-8 (Aug. 30, 2002).

356. Hoenig, J. & Heisey, D. The Abuse of Power: The Persuasive Fallacy of Power Calculations for Data Analysis.(Vol 55, Pg 10, 2001). *JOURNAL OF SPEECH LANGUAGE AND HEARING RESEARCH* **45,** 493–493 (2002).

357. Bennett, C. M., Miller, M. B. & Wolford, G. L. Neural Correlates of Interspecies Perspective Taking in the Post-Mortem Atlantic Salmon: An Argument for Multiple Comparisons Correction. *Neuroimage* **47,** S125 (Suppl 1 2009).

358. Beckmann, C. F., Jenkinson, M. & Smith, S. M. General Multilevel Linear Modeling for Group Analysis in FMRI. *NeuroImage* **20,** 1052–1063. doi:10.1016/S1053-8119(03)00435-X (Oct. 1, 2003).

359. Winkler, A. M., Ridgway, G. R., Webster, M. A., Smith, S. M. & Nichols, T. E. Permutation Inference for the General Linear Model. *NeuroImage* **92,** 381–397. doi:10.1016/j.neuroimage.2014.01.060 (May 2014).

360. Barnes, N. Publish Your Computer Code: It Is Good Enough. *Nature* **467,** 753–753. doi:10.1038/467753a (7317 Oct. 2010).

361. *Files · Master · Evan Edmond / Ping-Mrsi-Pooled · GitLab* GitLab. https://git.fmrib.ox.ac.uk/edmond/ping-mrsi-pooled/-/tree/master (2022).

362. *Evan Edmond / Biomox2 · GitLab* GitLab. https://git.fmrib.ox.ac.uk/edmond/biomox2 (2022).

363. *Notes/MRSI_recon_fitting_notebook_2021_11.Ipynb · Master · Evan Edmond / Ping-Mrsi-Pooled · GitLab* GitLab. https://git.fmrib.ox.ac.uk/edmond/ping-mrsi-pooled/-/blob/master/notes/MRSI_recon_fitting_notebook_2021_11.ipynb (2022).

364. Turner, M. R. *et al.* Distinct Cerebral Lesions in Sporadic and 'D90A' SOD1 ALS: Studies with [11C]Flumazenil PET. *Brain* **128,** 1323–1329. doi:10.1093/brain/awh509 (June 1, 2005).

365. Spreux-Varoquaux, O. *et al.* Glutamate Levels in Cerebrospinal Fluid in Amyotrophic Lateral Sclerosis: A Reappraisal Using a New HPLC Method with Coulometric Detection in a Large Cohort of Patients. *Journal of the Neurological Sciences* **193,** 73–78. doi:10.1016/S0022-510X(01)00661-X (Jan. 15, 2002).

366. Selvaraj, B. T. *et al.* C9ORF72 Repeat Expansion Causes Vulnerability of Motor Neurons to Ca2+-Permeable AMPA Receptor-Mediated Excitotoxicity. *Nature Communications* **9,** 347. doi:10.1038/s41467-017-02729-0 (1 Jan. 24, 2018).

367. Shimizu, T. *et al.* Sensory Cortex Hyperexcitability Predicts Short Survival in Amyotrophic Lateral Sclerosis. *Neurology* **90,** e1578–e1587. doi:10.1212/WNL.0000000000005424. pmid: 29602913 (Jan. 5, 2018).

368. McMackin, R. *et al.* Localization of Brain Networks Engaged by the Sustained Attention to Response Task Provides Quantitative Markers of Executive Impairment in Amyotrophic Lateral Sclerosis. *Cerebral Cortex,* bhaa076. doi:10.1093/cercor/bhaa076 (Apr. 21, 2020).

369. Smith, S. M. *et al.* Correspondence of the Brain's Functional Architecture during Activation and Rest. *Proceedings of the National Academy of Sciences* **106,** 13040–13045. doi:10.1073/pnas.0905267106. pmid: 19620724 (Aug. 4, 2009).

370. Beckmann, C. F. & Smith, S. M. Tensorial Extensions of Independent Component Analysis for Multisubject FMRI Analysis. *NeuroImage* **25,** 294–311. doi:10.1016/j.neuroimage.2004.10.043 (Mar. 1, 2005).

371. *FSLNets - FslWiki* https://fsl.fmrib.ox.ac.uk/fsl/fslwiki/FSLNets#Running_FSLNets (2023).

372. Brainard, D. H. The Psychophysics Toolbox. *Spatial Vision* **10,** 433–436. pmid: 9176952 (1997).

373. Jenkinson, M., Beckmann, C. F., Behrens, T. E. J., Woolrich, M. W. & Smith, S. M. FSL. *NeuroImage* **62,** 782–790. doi:10.1016/j.neuroimage.2011.09.015. pmid: 21979382 (Aug. 15, 2012).

374. Worsley, K. J. *Statistical Analysis of Activation Images* (Oxford University Press).

375. Beckmann, C. F., DeLuca, M., Devlin, J. T. & Smith, S. M. Investigations into Resting-State Connectivity Using Independent Component Analysis. *Philosophical Transactions of the Royal Society of London. Series B, Biological Sciences* **360,** 1001–1013. doi:10.1098/rstb.2005.1634. pmid: 16087444 (May 29, 2005).

376. Griffanti, L. *et al.* ICA-based Artefact Removal and Accelerated fMRI Acquisition for Improved Resting State Network Imaging. *NeuroImage* **95,** 232–247. doi:10.1016/j.neuroimage.2014.03.034 (July 2014).

377. Salimi-Khorshidi, G. *et al.* Automatic Denoising of Functional MRI Data: Combining Independent Component Analysis and Hierarchical Fusion of Classifiers. *NeuroImage* **90,** 449–468. doi:10.1016/j.neuroimage.2013.11.046 (Apr. 2014).

378. Abou-Elseoud, A. *et al.* The Effect of Model Order Selection in Group PICA. *Human Brain Mapping* **31,** 1207–1216. doi:10.1002/hbm.20929 (2010).

379. Suri, S. *et al.* Distinct Resting-State Functional Connections Associated with Episodic and Visuospatial Memory in Older Adults. *NeuroImage* **159,** 122–130. doi:10.1016/j.neuroimage.2017.07.049 (Oct. 1, 2017).

380. Beckmann, C. F., Mackay, C. E., Filippini, N. & Smith, S. M. Group Comparison of Resting-State FMRI Data Using Multi-Subject ICA and Dual Regression. *Neuroimage* **47,** S148 (Suppl 1 2009).

381. Smith, S. M. *et al.* Functional Connectomics from Resting-State fMRI. *Trends in Cognitive Sciences* **17,** 666–682. doi:10.1016/j.tics.2013.09.016. pmid: 24238796 (Dec. 1, 2013).

382. Smith, S. M. *et al.* Network Modelling Methods for FMRI. *NeuroImage* **54,** 875–891. doi:10.1016/j.neuroimage.2010.08.063 (Jan. 15, 2011).

383. Faul, F., Erdfelder, E., Lang, A.-G. & Buchner, A. G*Power 3: A Flexible Statistical Power Analysis Program for the Social, Behavioral, and Biomedical Sciences. *Behavior Research Methods* **39,** 175–191. doi:10.3758/BF03193146 (May 1, 2007).

384. Li, H. *et al.* Altered Cortical Activation during Action Observation in Amyotrophic Lateral Sclerosis Patients: A Parametric Functional MRI Study. *European Radiology* **25,** 2584–2592. doi:10.1007/s00330-015-3671-x (Sept. 1, 2015).

385. Jelsone-Swain, L., Persad, C., Burkard, D. & Welsh, R. C. Action Processing and Mirror Neuron Function in Patients with Amyotrophic Lateral Sclerosis: An fMRI Study. *PLOS ONE* **10,** e0119862. doi:10.1371/journal.pone.0119862 (Apr. 17, 2015).

386. Mohammadi, B. *et al.* Amyotrophic Lateral Sclerosis Affects Cortical and Subcortical Activity Underlying Motor Inhibition and Action Monitoring. *Human Brain Mapping* **36,** 2878–2889. doi:10.1002/hbm.22814 (2015).

387. Thorns, J. *et al.* Movement Initiation and Inhibition Are Impaired in Amyotrophic Lateral Sclerosis. *Experimental Neurology* **224,** 389–394. doi:10.1016/j.expneurol.2010.04.014 (Aug. 1, 2010).

388. Proudfoot, M. *et al.* Altered Cortical Beta-Band Oscillations Reflect Motor System Degeneration in Amyotrophic Lateral Sclerosis. *Human brain mapping* **38,** 237–254 (2017).

389. Amiez, C. & Petrides, M. Neuroimaging Evidence of the Anatomo-Functional Organization of the Human Cingulate Motor Areas. *Cerebral Cortex (New York, N.Y.: 1991)* **24,** 563–578. doi:10.1093/cercor/bhs329. pmid: 23131805 (Mar. 2014).

390. Procyk, E. *et al.* Midcingulate Motor Map and Feedback Detection: Converging Data from Humans and Monkeys. *Cerebral Cortex (New York, N.Y.: 1991)* **26,** 467–476. doi:10.1093/cercor/bhu213. pmid: 25217467 (Feb. 2016).

391. Agosta, F. *et al.* Resting State Functional Connectivity Alterations in Primary Lateral Sclerosis. *Neurobiology of Aging* **35,** 916–925. doi:10.1016/j.neurobiolaging.2013.09.041. pmid: 24211007 (Apr. 2014).

392. Meoded, A. *et al.* Cerebro-Cerebellar Connectivity Is Increased in Primary Lateral Sclerosis. *NeuroImage. Clinical* **7,** 288–296. doi:10.1016/j.nicl.2014.12.009. pmid: 25610792 (2015).

393. Littman, R. & Takács, Á. Do All Inhibitions Act Alike? A Study of Go/No-Go and Stop-Signal Paradigms. *PloS one* **12,** e0186774 (2017).

394. Aron, A. R. & Poldrack, R. A. The Cognitive Neuroscience of Response Inhibition: Relevance for Genetic Research in Attention-Deficit/Hyperactivity Disorder. *Biological Psychiatry* **57,** 1285–1292. doi:10.1016/j.biopsych.2004.10.026 (June 1, 2005).

395. Devine, M. S. *et al.* Exposing Asymmetric Gray Matter Vulnerability in Amyotrophic Lateral Sclerosis. *NeuroImage : Clinical* **7,** 782–787. doi:10.1016/j.nicl.2015.03.006. pmid: 25844330 (Mar. 14, 2015).

396. Konrad, C. *et al.* Pattern of Cortical Reorganization in Amyotrophic Lateral Sclerosis: A Functional Magnetic Resonance Imaging Study. *Experimental Brain Research* **143,** 51–56. doi:10.1007/s00221-001-0981-9 (Mar. 1, 2002).

397. Cappon, D., D'Ostilio, K., Garraux, G., Rothwell, J. & Bisiacchi, P. Effects of 10 Hz and 20 Hz Transcranial Alternating Current Stimulation on Automatic Motor Control. *Brain Stimulation* **9,** 518–524. doi:10.1016/j.brs.2016.01.001. pmid: 27038707 (2016 Jul-Aug).

398. Jack Jr, C. R. *et al.* Longitudinal Tau PET in Ageing and Alzheimer's Disease. *Brain* **141,** 1517–1528. doi:10.1093/brain/awy059 (May 1, 2018).

399. Lissek, S. *et al.* Sex Differences in Cortical and Subcortical Recruitment during Simple and Complex Motor Control: An fMRI Study. *Neuroimage* **37,** 912–926 (2007).

400. Verstraete, E., Turner, M. R., Grosskreutz, J., Filippi, M. & Benatar, M. Mind the Gap: The Mismatch between Clinical and Imaging Metrics in ALS. *Amyotrophic Lateral Sclerosis and Frontotemporal Degeneration* **16,** 524–529. doi:10.3109/21678421.2015.1051989. pmid: 26402254 (Nov. 27, 2015).

401. Dale, A. M., Fischl, B. & Sereno, M. I. Cortical Surface-Based Analysis. I. Segmentation and Surface Reconstruction. *NeuroImage* **9,** 179–194. doi:10.1006/nimg.1998.0395. pmid: 9931268 (Feb. 1999).

402. Fischl, B., Sereno, M. I. & Dale, A. M. Cortical Surface-Based Analysis: II: Inflation, Flattening, and a Surface-Based Coordinate System. *NeuroImage* **9,** 195–207. doi:10.1006/nimg.1998.0396 (Feb. 1, 1999).

403. Jolly, E. Pymer4: Connecting R and Python for Linear Mixed Modeling. *Journal of Open Source Software* **3,** 862. doi:10.21105/joss.00862 (Nov. 26, 2018).

404. Bates, D., Mächler, M., Bolker, B. & Walker, S. Fitting Linear Mixed-Effects Models Using Lme4. *Journal of Statistical Software* **67,** 1–48. doi:10.18637/jss.v067.i01 (Oct. 7, 2015).

405. Honey, C. J., Kötter, R., Breakspear, M. & Sporns, O. Network Structure of Cerebral Cortex Shapes Functional Connectivity on Multiple Time Scales. *Proceedings of the National Academy of Sciences* **104,** 10240–10245 (2007).

406. Kolasinski, J. *et al.* The Dynamics of Cortical GABA in Human Motor Learning. *The Journal of Physiology* **597,** 271–282. doi:10.1113/JP276626. pmid: 30300446 (Jan. 2019).

407. Floyer-Lea, A., Wylezinska, M., Kincses, T. & Matthews, P. M. Rapid Modulation of GABA Concentration in Human Sensorimotor Cortex during Motor Learning. *Journal of Neurophysiology* **95,** 1639–1644. doi:10.1152/jn.00346.2005. pmid: 16221751 (Mar. 2006).

408. Frangou, P. *et al.* Learning to Optimize Perceptual Decisions through Suppressive Interactions in the Human Brain. *Nature Communications* **10,** 474. doi:10.1038/s41467-019-08313-y (Dec. 2019).

409. Puts, N. A. J., Edden, R. A. E., Evans, C. J., McGlone, F. & McGonigle, D. J. Regionally Specific Human GABA Concentration Correlates with Tactile Discrimination Thresholds. *Journal of Neuroscience* **31,** 16556–16560. doi:10.1523/JNEUROSCI.4489-11.2011 (Nov. 16, 2011).

410. Cassady, K. *et al.* Sensorimotor Network Segregation Declines with Age and Is Linked to GABA and to Sensorimotor Performance. *NeuroImage* **186,** 234–244. doi:10.1016/j.neuroimage.2018.11.008 (Feb. 2019).

411. Schaller, B., Xin, L., O'Brien, K., Magill, A. W. & Gruetter, R. Are Glutamate and Lactate Increases Ubiquitous to Physiological Activation? A 1H Functional MR Spectroscopy Study during Motor Activation in Human Brain at 7Tesla. *NeuroImage* **93,** 138–145. doi:10.1016/j.neuroimage.2014.02.016 (June 2014).

412. Chen, C. *et al.* Activation Induced Changes in GABA: Functional MRS at 7T with MEGA-sLASER. *NeuroImage* **156,** 207–213. doi:10.1016/j.neuroimage.2017.05.044 (Aug. 1, 2017).

413. Mangia, S., Giove, F. & DiNuzzo, M. Metabolic Pathways and Activity-Dependent Modulation of Glutamate Concentration in the Human Brain. *Neurochemical Research* **37,** 2554–2561. doi:10.1007/s11064-012-0848-4 (Nov. 1, 2012).

414. Mullins, P. G. Towards a Theory of Functional Magnetic Resonance Spectroscopy (fMRS): A Meta-Analysis and Discussion of Using MRS to Measure Changes in Neurotransmitters in Real Time. *Scandinavian Journal of Psychology* **59,** 91–103. doi:10.1111/sjop.12411. pmid: 29356002 (Feb. 2018).

415. Kauppinen, R. A., Pirttilä, T. R., Auriola, S. O. & Williams, S. R. Compartmentation of Cerebral Glutamate in Situ as Detected by 1H/13C n.m.r. *The Biochemical Journal* **298 (Pt 1),** 121–127. doi:10.1042/bj2980121. pmid: 7907470 (Pt 1 Feb. 15, 1994).

416. Stagg, C. J. *et al.* Local GABA Concentration Is Related to Network-Level Resting Functional Connectivity. *Elife* **3,** e01465 (2014).

417. Bachtiar, V., Near, J., Johansen-Berg, H. & Stagg, C. J. Modulation of GABA and Resting State Functional Connectivity by Transcranial Direct Current Stimulation. *eLife* **4,** e08789. doi:10.7554/eLife.08789 (Sept. 18, 2015).

418. Kapogiannis, D., Reiter, D. A., Willette, A. A. & Mattson, M. P. Posteromedial Cortex Glutamate and GABA Predict Intrinsic Functional Connectivity of the Default Mode Network. *NeuroImage* **64,** 112–119. doi:10.1016/j.neuroimage.2012.09.029 (Jan. 2013).

419. Levar, N., Van Doesum, T. J., Denys, D. & Van Wingen, G. A. Anterior Cingulate GABA and Glutamate Concentrations Are Associated with Resting-State Network Connectivity. *Scientific Reports* **9,** 2116. doi:10.1038/s41598-018-38078-1 (1 Feb. 14, 2019).

420. Chen, X. *et al.* Regional GABA Concentrations Modulate Inter-network Resting-state Functional Connectivity. *Cerebral Cortex* **29,** 1607–1618. doi:10.1093/cercor/bhy059 (Apr. 1, 2019).

421. Kreis, R. Quantitative Localized 1H MR Spectroscopy for Clinical Use. *Progress in Nuclear Magnetic Resonance Spectroscopy* **31,** 155–195. doi:10.1016/S0079-6565(97)00014-9 (Sept. 1, 1997).

422. Tal, A., Kirov, I. I., Grossman, R. I. & Gonen, O. The Role of Gray and White Matter Segmentation in Quantitative Proton MR Spectroscopic Imaging. *NMR in biomedicine* **25,** 1392–1400. doi:10.1002/nbm.2812. pmid: 22714729 (Dec. 2012).

423. Frahm, J. *et al.* Localized Proton NMR Spectroscopy in Different Regions of the Human Brain in Vivo. Relaxation Times and Concentrations of Cerebral Metabolites. *Magnetic Resonance in Medicine* **11,** 47–63. doi:10.1002/mrm.1910110105 (1989).

424. Christiansen, P., Toft, P., Larsson, H. B. W., Stubgaard, M. & Henriksen, O. The Concentration of N-acetyl Aspartate, Creatine + Phosphocreatine, and Choline in Different Parts of the Brain in Adulthood and Senium. *Magnetic Resonance Imaging* **11,** 799–806. doi:10.1016/0730-725X(93)90197-L (Jan. 1, 1993).

425. Tedeschi, G. *et al.* Brain Regional Distribution Pattern of Metabolite Signal Intensities in Young Adults by Proton Magnetic Resonance Spectroscopic Imaging. *Neurology* **45,** 1384–1391. doi:10.1212/wnl.45.7.1384. pmid: 7617201 (July 1995).

426. Hennig, J., Pfister, H., Ernst, T. & Ott, D. Direct Absolute Quantification of Metabolites in the Human Brain with in Vivo Localized Proton Spectroscopy. *NMR in Biomedicine* **5,** 193–199. doi:10.1002/nbm.1940050406 (1992).

427. Kreis, R., Ernst, T. & Ross, B. D. Absolute Quantitation of Water and Metabolites in the Human Brain. II. Metabolite Concentrations. *Journal of Magnetic Resonance, Series B* **102,** 9–19. doi:10.1006/jmrb.1993.1056 (Aug. 1, 1993).

428. Ala-Korpela, M. *et al.* Quantification of Metabolites from Single-Voxelin Vivo 1 H NMR Data of Normal Human Brain by Means of Time-Domain Data Analysis. *Magnetic Resonance Materials in Physics, Biology and Medicine* **3,** 129–136 (1995).

429. Soher, B. J., van Zijl, P. C. M., Duyn, J. H. & Barker, P. B. Quantitative Proton MR Spectroscopic Imaging of the Human Brain. *Magnetic Resonance in Medicine* **35,** 356–363. doi:10.1002/mrm.1910350313 (1996).

430. Angelie, E. *et al.* Regional Differences and Metabolic Changes in Normal Aging of the Human Brain: Proton MR Spectroscopic Imaging Study. *American Journal of Neuroradiology* **22,** 119–127. pmid: 11158897 (Jan. 1, 2001).

431. Eylers, V. V. *et al.* Detection of Normal Aging Effects on Human Brain Metabolite Concentrations and Microstructure with Whole-Brain MR Spectroscopic Imaging and Quantitative MR Imaging. *American Journal of Neuroradiology* **37,** 447–454. doi:10.3174/ajnr.A4557. pmid: 26564440 (Mar. 1, 2016).

432. Cleeland, C., Pipingas, A., Scholey, A. & White, D. Neurochemical Changes in the Aging Brain: A Systematic Review. *Neuroscience & Biobehavioral Reviews* **98,** 306–319. doi:10.1016/j.neubiorev.2019.01.003 (Mar. 2019).

433. Kalra, S. Magnetic Resonance Spectroscopy in ALS. *Frontiers in neurology* **10,** 482. pmid: 31133975 (2019).

434. Clarke, W. T., Stagg, C. J. & Jbabdi, S. *FSL-MRS: An End-to-End Spectroscopy Analysis Package* preprint (Neuroscience, June 18, 2020). doi:10.1101/2020.06.16.155291.

435. Near, J. *et al.* Preprocessing, Analysis and Quantification in Single-voxel Magnetic Resonance Spectroscopy: Experts' Consensus Recommendations. *NMR in Biomedicine.* doi:10.1002/nbm.4257 (Feb. 21, 2020).

436. Smith, S. M. Fast Robust Automated Brain Extraction. *Human brain mapping* **17,** 143–155 (2002).

437. Jenkinson, M. & Smith, S. A Global Optimisation Method for Robust Affine Registration of Brain Images. *Medical Image Analysis* **5,** 143–156. doi:10.1016/s1361-8415(01)00036-6. pmid: 11516708 (June 2001).

438. Jenkinson, M., Bannister, P., Brady, M. & Smith, S. Improved Optimization for the Robust and Accurate Linear Registration and Motion Correction of Brain Images. *NeuroImage* **17,** 825–841. doi:10.1016/s1053-8119(02)91132-8. pmid: 12377157 (Oct. 2002).

439. Zhang, Y., Brady, M. & Smith, S. Segmentation of Brain MR Images through a Hidden Markov Random Field Model and the Expectation-Maximization Algorithm. *IEEE transactions on medical imaging* **20,** 45–57. doi:10.1109/42.906424. pmid: 11293691 (Jan. 2001).

440. Glasser, M. F. *et al.* A Multi-Modal Parcellation of Human Cerebral Cortex. *Nature* **536,** 171–178. doi:10.1038/nature18933. pmid: 27437579 (7615 Aug. 2016).

441. Horn, A. HCP-MMP1.0 Projected on MNI2009a GM (Volumetric) in NIfTI Format. doi:10.6084/m9.figshare.3501911.v5 (Aug. 2016).

442. Nickerson, L. D., Smith, S. M., Öngür, D. & Beckmann, C. F. Using Dual Regression to Investigate Network Shape and Amplitude in Functional Connectivity Analyses. *Frontiers in Neuroscience* **11.** doi:10.3389/fnins.2017.00115 (Mar. 13, 2017).

443. Klein, A. *et al.* Evaluation of 14 Nonlinear Deformation Algorithms Applied to Human Brain MRI Registration. *NeuroImage* **46,** 786–802. doi:10.1016/j.neuroimage.2008.12.037. pmid: 19195496 (July 1, 2009).

444. Kreis, R. The Trouble with Quality Filtering Based on Relative Cramér-Rao Lower Bounds: The Trouble with Quality Filtering Based on Relative CRLB. *Magnetic Resonance in Medicine* **75,** 15–18. doi:10.1002/mrm.25568 (Jan. 2016).

445. Stagg, C. J. *et al.* Relationship between Physiological Measures of Excitability and Levels of Glutamate and GABA in the Human Motor Cortex. *The Journal of Physiology* **589,** 5845–5855. doi:10.1113/jphysiol.2011.216978 (2011).

446. Capper-Loup, C., Rebell, D. & Kaelin-Lang, A. Hemispheric Lateralization of the Corticostriatal Glutamatergic System in the Rat. *Journal of Neural Transmission* **116,** 1053–1057. doi:10.1007/s00702-009-0265-2 (Sept. 1, 2009).

447. Karlebach, G. & Francks, C. Lateralization of Gene Expression in Human Language Cortex. *Cortex* **67,** 30–36. doi:10.1016/j.cortex.2015.03.003 (June 1, 2015).

448. Ocklenburg, S. *et al.* Variation in the NMDA Receptor 2B Subunit Gene GRIN2B Is Associated with Differential Language Lateralization. *Behavioural Brain Research* **225,** 284–289. doi:10.1016/j.bbr.2011.07.042 (Nov. 20, 2011).

449. Kaiser, L. G., Schuff, N., Cashdollar, N. & Weiner, M. W. Age-Related Glutamate and Glutamine Concentration Changes in Normal Human Brain: 1H MR Spectroscopy Study at 4 T. *Neurobiology of Aging* **26,** 665–672. doi:10.1016/j.neurobiolaging.2004.07.001 (May 1, 2005).

450. Hädel, S., Wirth, C., Rapp, M., Gallinat, J. & Schubert, F. Effects of Age and Sex on the Concentrations of Glutamate and Glutamine in the Human Brain. *Journal of Magnetic Resonance Imaging* **38,** 1480–1487. doi:10.1002/jmri.24123 (2013).

451. Marjańska, M. *et al.* Region-Specific Aging of the Human Brain as Evidenced by Neurochemical Profiles Measured Noninvasively in the Posterior Cingulate Cortex and the Occipital Lobe Using 1H Magnetic Resonance Spectroscopy at 7 T. *Neuroscience* **354,** 168–177. doi:10.1016/j.neuroscience.2017.04.035 (June 23, 2017).

452. Suri, S. *et al.* Effect of Age and the APOE Gene on Metabolite Concentrations in the Posterior Cingulate Cortex. *NeuroImage* **152,** 509–516. doi:10.1016/j.neuroimage.2017.03.031 (May 15, 2017).

453. Zahr, N. M. *et al.* In Vivo Glutamate Measured with Magnetic Resonance Spectroscopy: Behavioral Correlates in Aging. *Neurobiology of Aging* **34,** 1265–1276. doi:10.1016/j.neurobiolaging.2012.09.014 (Apr. 1, 2013).

454. Sailasuta, N., Ernst, T. & Chang, L. Regional Variations and the Effects of Age and Gender on Glutamate Concentrations in the Human Brain. *Magnetic Resonance Imaging* **26,** 667–675. doi:10.1016/j.mri.2007.06.007 (June 1, 2008).

455. Enzi, B. *et al.* Glutamate Modulates Resting State Activity in the Perigenual Anterior Cingulate Cortex – A Combined fMRI–MRS Study. *Neuroscience* **227,** 102–109. doi:10.1016/j.neuroscience.2012.09.039 (Dec. 27, 2012).

456. Falkenberg, L. E., Westerhausen, R., Specht, K. & Hugdahl, K. Resting-State Glutamate Level in the Anterior Cingulate Predicts Blood-Oxygen Level-Dependent Response to Cognitive Control. *Proceedings of the National Academy of Sciences* **109,** 5069–5073. doi:10.1073/pnas.1115628109. pmid: 22411802 (Mar. 27, 2012).

457. Wu, T. *et al.* Aging Influence on Functional Connectivity of the Motor Network in the Resting State. *Neuroscience Letters* **422,** 164–168. doi:10.1016/j.neulet.2007.06.011 (July 18, 2007).

458. Michely, J. *et al.* Network Connectivity of Motor Control in the Ageing Brain. *NeuroImage: Clinical* **18,** 443–455. doi:10.1016/j.nicl.2018.02.001 (Jan. 1, 2018).

459. Weinberg, B. D., Kuruva, M., Shim, H. & Mullins, M. E. Clinical Applications of Magnetic Resonance Spectroscopy (MRS) in of Brain Tumors: From Diagnosis to Treatment. *Radiologic clinics of North America* **59,** 349–362. doi:10.1016/j.rcl.2021.01.004. pmid: 33926682 (May 2021).

460. Giroud, M. *et al.* Reduced Brain N-acetyl-aspartate in Frontal Lobes Suggests Neuronal Loss in Patients with Amyotrophic Lateral Sclerosis. *Neurological Research* **18,** 241–243. doi:10.1080/01616412.1996.11740412. pmid: 8837060 (June 1996).

461. Gredal, O. *et al.* Quantification of Brain Metabolites in Amyotrophic Lateral Sclerosis by Localized Proton Magnetic Resonance Spectroscopy. *Neurology* **48,** 878–881. doi:10.1212/wnl.48.4.878. pmid: 9109871 (Apr. 1997).

462. Jones, A. P. *et al.* Preliminary Results of Proton Magnetic Resonance Spectroscopy in Motor Neurone Disease (Amytrophic Lateral Sclerosis). *Journal of the Neurological Sciences* **129 Suppl,** 85–89. doi:10.1016/0022-510x(95)00072-a. pmid: 7595630 (May 1995).

463. Pioro, E. P., Antel, J. P., Cashman, N. R. & Arnold, D. L. Detection of Cortical Neuron Loss in Motor Neuron Disease by Proton Magnetic Resonance Spectroscopic Imaging in Vivo. *Neurology* **44,** 1933–1938. doi:10.1212/wnl.44.10.1933. pmid: 7936250 (Oct. 1994).

464. Simmons, M. L., Frondoza, C. G. & Coyle, J. T. Immunocytochemical Localization of N-acetyl-aspartate with Monoclonal Antibodies. *Neuroscience* **45,** 37–45. doi:10.1016/0306-4522(91)90101-s. pmid: 1754068 (1991).

465. Srivastava, O. *et al.* Cerebral Degeneration in Amyotrophic Lateral Sclerosis: A Prospective Multicenter Magnetic Resonance Spectroscopy Study. *Neurology. Clinical Practice* **9,** 400–407. doi:10.1212/CPJ.0000000000000674. pmid: 31750025 (Oct. 2019).

466. Ta, D. *et al.* Progressive Neurochemical Abnormalities in Cognitive and Motor Subgroups of Amyotrophic Lateral Sclerosis: A Prospective Multicenter Study. *Neurology* **97,** e803–e813. doi:10.1212/WNL.0000000000012367. pmid: 34426551 (Aug. 24, 2021).

467. Suhy, J. *et al.* Early Detection and Longitudinal Changes in Amyotrophic Lateral Sclerosis by (1)H MRSI. *Neurology* **58,** 773–779. doi:10.1212/wnl.58.5.773. pmid: 11889242 (Mar. 12, 2002).

468. Verma, G. *et al.* Whole-Brain Analysis of Amyotrophic Lateral Sclerosis by Using Echo-Planar Spectroscopic Imaging. *Radiology* **267,** 851–857. doi:10.1148/radiol.13121148. pmid: 23360740 (June 2013).

469. Yin, H. *et al.* Combined MR Spectroscopic Imaging and Diffusion Tensor MRI Visualizes Corticospinal Tract Degeneration in Amyotrophic Lateral Sclerosis. *Journal of Neurology* **251,** 1249–1254. doi:10.1007/s00415-004-0526-9 (Oct. 1, 2004).

470. Cervo, A. *et al.* The Combined Use of Conventional MRI and MR Spectroscopic Imaging Increases the Diagnostic Accuracy in Amyotrophic Lateral Sclerosis. *European Journal of Radiology* **84,** 151–157. doi:10.1016/j.ejrad.2014.10.019. pmid: 25466774 (Jan. 2015).

471. Stagg, C. J. *et al.* Whole-Brain Magnetic Resonance Spectroscopic Imaging Measures Are Related to Disability in ALS. *Neurology* **80,** 610–615. doi:10.1212/WNL.0b013e318281ccec. pmid: 23325907 (Feb. 12, 2013).

472. Kalra, S., Tai, P., Genge, A. & Arnold, D. L. Rapid Improvement in Cortical Neuronal Integrity in Amyotrophic Lateral Sclerosis Detected by Proton Magnetic Resonance Spectroscopic Imaging. *Journal of Neurology* **253,** 1060–1063. doi:10.1007/s00415-006-0162-7. pmid: 16609809 (Aug. 2006).

473. Andronesi, O. C. *et al.* Imaging Neurochemistry and Brain Structure Tracks Clinical Decline and Mechanisms of ALS in Patients. *Frontiers in Neurology* **11,** 590573. doi:10.3389/fneur.2020.590573. pmid: 33343494 (2020).

474. Vucic, S., Pavey, N., Haidar, M., Turner, B. J. & Kiernan, M. C. Cortical Hyperexcitability: Diagnostic and Pathogenic Biomarker of ALS. *Neuroscience Letters* **759,** 136039. doi:10.1016/j.neulet.2021.136039. pmid: 34118310 (June 10, 2021).

475. Carew, J. *et al.* Presymptomatic Spinal Cord Neurometabolic Findings in SOD1-positive People at Risk for Familial ALS. *Neurology* **77,** 1370–1375. doi:10.1212/WNL.0b013e318231526a. pmid: 21940617 (Oct. 4, 2011).

476. Wismans, C. *In Vivo Imaging of Brain Metabolism in Asymptomatic C9orf72 Repeat Expansion Carriers* Sept. 2016.

477. Pollard, T. J., Johnson, A. E. W., Raffa, J. D. & Mark, R. G. Tableone: An Open Source Python Package for Producing Summary Statistics for Research Papers. *JAMIA open* **1,** 26–31. doi:10.1093/jamiaopen/ooy012. pmid: 31984317 (July 2018).

478. Querin, G. *et al.* Presymptomatic Spinal Cord Pathology in C9orf72 Mutation Carriers: A Longitudinal Neuroimaging Study. *Annals of Neurology* **86,** 158–167. doi:10.1002/ana.25520 (2019).

479. Proudfoot, M., Bede, P. & Turner, M. R. Imaging Cerebral Activity in Amyotrophic Lateral Sclerosis. *Frontiers in Neurology* **9** (2019).

480. Steel, A. *Examining Functional Plasticity in the Human Brain* (University of Oxford / University of Oxford, 2019).

481. Murphy, N. A. *et al.* Age-Related Penetrance of the C9orf72 Repeat Expansion. *Scientific Reports* **7,** 2116. doi:10.1038/s41598-017-02364-1 (1 May 18, 2017).

482. Byrne, S. *et al.* Cognitive and Clinical Characteristics of Patients with Amyotrophic Lateral Sclerosis Carrying a C9orf72 Repeat Expansion: A Population-Based Cohort Study. *The Lancet Neurology* **11,** 232–240. doi:10.1016/S1474-4422(12)70014-5 (Mar. 1, 2012).

483. Cooper-Knock, J., Shaw, P. J. & Kirby, J. The Widening Spectrum of C9ORF72-related Disease; Genotype/Phenotype Correlations and Potential Modifiers of Clinical Phenotype. *Acta Neuropathologica* **127,** 333–345. doi:10.1007/s00401-014-1251-9 (Mar. 1, 2014).

484. Bzdok, D., Varoquaux, G. & Thirion, B. Neuroimaging Research: From Null-Hypothesis Falsification to Out-of-Sample Generalization. *Educational and Psychological Measurement* **77,** 868–880. doi:10.1177/0013164416667982 (Oct. 1, 2017).

485. Douaud, G., Filippini, N., Knight, S., Talbot, K. & Turner, M. R. Integration of Structural and Functional Magnetic Resonance Imaging in Amyotrophic Lateral Sclerosis. *Brain* **134,** 3470–3479. pmid: 22075069 (2011).

486. Geevasinga, N. *et al.* Brain Functional Connectome Abnormalities in Amyotrophic Lateral Sclerosis Are Associated with Disability and Cortical Hyperexcitability. *European Journal of Neurology* **24,** 1507–1517. doi:10.1111/ene.13461. pmid: 28926154 (Dec. 2017).

487. Bueno, A. P. A. *et al.* Structural and Functional Papez Circuit Integrity in Amyotrophic Lateral Sclerosis. *Brain Imaging and Behavior* **12,** 1622–1630. doi:10.1007/s11682-018-9825-0 (Dec. 1, 2018).

488. Bharti, K. *et al.* Involvement of the Dentate Nucleus in the Pathophysiology of Amyotrophic Lateral Sclerosis: A Multi-Center and Multi-Modal Neuroimaging Study. *NeuroImage. Clinical* **28,** 102385. doi:10.1016/j.nicl.2020.102385. pmid: 32871387 (Aug. 16, 2020).

489. Cheng, L. *et al.* Structural and Functional Underpinnings of Precentral Abnormalities in Amyotrophic Lateral Sclerosis. *European Journal of Neurology.* doi:10.1111/ene.14717. pmid: 33404153 (Jan. 6, 2021).

490. Van der Burgh, H. K. *et al.* Multimodal Longitudinal Study of Structural Brain Involvement in Amyotrophic Lateral Sclerosis. *Neurology* **94,** e2592–e2604. doi:10.1212/WNL.0000000000009498. pmid: 32414878 (June 16, 2020).

491. Borsodi, F. *et al.* Multimodal Assessment of White Matter Tracts in Amyotrophic Lateral Sclerosis. *PloS One* **12,** e0178371. doi:10.1371/journal.pone.0178371. pmid: 28575122 (2017).

492. Broad, R. J. *et al.* Neurite Orientation and Dispersion Density Imaging (NODDI) Detects Cortical and Corticospinal Tract Degeneration in ALS. *Journal of Neurology, Neurosurgery, and Psychiatry* **90,** 404–411. doi:10.1136/jnnp-2018-318830. pmid: 30361295 (Apr. 2019).

493. Foerster, B. R. *et al.* Multimodal MRI as a Diagnostic Biomarker for Amyotrophic Lateral Sclerosis. *Annals of Clinical and Translational Neurology* **1,** 107–114. doi:10.1002/acn3.30. pmid: 25356389 (Feb. 2014).

494. Bede, P., Iyer, P. M., Finegan, E., Omer, T. & Hardiman, O. Virtual Brain Biopsies in Amyotrophic Lateral Sclerosis: Diagnostic Classification Based on in Vivo Pathological Patterns. *NeuroImage. Clinical* **15,** 653–658. doi:10.1016/j.nicl.2017.06.010. pmid: 28664036 (2017).

495. Dai, Z. *et al.* Amide Signal Intensities May Be Reduced in the Motor Cortex and the Corticospinal Tract of ALS Patients. *European Radiology* **31,** 1401–1409. doi:10.1007/s00330-020-07243-4. pmid: 32909054 (Mar. 2021).

496. Kocar, T. D., Behler, A., Ludolph, A. C., Müller, H.-P. & Kassubek, J. Multiparametric Microstructural MRI and Machine Learning Classification Yields High Diagnostic Accuracy in Amyotrophic Lateral Sclerosis: Proof of Concept. *Frontiers in Neurology* **12,** 745475. doi:10.3389/fneur.2021.745475. pmid: 34867726 (2021).

497. Thome, J., Steinbach, R., Grosskreutz, J., Durstewitz, D. & Koppe, G. Classification of Amyotrophic Lateral Sclerosis by Brain Volume, Connectivity, and Network Dynamics. *Human Brain Mapping* **43,** 681–699. doi:10.1002/hbm.25679. pmid: 34655259 (Feb. 1, 2022).

498. Schuster, C., Hardiman, O. & Bede, P. Survival Prediction in Amyotrophic Lateral Sclerosis Based on MRI Measures and Clinical Characteristics. *BMC neurology* **17,** 73. doi:10.1186/s12883-017-0854-x. pmid: 28412941 (Apr. 17, 2017).

499. Agosta, F. *et al.* Survival Prediction Models in Motor Neuron Disease. *European Journal of Neurology* **26,** 1143–1152. doi:10.1111/ene.13957. pmid: 30920076 (Sept. 2019).

500. Johannesen, S. *et al.* Modeling and Bioinformatics Identify Responders to G-CSF in Patients With Amyotrophic Lateral Sclerosis. *Frontiers in Neurology* **12** (2021).

501. Guyon, I. & Elisseeff, A. An Introduction to Variable and Feature Selection. *Journal of machine learning research* **3,** 1157–1182 (Mar 2003).

502. Jollans, L. *et al.* Quantifying Performance of Machine Learning Methods for Neuroimaging Data. *NeuroImage* **199,** 351–365. doi:10.1016/j.neuroimage.2019.05.082. pmid: 31173905 (Oct. 1, 2019).

503. Pedregosa, F. *et al.* Scikit-Learn: Machine Learning in Python. *Journal of Machine Learning Research* **12,** 2825–2830 (2011).

504. Fan, R.-E., Chang, K.-W., Hsieh, C.-J., Wang, X.-R. & Lin, C.-J. LIBLINEAR: A Library for Large Linear Classification. *the Journal of machine Learning research* **9,** 1871–1874 (2008).

505. Friedman, J., Tibshirani, R. & Hastie, T. *The Elements of Statistical Learning: Data Mining, Inference, and Prediction* (Springer-Verlag New York New York, 2009).

506. Spring, S., Food, Administration, D., *et al.* Bethesda (MD): National Institutes of Health (US). FDA-NIH Biomarker Working Group. BEST (Biomarkers, EndpointS, and Other Tools) Resource. BEST (Biomarkers, EndpointS, and Other Tools) Resource [Internet]. BEST (Biomarkers, EndpointS, and Other Tools) Resource. *Food and Drug Administration (US)* (2016).

507. Abeysuriya, R. G. *et al.* A Biophysical Model of Dynamic Balancing of Excitation and Inhibition in Fast Oscillatory Large-Scale Networks. *PLOS Computational Biology* **14,** e1006007. doi:10.1371/journal.pcbi.1006007 (Feb. 23, 2018).

508. Duque, J., Greenhouse, I., Labruna, L. & Ivry, R. B. Physiological Markers of Motor Inhibition during Human Behavior. *Trends in Neurosciences* **40,** 219–236. doi:10.1016/j.tins.2017.02.006. pmid: 28341235 (Apr. 1, 2017).

509. Greenhouse, I., Sias, A., Labruna, L. & Ivry, R. B. Nonspecific Inhibition of the Motor System during Response Preparation. *Journal of Neuroscience* **35,** 10675–10684. doi:10.1523/JNEUROSCI.1436-15.2015. pmid: 26224853 (July 29, 2015).

510. Burle, B., Vidal, F., Tandonnet, C. & Hasbroucq, T. Physiological Evidence for Response Inhibition in Choice Reaction Time Tasks. *Brain and Cognition. Neurocognitive Mechanisms of Performance Monitoring and Inhibitory Control* **56,** 153–164. doi:10.1016/j.bandc.2004.06.004 (Nov. 1, 2004).

511. Bagiella, E., Bhatt, D. L. & Gaudino, M. The Consequences of the COVID-19 Pandemic on Non-COVID-19 Clinical Trials. *Journal of the American College of Cardiology* **76,** 342–345. doi:10.1016/j.jacc.2020.05.041 (July 21, 2020).

512. Jack, C. R. *et al.* Tracking Pathophysiological Processes in Alzheimer's Disease: An Updated Hypothetical Model of Dynamic Biomarkers. *The Lancet. Neurology* **12,** 207–216. doi:10.1016/S1474-4422(12)70291-0. pmid: 23332364 (Feb. 2013).

513. Kubera, K. M., Schmitgen, M. M., Hirjak, D., Wolf, R. C. & Orth, M. Cortical Neurodevelopment in Pre-Manifest Huntington's Disease. *NeuroImage : Clinical* **23,** 101913. doi:10.1016/j.nicl.2019.101913. pmid: 31491822 (June 29, 2019).

514. Turner, M. R. The Early Biomarker Challenge in Neurodegenerative Disorders. *Journal of Neurology, Neurosurgery, and Psychiatry* **90,** 1190–1191. doi:10.1136/jnnp-2019-321145. pmid: 31243045 (Nov. 2019).

515. Nakken, O., Meyer, H. E., Stigum, H. & Holmøy, T. High BMI Is Associated with Low ALS Risk: A Population-Based Study. *Neurology* **93,** e424–e432. doi:10.1212/WNL.0000000000007861. pmid: 31243073 (July 30, 2019).

516. Benatar, M. *et al.* Preventing Amyotrophic Lateral Sclerosis: Insights from Pre-Symptomatic Neurodegenerative Diseases. *Brain* **145,** 27–44. doi:10.1093/brain/awab404. pmid: 34677606 (Jan. 1, 2022).

517. Day, J. W. *et al.* Onasemnogene Abeparvovec Gene Therapy for Symptomatic Infantile-Onset Spinal Muscular Atrophy in Patients with Two Copies of SMN2 (STR1VE): An Open-Label, Single-Arm, Multicentre, Phase 3 Trial. *The Lancet. Neurology* **20,** 284–293. doi:10.1016/S1474-4422(21)00001-6. pmid: 33743238 (Apr. 2021).

518. Biogen. *A Phase 1 Multiple-Ascending-Dose Study to Assess the Safety, Tolerability, and Pharmacokinetics of BIIB078 Administered Intrathecally to Adults With C9ORF72-Associated Amyotrophic Lateral Sclerosis* Clinical trial registration NCT03626012 (clinicaltrials.gov, Jan. 13, 2022).

519. *Biogen and Ionis Announce Topline Phase 1 Study Results of Investigational Drug in C9orf72 Amyotrophic Lateral Sclerosis | Biogen* https://investors.biogen.com/news-releases/news-release-details/biogen-and-ionis-announce-topline-phase-1-study-results (2022).

520. Biogen. *A Phase 3 Randomized, Placebo-Controlled Trial With a Longitudinal Natural History Run-In and Open-Label Extension to Evaluate BIIB067 Initiated in Clinically Presymptomatic Adults With a Confirmed Superoxide Dismutase 1 Mutation* Clinical trial registration NCT04856982 (clinicaltrials.gov, July 20, 2022).

521. Oskarsson, B., Mauricio, E. A., Shah, J. S., Li, Z. & Rogawski, M. A. Cortical Excitability Threshold Can Be Increased by the AMPA Blocker Perampanel in Amyotrophic Lateral Sclerosis. *Muscle & Nerve* **64,** 215–219. doi:10.1002/mus.27328. pmid: 34008857 (Aug. 2021).

522. Polanía, R., Nitsche, M. A. & Ruff, C. C. Studying and Modifying Brain Function with Non-Invasive Brain Stimulation. *Nature Neuroscience* **21,** 174–187. doi:10.1038/s41593-017-0054-4 (2 Feb. 2018).